DOT/FAA/TC-15/25

Federal Aviation Administration
William J. Hughes Technical Center
Aviation Research Division
Atlantic City International Airport
New Jersey 08405

Crushing Behavior of Laminated Composite Structural Elements: Experiment and LS-DYNA Simulation

December 2016

Final Report

This document is available to the U.S. public through the National Technical Information Services (NTIS), Springfield, Virginia 22161.

This document is also available from the Federal Aviation Administration William J. Hughes Technical Center at actlibrary.tc.faa.gov.

U.S. Department of Transportation
Federal Aviation Administration

NOTICE

Technical Report Documentation Page

1. Report No.
DOT/FAA/TC-**15/25**

2. Government Accession No.

3. Recipient's Catalog No.

4. Title and Subtitle
CRUSHING BEHAVIOR OF LAMINATED COMPOSITE STRUCTURAL ELEMENTS: EXPERIMENT AND LS-DYNA SIMULATION

5. Report Date
December 2016

6. Performing Organization Code

7. Author(s)
Bonnie Wade and Paolo Feraboli

8. Performing Organization Report No.

9. Performing Organization Name and Address
Automobili Lamborghini Advanced Composite Structures Laboratory
Department of Aeronautics and Astronautics
University of Washington
Seattle, WA 98195-2400

10. Work Unit No. (TRAIS)

11. Contract or Grant No.

12. Sponsoring Agency Name and Address
U.S. Department of Transportation
Federal Aviation Administration
Office of Aviation Research
Washington, DC 20591

13. Type of Report and Period Covered

14. Sponsoring Agency Code
AIR-100

15. Supplementary Notes
The Federal Aviation Administration William J. Hughes Technical Center Aviation Research Division COR was Allan Abramowitz.

16. Abstract

The energy absorbing behavior of a composite structure is not easily predicted because of the great complexity of the failure mechanisms that occur within the material. Challenges arise both in the experimental characterization and numerical modeling of the material/structure combination. This report addresses both the experimental characterization of composite energy absorption mechanisms and the numerical simulation of composite materials undergoing crushing.

Quasi-static crush tests of several carbon fiber/epoxy prepreg fabric structural elements with different shapes representative of those that can be implemented into an aircraft subfloor crashworthy structure are performed to measure the specific energy absorption (SEA) of the material and shape combination. Experimental results show a direct correlation between curvature of the structural element cross section and its energy absorption, where a higher degree of curvature in the cross section suppresses delamination failure and promotes fragmentation failure, thereby resulting in greater energy absorption. A relationship between the crush element geometry and SEA has been developed, which allows for a reduced number of element-level crush tests to characterize the energy absorption capability of a particular composite material system.

A finite element model for each element shape is generated using the commercially available explicit software LS-DYNA and the built-in progressive failure material model MAT54. This model has been extensively used by the aircraft industry to simulate composite materials undergoing progressive damage under crash conditions as well as other foreign object impact scenarios. The MAT54 softening reduction factor (SOFT) is the key modeling parameter, which requires a different value for each shape while using the experimental crush data for the calibration. By adjusting this parameter, good agreement between simulation and experiment is achieved. The modeling approach cannot be considered to be truly predictive because the element-level experiments must be used for model calibration and not validation within the certification strategy by analysis supported by test evidence.

Finally, the source code of the MAT54 material model is modified to improve the model for crush simulation. The modified model offers better simulation of the material in single-element studies, but not significant benefit to the crush simulations. The modeling strategy developed using the built-in MAT54 while adjusting the SOFT, which itself is directly dependent on the experimental energy absorption, is successful without further modifications to the material model.

17. Key Words
Crashworthiness, Energy absorption, Finite element modeling, Impact, Damage modeling, Carbon fiber

18. Distribution Statement
This document is available to the U.S. public through the National Technical Information Service (NTIS), Springfield, Virginia 22161. This document is also available from the Federal Aviation Administration William J. Hughes Technical Center at actlibrary.tc.faa.gov.

19. Security Classif. (of this report)
Unclassified

20. Security Classif. (of this page)
Unclassified

21. No. of Pages
202

22. Price

ACKNOWLEDGEMENTS

The research was performed at the Automobili Lamborghini Advanced Composite Structures Laboratory at the University of Washington in Seattle, Washington.

Funding for this research was provided by the Federal Aviation Administration. Matching funds were provided by The Boeing Company and additional funds were provided by Automobili Lamborghini S.p.A.

The authors would like to thank Dr. Mostafa Rassaian and his Advanced Analysis team: Alan Byar, Michael Rucki, and Mark Higgins. Dr. Rassaian was instrumental in establishing the LS-DYNA modeling capabilities and strengthening the ongoing projects concerned with crash simulation.

The authors would also like to thank Dr. Xinran Xiao (previously of General Motors) for his guidance with the fundamentals of explicit finite element modeling, as well as the active members of the Crashworthiness Working Group of the CMH-17 (Composite Materials Handbook, formerly MIL-HDBK-17); Paul Robertson and Aeronautical Testing Services of Arlington, Washington, for providing the corrugated mold design and manufacturing; and Andrea Dorr and Leslie Cooke (Toray Composites) for donating the prepreg materials and providing the tubular mandrel mold design and manufacturing.

TABLE OF CONTENTS

Page

LIST OF FIGURES

LIST OF TABLES

LIST OF ACRONYMS

AGATE	Advanced General Aviation Transport Experiments
BBA	Building block approach
CDM	Continuum damage mechanics
CFC	Channel frequency class
CFRP	Carbon fiber-reinforced plastic (or polymers)
CMH-17	Composite Materials Handbook, formerly MIL-HDBK-17
COV	Coefficient of variation
CRASURV	Commercial Aircraft Design for Crash Survivability
DLR	German Aerospace Center
EA	Energy absorbed (the total area under the load-displacement curve)
EFS	Effective failure strain
FE	Finite element
FEA	Finite element analysis
INN	Invariant node numbering
LaRC	Langley Research Center
LP	Load-penetration (curve for LS-DYNA contact formulation)
NASA	National Aeronautics and Space Administration
NEIPS	Number of extra history variables
NDGRAD	Number of degradation iterations following failure for STROPT = 2, 3; determines the slope of the linear decay
NLR	Dutch National Aerospace Laboratory (Netherlands)
PCWL	Piecewise linear
PDM	Progressive damage model
PW	Plain-weave
RR	Round robin
SEA	Specific energy absorption (the energy absorbed per unit mass of crushed structure)
SIGLIM	Percentage of maximum stress allowed during plastic deformation for STROPT = 3
SOFT	Softening reduction factor
STROPT	Specifies which stress degradation option to use
UD	Unidirectional
UMAT	(User-defined) material model
WWFE	World Wide Failure Exercise

EXECUTIVE SUMMARY

The behavior of composite materials under crush conditions poses particular challenges for engineering analysis because it requires modeling beyond the elastic region and into failure initiation and propagation. Crushing is the result of a combination of several failure mechanisms, such as matrix cracking and splitting, delamination, fiber tensile fracture and compressive kinking, frond formation and bending, and friction. With current computational power, it is not possible to capture each of the failure mechanisms; therefore, simplifications are required. Macro-mechanical models based on lamina-level properties have been used, notwithstanding the well-accepted limitations for composite failure criteria in predicting the onset of damage within laminate codes. This report investigates the ability of a commercially available, mainstream industry analytical tool to predictively simulate composites under crash conditions. This research is part of the multiyear project, "Standardization of Analytical and Experimental Methods for Crashworthiness Energy Absorption of Composite Materials."

The first part of the report contains the results of element-level experiments, consisting of the quasi-static crushing of corrugated specimens manufactured with carbon fiber/epoxy prepreg tape. The tests were performed to measure the specific energy absorption and validate the numeric simulation. The corrugated shape is representative of subfloor crashworthy structures, as used in general aviation, large commercial transport, and rotorcraft. The corrugated geometry is also appealing from a test perspective because it is self-supporting (i.e., it does not require a stabilizing fixture), it does not feature hoop tensile stress phenomena typical of tubular structures, and it is easy to manufacture.

The second part of the report includes a detailed explanation of the modeling approach used to simulate the crush test. The finite element model was generated using the commercially available explicit software, LS-DYNA. The built-in progressive failure material model MAT54 was successfully used to obtain excellent agreement with the experiment. The material model MAT54 has been used extensively by the aircraft industry to simulate composite materials undergoing progressive damage under crash conditions as well as other foreign object impact scenarios.

The modeling strategy's strengths and shortcomings were identified through a sensitivity study. Several modeling parameters, which have no physical meaning or cannot otherwise be measured experimentally, have a strong influence on the success of the simulation. For example, the softening reduction factor (crush front parameter) is the single most influential parameter for determining the success of the simulation. These parameters need to be calibrated by trial and error to match the experimental results, and, therefore, cannot be determined a priori. From this investigation, it becomes evident that the modeling approach cannot be considered to be truly predictive. The implications are that the element-level tests (i.e., the crushing of a single-element absorber, such as the corrugated specimen) should be used for model calibration, and not validation, within the certification strategy by analysis supported by test evidence. Once the model is calibrated at this level, the analysis model can be used to predict the crash response of subcomponents, components, and full-scale test ar ticles.

1. INTRODUCTION

The increasing use of advanced carbon fiber-reinforced plastic (or polymers) (CFRP) composites in the primary structure of modern aircraft presents certain complications for the designer dealing with occupant safety and crashworthiness. The energy absorption provided by a composite structure is not easily predicted because of the complexity of the crush failure mechanisms that occur within the material. To be a feasible design choice, advanced composite vehicle structures must be able to provide a similar level of crash safety as their metallic predecessors, such that the crash certification requirements are satisfied.

The basis of crash certification tests is to verify that the five necessary conditions for survival during a vehicle collision are preserved. These conditions are: 1) maintaining sufficient occupant space, 2) providing adequate occupant restraint, 3) limiting acceleration and loads experienced by the occupants, 4) providing protection from the release of items of mass, and 5) allowing for a safe post-crash egress from the vehicle [1]. In general, the total structural deformation in a crash will determine the satisfaction of these conditions; however, individual structural subcomponents that are specifically designed to absorb crash energy can provide a great increase in structural crashworthiness and survivability. For this reason, structural energy absorbers can be found in all modern vehicles—in the form of collapsible tubular rails in the front end of passenger cars [2–5] and in the form of collapsible floor stanchions and beams in aircraft subfloor and cargo structures [6–8] (see figure 1).

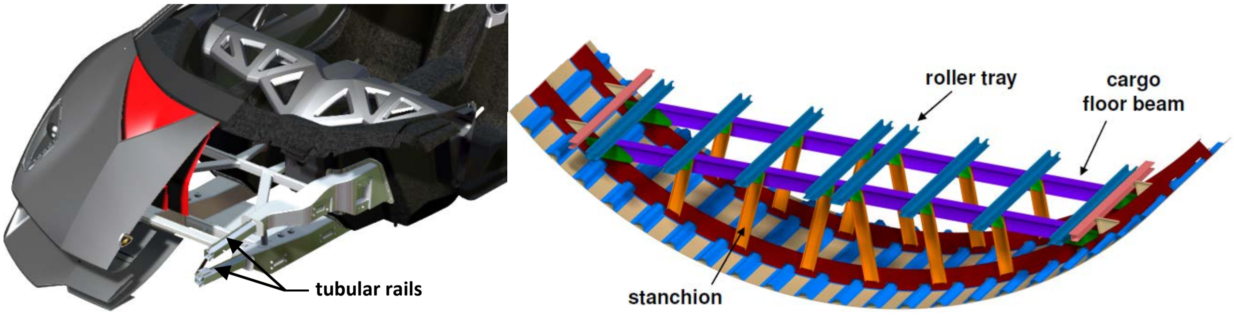

(a) (b)

Figure 1. Crash structures in (a) the front end of a passenger car and (b) in the subfloor of a typical part 25 twin aisle aircraft

Structural crash elements have traditionally been made from aluminum, which absorbs energy through controlled collapse by folding and hinging, involving extensive local plastic deformation. The fold geometry and energy absorption of metallic elements depend on its geometry and can be predicted with accuracy using finite element analysis (FEA) numerical methods. However, composite structures fail in a crash through a complex combination of fracture mechanisms, including fiber fracture, matrix cracking, fiber-matrix debonding, and interlaminar damage (delamination), all of which can occur alone or together [9]. The combination of several brittle and plastic failure modes makes the design of composite energy-absorbing crash structures difficult, and the energy-absorbing behavior of composites cannot be easily predicted. Thus, extensive substructure testing is usually required in the design of crashworthy composite structures to verify that a proposed configuration will perform as intended.

While experimental crash testing remains an integral part of safety and certification, both the aerospace and automotive industries increasingly rely on the capability of FEA codes to preemptively simulate structural tests to identify problems early in the design process, optimize the vehicle, and avoid excessive crash testing of costly prototype vehicles. Following a successful certification crash test, the validated FEA model is used to simulate a variety of other crash scenarios by varying parameters, such as impact angle, velocity, impactor, etc. The FEA models have been proven to simulate the elastic and plastic deformation of metallic structures very well, and simulation is currently an indispensable part of the design and certification process, while limited experimental prototype testing is conducted to validate these simulated models [10–11].

As metallic structures are replaced by composite structures, there is a need for a better understanding of the energy-absorbing mechanisms that occur during composite crush failure. Currently, there is no standardized test method to characterize the energy-absorbing capability of a composite material system because its energy-absorbing mechanisms are not well understood. In addition, there is a need for increased development of predictive tools to simulate the energy absorption capability of composite materials in FEA models. These issues pose a limitation on the wider introduction of composites in primary crashworthy structures and impede the optimum design, safety, and performance of composite structures. This report addresses both the experimental energy absorption characterization of composite materials and the numerical simulation of the energy-absorbing capability of composites undergoing crushing. The goal of this research is to: 1) develop and demonstrate a procedure that defines a set of experimental crush results that characterize the energy absorption capability of a composite material system; 2) use the experimental results in the development and refinement of a composite material model for crush simulation; 3) explore modifying the material model to improve its use in crush modeling; and 4) provide experimental and modeling guidelines for composite structures under crush at the element-level in the scope of the building block approach (BBA). This research is part of the multiyear project, “Standardization of Analytical and Experimental Methods for Crashworthiness Energy Absorption of Composite Materials.”

2. LITERATURE REVIEW

2.1 EXPERIMENTAL CHARACTERIZATION OF COMPOSITE ENERGY ABSORPTION

Research began in the 1980s to understand the energy-absorbing mechanisms of composite material systems undergoing crush failure. To this day, research in this field has focused exclusively on experimental investigation because the fundamental mechanisms that control the crushing behavior and energy absorption in composite materials are technically challenging and not well understood. To focus on advanced structural composites, this review considers only CFRP systems that use a thermoset resin, as these are traditionally the most common type of composite found in primary vehicle structures. These types of composite material systems experience a brittle crush failure response, referred to as progressive crushing.

Before reviewing the literature on progressive crushing of composites, a brief discussion is necessary to identify the experimental parameters that define energy absorption. A simple cross-section schematic of a square tube undergoing progressive crushing due to the force *F*, along with a typical load-displacement curve representative of such failure, is shown in figure 2. The cross section in figure 2 features the chamfered end, called a crush trigger, which prevents global buckling failure and allows for progressive crushing to initiate. The crush trigger is a necessary design feature for composites progressive crushing. It can take the form of a steeple, saw tooth, or chamfered edge machined into the coupon, or ply drop offs that also form a natural chamfer of the structure. Without the crush initiator, composite materials have a tendency to reach unacceptably high peak forces upon impact and often buckle in an unstable manner. Across experimental crush studies, it is widely accepted that a crush trigger is crucial for composite materials, although the trigger geometry that produces the best result is not agreed upon [12–13].

When evaluating the crush performance of a structure, the load-displacement curve from the crush experiment is analyzed, from which some key parameters can be determined:

- Peak load: The maximum point on the load-displacement diagram that initiates progressive crushing failure, noted as $P_{\max}$ in figure 2.
- Average crush load (also referred to as the sustained crush force): The displacement-average value of the load history, noted as $\bar{P}$ in figure 2.
- Energy absorbed (EA): The total area under the load-displacement diagram.

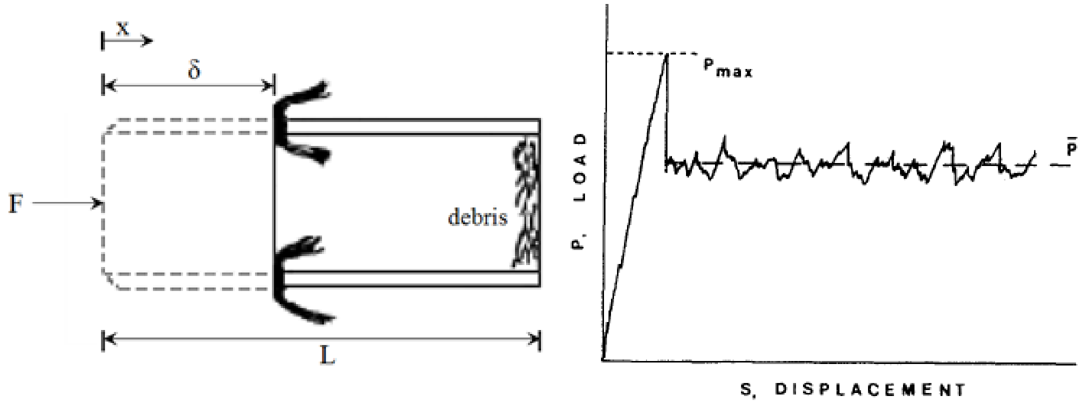

Figure 2. Schematic of composite tube with a chamfered crush initiator undergoing progressive crushing and the resulting load-displacement crush curve, from Hull [9]

Referring to the notation provided in figure 2, the *EA* is given by:

$$EA = \int_0^{\delta} F \cdot dx \qquad (1)$$

The capability of a material to dissipate energy can be expressed in terms of specific energy absorption (SEA), which is the EA per unit mass of crushed structure and is measured in joule/gram (J/g). Considering the mass of a structure that undergoes crushing as the product of the density, ρ, displacement, δ, and cross-sectional area, A (which, in turn, is the product of the section length, S, and the thickness, t), the SEA is given by:

$$SEA = \frac{EA}{\rho \cdot \delta \cdot A} = \frac{\int F \cdot dx}{\rho \cdot \delta \cdot S \cdot t} \tag{2}$$

The SEA measured from crush testing is the primary value used to characterize the energy absorption capability of a material, and is reported by most authors reviewed here to quantify crush performance.

Most experimental research has focused on the axial crushing of thin-walled tubular specimens with chamfered crush initiators that are representative of elements found within crash structures, such as that shown in figure 2. Such specimens are self-supporting and are therefore easy to subject to axial crush testing. Work performed to understand the physical energy absorbing failure mechanisms of progressive crushing using tubular specimens has been published by Farley and Jones [14–15], Hull [9], and Carruthers [16], and has most recently been reported by Bisagni [4].

To provide some perspective on the technical challenge presented by this topic, Hull [9] states that a detailed understanding of the physical geometry of the crush zone (also called the crush front by other authors) is necessary to characterize progressive crushing. He identifies a list of several interacting variables, which ultimately define the physical crush zone geometry, and concludes in his paper that “a complete description of the interaction of all of these variables is impossible.” This is a common conclusion among experimentalists in this area who uniformly recognize the technical challenge presented by composite crush failure.

In 1989, Farley and Jones [14] were two of the first researchers to attempt to develop a scientific understanding of the physical energy absorption mechanisms occurring during progressive crushing. Prior to this, the studies on composite energy absorption had consisted of reporting the results from specific test matrices comparing the energy absorption of one design against another. Farley and Jones identified three distinct crushing modes, combinations of which described progressive crushing failure. These modes are transverse shearing, brittle fracturing, and lamina bending. In later publications, Farley and Jones [15] stated that the brittle fracturing mode is, in fact, a combination of the transverse-shearing and lamina-bending modes, making these two the only distinct modes. As described by Farley and Jones, the transverse shearing mode, shown in figure 3(a), is characterized by short interlaminar and longitudinal cracks, which coalesce to form partial lamina bundles. The principal energy-absorbing mechanism is the transverse shearing of the edges of the lamina bundles. The length of these cracks is typically less than the laminate thickness, but ultimately the number, location, and length of the cracks are functions of the specimen structure and constituent material properties. The lamina bending failure mode, shown in figure 3(b), is characterized by long interlaminar, intralaminar, and parallel-to-fiber cracks, which do not coalesce, and the lamina bundles formed do not fracture. Instead, the lamina bundles exhibit significant bending deformation. The main energy-absorbing mechanism of this failure mode is crack growth, which Farley and Jones describe as an inefficient crushing mode, alluding to its low-energy absorption capability due to minimal fiber fracture.

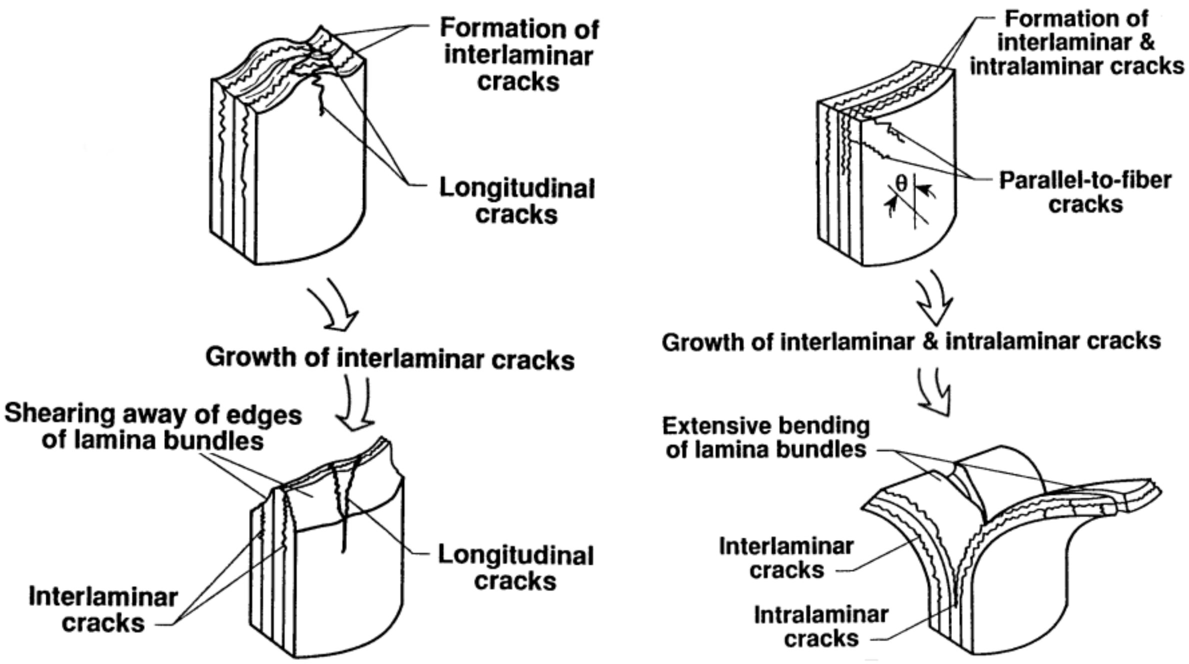

(a) (b)

Figure 3. From Farley and Jones [14], (a) transverse shearing and (b) lamina bending failure modes of progressive crushing failure

Hull [9] soon followed the work of Farley and Jones, and provided his own scientific analysis of the energy-absorbing mechanisms occurring during progressive crushing. Hull identified eight theoretical failure modes relevant to crush failure, stating that fracture occurs in tension, compression, shear parallel, and normal to the fiber direction, and that failure may also involve interlaminar fracture in tension and shear. In practice, Hull identified two general modes of progressive crushing failure: splaying and fragmentation. Crush failure is often a combination of differing degrees of both modes. The splaying mode is characterized by long cracks, which propagate through the matrix and between plies while leaving most of the fiber bundles intact. Conversely, the fragmentation mode is characterized by abundant fiber fracture and matrix cracking, rendering most of the material as debris with little left intact. These two modes are shown in figure 4 and are essentially the same as those identified by Farley and Jones, as later noted by Carruthers [16].

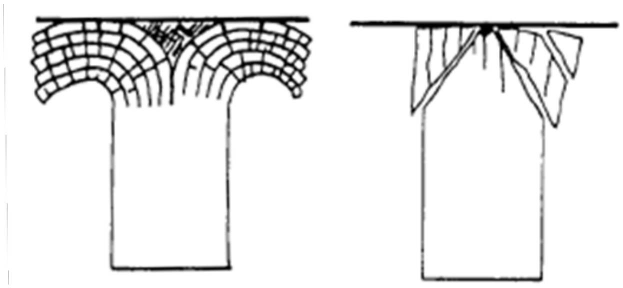

(a) (b)

Figure 4. Schematics of the two extremes of composite crush failure modes: (a) splaying mode and (b) fragmentation mode [9]

By using micrographic analysis, Hull [9] identified several of the eight theoretical fracture modes as prevalent within both the splaying and fragmentation crushing failures. From this analysis, the impossibility of characterizing the crush zone is evident, given its dependence on the microfracturing processes; forces acting at the crush zone; microstructural variables associated with the composite constituents; shape and dimensions of the crush specimen; and testing variables, such as temperature and speed. Hull does not describe a difference in energy absorption potential between these two crushing modes. Hull shows that the arrangement of fibers (i.e., laminate layup) influences which failure mode is more dominant during progressive crushing. By increasing the ratio of hoop to axial fibers in the composite tube layup, Hull is able to change the failure mode from portraying primarily splaying failure to primarily fragmentation failure, proposing that hoop fibers contain the splaying of axial fibers during crushing. This conclusion is applicable only to closed section crush articles with hoop fibers, such as the tubes Hull used in his investigation.

Carruthers [16] provides a review of several experimental studies of composite crush tubes conducted through its publication in 1998. This review summarizes that, of the many failure modes described, the most prominent include transverse shearing, brittle fracturing (both of the fiber and of the matrix), lamina bending, delamination, and local buckling. Carruthers concludes that the many failure modes identified by several authors are bounded by the two extremes identified independently by Farley and Hull: splaying/lamina bending and fragmentation. Carruthers continues, “of the two brittle fracture failure modes, there is some evidence to suggest that the fragmentation mode of failure generally results in higher energy absorptions than the splaying mode” and refers the reader to the crush tube work of Hamada [17]. Determining which failure mode will be dominant during tube crushing, however, depends on several factors, including the selection of fiber and matrix constituents, lamina angle, specimen geometry, layup, and testing speed. This result appears to be the consensus among experimental investigations to identify composite crush failure modes; however, among these investigations, there are conflicting data over what parameters influence the physical preference of one failure mode over the other, and how each parameter influences the result. The common conclusion among researchers to this day is that there are several different failure modes occurring simultaneously during composite material crushing, each of which provides a different capability for energy absorption, but a general disagreement of what parameters most influence these modes, and how their influence takes effect.

Beyond the extensive work of these authors, not much additional work has been done to scientifically characterize the physical energy-absorbing mechanisms in progressive crushing. In more recent publications, authors often report observations of different failure modes as they appear within the context of a particular test matrix without delving into a scientific explanation of these modes. In this way, several crush failure modes are named, but they are often not characterized within the greater context of the two established boundary modes of splaying and fragmentation. Most recently, for instance, Bisagni [4] presented a brief description of four failure modes observed from crush testing circular carbon fiber tubes. These are the tearing, socking, splaying, and microfragmentation modes, as shown from Bisagni in figure 5. While Bisagni’s microfragmentation mode appears to be the one identified by Hull, the other three modes appear to include combinations of fragmentation and bending crush modes.

Tearing mode Socking mode

Splaying mode Microfragmentation mode

Figure 5. Four progressive crush failure modes as identified by Bisagni [4]

Underlying the scientific efforts to characterize the physical energy-absorbing mechanisms present in composite progressive crushing has always been the fundamental desire to quantify and measure the energy-absorbing capability of composites. As given in equation 2, the SEA measured from crush testing is the primary value used to characterize the energy-absorption capability of a material. Unfortunately, there is no standardized test method for SEA measurement and, therefore, no way to systematically compare the energy-absorption capability of different composite material systems. This means that the SEA values reported by different research efforts cannot be directly compared because they likely used different test methods, which can influence SEA results significantly.

The manner in which coupon-level testing is conducted for SEA characterization of composites varies greatly and has been the topic of recent research efforts. Few attempts have been made at developing a coupon-sized test method to determine the SEA of composite materials. Such efforts are being made by the Crashworthiness Working Group of the Composite Materials Handbook (CMH-17), formerly MIL-HDBK-17 [18], while operating in parallel with the ASTM International Committee D-30 on Composite Materials. Similarly, the Energy Management Working Group of the ACC [2], which comprises members of the three largest U.S. automotive manufacturers and the U.S. Department of Energy, has worked for over two decades on the topic of composite crash structures for automobiles. In addition, government organizations, such as the National Aeronautics and Space Administration (NASA) [19] in the U.S., the German Aerospace Center (DLR) [20], and the National Aerospace Laboratory of the Netherlands (NLR) [7], have also dedicated resources towards the experimental characterization of composite crash energy absorption.

One method for SEA measurement is to use a flat material coupon, similar to those used for standardized mechanical material property testing. Flat test coupons have the advantage of being easily manufactured with no requirement for special tooling. Because of the loading conditions required and failure modes desired, however, characterizing crush energy absorption using a flat coupon is a challenging and controversial task. A specialized fixture is required, which must provide anti-buckling support for the flat coupon without inducing friction or suppressing crush failure. Several fixtures for flat coupon crush testing have been proposed over the years, and a good review of this work is provided by Feraboli [12]. Four such flat crush coupon fixtures are shown in figure 6. Each of these fixtures features different mechanisms to provide lateral anti-buckling support, such as two vertical knife edge supports, which pinch the flat test coupon vertically in place during crushing in the NASA fixture, as shown in figure 6(a), or the roller bearings, which facilitate both vertical movement and lateral support of the test coupon in the University of Stuttgart fixture, as shown in figure 6(d). The University of Washington fixture uses knife edge supports in a similar fashion to the NASA fixture; however, these supports do not constrain the entire length of the specimen, and an adjustable length of unsupported height of the coupon at the crush front is allowed, as highlighted in figure 7.

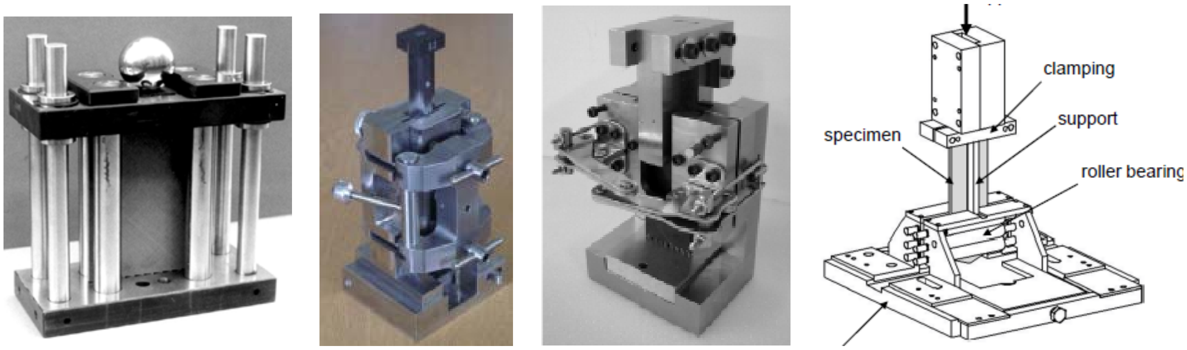

(a) (b) (c) (d)

Figure 6. Flat coupon crush test fixtures from (a) NASA [19], (b) Engenuity [1], (c) Oakridge National Laboratory [21], and (d) University of Stuttgart [22]

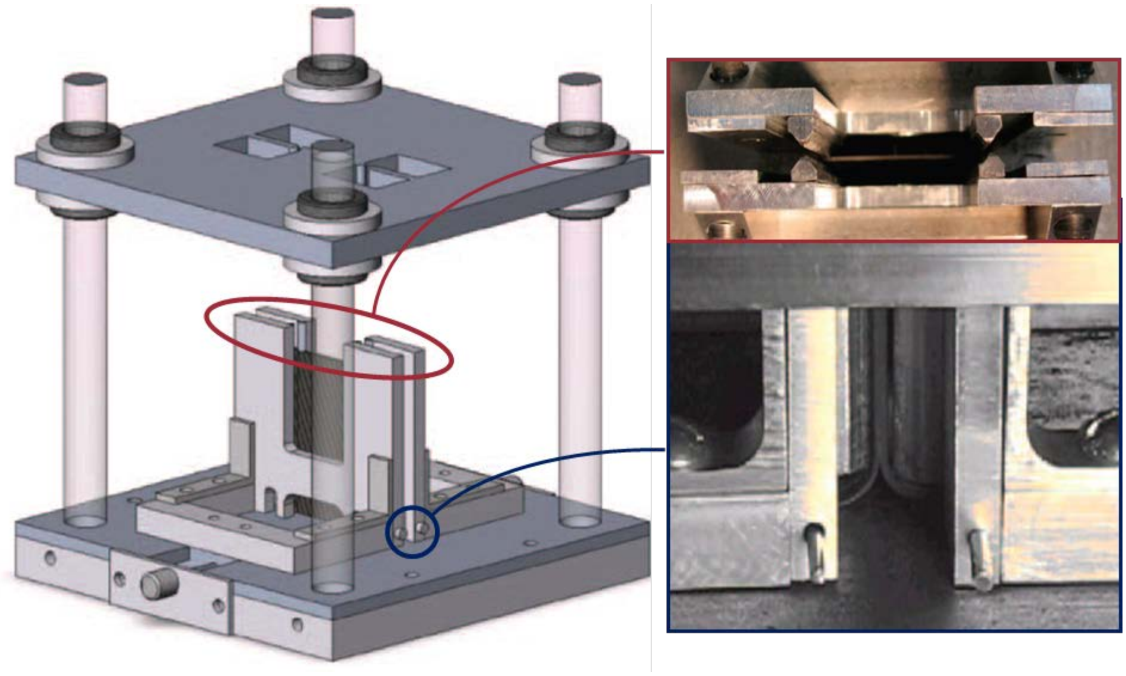

Figure 7. University of Washington flat crush coupon fixture highlighting the details of the knife-edge supports (top right) and unsupported height of the crush coupon (bottom right) [12]

With the exception of the NASA flat coupon crush fixture, all fixtures feature a laterally unsupported distance at the crush front where the crushed material is free to naturally bend and form fronds, and the evacuation of debris is allowed to minimize interference with the remainder of the test coupon undergoing crushing. Crush tests conducted using the NASA fixture determined that without an unsupported region, a flat coupon is over-constrained at the crush-front. The collection of growing debris impedes the natural crushing of the coupon and causes great reaction forces. Consequently, an artificially high SEA is measured because of these fixture effects [12]. Research conducted using two of the fixtures, from the University of Stuttgart [22] and University of Washington [12], indicates the importance of the unsupported height distance on the measured SEA and crushing stress. While providing too little unsupported height causes an over-constrained situation, such as experienced using the NASA fixture, providing too much unsupported height allows for buckling, and crushing is not achieved, as shown in figures 8 and 9. Comparing these two results, the unsupported height threshold at which the energy absorption trend changes is different, and may depend on either the material system tested or the test fixture itself. Several unsupported height distances must be tested to find the proper amount that allows for sustained crushing and from which the flat coupon SEA can be measured. For all flat coupon anti-buckling test fixtures, however, the influence of the test fixture cannot be definitively identified and the adoption of a self-supporting element-level crush specimen is preferable to that of a flat specimen.

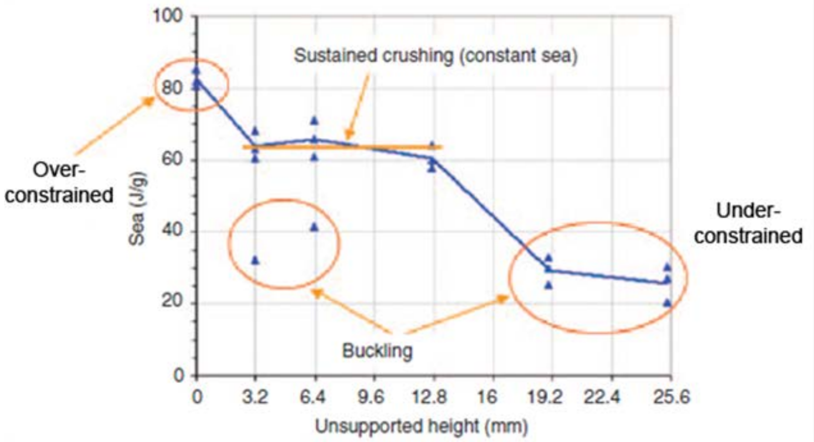

Figure 8. Influence of the unsupported height of the University of Washington flat crush test fixture on the SEA measurement, from Feraboli [12]

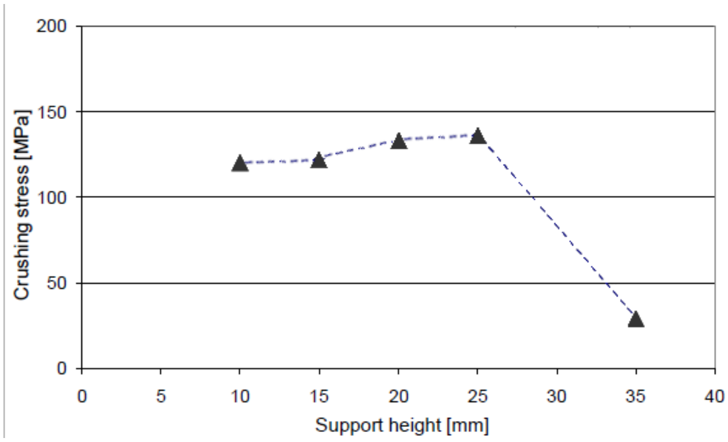

Figure 9. Influence of the unsupported height of the University of Stuttgart flat crush test fixture on the crushing stress measurement, from Feindler et al. [22]

The majority of the experimental research to determine the crush energy absorption of composite materials has used thin-walled tubular specimens rather than flat coupons or other shapes. Such research was underway prior to the development of flat coupon crush test fixtures. Tubes were selected because they are self-supporting and, therefore, do not require dedicated test fixtures, and also because they are representative of the tubular front rails usually found in automotive crash structures. Most work completed to date consists of reporting SEA results from varying test parameters, fiber and matrix constituent materials, the laminate layup, and geometric features of the tubes. Among this work, a wide range of experimental setups have been used, making comparisons across different test programs difficult. Furthermore, some of the observed trends reported by authors are contradictory to those reported by others, leaving questions as to exactly how certain parameters influence results. For instance, some research has shown that the SEA can double between the dynamic and quasi-static crush tests of the same geometry [5], whereas other authors have reported a decrease over dynamic results [16]. Thornton [23] reports no rate dependency across a velocity range of six orders of magnitude, and Mamalis [24] maintains that the strain-rate sensitivity of energy absorption depends on the dominant failure mode experienced by the composite crush coupon, for which only particular crush failure modes are sensitive. The only consensus about the influence of test speed on energy absorption is that there is no consensus [16 and 25]. The lack of an agreed-upon test method makes the comparison of test results and research findings across the literature a challenge.

To further illustrate this point, key findings from a review of more than 50 composite crush tube test programs published by Carruthers et al. [16] and Jacob et al. [25] were reviewed. Among these test programs, the effect of various constituents, layups, specimen geometries, loading rates, and other test parameters were investigated. The findings from Thornton [23], Farley [26], and Schmueser and Wickcliffe [27] reveal that carbon tubes consistently have a higher SEA than glass and aramid tubes. Regarding the matrix constituent, there is widespread disagreement of its direct influence on energy absorption and, in particular, which matrix properties constitute good energy absorption. For instance, Thornton [23] reports that higher tensile strength and modulus of the matrix contributes to higher energy absorption, while noting that there is no dependence of SEA upon the resin fracture toughness. Contrarily, Hamada et al. [28] report that the high fracture toughness of a matrix directly resulted in the highest energy absorption of any CFRP. Finally, Tao et al. [29] report that the increased compressive strength of a matrix is the most influential matrix property in providing better energy absorption. The influence of material layup upon energy absorption appears to be dependent on the constituent materials, as contrasting trends between ply angles and energy absorption capability of carbon composites versus glass and aramid composites have been reported by Carruthers et al. [16]. In this area, there is also disagreement in that Schmueser and Wickcliffe [27] report that ply angle influence on energy absorption remains the same among all fiber types. Whenever there is disagreement of the general energy absorption data trends, each author has used a different test method that implements different loading rates and trigger mechanisms (for instance, making comparisons and drawing meaningful conclusions difficult).

Upon review of the relative available literature, studies of the effect of crush specimen geometry on SEA have focused on changes of small geometric features, such as tube diameters and thicknesses. Among tubular specimens, several geometric features have been reported by several authors as influencing SEA, leading to the overall conclusion that geometry strongly influences energy absorption. In particular, Thornton [23], Mamalis et al. [24], and Kindervater [30] each reported that circular tubes had higher energy absorption than square tubes of the same composite system. Farley [31] and Mamalis et al. [32] individually reported that increasing the diameter-to-thickness ratio of circular tubes nonlinearly decreased the energy absorption. Farley and Jones [15] reported upper and lower bounds for the thickness of the tube, for which overly thick tubes tended to fail catastrophically when the hoop stress in the tube reached the strength of the material and overly thin tubes tended to buckle. In a separate publication, Farley and Jones [33] reported the influence of the eccentricity of near elliptical tubes as determined by the included angle of the cross section. As the tubes became more elliptical (i.e., the included angle decreased), the energy absorption of these tubes increased by up to 30%. Studies on the effect of crush specimen geometry were also carried out by Hanagud et al. [34] using corrugated plate specimens. Hanagud found that the web amplitude had a destabilizing effect when too low, but the number of repeated waves was not influential. In general, each study of the effect of crush specimen geometry on SEA has focused on small and specific geometric features, and there has been no work reported that compared the macro effects of different geometries upon energy absorption (i.e., comparing tubes to corrugated webs).

Carruthers et al. [16] suggested that the closed-section nature of tubes has unknown but evident effects on the crush performance. In particular, it is thought that the stacking sequence affects the crush behavior because the hoop fibers constrain the axial fibers and prevent them from splaying, thereby suppressing the propagation of the crush front. Only a limited number of element-level crush experiments have used test specimens of geometries other than tubes. The aerospace community has focused mostly on test specimens that resemble subfloor structures, such as floor beams, longerons, stanchions, and stiffeners. Corrugated web geometries have a history of being employed as energy absorbers in the subfloors of aircraft to improve crashworthiness in both rotorcraft [20 and 35] and large commercial transport aircraft [36]. Corrugation increases the stability of a vertical web, thereby increasing its crippling strength, and enables floor beams to carry higher design loads. By reducing the likelihood of macroscopic buckling, the corrugated geometry promotes stable crushing and significant energy absorption in a crash scenario [34]. Other possible test element geometries are open section and partially self-supporting and are, therefore, more versatile from a manufacturing viewpoint. They also do not exhibit the same hoop fiber constraint as tubular shapes and do not require a dedicated test fixture like flat coupons. Such geometries include semicircular segments [5], channel stiffeners [2], and the DLR omega specimen [37]. Like the crush tube studies, the goal within these individual test programs is often focused on understanding the influence of a specific effect from material, layup, loading rate, geometry effects, etc., and the issue among these test programs remains the lack of an agreed-upon test method. There has not been a systematic study of the influence of large geometric changes (i.e., using different shapes rather than different dimensions of the same shape) upon the SEA of a composite material system, and, therefore, there is no clear way to compare the results of the corrugated web tests against the tubular tests. In the absence of a standardized experimental test method, there is a need to understand the influence on the crashworthiness of composite specimens with such large geometric differences.

Finally, the variability in SEA measurements for composite materials has been shown to be dependent on numerous testing variables, and this can make it difficult to understand exactly how composites perform with respect to crashworthiness. For this reason, it is useful to compare the performance of composite material systems against their predecessors (i.e., metals) to develop a better understanding of composites. Indeed, most of the composite crush test programs reviewed often use an isotropic metal, such as steel or aluminum, as a baseline against which the composite SEA measurement is compared. Across these studies, it is shown that the SEA measurement of carbon fiber-epoxy composites in particular is consistently higher than that of isotropic metals, unless given very unfavorable conditions (e.g., poor layup, unstable geometry, etc.). Carruthers et al. [16] report that for axially compressed tubes, carbon fiber-epoxy tubes with a 0-degree biased layup have SEA measurements 1.6–2.2 times higher than metallic tubes, In table 1, Jacob et al. [25] compile a history of tube crush experiments, and report that the SEA of a carbon fiber-epoxy crush tube is 110 J/g compared against 78–89 J/g for aluminum tubes of different diameters.

Table 1. Comparison of SEA of carbon and glass composite tubes against steel and aluminum tubes, from Carruthers et al. [16]

Material	Layup	Thickness: outside diameter ratio	SEA [J/g]
Carbon-epoxy	$[0/\pm15]_3$	0.033	99
Carbon-epoxy	$[\pm45]_3$	0.021	50
Glass-epoxy	$[0/\pm15]_2$	0.060	30
1015 Steel		0.070	45
6061 Aluminum		0.070	60

The data from Carruthers et al. and Jacob et al. is in agreement with a chart published by the Advanced General Aviation Transport Experiments (AGATE) Small Airplane Crashworthiness Design Guide [38], which clearly shows the outperformance of graphite (carbon) tubes for SEA compared against various metals, reproduced in figure 10. It is generally acknowledged that carbon fiber composites offer the increased capability for energy absorption over both isotropic materials and other composite types, although the variables that influence this capability are numerous and not well understood.

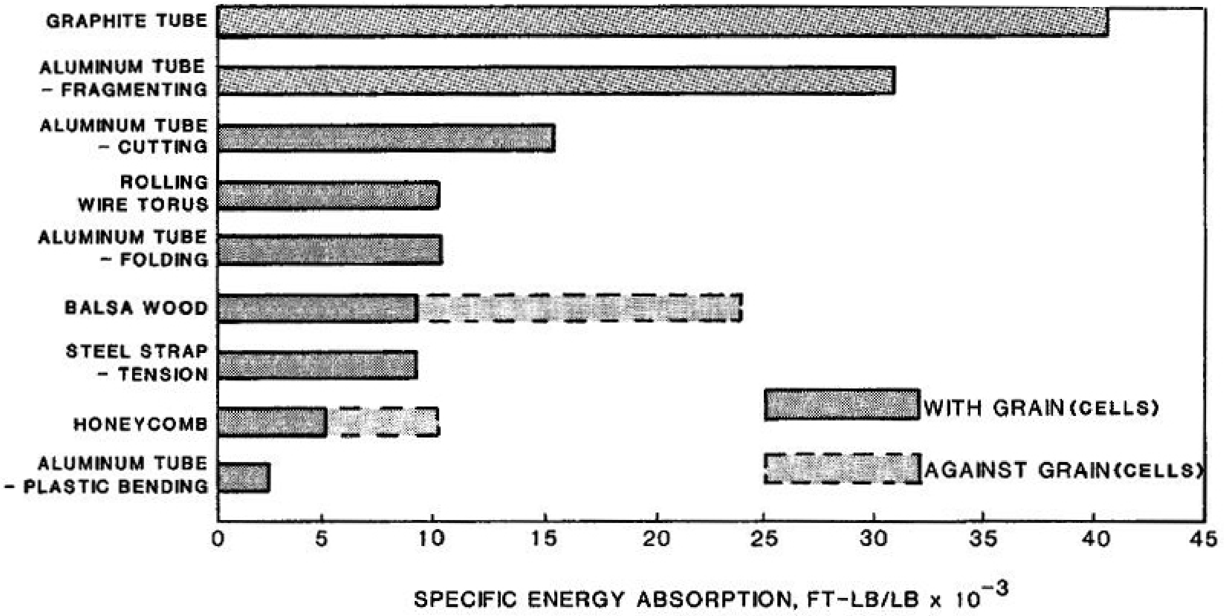

Figure 10. SEA values from tube crush testing of different materials, showing the outperformance of graphite (carbon) in the AGATE Design Guide [38]

2.2 COMPOSITE MATERIAL MODELS FOR CRASH SIMULATION

The significant challenge presented by the simulation of composite material systems beyond the elastic region is the complex nature of the combination of individual failure mechanisms occurring in the damaged material. Each failure mechanism is demonstrably unique, and it has been shown that even in the experimental field of investigation, there is disagreement concerning the prevalence of one failure mode over another given different material types, layups, boundary conditions, etc. The development of composite materials capable of crash simulation has been pursued in two general areas: 1) models that attempt to capture the detailed behavior of simple test specimens and to model the individual crush failure mechanisms occurring within the material [39–46], and 2) crash modeling of large-scale composite components and structures using calibrated composite material models, which capture the overall behavior of the crushing material rather than the details of the failure mechanisms [47–50]. While the detailed damage mechanism models are important for developing a better understanding of the fundamental material failure behaviors, computational limitations are such that capturing detail in a large-scale composite crash model is not yet feasible and is not currently being attempted. Such small-scale models are not within the scope of this research.

Composite material models that are suitable for full-scale crash simulations are often lamina-level models whose material properties are that of the lamina. The layup of the laminate is specified by the element formulation (not by the material model). Classical laminate theory is used within the element formulation to calculate laminate stress and strains from the lamina stresses and strains determined by the material model. These models have three features: the elastic model, the failure criterion, and the post-failure damage model, which include progressive damage and ultimate material failure. The elastic model uses stress-strain relations based on Hooke's Law and constitutive properties measured from standardized material property experiments. The failure criterion and damage model are the two features that distinguish most composite material models and will be the focus of this review.

Predicting the initial failure of a composite lamina and developing failure criterion have been a topic of research since the 1960s. All failure criteria rely on extensive experimental data to define strength and strain parameters, and are therefore semi-empirical in nature. A review of early composite failure theory [51–54] reveals that numerous criteria have been developed with various degrees of success. Among these criteria, there has been a lack of evidence to show whether any analysis method provides accurate and meaningful predictions for failure over anything other than a very limited range of conditions. To address this issue, Hinton et al. launched the first World Wide Failure Exercise (WWFE) in 1998 to assess and compare the prediction capabilities of a wide variety of composite failure theories. This large scale, multiyear collaborative effort demonstrated in its conclusion in 2004 that failure criteria for composites have several shortcomings, making it a challenge to predict even the onset of damage, with particular deficiencies for predicting nonlinear responses [55]. Although crush failure was not addressed by the WWFE, crushing is a more complex failure mode than any of the nonlinear loading conditions investigated by the WWFE for which none of the failure criteria could adequately predict. This evaluation of composite failure criteria reveals the technical challenge presented by the development of a composite material model suitable for crash simulation for which even the prediction of the onset of damage is a great challenge, not to mention the post-failure material deformation. For a more current and broad catalogue of existing failure criterion actively used in composite material models, a review published by Orifici et al. [56] is referenced.

Because of their anisotropic nature, failure criteria for composite materials treat different failure modes separately, at the very least defining unique criteria for fiber rupture and matrix failure. Typically, these modes are separated further into different load cases of tension, compression, and shear, and can also include additional interactive criterion for complete ply failure. For both fiber and matrix failures, the most simple and most commonly used composite failure criteria are the maximum strain and maximum stress criteria [52 and 56]. The maximum strain criterion states that a material fails under a stress state when any of the principal strains reach an ultimate value. The expression for this in terms of 2D principle stresses is:

$$max\{|\sigma_1 - v\sigma_2|, |\sigma_2 - v\sigma_1|\} = \sigma_u \tag{3}$$

where v is the Poisson's ratio of the material. Similarly, the maximum stress criterion states that a material fails when any of the principal stresses reaches the ultimate value, as given by:

$$max\{|\sigma_1|, |\sigma_2|, |\sigma_{12}|\} = \sigma_u \tag{4}$$

Either of these criteria can be used to define tensile and compressive failures in the fiber and matrix by using the appropriate tensile and compressive strengths measured from coupon testing of the lamina in the axial, transverse, and shear directions.

In 1980, Hashin [57] modified a general tensor polynomial criterion from which four distinct failure modes for a composite lamina were developed, each a quadratic interaction criterion involving an in-plane shear term. The Hashin failure criteria are given by:

Tensile fiber mode:

$$\left(\frac{\sigma_{11}}{{F_1}^{tu}}\right)^2 + \left(\frac{\tau_{12}}{{F_{12}}^{u}}\right)^2 = 1 \qquad for\ \sigma_{11} > 0 \tag{5}$$

Compressive fiber mode:

$$\left(\frac{\sigma_{11}}{{F_1}^{cu}}\right)^2 = 1 \qquad for\ \sigma_{11} < 0 \tag{6}$$

Tensile matrix mode:

$$\left(\frac{\sigma_{22}}{{F_2}^{tu}}\right)^2 + \left(\frac{\tau_{12}}{{F_{12}}^{u}}\right)^2 = 1 \qquad for\ \sigma_{22} > 0 \tag{7}$$

Compressive matrix mode:

$$\left(\frac{\sigma_{22}}{2{F_{12}}^{u}}\right)^2 + \left[\left(\frac{{F_2}^{cu}}{2{F_{12}}^{u}}\right)^2 - 1\right]\frac{\sigma_{22}}{{F_2}^{cu}} + \left(\frac{\tau_{12}}{{F_{12}}^{u}}\right)^2 = 1 \qquad for\ \sigma_{22} < 0 \tag{8}$$

In 1987, Chang and Chang [58] augmented Hashin's failure criteria to have a fiber-matrix shearing term in place of the in-plane shear term as follows:

$$\bar{\tau} = \frac{(\tau_{12}{}^{2}/2G_{12}) + \frac{3}{4}\alpha\tau_{12}{}^{4}}{((F_{12}{}^{u})^{2}/2G_{12}) + \frac{3}{4}\alpha(F_{12}{}^{u})^{4}} \tag{9}$$

where α is a nonlinear shear factor on the third-order term of the shear stress-strain elastic relation:

$$\varepsilon_{12} = \frac{1}{G_{12}}\tau_{12} + \alpha\tau_{12}{}^{3} \tag{10}$$

The Hashin failure criteria with Chang and Chang's augmentation will receive considerable attention in this report because these are the failure criteria used by the material model investigated in this body of research.

Another way to define mode-based lamina failure is to use phenomenological failure criteria, most notably Puck's criteria [59]. These types of models attempt to simulate the unique physical phenomena of different lamina failure modes and rely heavily on empirical data that requires specialized testing and curve fitting. Puck's criteria were evaluated in the WWFE, which reported a relatively positive performance in the exercise; however, it was also acknowledged that the experimental requirement to define numerous fitting parameters of such phenomenological models is both burdensome and difficult to validate [60].

Finally, there is a category of interactive failure criteria that considers the failure of the entire ply rather than separating criteria into fiber and matrix modes. Orifici et al. [56] offer an interesting commentary on such criteria, which are often criticized because of "their origins in theories originally proposed for metals." They continue, "however, interactive criteria have demonstrated accuracy comparable with leading theories in which the failure modes are considered, and continue to be commonly applied in industry and widely available in FE codes." One such failure criterion that is of interest for crash simulation is Wolfe's strain-energy-based criterion [61]. Although it was not any more successful than any of the other simulation methods in the WWFE in predicting simple laminate-loading conditions [62], it is suggested here that an energy-based criterion could be useful in predicting the energy-absorbing capability of composite structures in crash. Wolfe's criterion relies on the axial, transverse, and shear components of strain energy as measured by the area under the material coupon-level stress-strain curves of the lamina. Each component is expressed as an integral of the stress in terms of strain, divided by its ultimate strain-energy value (as measured by coupon-level experiment), and raised by a power of m_i, a shape function. The sum of the three components becomes Wolfe's strain-energy failure criterion:

$$\left(\frac{\int_{\varepsilon_1}\alpha_1 d\varepsilon_1}{\int_{\varepsilon_1^u}\alpha_1 d\varepsilon_1}\right)^{m_1} + \left(\frac{\int_{\varepsilon_2}\alpha_2 d\varepsilon_2}{\int_{\varepsilon_2^u}\alpha_2 d\varepsilon_2}\right)^{m_2} + \left(\frac{\int_{\varepsilon_6}\alpha_6 d\varepsilon_6}{\int_{\varepsilon_6^u}\alpha_6 d\varepsilon_6}\right)^{m_6} = 1 \tag{11}$$

The shape function values determine the shape of the failure surface in strain energy space and are unique for every material system. These values have an upper bound of $m_i = 2$ and cannot be determined without curve fitting to biaxial test data. These values are suggested to be set equal to 1 without such data; however, it was shown during the WWFE that Wolfe's predictions required extensive updating after experimental data were made available. While several changes were made to improve the predicted results, for some cases the shape function values were each changed to a value of 2, such that the prediction better matched the experiment. The resulting improved model concluded that, in particular for non-linear behavior, "the strain energy-based model generally predicts lower failure strengths than those from experimental testing," [62].

Following initial lamina failure, each composite material model must specify a damage model to degrade the performance of the material until ultimate failure is specified. There are two types of damage models for composites: continuum damage mechanics (CDM) and progressive damage models (PDMs) [56]. In a CDM model, material damage is defined using internal-state variables contained in a set of equations that allow the material to remain a continuum with smooth, continuous field equations. The internal damage variables are incorporated into the material constitutive equations to degrade the material performance as damage progresses. Talreja [63] was one of the first to develop a CDM model, and more current examples of CDM models are given by Johnson et al. [64] and Sokolinsky et al. [65]. In each of these models, damage factors are introduced into the ply stress-strain equations, which have an inverse relationship with the material constitutive properties. This has the effect of degrading the ply stresses following failure according to the damage evolution function defined by the material model. The analysis continues until the stress is degraded to zero, or until another condition specified for ultimate failure is satisfied.

In a PDM, damage is simulated using a ply discount method for which, when the failure criterion is violated in a ply, specified constitutive properties in that ply are reduced (often stiffness is set to zero) and the analysis continues. This continues until all plies have failed and the material is considered to have reached ultimate failure. Orifici et al. [56] report that the progressive damage approach is simple and that the binary reduction of constitutive properties is "particularly suited to the quasi-brittle nature of fibre-reinforced composites, and numerous researchers have recorded significant success in applying this approach to represent ply damage mechanisms." A PDM is used in the composite material model, which is the main focus of this body of research and is discussed at length in the main sections of this report.

While material models that implement lamina-level failure criteria and damage models are computationally feasible and an appropriate choice for composite crash simulation, predictions often suffer from the oversimplification that arises as a consequence of modeling an anisotropic, heterogeneous material as a laminate of orthotropic, homogeneous layers [66]. The true physical nature and interaction of failure mechanisms occurring within the crush front cannot be directly modeled using such an approach, which consequently can impair the predictive capability of these models. This is an important feature of composite material models that requires a strategic approach to their use in crash simulation, which this body of research will directly address.

2.3 CRASH SIMULATION OF COMPOSITE STRUCTURES

The state-of-the-art explicit FEA codes used to simulate the dynamic crushing deformation and damage of composite and metallic structures alike include LS-DYNA, Abacus/Explicit, RADIOSS, and PAM-CRASH [1]. The crash simulation of metallic structures using these codes has matured into a reliable tool over the past decade in the automotive industry [11]. Given the technical challenge presented by the ongoing development of composite material models, the use of such models in full-scale FEA crash simulations requires an intelligent approach and strategic implementation such that these advanced material models can be effective in providing useful results that are much needed as the use of composites in vehicle structures grows. The BBA is the method that allows for the strategic use of composite damage material models in crash simulation.

The BBA is outlined in great detail in the CMH-17 handbook [1], and was developed to substantiate the design of composite structures using both analysis and testing in an optimized fashion. In addition to the CMH-17 handbook, in 2009, Feraboli [66] published a concise description of the use of the BBA in composite aircraft certification, while Rassaian and Davis [67] made a presentation on the use of the BBA specifically for composites crashworthiness certification in 2012. These three resources are used to form the following discussion on the BBA.

The BBA uses experimental test data to support the development of the numerical model at increasing levels of structural complexity, as shown in figure 11, beginning with material coupons and progressing through structural elements, subcomponents, components, and finally, the complete full-scale structure. Each level builds on knowledge gained in the previous, less-complex levels. Progressing through the BBA, the specimen and experiment increase in both scale and complexity; however, the number of test repetitions decreases. By combining testing and analysis, analysis predictions are verified by experiment, test plans are guided by analysis needs, and the degree of knowledge, safety, and confidence in the design is increased.

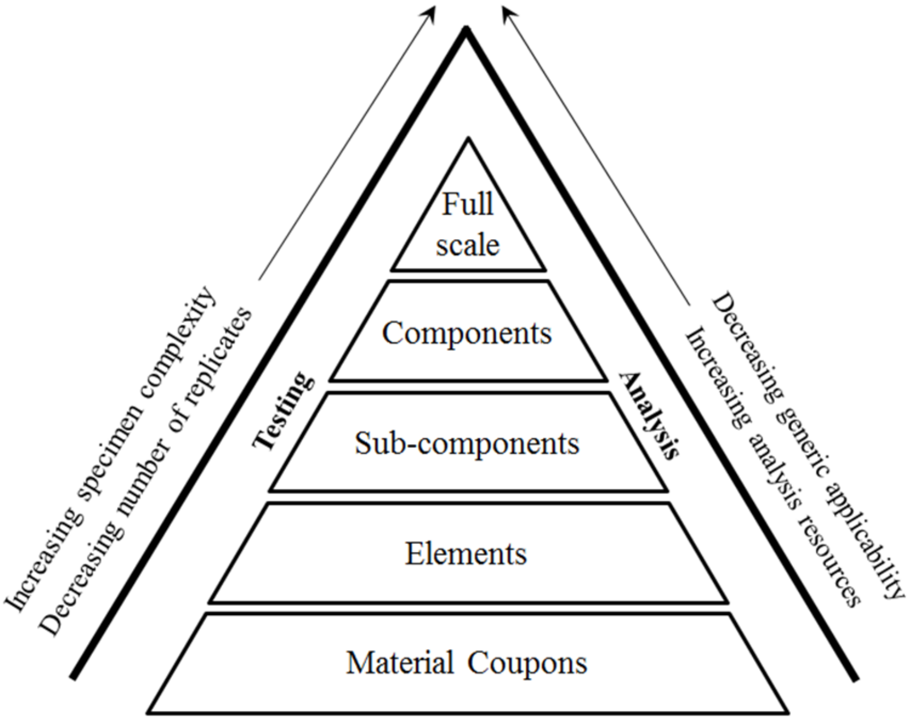

Figure 11. The BBA for composite structural development

At the lowest level of the BBA, material coupon test data are directly input into the material model to form its initial definition. At this level, many coupon data are necessary to form design allowables data for the composite material system [66], but very little is done in the analysis other than to initialize the material model. In intermediate levels, experimental data support the development of the analysis by calibrating simulated results against the test evidence. At the elements level of the BBA, testing includes the characterization of structural details, such as bolted and bonded joints, radius details, and stress concentrations. Test data collected at this level can either be directly input into the material model or used to calibrate it, depending on the capability of the individual material model. The test matrix at the element level is guided by the needs of the analysis model, such that it can be properly calibrated to be used at the higher levels of the BBA.

At the subcomponent and components levels, tests are used almost exclusively to validate the analysis method previously calibrated. From Rassaian and Davis [67], an example of the subcomponent test for a crashworthy structure is a 2-stanchion subfloor assembly from a fuselage section with the skin, stringers, stanchions, and cargo floor included. From Feraboli [66], component testing for an aircraft would include 3- and 5-stringer panels to characterize skin/stringer interactions, major bolted joint assemblies, and spar, stringer, and rib tests. The testing done at these levels is used for validation of the analysis model and to minimize the risks associated with the last level of the pyramid—full-scale validation of the complete assembly. By the time the analysis model reaches the validation stage, the model is not calibrated further and must rely on the work done at lower levels. For this reason, the modeling strategy used for the full-scale final model must be the same as that used all the way down to the coupon-level. This means that the heavily detailed composite material model that is not capable of scaling up to the full-scale analysis is not feasible.

While the BBA is widely acknowledged in the composites industry, most of the development and expertise of its engineering application to composite crash modeling have been conducted in the private sector. One notable example of a publication on the topic of using the BBA for composite impact simulation comes from Feraboli et al. [68], in which a deep composite sandwich beam was impacted against a large pole, representative of a side-pole impact required for automotive crash certification. The event was simulated using an explicit analysis in LS-DYNA. In this effort, the model definitions for different parts of the sandwich structure were developed through tests and correlated analysis at lower levels of the BBA to build up to the final model, which could be considered a subcomponent model. The material model for the composite facesheets, MAT54, was calibrated from tests and simulation of three-point bending tests. The material model for the aluminum honeycomb was calibrated from quasistatic crush tests and simulation of smaller honeycomb specimens. Finally, the adhesive between the facesheets and the honeycomb was calibrated from single lap shear tests and their simulation. These three calibrated components were then incorporated into the final model of the large honeycomb beam and validated against the experiment of the pole impact. By following the BBA, good correlation between experiment and the validated simulation was observed, as shown in figure 12.

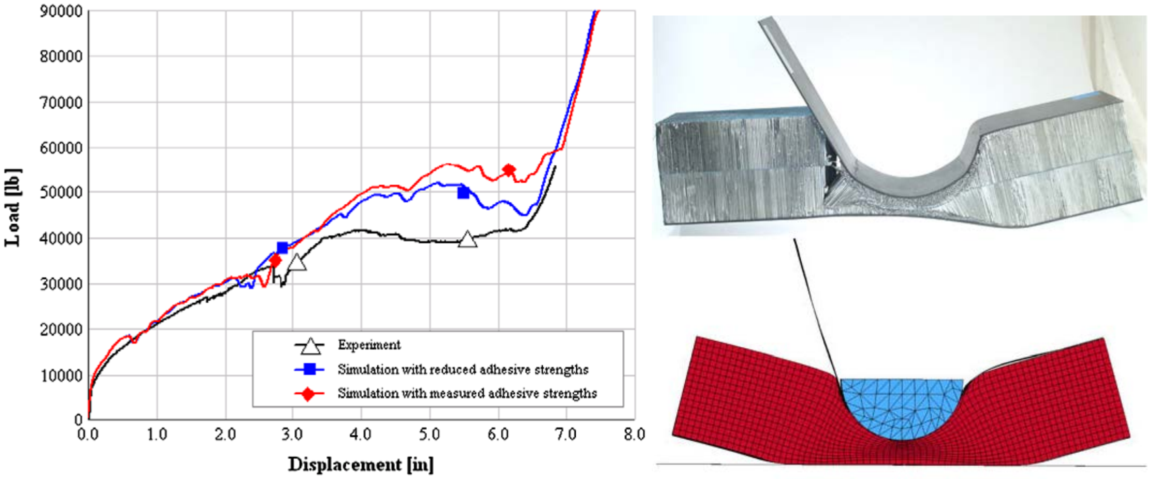

Figure 12. Successful test-analysis correlation from using the BBA to model a composite sandwich pole impact, from Feraboli et al. [68]

The other notable and most recent example of the use of the BBA for composites crash simulation comes from Heimbs et al. at DLR in 2013 [69]. In this study, a full-scale composite fuselage section subjected to crash conditions is simulated using Abaqus/Explicit. To build up to this simulation, composite coupons are subjected to three-point bend tests, which are used to validate the elastic properties input into the material model from standardized coupon testing. The material model uses the Hashin failure criteria to determine failure initiation, similarly to the LS-DYNA MAT54 model, and fracture energy criteria for damage modeling until ply erosion. The out-of-plane deflection of the test is also relevant to the skin-bending failure mode expected of the fuselage section crash simulation. The minimum 0.2″ (5 mm) mesh size used is particularly large for the coupon simulations, but appropriate when scaled up to the full-scale fuselage section. Pull-through, single lap shear, and coach peel tests are performed at the coupon-level as well to fully characterize the performance of the bolted joints. The results from these tests were used to calibrate the beam elements used to simulate joints in Abaqus/Explicit. At the element-level of the BBA, composite C-channels representative of the circumferential frames are subjected to four-point bending tests. The analysis of this experiment proved to be difficult because of the complicated experimental setup. After a detailed model of the entire test rig was complete, the corresponding load-displacement curve corresponded fairly well to the experiment, and the failure mode was exactly as it was observed in the experiment, as shown in figure 13. The DLR study concluded that several features of the fuselage section model have been calibrated and validated for use at higher levels of the BBA.

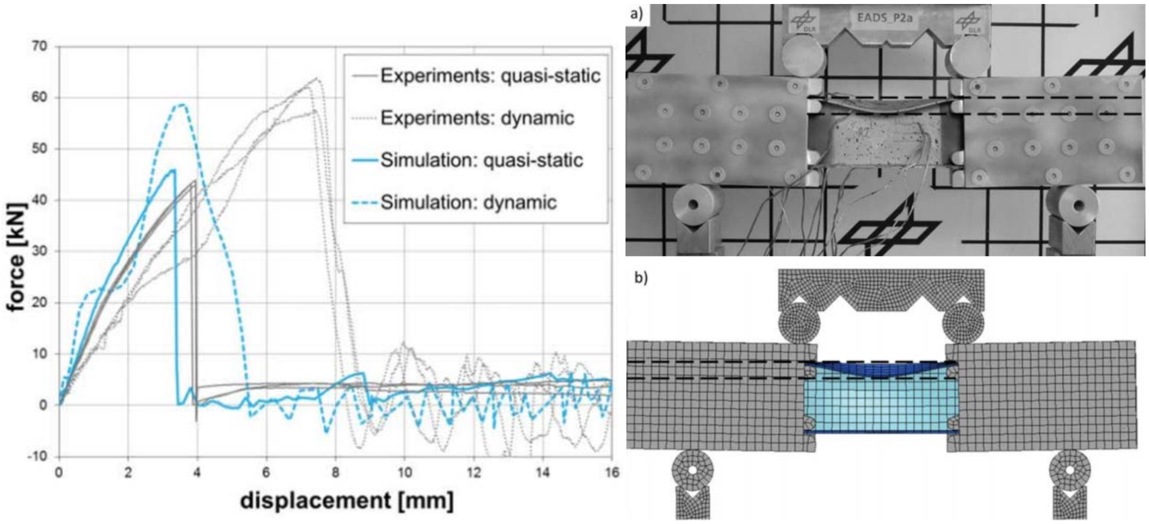

Figure 13. Successful test-analysis correlation from using the BBA to model a composite C-channel representative of a circumfrential frame, from Heimbs, et al. [69]

Although the focus of this report is the lower levels of the BBA, the ultimate goal is to use this work to build up to the higher levels. A review of the full-scale composite structure crashworthiness simulation efforts is briefly presented here. It is useful to review these full-scale simulations, not only to provide a greater scope as to where the element-level testing and simulation efforts are heading, but also to define some limitations imposed by the large scale of the upper level simulations (e.g., mesh sizes, element types, general complexity, etc.) There are only a select number of large-scale composites crashworthiness simulation efforts available in the public domain, all of which have been generated from government-sponsored research programs. These include investigations conducted at the NASA Langley Research Center (LaRC) during the past 15 years [70–72] and the European Commercial Aircraft Design for Crash Survivability (CRASURV) program [73].

The earliest work comes from the U.S. Army, which initiated a research program in 1996 to evaluate the capabilities of commercial crash simulation codes for modeling the impact response of a composite helicopter drop tested at NASA LaRC [70]. Although this is the first example available of a full-scale crash simulation of a composite structure, the crush failure of the composite material was not a focal point of this research effort. Instead, the correlation between the experiment and the MSC.Dytran simulation focused on the energy absorption of the aluminum landing gear and the overall deformation of the full structure. Failure criteria and post-failure material characteristics were provided only for the metallic material models, and the composite models were assumed to remain elastic. Similarly, an MSC.Dytran model of a composite fuselage concept drop tested at NASA LaRC in 2000 [74] did not contain a damage model for the carbon composite materials. The crash model instead focused on the simulation of foam block energy absorbers placed in the subfloor of the fuselage section. Foam blocks were also used in the drop test and analysis of the AGATE composite aircraft in 2002 [72]. In these early days, just over 10 years ago, only the elastic model of carbon composite material systems was used because damage models were not yet mature enough to be used in full-scale simulations.

One of the only examples of a large-scale composite structure crash simulation that uses a composite damage material model comes from the CRASURV program. The drop test of a prototype composite fuselage section in this program was performed, and the simulation of the event was constructed using RADIOSS. The simulation built upon previous work within the CRASURV program to develop crashworthy composite subfloor designs of helicopters [8], which produced analysis data for the composite material model at lower levels of the BBA. Results from the fuselage section simulation were presented in 2004 by Delsart et al. [73]. The composite fuselage section that was drop tested used composite sinusoidal beams in the subfloor of the cargo bay as designed crash energy absorbers. The composite material model was calibrated using 0- and 90-direction coupon-level simulations in tension and compression, as well as +/-45 shear coupons of the unidirectional (UD) composite. A critical parameter of the material model was determined to be “I_{off},” which prescribes a condition for element erosion following failure. This parameter was not able to be calibrated at lower levels. A section of the cargo beam, as well as the relevant joining plates, brackets, and frame it was attached to, was modeled separately as a subcomponent model. Unfortunately, there were no experimental data to validate these models, and the subcomponent models served only to provide relative results of parametric trends of the modeling inputs and mesh sensitivity studies. The full fuselage section model was made up of shell and spring elements, with the finest elements used for the sinusoidal beams having a shell mesh size of 0.16″ (4 mm). The critical parameter was shown to be the I_{off} element erosion parameter within the RADIOSS material model, and only after comparison of the full-scale drop test results could appropriate values for this parameter in each section of the fuselage be determined. Delsart et al. concluded, “One can therefore estimate that the RADIOSS code may be used as a predesign tool insofar it permits—if not to precisely predict the right structural behavior—to cover a realistic range of crash behaviors, by activating the rupture criteria I_{off} on the different components of the structure.”

From each of these examples, certain similarities arise in the crash simulation model definitions, which can be considered to be well established and useful to know for the element-level simulations. For instance, in all cases, crash simulation always uses an explicit formulation of the FEA solver, which is conditionally stable, but computationally very expensive [47, 50, 64, and 75]. For that reason, shell (2D) elements are preferred over the more difficult brick (3D) elements, and, for composites, the approach has been to use orthotropic four-noded shell elements. In their review of FEA simulation of aircraft crashworthiness, Maia and de Oliveira [75] confirm that four-noded Belytschko-Tsay shell elements are the basis of all crashworthiness simulations, and that the results obtained from thousands of crashworthiness simulations over the course of two decades have established the reliability and usefulness of such elements. These elements are remarkably efficient and rely on the local material coordinate system, which greatly reduces spurious stresses and strains when subjected to large deformations. To model a laminated composite material, the plies are grouped into a single shell element in which each lamina is represented by one or more integration points virtually existing through the thickness [68–69]. This reduces the level of computational effort but prevents the simulation of interlaminar behavior. Models have been developed that use stacked shells to simulate groupings of plies in the laminate with tiebreak contacts in between the shell layers such that delamination modeling is possible [8, 9, 48, and 76]. The stacked shell element laminate, however, is too computationally expensive to use in large-scale models, and material delamination modeling has not yet been directly implemented at the full scale [77].

The current approach used in the aircraft industry requires adjustment and calibration of composite material models within the scope of the BBA to reach an agreement between experiment and crash simulation. As previously discussed, most of the development and expertise of the engineering application of the BBA to composite crash modeling has been conducted in the private sector. The privatized localization of expertise is an impediment upon the broader use of composites in primary crashworthy structures. It has also presented a problem to regulatory agencies, such as the FAA, which ultimately must regulate the safety of all aircraft that are beginning to implement emerging composite technologies. For this reason, a coordinated cross-organizational effort within the Crashworthiness Working Group of CMH-17, formerly MIL-HDBK-17 [1], was formed in 2005 by Feraboli and Rassaian [5]. This Working Group is comprised of representatives from the aerospace and automotive industries, academia, government laboratories, and regulatory agencies. In 2008, Dr. Rassaian launched a Numerical Round Robin (RR) exercise within the CMH-17 Crashworthiness Working Group, specifically to address crash simulation, with the goal of assessing the predictive capability of commercially available FEA codes for composite crash simulation, and to provide numerical best practices guidelines. Participants of the RR are from the automotive and aerospace industries (The Boeing Company—Research & Technology and Ford Motor Company), numeric analysis tool developers (Altair Engineering and SIMULIA), government agencies (the FAA), and academia (the University of Washington, the University of Utah, and Wichita State University). The research presented here was conducted within the context of the CMH-17 Crashworthiness Working Group.

Each participant of the RR developed a crash simulation strategy with its own solver, material model, contact definition, element type, and other modeling parameters specific to the individual strategy. The first two rounds of the RR exercise represent the first two levels of the BBA, shown in figure 11. Subsequent rounds focused on higher levels of the BBA, as shown in the RR roadmap in figure 14. In Round I, participants were asked to make blind predictions of the result of an element-level crush experiment using their chosen modeling strategy. The objective of Round I was to evaluate whether any modeling strategy could be purely predictive of the composite crushing behavior given only standardized coupon-level material property input values. The result of Round I showed that no such strategy existed, and that crush data were necessary to calibrate each material model. At the conclusion of Round I, participants were given the experimental data from the Round I crush element to calibrate their modeling strategies.

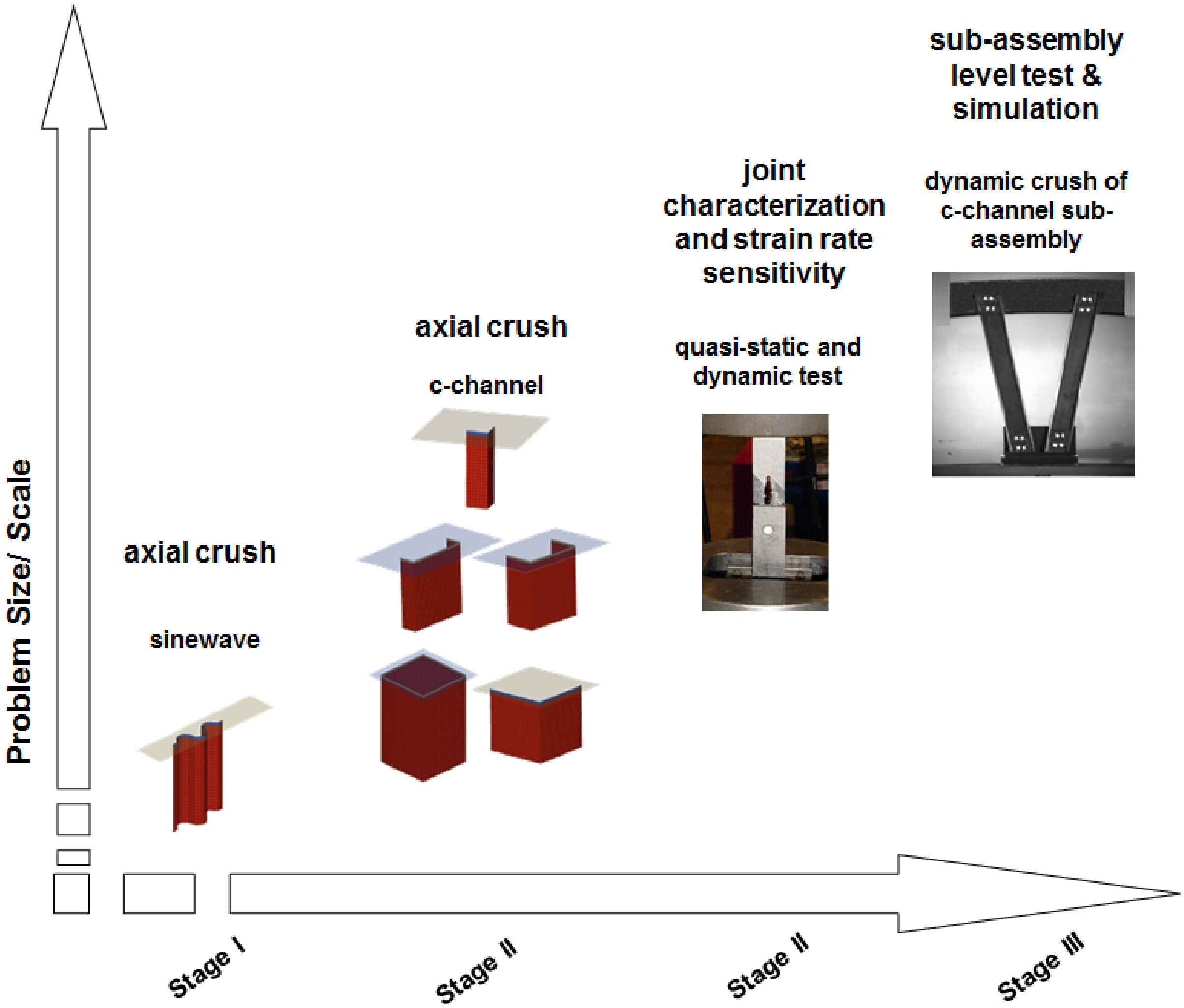

Figure 14. Roadmap of the CMH-17 crashworthiness working group numerical round robin exercise [78]

In Round II, participants were challenged to make blind predictions of various element-level crush experiments based on their modeling strategy, which had been calibrated using only the Round I experimental data. These predictions were not able to be made, and it was revealed that the experimental SEA measured from each element-level test varied considerably, even though the material system remained the same. The participants were then given all the element-level experimental results from Round II and were challenged to calibrate their modeling strategy such that it produced results that matched the experiments well. The first two rounds of the RR exercise represent the first two levels of the BBA shown in figure 11. Subsequent rounds focused on higher levels of the BBA to test the predictive capability composite crash modeling strategies following their calibration at the element-level.

The crash modeling strategy developed by the author at the University of Washington with Boeing Research and Technology for the CMH-17 RR exercise uses the LS-DYNA built-in composite material model MAT54. Although several other codes are available, LS-DYNA has traditionally been considered the benchmark for composite crash simulations and is extensively used in the automotive and aerospace industries to perform explicit dynamic post-failure simulations [6, 68, 79, and 80]. The LS-DYNA MAT54 material model is a good candidate for large, full-scale structural composite damage simulations because it is specifically meant for shell elements, for which all full-scale crash simulations are modeled with, and it relies on relatively few input parameters, most of which can be simply measured using standard material property testing. MAT54 therefore requires a reduced computational load that is appropriate for large-scale simulations, and was previously used in the BBA publication of Feraboli et al. [68].

3. PART I—EXPERIMENT

3.1 DESIGN OF EXPERIMENT

The material system selected for this study is carbon fiber/epoxy T700–2510 12k tow plain-weave (PW) prepreg supplied by Toray Composites America. This material system has a 270°F cure resin (132°C) designated for a vacuum bag and oven cure only. This material is used extensively for general aviation primary structures, and its properties are well documented as part of the FAA-sponsored AGATE program [81]. These properties are reproduced in table 2. An idealized stress-strain curve in both the axial and transverse directions is generated for the material system in figure 15 from the properties listed in table 2. A layup of $[(0/90)]_{8f}$ is used, which yields average cured laminate thicknesses of 0.073″ (1.85 mm).

Table 2. Material properties provided by the AGATE design allowables for T700SC 12k/2510 plain weave (PW) fabric [81]

	PW
Density	1.48-1.52 g/cc
F_1^{tu}	132 ksi
E_1^{t}	8.11 Msi
v_{12}	0.043
F_2^{tu}	112 ksi
E_2^{t}	7.96 Msi
F_1^{cu}	103 ksi
E_1^{c}	8.09 Msi
F_2^{cu}	102 ksi
E_2^{c}	7.77 Msi
F_{12}^{su}	19.0 ksi
G_{12}^{s}	0.609 Msi

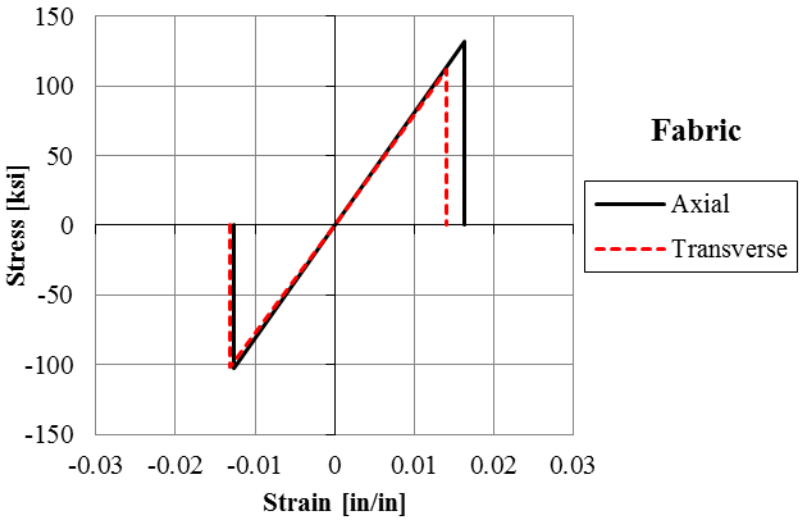

Figure 15. Idealized material stress-strain curves generated from published material properties for the fabric material system

3.2 CORRUGATED CFRP ELEMENT CRUSH TESTS

Three different corrugated web geometries are used to investigate how the degree and shape of the corrugation affect both stability and crush performance of the composite specimen. The design of the corrugated crush specimens comes from a previous experimental investigation that used various UD material systems, as published by Feraboli [82]. Each corrugated section features three half-periods repeated on alternate sides of the mid-plane and a short amount of flat material on either side of the corrugation for additional axial stability. The low-sine geometry features a sinusoid function of amplitude of 0.125″ (3.2 mm), and the high-sine geometry features a sinusoid function of amplitude of 0.25″ (6.4 mm). The semicircular specimen features a semicircular segment with a radius of 0.25″ (6.4 mm) repeated three times on alternate sides of the mid-plane. Detailed dimensions of all three geometries are shown in figure 16. The semicircular specimen was also the focus of earlier experimental and analytical research completed in this project, published by Feraboli and Wade [83–84].

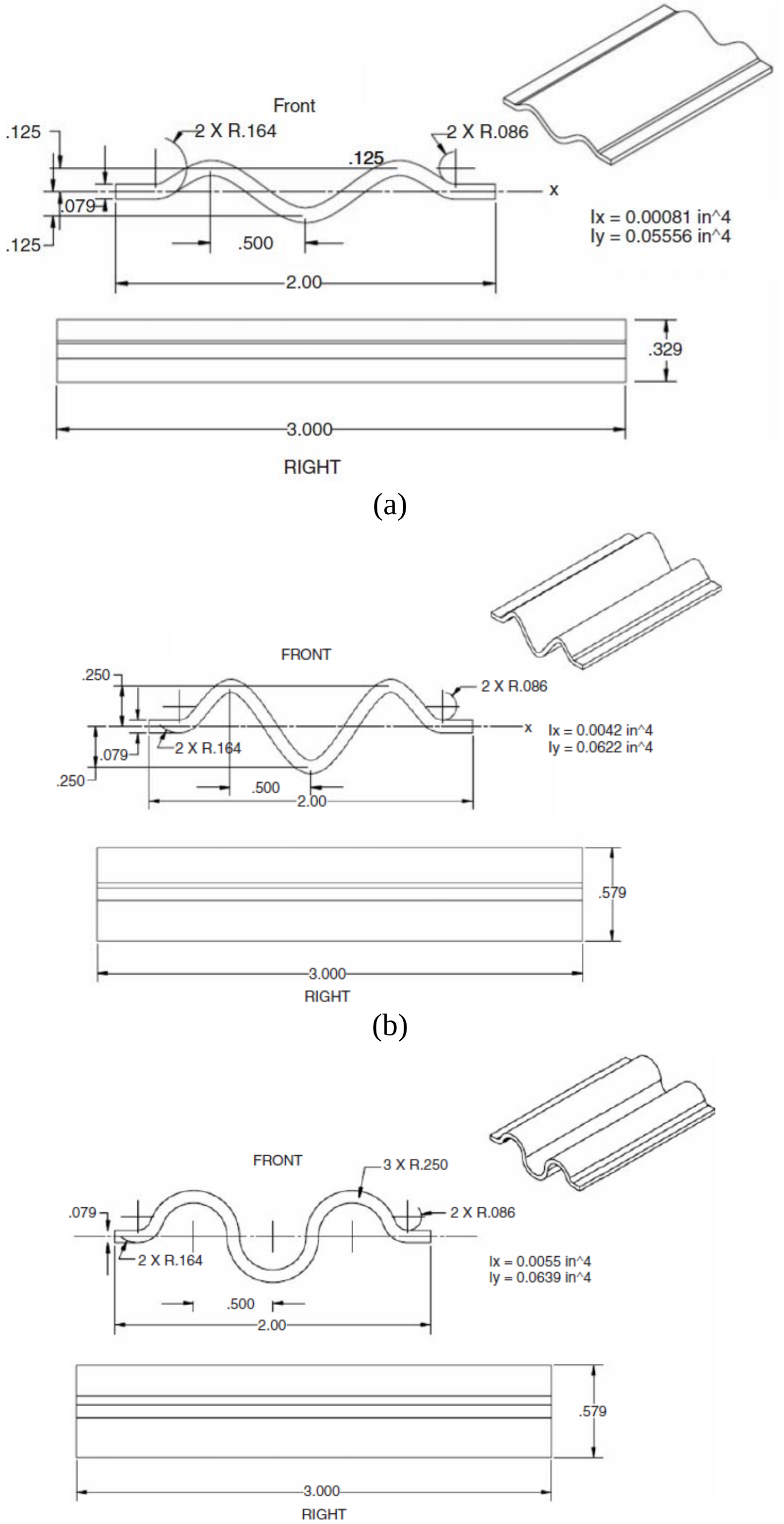

(a)

(b)

(c)

Figure 16. Three corrugated geometries and dimensions (all in inches) (a) low sine, (b) high sine, and (c) semicircular

Corrugated specimens are manufactured by press-molding through a set of aluminum matching tools, shown in figure 17. Each specimen is trimmed to be 3.0″ (76.2 mm) long with a 45-degree steeple machined along the top edge to initiate crushing behavior, a required feature when crush testing composite coupons [85–86].

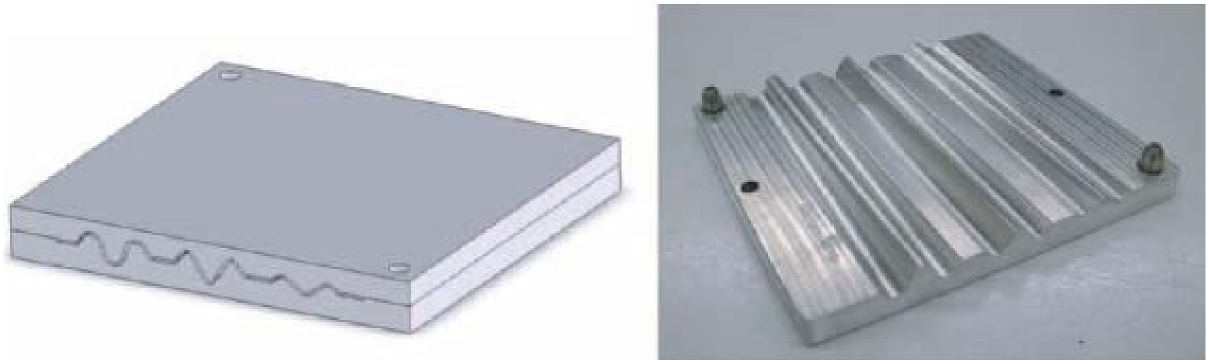

Figure 17. Aluminum tool used to make all three corrugated geometries

The corrugated specimens, which are self-supporting and do not require additional stabilization [25–29], are tested under quasi-static axial crushing. The test fixture is comprised of two flat steel plates: the base plate and the load plate. The specimen rests vertically between the two plates, with the triggered end facing upwards toward the loading platen, as shown in figure 18. Four posts with linear bearings are used to keep the plates aligned with respect to each other, and a self-aligning steel sphere is used to introduce the load from the crosshead into the load plate. Tests are conducted at a crosshead displacement rate of 2.0 in/min (50.8 mm/min) in an electromechanical universal test frame under displacement control. During the test, the load and crosshead displacement values are recorded. Five specimens were tested for repeatability.

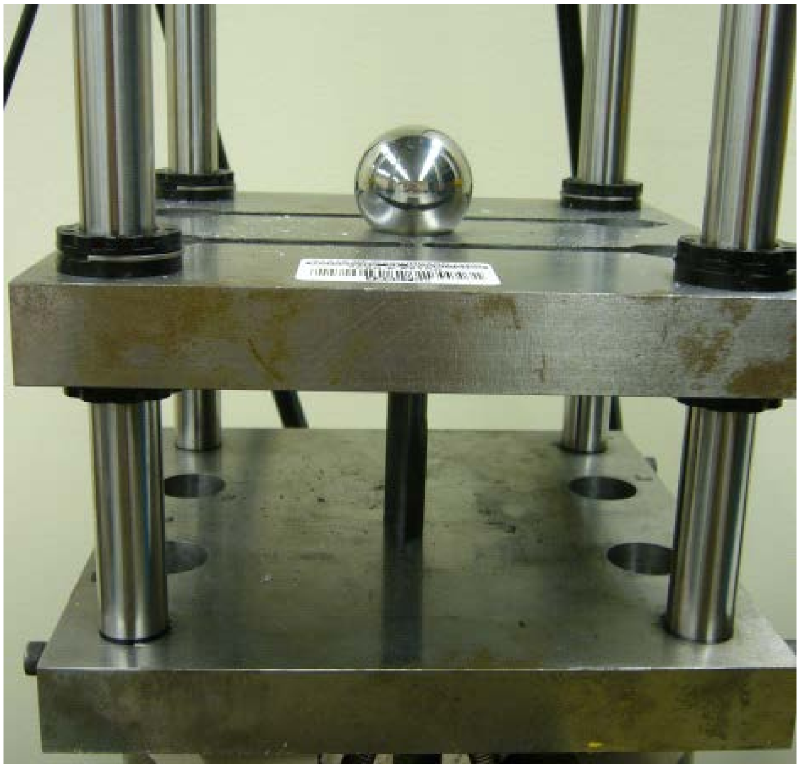

Figure 18. Crush coupon test fixture with corrugated specimen installed

3.3 TUBULAR CFRP ELEMENT CRUSH TESTS

The design motivation of the tubular crush elements is that the square tube element is representative of the classic tubular automotive crush structure element, while other shapes, such as C-channels and corners, can be easily manufactured as derivatives of the tube. In particular, the C-channel shape is a modern feature in the design of subfloor stanchions in large commercial transport aircraft designed to provide energy absorption [87]. Five tubular element shapes are crush tested to continue the study of the effect of cross-sectional geometry on the overall crush behavior and energy absorption. Each specimen uses the same AGATE fabric material and layup such that the geometry is the only variable in the experiment. At least four repetitions of each specimen are quasi-statically crush tested using the same test setup as the corrugated specimens. The five new element shapes are derivatives of a common square composite tube with rounded corners: a small and a large C-channel, a small and a large corner, and the tube itself. Schematics for these geometries and their dimensions are shown in figure 19.

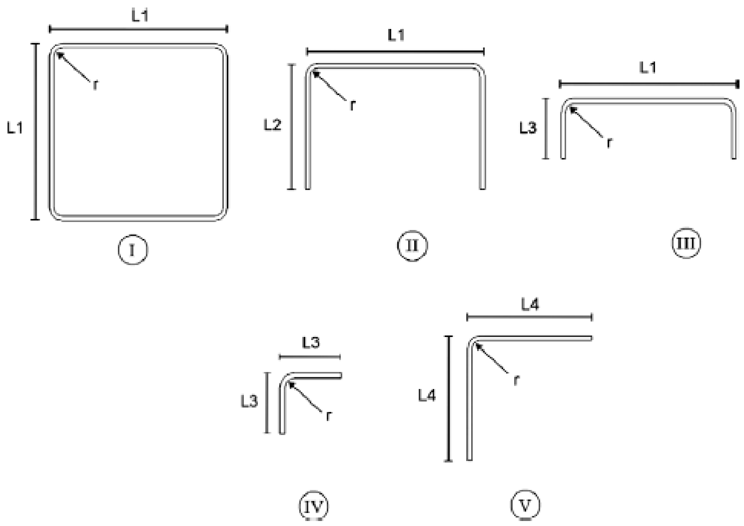

Dimension	Value	
L1	2.50 in.	(63.5 mm)
L2	1.75 in.	(44.5 mm)
L3	0.75 in.	(19.0 mm)
L4	2.00 in.	(50.8 mm)
r	0.175 in.	(4.45 mm)

Figure 19. Five channel geometries and dimensions (I) tube, (II) large C-channel, (III) small C-channel, (IV) small corner, and (V) large corner

To make the tubular derived shape elements, portions of the square tube specimen are cut using a diamond-coated tile saw. With a single cut performed off-axis on the square cross section, the large and small C-channels are obtained (see figure 20-II and 20-III, respectively). A second off-axis cut is performed on the small C-channel (see figure 20-IV), which isolates a single corner element whose dimensions are L3 x L3 (see figure 19-IV). The fifth channel specimen is obtained by performing two cuts on the original square tube section I (see figure 20-V), in the proximity of two opposing corners. What results is the large corner specimen with dimensions L4 x L4 (see figure 19-V).

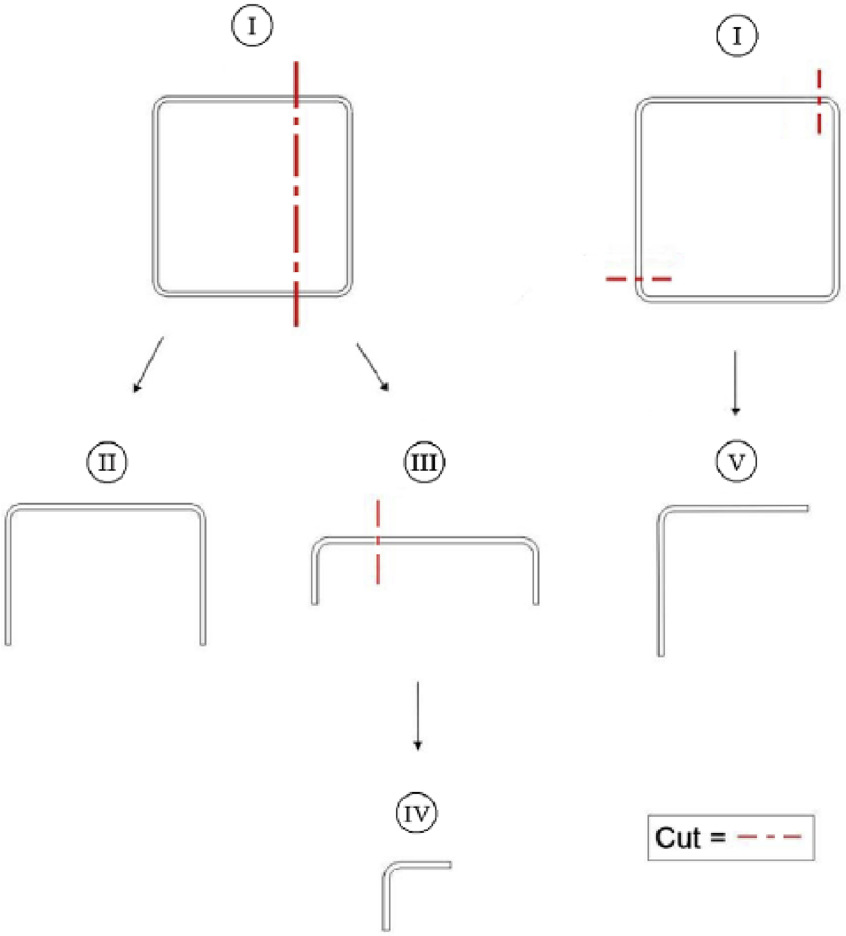

Figure 20. Schematic of machining operation performed to obtain channel test specimens II–V from the tubular specimen I

The total section lengths, or perimeters, for each of the five channel section geometries are shown in figure 21. Each of the five channel sections considered is comprised of one or more corner details and additional segments of flat material. If the small corner geometry, specimen IV, is used as a repetitive unit, each cross section can be subdivided into sections that are influenced by a single corner detail. These divisions are also shown in figure 21.

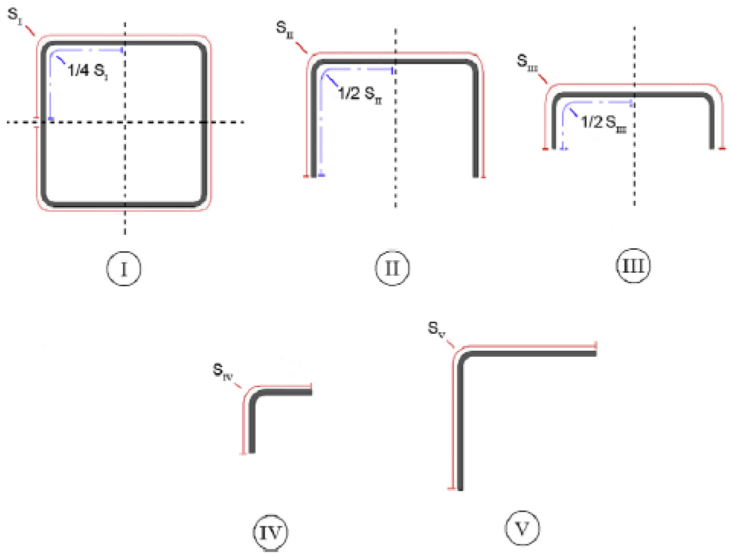

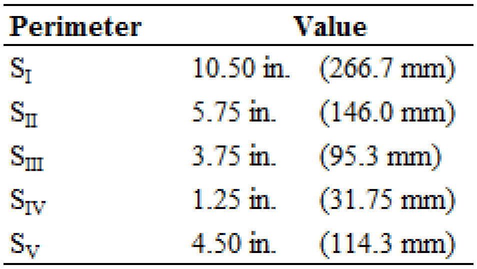

Perimeter	Value	
S_I	10.50 in.	(266.7 mm)
S_{II}	5.75 in.	(146.0 mm)
S_{III}	3.75 in.	(95.3 mm)
S_{IV}	1.25 in.	(31.75 mm)
S_V	4.50 in.	(114.3 mm)

Figure 21. The total section length (perimeter) for each channel geometry considered and the portion of each geometry influenced by a single corner detail

The repeating corner unit is defined as the small corner geometry (see figure 19-IV), and each cross section is subdivided into sections that are influenced by that single corner detail plus additional flat segments. For instance, the square tube (see figure 19-I) is subdivided into a quarter section, comprised of a single corner detail plus two additional flat segments on either side of the corner. This quarter section represents the portion of the square cross section that is influenced by a single corner detail because the double symmetry accounts for the other three corner elements. For the large and small C-channels, the half section comprises the single corner detail plus additional flat segments. In the case of the small C-channel, there is only one additional flat segment because the length of the small C-channel flange is equal to the small corner detail flange. For the large C-channel, the longer flange means that there are additional flat segments on both sides of the corner detail. The large corner element is not subdivided because it is comprised of a single corner detail with longer flat segments on both sides. The subdivided sections for each geometry that represents the portion influenced by a single corner element are shown for each of the five channel-type geometries in figure 22, where S_{IV} is the perimeter length of the small corner element, and the $\Delta S'$, $\Delta S''$, and $\Delta S'''$ quantities are the lengths of additional flat segments added for each geometry.

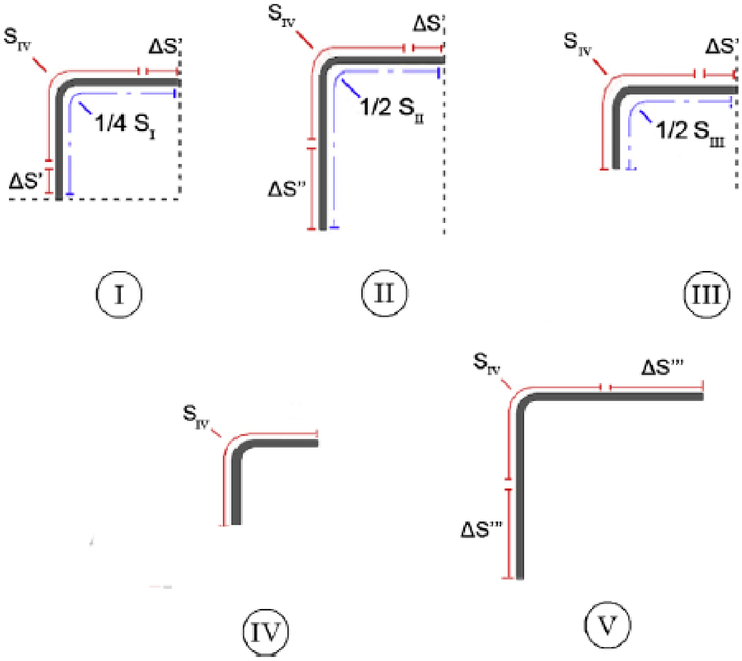

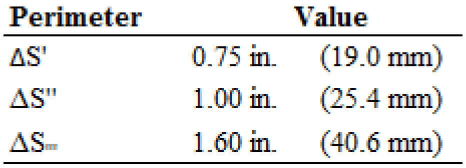

Perimeter	Value	
ΔS'	0.75 in.	(19.0 mm)
ΔS''	1.00 in.	(25.4 mm)
ΔS'''	1.60 in.	(40.6 mm)

Figure 22. Subdivision of section length into a corner detail, S_{iv}, and a portion of flat segments, δs, for each of the five channel-type cross-section geometries considered

The purpose of this effort is to be able to measure the SEA and crush behavior of a standalone corner element, S_{IV}, and then extrapolate the actual in-situ SEA and crush behavior of the flat sections, which is otherwise difficult to assess experimentally [12, 19, and 88]. In this way, creating derivative geometries from the common square tube geometry is advantageous to determine the influence of the cross-sectional geometry on crush behavior.

The tubular specimens are manufactured on an aluminum square tubular mandrel with 0.175″ (4.45 mm) radius rounded corners, shown in figure 23, and cured in an oven under vacuum pressure. Unlike for the corrugated shape elements, this tool is only one sided and therefore yields a different average cured thickness of 0.065″. (1.65 mm). After trimming, each specimen is 3.50″ (88.9 mm) long. A single-sided 45-degree chamfer is machined along the upper edge of every specimen to initiate crushing behavior during testing, as is done for the corrugated crush specimens.

Figure 23. Square aluminum mandrel with carbon composite tube

Specimens are crush tested between two aluminum plates with at least four repetitions per geometry. The upper plate travels at the same quasi-static rate of 2.0 in/min (50.8 mm/min) as used for the corrugated crush specimens. All section specimens except for the square tube are potted into an epoxy resin base to provide additional stability during crushing; therefore, their effective length is reduced by at least 0.5″ (12.5 mm).

4. EXPERIMENTAL RESULTS

The ability of a material to absorb energy can be expressed in terms of SEA, defined as the EA per unit mass of crushed structure. The EA is calculated as the total area under the force-stroke diagram, whereas the mass of the structure that undergoes crushing is given by the product of stroke l, cross-sectional area A, and density ρ:

$$SEA = \frac{\int F \cdot dl}{\rho \cdot A \cdot l} = \frac{F_{avg}}{\rho \cdot A} \tag{12}$$

Where F is the instantaneous crush force, and F_{avg} is the sustained crush force, which is the displacement-average value of the crush force and a direct indicator of the EA. The SEA is typically measured in J/g or kJ/kg units. The SEA is a well-accepted parameter used to quantify the ability of the material and structure to absorb energy. SEA is the primary metric used to characterize the energy absorption capability of the three corrugated and five tubular element shapes manufactured from the same carbon fiber composite material system. Additional metrics to compare the results of the crush tests include the observed crush failure mechanisms that occur in the failed material, as well as the shape of the load-displacement curve, including the initial peak load and average crush load.

4.1 CORRUGATED ELEMENT CRUSH TEST RESULTS

The corrugated geometries were successful in achieving stable sustained crushing associated with high energy absorption. The three corrugated crush specimens, before and after crush tests, are shown in figure 24. These images reveal a primarily fragmentation-based failure mode, as evidenced by the small dust-like remains of the crushed material, with little resemblance to the initial shape of the specimen. Experimental load, energy, and SEA curves from every corrugated element shape tested are shown in figures 25–27. The initial peak load, average crushing load, and SEA data for each corrugated test specimen is shown in table 3.

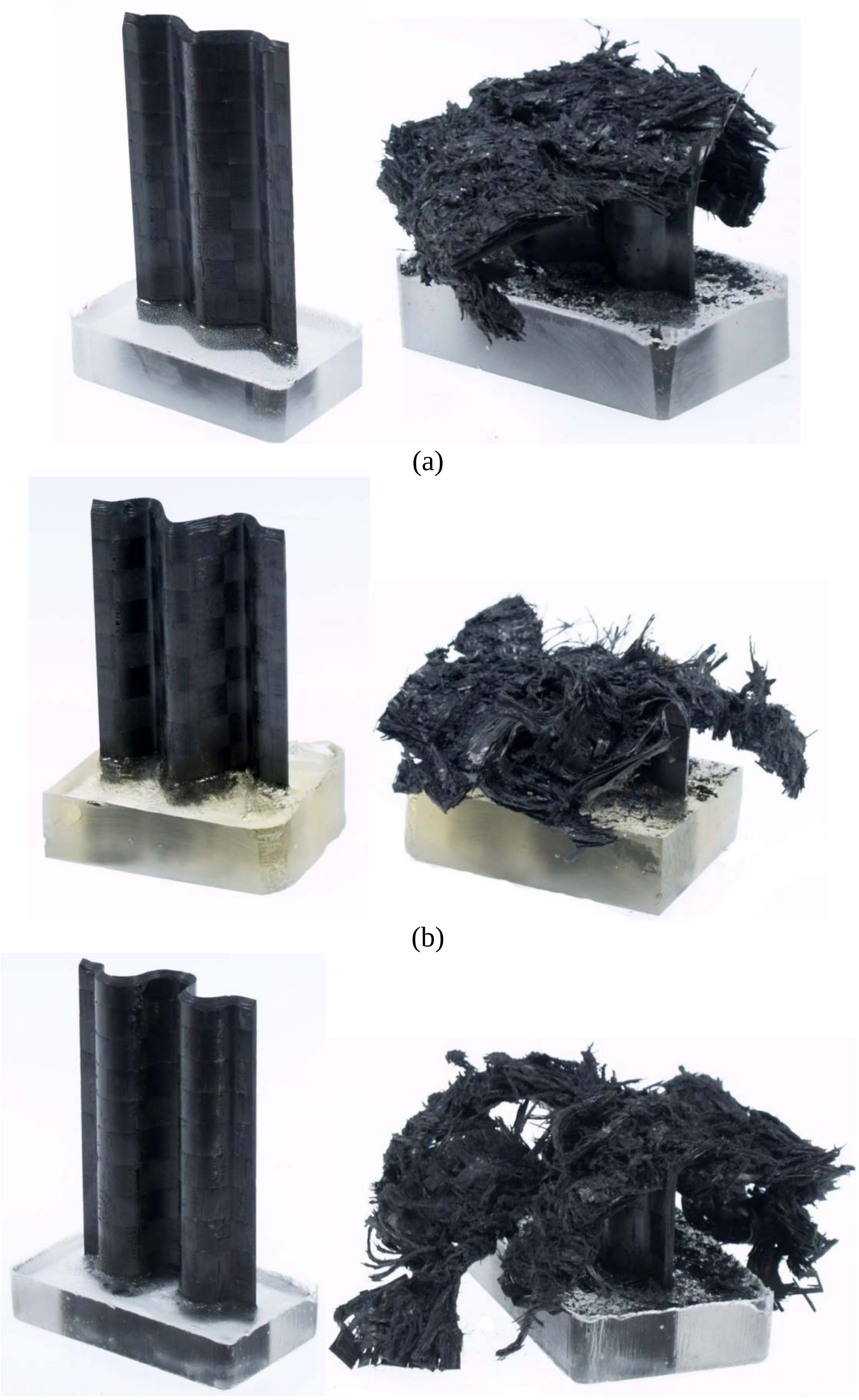

(a)

(b)

(c)

Figure 24. The (a) low sinusoid, (b) high sinusoid, and (c) semicircular corrugated crush specimens before and after testing

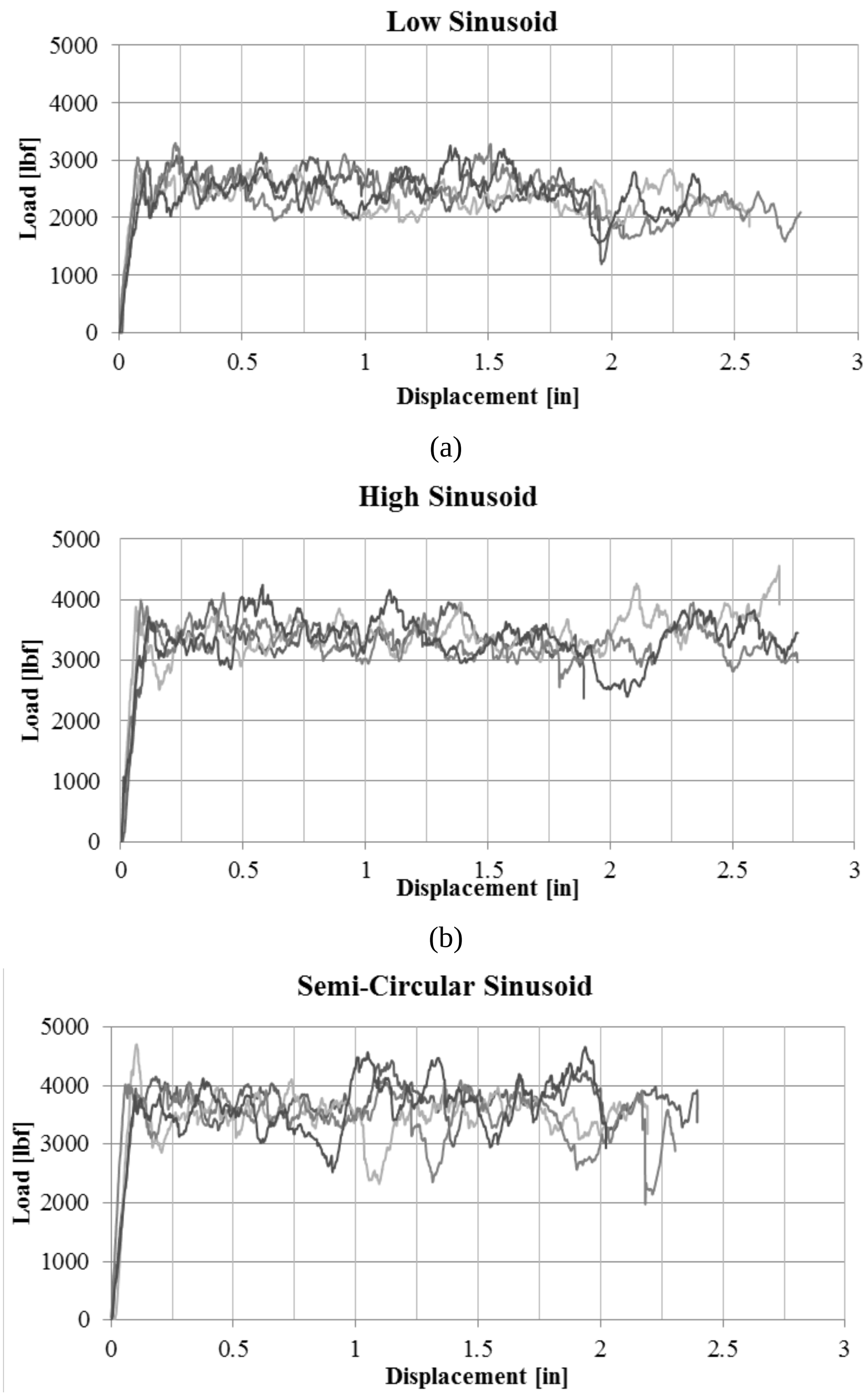

(a)

(b)

(c)

Figure 25. Load-displacement data from crush experiments of the (a) low, (b) high, and (c) semicircular sinusoid elements made from the fabric material system

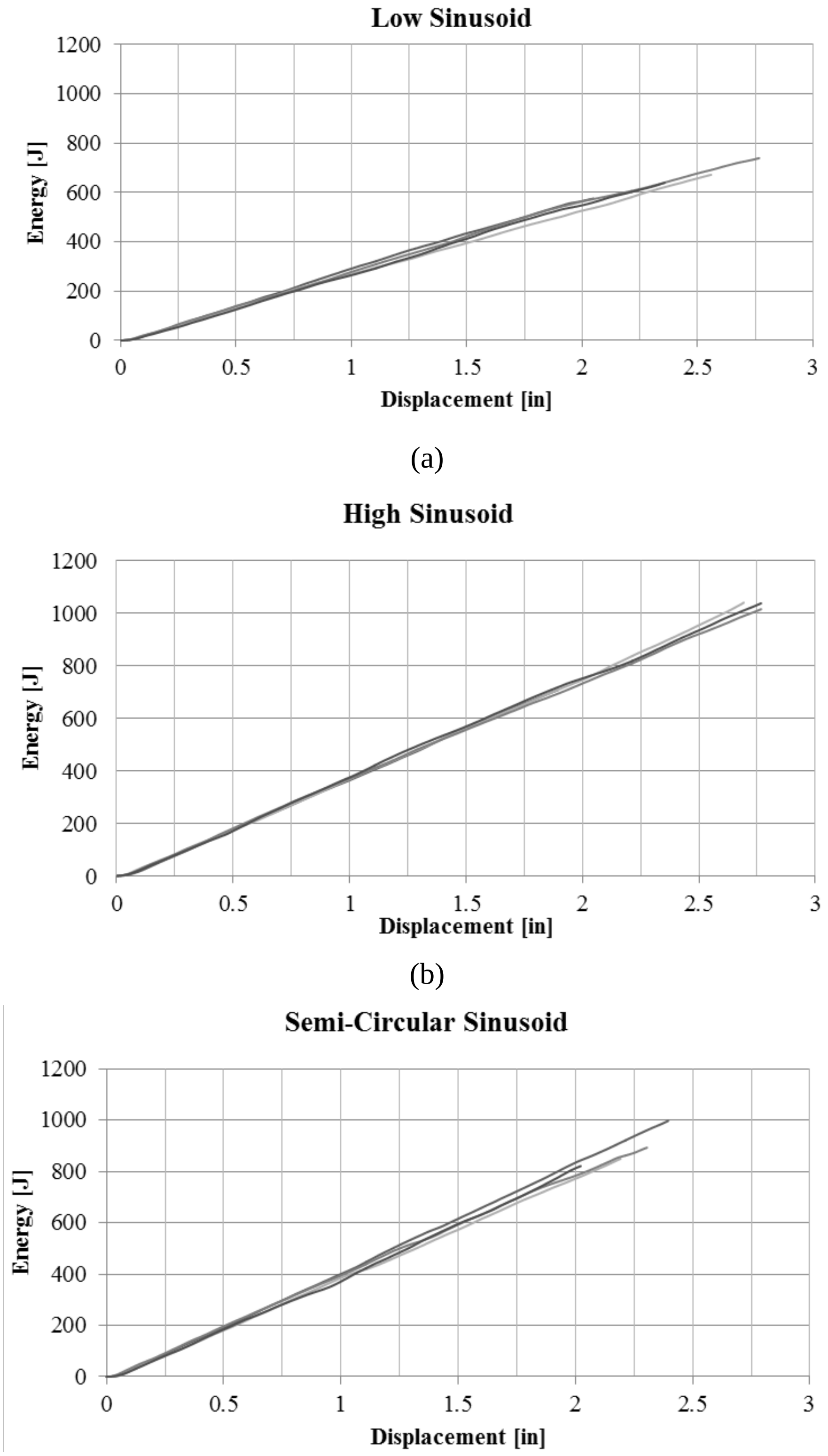

(c)

Figure 26. EA vs. displacement data from crush experiments of the (a) low, (b) high, and (c) semicircular sinusoid elements made from the fabric material system

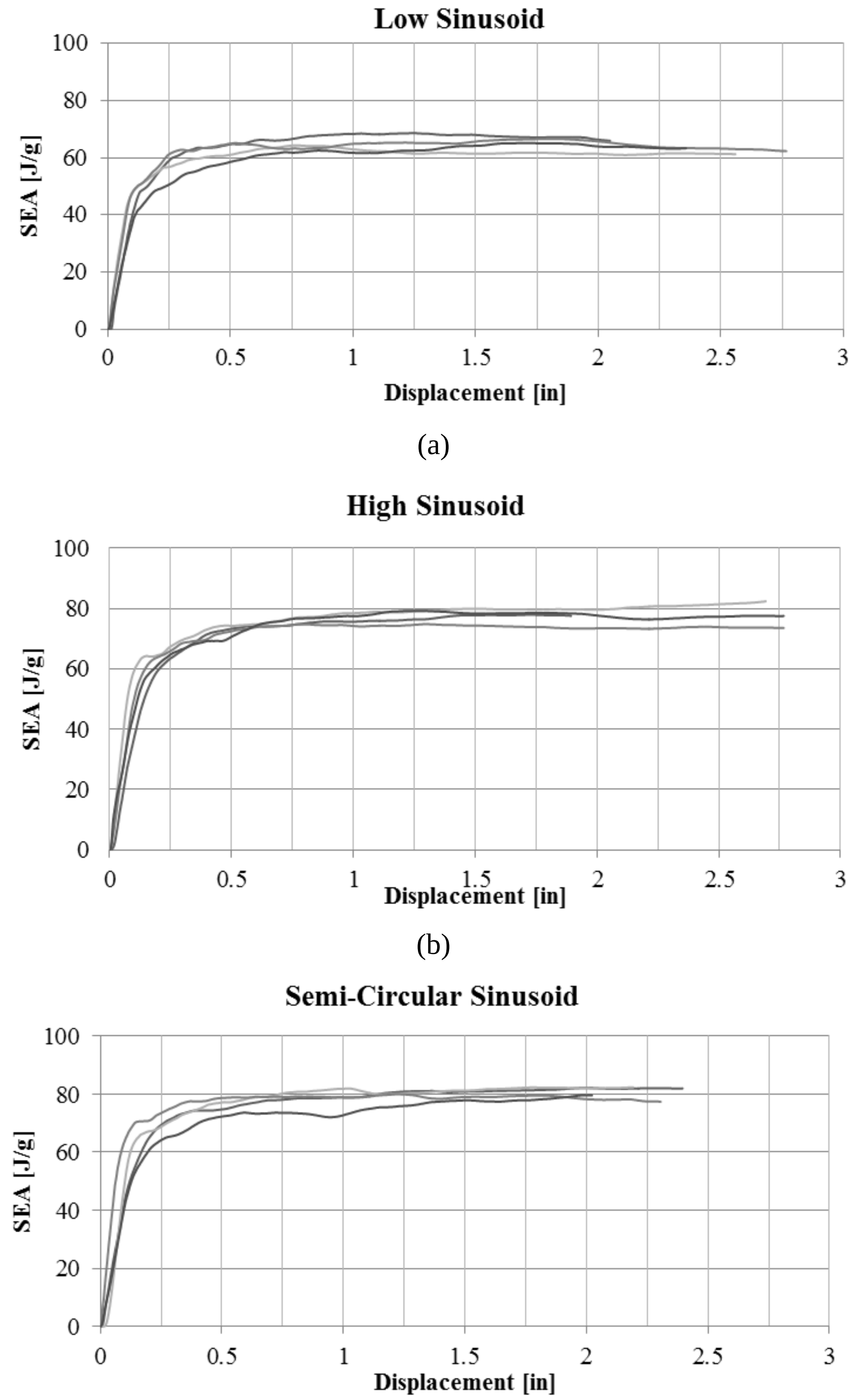

(a)

(b)

(c)

Figure 27. SEA vs. displacement data from crush experiments of the (a) low, (b) high, and (c) semicircular sinusoid elements made from the fabric material system

Table 3. Experimental load and SEA results from the sinusoid crush elements

		Initial Peak	Average Crush Load	SEA
		[lbf]	*[lbf]*	*[J/g]*
Low Sinusoid	Specimen 1	2860	2346	61.5
	Specimen 2	3048	2391	64.3
	Specimen 3	2767	2446	62.4
	Specimen 4	2983	2584	66.6
	Average	2915	2442	63.7
	CoV	4%	4%	4%
High Sinusoid	Specimen 1	3883	3457	78.4
	Specimen 2	3997	3285	73.1
	Specimen 3	3624	3395	75.1
	Specimen 4	3713	3367	76.4
	Average	3804	3376	75.8
	CoV	4%	2%	3%
Semi-circular Sinusoid	Specimen 1	4705	3483	79.5
	Specimen 2	4025	3399	77.8
	Specimen 3	3842	3681	74.7
	Specimen 4	3948	3761	79.2
	Average	4130	3581	77.8
	CoV	9%	5%	3%

CoV = coefficient of variation

The load-displacement curves, shown in figure 25, demonstrate the typical variability of experimental crush elements because the initial load peaks all fall within 4%–9% of one another, and the average crushing load falls within 2%–5%. These low variations are evidence of stable and repeatable composite crush elements. The energy-absorption data for the three sinusoid elements, shown in figure 26, confirm the test stability and repeatability. The rate of energy absorption is nearly constant within each family, with little variation between test specimens. In general, the semicircular and high sinusoid specimens absorb more energy at a faster rate than the low sinusoid specimen, but all three families are very similar. Finally, the SEA data, shown in figure 27, also demonstrate a low variability between test specimens within each sinusoid family; however, the low sinusoid element achieved consistently lower SEA measurement than the high and semicircular sinusoid elements. With only a slight change in the specimen geometry, the average crush load and SEA measurements are clearly affected.

4.2 TUBULAR ELEMENT CRUSH TEST RESULTS

Pictures of the tubular crush elements before and after crush testing are shown in figures 28–32. All tubular crush specimens presented in this study crushed in a stable manner, although their observed crush failure mode is evidently different from that of the corrugated elements. The general trend among the tubular specimens was that tearing failure occurs at the corners of the element shape, while most flat sections, such as flanges, bend and splay open, leaving the material damaged but partially intact. Along longer flat sections enclosed by corners, such as the C-channel webs and the square tube walls, progressive accordion-like folding occurs, where the material fractures at the folds, but significant portions of the flat material are damaged but remain partially intact.


(a) (b)

Figure 28. Square tube, specimen I, (a) before and (b) after crush testing

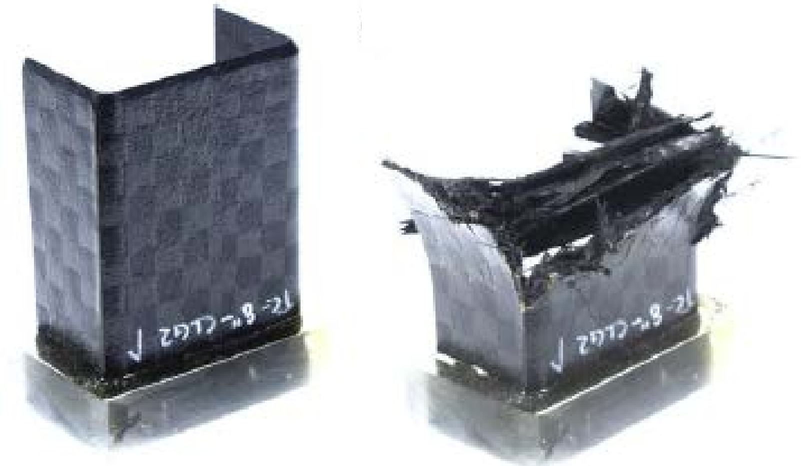
(a) (b)

Figure 29. Large C-channel, specimen II, (a) before and (b) after crush testing

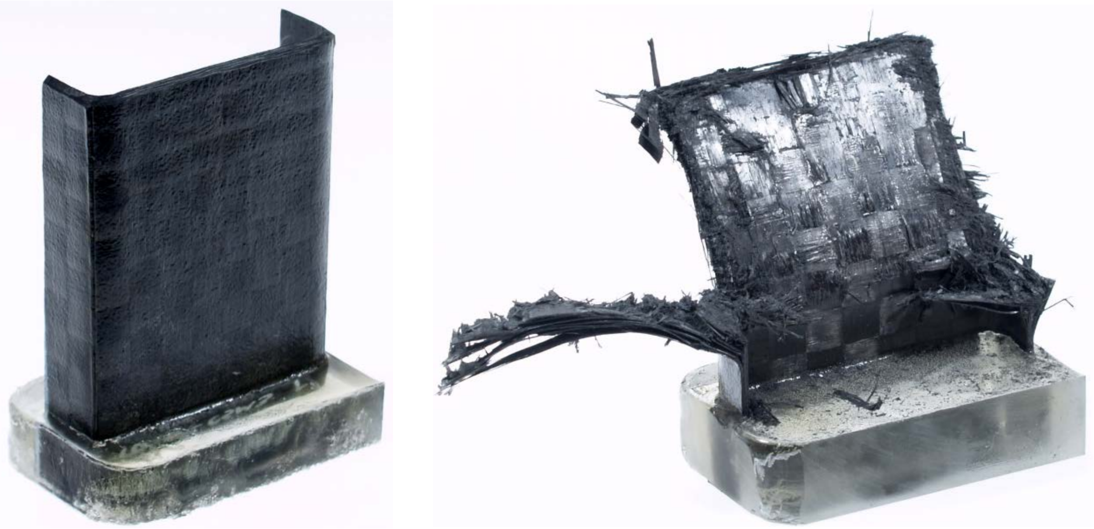
(a) (b)

Figure 30. Small C-channel, specimen III, (a) before and (b) after crush testing

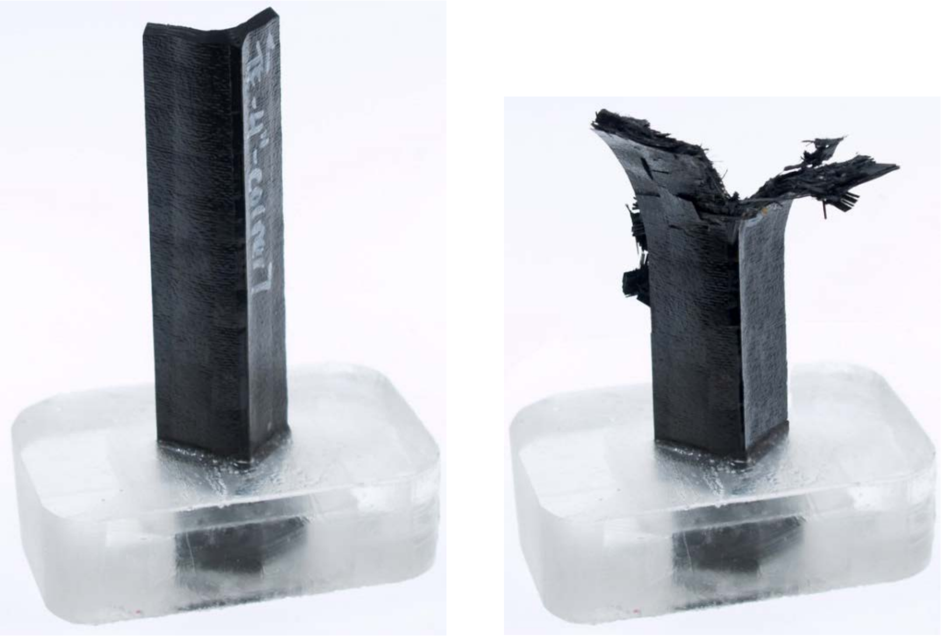
(a) (b)

Figure 31. Small corner, specimen IV, (a) before and (b) after crush testing

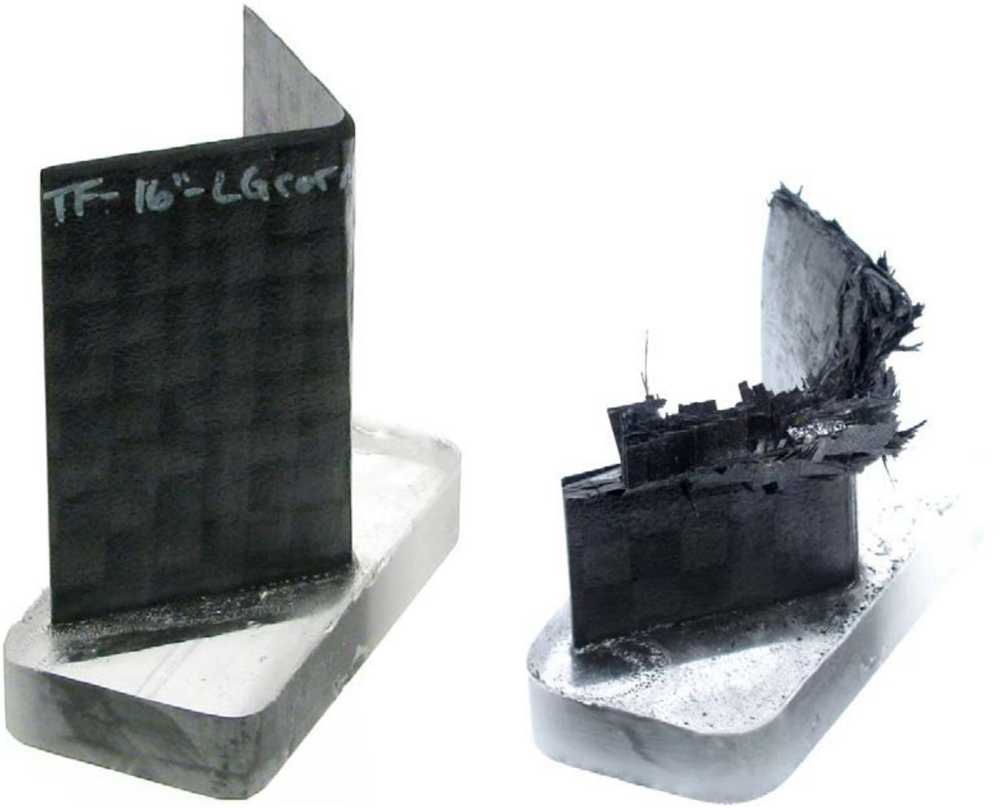

(a) (b)

Figure 32. Large corner, specimen V, (a) before and (b) after crush testing

The experimental load, energy, and SEA curves for each of the five tubular element shapes are shown in figures 33–35. In general, greater variability was observed in the crush results from the tubular specimens than from the corrugated specimens, as best evidenced by the percent variability of the initial peak load, average crush loads, and SEA measurements shown in table 4.

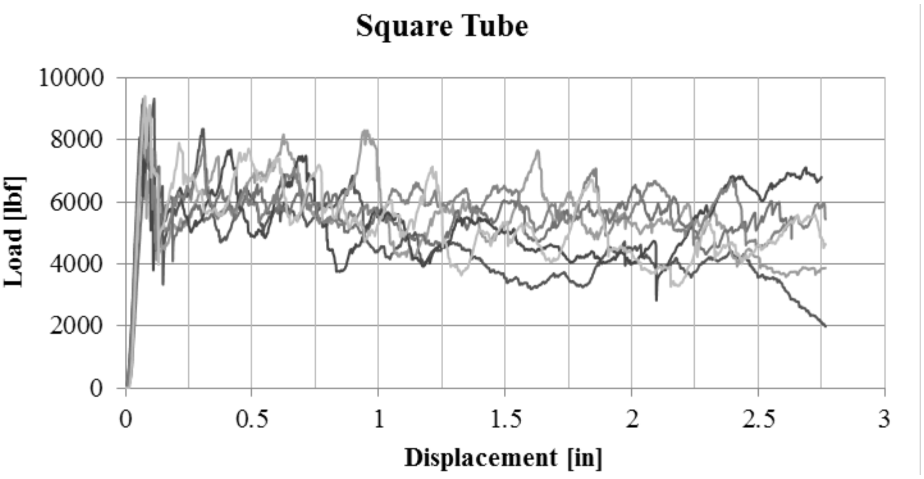

(a)

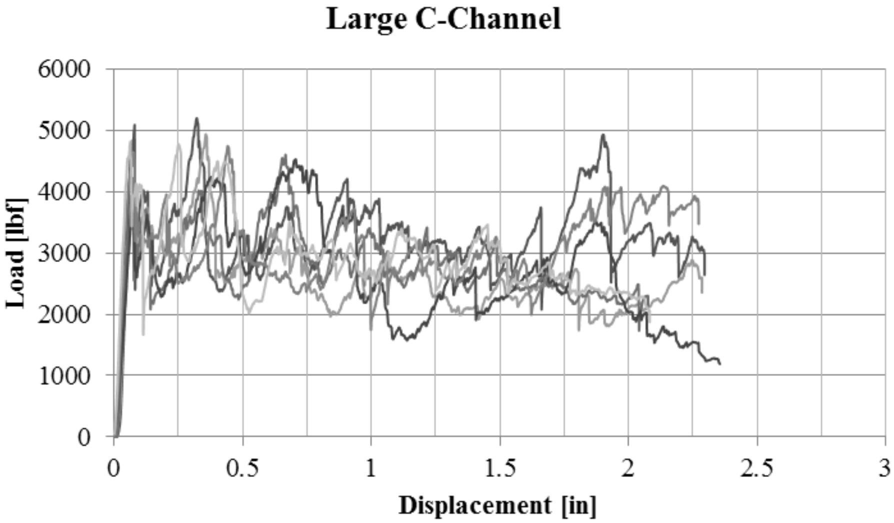

(b)

Figure 33. Load-displacement curves measured from crush experiments of (a) square tube, (b) large C-channel, (c) small C-channel, (d) small corner, and (e) large corner elements

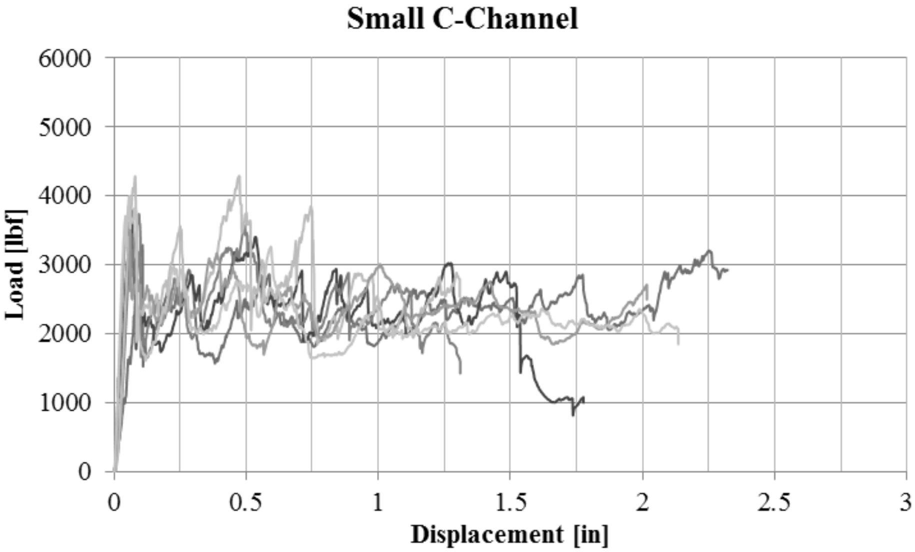

(c)

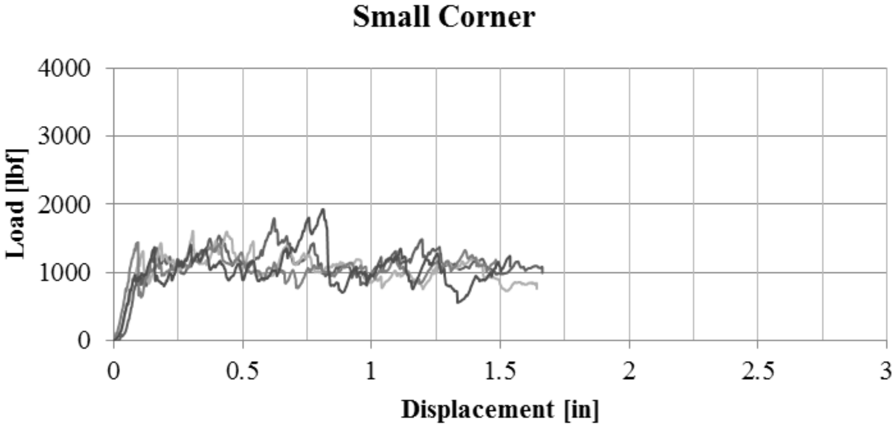

(d)

Figure 33. Load-displacement curves measured from crush experiments of (a) square tube, (b) large C-channel, (c) small C-channel, (d) small corner, and (e) large corner elements (continued)

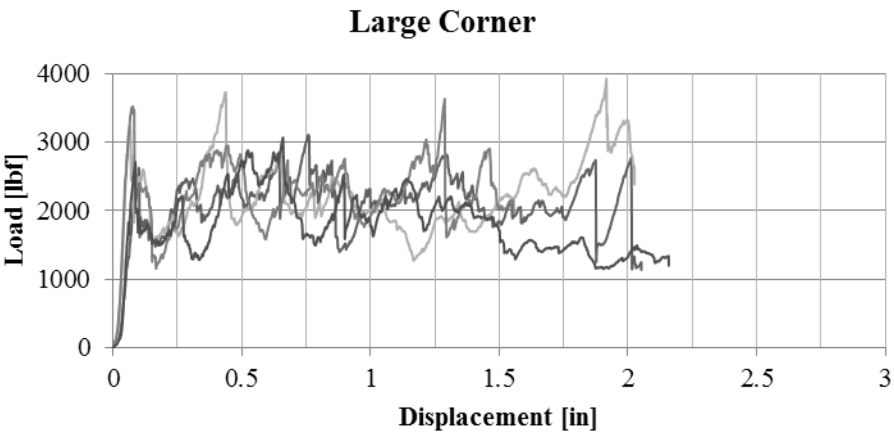

(e)

Figure 33. Load-displacement curves measured from crush experiments of (a) square tube, (b) large C-channel, (c) small C-channel, (d) small corner, and (e) large corner elements (continued)

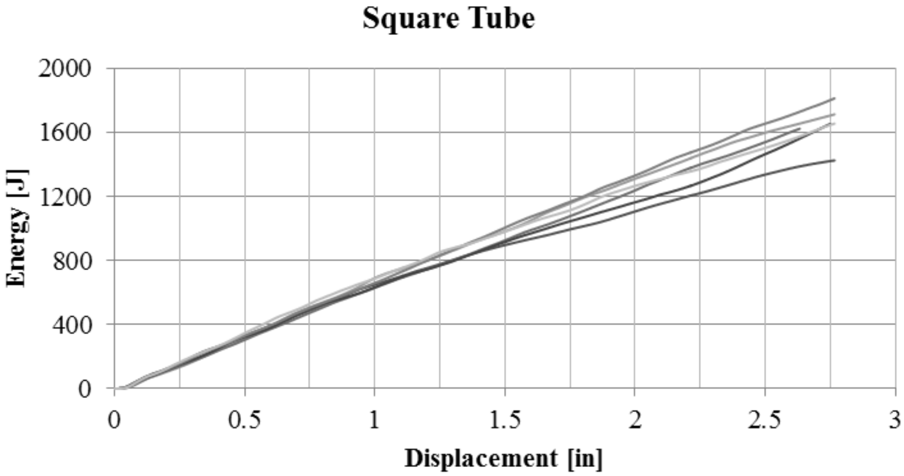

(a)

Figure 34. Energy absorption curves measured from crush experiments of (a) square tube, (b) large C-channel, (c) small C-channel, (d) small corner, and (e) large corner elements

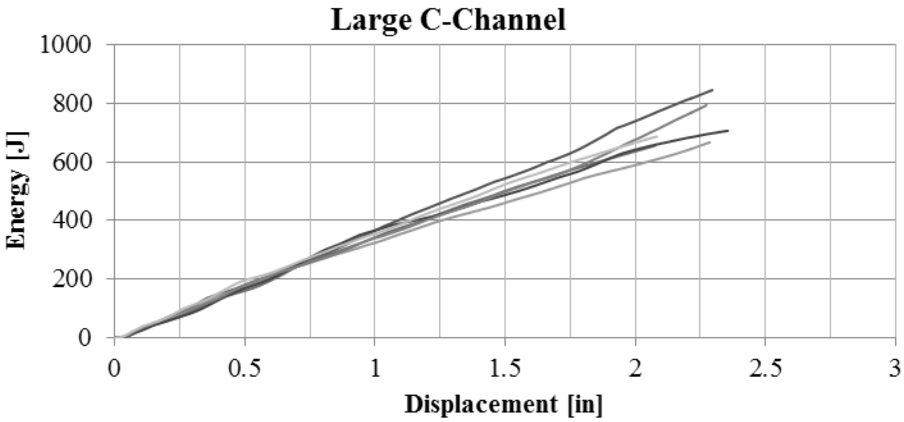

(b)

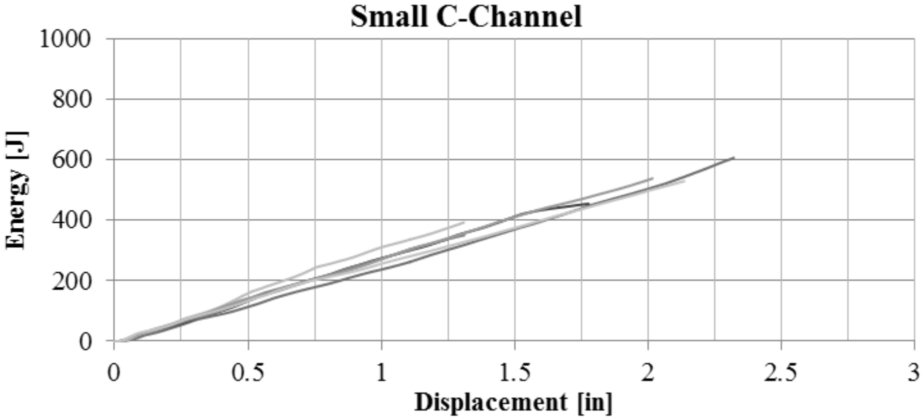

(c)

Figure 34. Energy absorption curves measured from crush experiments of (a) square tube, (b) large C-channel, (c) small C-channel, (d) small corner, and (e) large corner elements (continued)

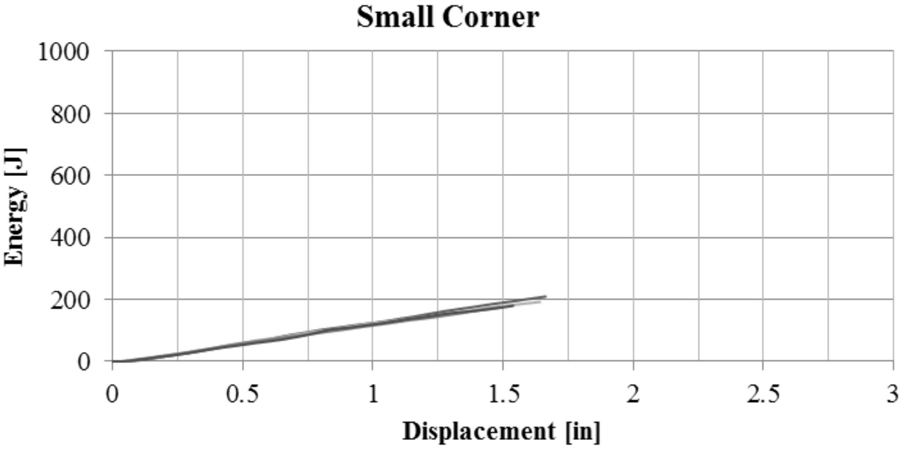

(d)

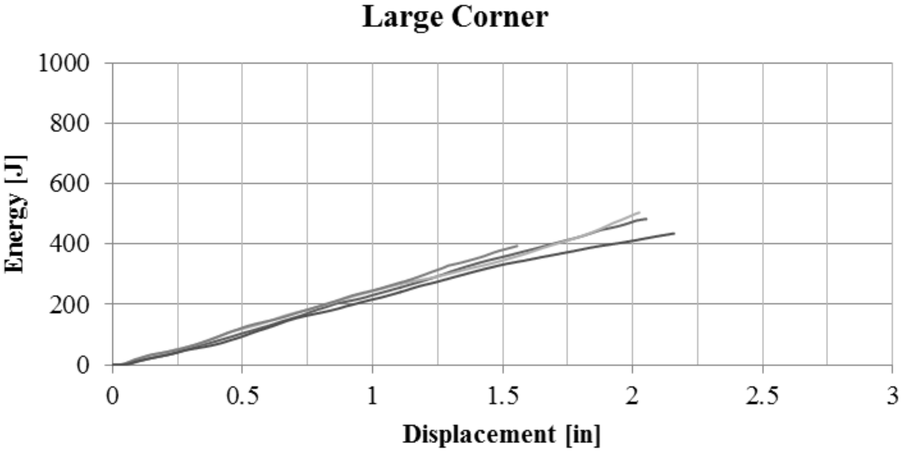

(e)

Figure 34. Energy absorption curves measured from crush experiments of (a) square tube, (b) large C-channel, (c) small C-channel, (d) small corner, and (e) large corner elements (continued)

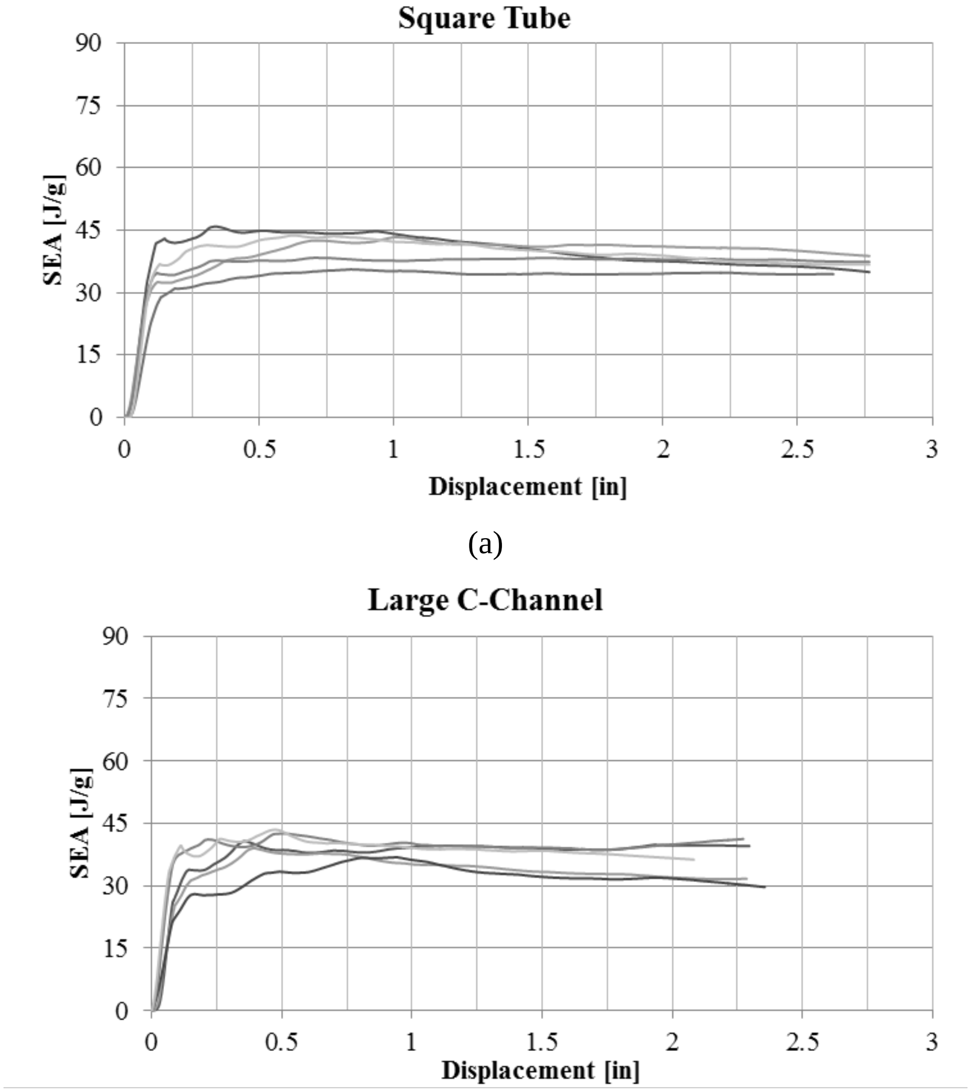

(a)

(b)

Figure 35. SEA curves measured from crush experiments of (a) square tube, (b) large C-channel, (c) small C-channel, (d) small corner, and (e) large corner elements

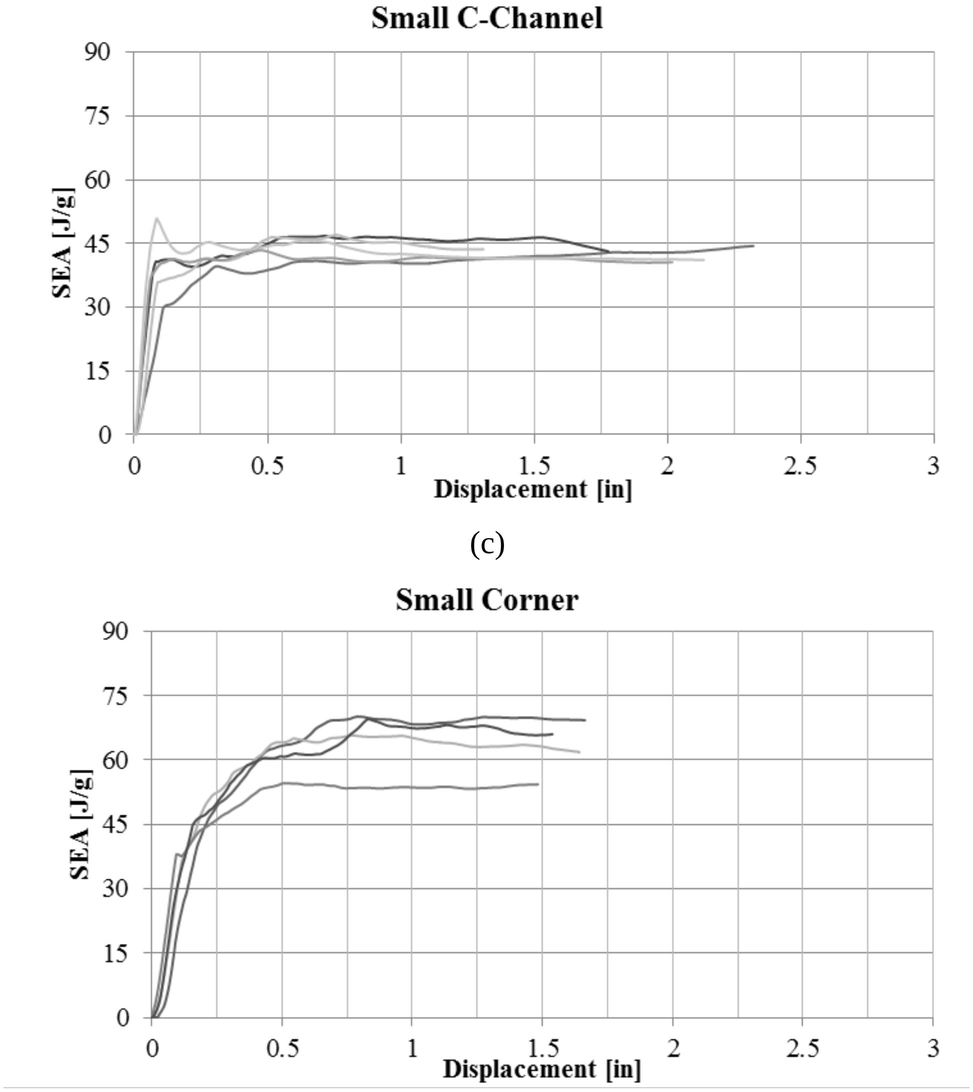

(c)

(d)

Figure 35. SEA curves measured from crush experiments of (a) square tube, (b) large C-channel, (c) small C-channel, (d) small corner, and (e) large corner elements (continued)

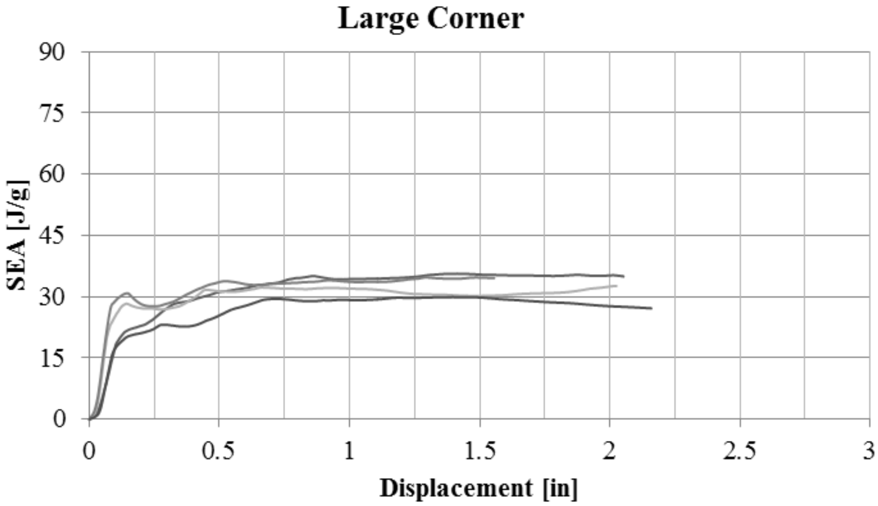

(e)

Figure 35. SEA curves measured from crush experiments of (a) square tube, (b) large C-channel, (c) small C-channel, (d) small corner, and (e) large corner elements (continued)

Table 4. Experimental load and SEA results from the tubular crush elements

		Initial Peak	Average Crush Load	SEA
		[lbf]	*[lbf]*	*[J/g]*
Square Tube	Specimen 1	7655	5544	34.4
	Specimen 2	9122	5377	31.7
	Specimen 3	9325	5866	37.7
	Specimen 4	9414	5366	40.1
	Specimen 5	9037	4605	40.6
	Average	8911	5352	36.9
	CoV	8%	9%	10%
Large C-Channel	Specimen 1	4112	2616	34.5
	Specimen 2	3682	2604	32.4
	Specimen 3	4637	3126	39.9
	Specimen 4	4816	2940	39.0
	Specimen 5	5083	3312	38.7
	Average	4466	2920	36.9
	CoV	13%	11%	9%
Small C-Channel	Specimen 1	3283	2431	41.4
	Specimen 2	3780	2288	44.8
	Specimen 3	4277	2721	43.4
	Specimen 4	3837	2386	41.3
	Specimen 5	3993	2208	42.8
	Average	3834	2407	42.7
	CoV	9%	8%	3%
Small Corner	Specimen 1	1309	1067	63.3
	Specimen 2	1440	1067	52.8
	Specimen 3	981	1068	65.1
	Specimen 4	1360	1161	67.9
	Average	1272	1091	62.3
	CoV	16%	4%	11%

Table 4. Experimental load and SEA results from the tubular crush elements (continued)

		Initial Peak	Average Crush Load	SEA
		[lbf]	*[lbf]*	*[J/g]*
Large Corner	Specimen 1	3242	2241	30.7
	Specimen 2	3505	2283	33.3
	Specimen 3	2701	1818	28.2
	Specimen 4	2623	2133	34.1
	Average	3018	2119	31.6
	CoV	14%	10%	8%

5. DISCUSSION OF EXPERIMENTAL RESULTS

To easily compare the results across the five different tubular and three corrugated crush specimen geometries, a representative load-displacement curve that best exemplifies the average peak and crush loads from each family is selected for each geometry. These curves are plotted in groups and are shown in figure 36. Average SEA values from all stable repetitions are given in table 5. Table 5 includes a value for a flat crush coupon SEA for this material system. Flat crush coupon testing was previously investigated as a part of this crashworthiness research, results from which were published by Feraboli [12]. The SEA results have clearly demonstrated that the crush element geometry has a significant influence on SEA, and that for composite materials, SEA is a structural, not material, property. For the fabric carbon fiber composite material system investigated, the energy absorption capability lies within the range of 23 J/g (flat, see [12]) to 78 J/g (corrugated).

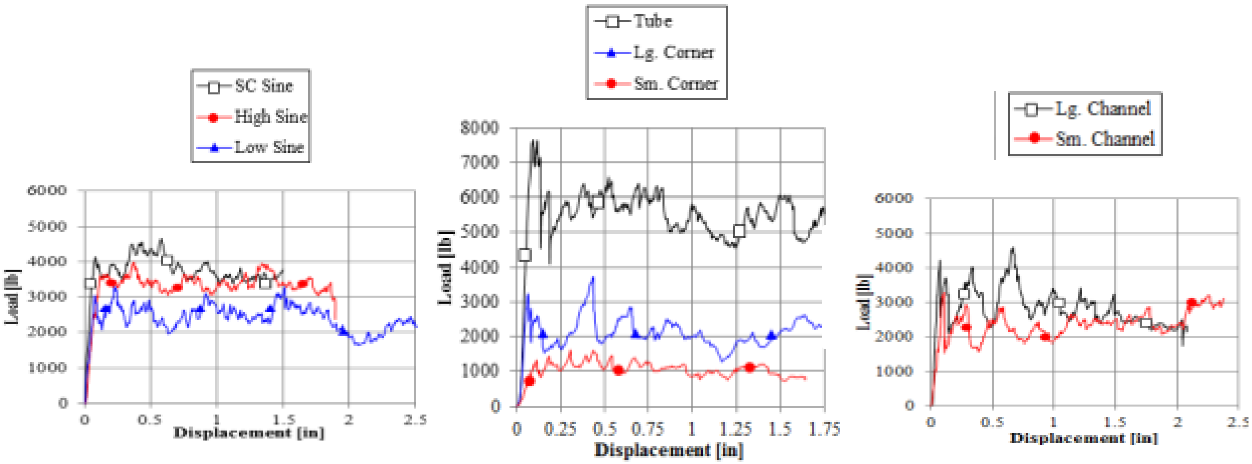

Figure 36. A sample load-displacement curve from crush tests of eight geometries

Table 5. SEA results from each of the nine crush-tested geometries

SC Sine	78 J/g	Tube	37 J/g	Large Channel	37 J/g
High Sine	76 J/g	Large Corner	32 J/g	Small Channel	43 J/g
Low Sine	70 J/g	Small Corner	62 J/g	Flat [12]	23 J/g

Given the clear influence of specimen geometry on the resulting SEA measurement demonstrated in the crush experiments, a relationship is sought that connects the geometric features of the crush specimens to the SEA. A deeper understanding of how the geometry influences the energy absorbing mechanisms occurring during crush failure was conducted

To relate the geometry to the SEA, the geometry is expressed in a mathematical form that is then compared against SEA results. One way to describe the geometry in terms of mathematics that differentiate each crush specimen by a different value is to consider the amount of curvature of the cross section relative to the total length, which can be expressed by a simple ratio. For the tubular specimens, the length of each curved section is equal to the length around one of the 90-degree corners, given by the quantity $({}^{\pi}/_{2})r$. The degree of curvature ratio is therefore defined to be the arc length of one corner divided by the length of the cross section influenced by that corner, as follows:

$$\varphi = \frac{(\pi / 2) r}{(S_i / n)} \tag{13}$$

Where r is the radius of the corner, S_i is the length of the cross section (along the mid-plane), and n is the number of corners in the geometry. Because this value is a length scale divided by another length scale, it is a nondimensional parameter. To calculate the degree of curvature of the corrugated geometries, the length of the corrugated portion of the section is divided by the total length, for which the only flat portions of the cross sections are the end flanges. The resulting degree of curvature values calculated for each geometry are given in table 6.

Table 6. Degree of curvature (φ) values for each of the nine geometries crush tested

SC Sine	0.895	Tube	0.105	Large Channel	0.096
High Sine	0.891	Large Corner	0.061	Small Channel	0.147
Low Sine	0.829	Small Corner	0.220	Flat	0.000

The SEA is plotted versus the degree of curvature for each geometry, which reveals a linear trend among the tubular shapes, which have lower degrees of curvature, as shown in figure 37(a). The corrugated shapes have a much higher degree of curvature, and at such values, the SEA reaches a maximum threshold at 70–80 J/g for this material type, as shown in figure 37(b). This result shows that more curvature in the cross-sectional geometry provides a better efficiency in crushing, and that a threshold exists for which increasing the amount of curvature of the geometry no longer contributes to raising the energy absorption capability.

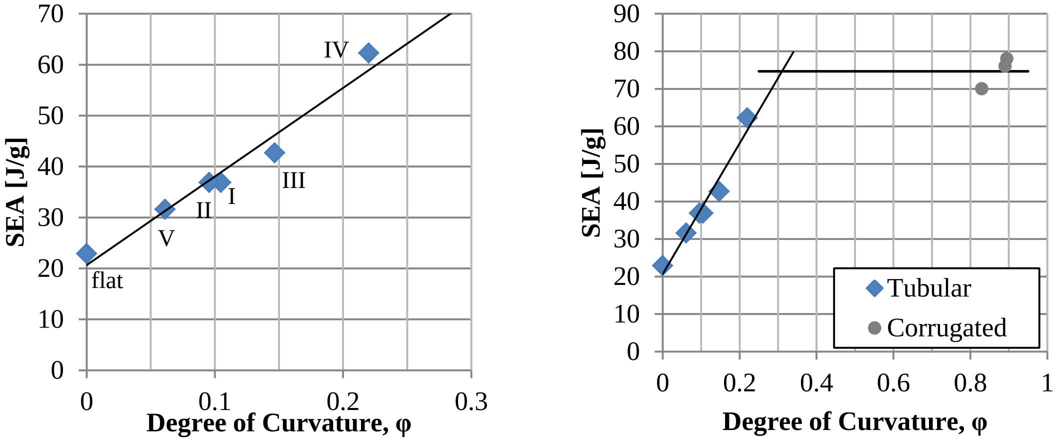

(a) (b)

Figure 37. SEA vs. φ for different crush geometries: (a) tubular only (b) all geometries

To better understand this phenomenon, a micrographic analysis of the crushed specimens was conducted to compare the higher SEA curve sections against the lower SEA flat sections. The analysis showed that the damaged region following the crush-front of curved sections was very small, and most of the specimen was intact and undamaged behind the crush-front. Micrographic analysis of flat sections revealed long cracks that had propagated beyond the crush-front through-material. A micrographic image from each curved (from a semicircular sinusoid specimen) and flat segment (from the web of a C-channel) in figure 38 shows both of these failure mechanisms. In the flat specimen, the damage had propagated more than five times the distance from the crush front than the damage in the curved specimen.

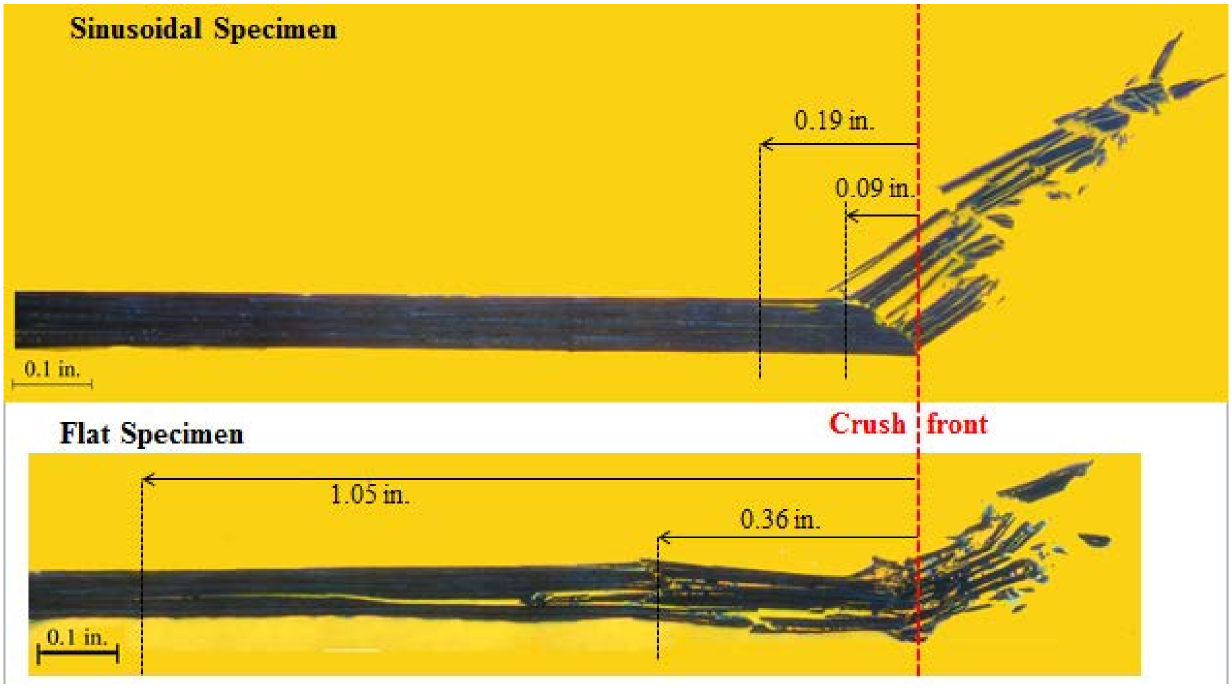

Figure 38. Micrographic analysis showing a short damage zone following tearing failure at the corners (top) and a large damage zone following ply splaying at the flat sections (bottom)

The key result is that the failure mechanisms of the curved and flat segments were observed to be very different. Referring to the energy-absorbing mechanisms identified by Hull [9], the flat sections of the tubular geometries splayed open, as shown in figure 30(b), and allowed crack propagation deep down into the interior of the material, as shown in figure 38. Material at the corners of the tubular sections, as shown in figure 31(b), and in the corrugated specimens, as shown in figure 24, experienced abundant fragmentation and tearing.

The distinct failure mechanisms of the flat and curved segments each have a different energy-absorbing capacity. The delamination failure mode observed in the flat segment absorbed little energy because most of the material remained intact, but a large crack propagated between plies, causing little fiber breakage. The fragmentation observed at the corners, however, absorbed a lot of energy in the process of breaking up the material, both fiber and matrix, into pieces as small as dust particles. The greater the delamination suppression provided by a geometry, the more fragmentation failure occurs and the higher the SEA. The amount of delamination suppression can be estimated by considering the degree of curvature of the geometry, as given in equation 13.

The estimation of SEA given by the degree of curvature must be considered with caution, however, as there is a material scale factor in terms of the specimen thickness and the local fiber buckling length, which affects the favored failure mechanism in the material. For instance, a large, perfectly circular specimen with a large diameter-to-thickness aspect ratio will have a geometric degree of curvature value $\phi = 1.0$, which would indicate a high SEA based on figure 37. With a large enough diameter, this hypothetical circular specimen would locally have a flat geometry (to the limit, locally $\phi = 0.0$), and experience splaying and delamination failure mechanisms, which would result in a low SEA. In the case of the crush experiments presented in this report, the aspect ratio of length to thickness for all nine specimens had similar values, and the material scale factor is not evident in the results. It would be appropriate to consider the geometric degree of curvature value ϕ a local phenomenon, for which the relevant scale factor must be determined for the material system tested.

6. EXPERIMENTAL CONCLUSIONS

In the process of investigating experimental methods to characterize the energy absorption capability of composite material systems, several key findings were made. First, unlike isotropic materials, SEA is not a material property of a composite material system, and SEA measurements vary significantly according to the geometry of the crush test element. This means that no single crush test can fully characterize the energy absorption capability of a composite material system, as several configurations must be tested that are each representative of geometric elements from the full structure for a range of SEA values to be collected. The underlying reason that there is a range of energy absorption capability in a single composite material system is because of the variety of crush failure modes observed during crush testing, which are each capable of absorbing different amounts of energy. These failure modes change according to the degree of curvature of the geometry of the crush test element.

Composite crush energy absorption mechanisms can be divided into two extreme behaviors, delamination/splaying and fragmentation, for which crush failure is a combination of varying degrees of both. In the delamination mode, little energy is expelled in splitting the material along an interlaminar crack front into two fronds, and the resulting SEA measurement is relatively low. This mode was observed for flat segments of the crush elements, where the geometry provides no delamination suppression, and a crack front can easily propagate through the material. Fragmentation failure is a more comprehensively destructive failure mode, which leaves little material intact and requires significant energy to break the material in such a manner, resulting in a high SEA measurement. Such failure occurs when crack propagation is suppressed by a highly curvaceous geometry.

As a result of these different crush failure modes, the energy-absorbing capability of the single composite material system investigated varied from 23 J/g (flat) to 78 J/g (corrugated). From the eight crush geometries tested, a relationship between the SEA and the degree of curvature of the crush test element geometry was developed. This curve describes the energy-absorption capability of the material according to the geometry of the crush element. This curve cannot be derived from a single test, and crush elements with different degrees of curvatures must be tested to develop such a curve for any other material, layup, thickness, etc. It is recommended that a flat coupon, low degree of curvature specimen (e.g., tube), and high degree of curvature specimen (e.g., corrugated) each be experimentally crush tested to develop this curve so the material SEA is fully characterized. Such a comprehensive characterization of the energy-absorbing capability of a composite material system is necessary so the analysis material model can be calibrated to match the varying experimental results at the element level (e.g., sinusoidal and tube specimens).

7. PART II—ANALYTICAL MODEL

LS-DYNA has traditionally been considered the benchmark for composite crash simulations and is extensively used in the automotive and aerospace industries to perform explicit dynamic post-failure simulations [6, 68, 79, and 80]. The LS-DYNA MAT54 material model is a great candidate for large, full-scale structural composite damage simulations because it is specifically meant for shell elements, with which all full-scale crash simulations are modeled, and it relies on relatively few input parameters, most of which can be simply measured using standard material property testing. MAT54 therefore requires a reduced computational load that is appropriate for large-scale simulations. A portion of this research effort has been dedicated to the full characterization and documentation of this material model, which is a good candidate for composite crash simulation. This was accomplished through single-element studies (published in FAA report DOT/FAA/TC-14/19 [89]), parametric studies of crush simulations, and the careful study and interpretation of the MAT54 source code generously provided by LSTC. The result of this effort is a more comprehensive description of MAT54, its parameters, and its governing equations, which was previously published [89–90], and is replicated in section 7.1.

The crush simulation of the semicircular corrugated shape was developed first, and results of its development and the subsequent parametric studies performed on the user input parameters have been published in the FAA report DOT/FAA/AR-11/21 [83]. Using the fully developed corrugation crush model, the eight different structural crush element shapes, whose experimental crush test results are presented in this report, are modeled to investigate the predictive capability of this modeling approach given new structural element geometries. From this comprehensive set of investigations using MAT54 to model a composite material undergoing crush failure, a detailed protocol describing the procedure to calibrate the MAT54 model for crush simulation, as well as a definition of the required experimental data necessary to achieve a calibrated material model, has been established, and is presented at the conclusion of part II of the report.

7.1 DESCRIPTION OF THE MAT54 MATERIAL MODEL

LS-DYNA has a handful of preexisting composite material models, such as MAT22 and MAT54/55, which are progressive failure models that use a ply-discount method to degrade elastic material properties; and MAT58, MAT158, and MAT162, which use CDM to degrade the elastic properties after failure. The LS-DYNA MAT54 material model is of interest for large full-scale structural damage simulations because it is a relatively simple material model, which requires minimal input parameters. Not only does this reduce the computational requirement of a simulation, but it also reduces the difficulty and amount of material testing necessary to generate input parameters.

MAT54 is a progressive failure model, which is designed specifically to handle orthotropic materials, such as UD tape composite laminates. To support the following discussion, the entire MAT54 input deck is shown in figure 39, with all 43 user-defined input parameters grouped into seven categories for clarity. The definitions for all of these parameters are listed in table 7.

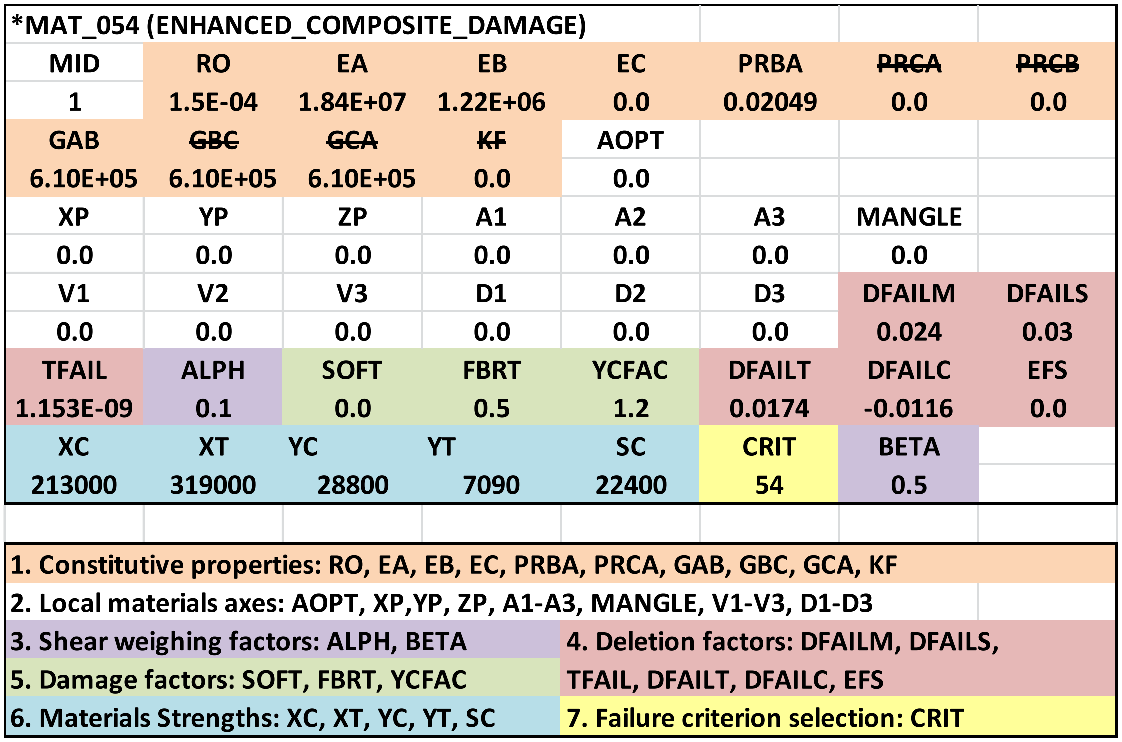

*MAT_054 (ENHANCED_COMPOSITE_DAMAGE)							
MID	RO	EA	EB	EC	PRBA	~~PRCA~~	~~PRCB~~
1	1.5E-04	1.84E+07	1.22E+06	0.0	0.02049	0.0	0.0
GAB	~~GBC~~	~~GCA~~	~~KF~~	AOPT			
6.10E+05	6.10E+05	6.10E+05	0.0	0.0			
XP	YP	ZP	A1	A2	A3	MANGLE	
0.0	0.0	0.0	0.0	0.0	0.0	0.0	
V1	V2	V3	D1	D2	D3	DFAILM	DFAILS
0.0	0.0	0.0	0.0	0.0	0.0	0.024	0.03
TFAIL	ALPH	SOFT	FBRT	YCFAC	DFAILT	DFAILC	EFS
1.153E-09	0.1	0.0	0.5	1.2	0.0174	-0.0116	0.0
XC	XT	YC	YT	SC	CRIT	BETA	
213000	319000	28800	7090	22400	54	0.5	

1. Constitutive properties: RO, EA, EB, EC, PRBA, PRCA, GAB, GBC, GCA, KF	
2. Local materials axes: AOPT, XP,YP, ZP, A1-A3, MANGLE, V1-V3, D1-D3	
3. Shear weighing factors: ALPH, BETA	4. Deletion factors: DFAILM, DFAILS,
5. Damage factors: SOFT, FBRT, YCFAC	TFAIL, DFAILT, DFAILC, EFS
6. Materials Strengths: XC, XT, YC, YT, SC	7. Failure criterion selection: CRIT

Figure 39. Material deck for MAT54 and the 43 parameters shown in seven categories; strikethrough parameters are inactive

Table 7. MAT54 user input definitions and required experimental data

Name	Definition	Type	Measurement
MID	Material identification number	Computational	N/A
RO	Mass per unit volume	Experimental	Density test
EA	Axial Young’s modulus	Experimental	0-degree tension test
EB	Transverse Young’s modulus	Experimental	90-degree tension test
EC	Through-thickness Young’s modulus	(Inactive)	
PRBA	Minor Poisson’s ratio v_{21}	Experimental	0-degree tension test with biaxial strain measurement
PRCA	Minor Poisson’s ratio v_{31}	(Inactive)	
PRCB	Major Poisson’s ratio v_{12}	(Inactive)	
GAB	Shear modulus G_{12}	Experimental	Shear test
GBC	Shear modulus G_{23}	(Inactive)	
GCA	Shear modulus G_{31}	(Inactive)	
KF	Bulk modulus	(Inactive)	
AOPT	Local material axes option	Computational	N/A
XP,YP,ZP	Used for AOPT = 1	(Inactive)	
A1,A2,A3	Vector ‘a’ used for AOPT = 2	Computational	N/A
MANGLE	Angle used for AOPT = 3	Computational	N/A
V1,V2,V3	Vector used for AOPT = 3	Computational	N/A
D1,D2,D3	Used for AOPT = 2, solid elements	(Inactive)	
ALPH	Elastic shear stress non-linear factor	Shear factor	None; Default 0.1 recommended
BETA	Shear factor in tensile axial failure criterion	Shear factor	None; Default 0.5 recommended
DFAILT	Axial tensile failure strain	Experimental	0-degree tension test
DFAILC	Axial compressive failure strain	Experimental	0-degree compression test
DFAILM	Transverse failure strain	Experimental	90-degree tension and compression tests; May require adjustment for stability
DFAILS	Shear failure strain	Experimental	Shear test
EFS	Effective failure strain	Optional	Combination of standard tests
TFAIL	Time step failure value	Computational	Derived from numeric time-step
FBRT	Axial tensile strength factor after 2-dir failure	Damage factor	None; Default 0.5 recommended
SOFT	Material strength factor after crushing failure	Damage factor	Requires calibration against element-level crush data
YCFAC	Axial compressive strength factor after 2-dir failure	Damage factor	None; Default 1.2 recommended
XT	Axial tensile strength	Experimental	0-degree tension test
XC	Axial compressive strength	Experimental	0-degree compression test
YT	Transverse tensile strength	Experimental	90-degree tension test
YC	Transverse compressive strength	Experimental	90-degree compression test
SC	Shear strength	Experimental	Shear test
CRIT	Specification of failure criterion	Computational	N/A; Requires value of 54 for MAT54

In the elastic region, the material stress-strain behaviors for fiber (axial, one-direction), matrix (transverse, two-direction), and shear (12-direction) are given by:

$$\varepsilon_{11} = \frac{1}{E_1}\left(\sigma_{11} - v_{12}\sigma_{22}\right) \tag{14}$$

$$\varepsilon_{22} = \frac{1}{E_2}\left(\sigma_{22} - v_{21}\sigma_{11}\right) \tag{15}$$

$$2\varepsilon_{12} = \frac{1}{G_{12}}\sigma_{12} + \alpha\sigma_{22}{}^{3} \tag{16}$$

In equation 16, the α (ALPH in table 7) input parameter is a weighting factor for the nonlinear shear stress term. ALPH cannot be experimentally determined, but needs to be calibrated by trial and error whenever shear is present. Table 7 provides a recommended value for ALPH, which was found to provide consistently stable results in crush simulations.

Beyond the elastic region, MAT54 uses the Hashin [57] failure criteria to determine individual ply failure, as given by equations 17–20 using MAT54 user input notations defined in table 7, where *ef*, *ec*, *em*, and *ed* are called history variables. History variables are failure flags, which represent tension and compression for the fiber direction, and tension and compression for the matrix direction, respectively. It should be noted that all of these quantities assume that the one-direction (axial) is the fiber direction, while the two-direction (transverse) is the matrix direction.

For the tensile fiber mode where $\sigma_{11} \geq 0$:

$$ef^{2} = \left(\frac{\sigma_{11}}{XT}\right)^{2} + \beta\left(\frac{\sigma_{12}}{SC}\right)^{2} - 1\begin{cases} \geq 0 & failed \\ < 0 & elastic \end{cases} \tag{17}$$

Upon failure: $E_1 = E_2 = G_{12} = v_{12} = v_{21} = 0$.

The shear stress weighting factor β (BETA in table 7) allows the user to explicitly define the influence of shear in the tensile fiber mode. Setting BETA = 0 reduces equation 17 to the Maximum Stress failure criterion. Selecting the BETA value is a matter of preference and can otherwise be done by trial and error. Table 7 provides a recommended value for BETA, which was found to provide consistently stable results in crush simulations.

For the compressive fiber mode where $\sigma_{11} < 0$:

$$ec^{2} = \left(\frac{\sigma_{11}}{XC}\right)^{2} - 1\left(\frac{\sigma_{11}}{XC}\right)^{2} - 1\begin{cases} \geq 0 & failed \\ < 0 & elastic \end{cases} \tag{18}$$

Upon failure: $E_1 = v_{12} = v_{21} = 0$.

For the tensile matrix mode where $\sigma_{22} \geq 0$:

$$em^2 = \left(\frac{\sigma_{22}}{YT}\right)^2 + \left(\frac{\sigma_{12}}{SC}\right)^2 - 1 \begin{cases} \geq 0 & failed \\ < 0 & elastic \end{cases} \tag{19}$$

Upon failure: $E_2 = v_{21} = G_{12} = 0$.

For the compressive matrix mode where $\sigma_{22} < 0$:

$$ed^2 = \left(\frac{\sigma_{22}}{2SC}\right)^2 + \left[\left(\frac{YC}{2SC}\right)^2 - 1\right]\frac{\sigma_{22}}{YC} + \left(\frac{\sigma_{12}}{SC}\right)^2 - 1 \begin{cases} \geq 0 & failed \\ < 0 & elastic \end{cases} \tag{20}$$

Upon failure: $E_2 = v_{12} = v_{21} = G_{12} = 0$.

When one of the above conditions is exceeded in a ply within the element, the specified elastic properties for that ply are set to zero. The mechanism by which MAT54 applies this elastic property reduction, however, only prevents the failed ply from carrying increased stress rather than reducing the stress to zero or a near-zero value. The equation used by MAT54 to determine one- and two-direction element stresses in the i^{th} time step provides insight into this mechanism:

$$\begin{bmatrix} \sigma_{11} \\ \sigma_{22} \end{bmatrix}_i = \begin{bmatrix} \sigma_{11} \\ \sigma_{22} \end{bmatrix}_{i-1} + \begin{bmatrix} C_{11} & C_{12} \\ C_{21} & C_{22} \end{bmatrix}_i \begin{bmatrix} \Delta\varepsilon_{11} \\ \Delta\varepsilon_{22} \end{bmatrix}_i \tag{21}$$

When ply failure occurs in the i^{th} time step, constitutive properties in the stiffness matrix C go to zero, but the stresses from the i-1 time step are non-zero. This leads the failed ply stresses to be constant and unchanged from the stress state just prior to failure. The resulting plastic behavior, shown in figure 40, occurs only when the strength is reached before the failure strain (DFAIL in figure 40). Elastic property degradation following failure in MAT54 works in this way, rather than degrading properties in the elastic equations, equations 14–16, which would result in a reduced or zero-stress state in a failed ply.

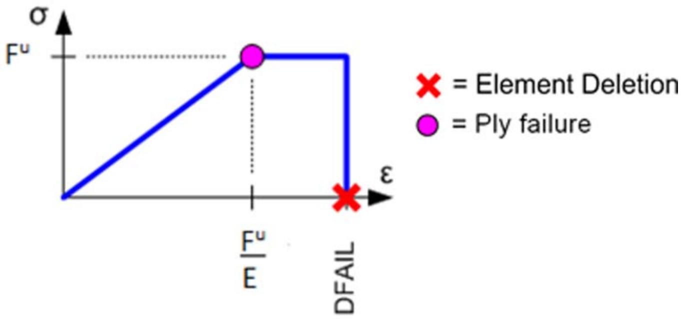

Figure 40. Elastic-plastic stress-strain behavior of MAT54

The MAT54 FBRT and YCFAC strength-reduction parameters are used to degrade the pristine fiber strengths of a ply if compressive matrix failure takes place. This strength reduction simulates damage done to the fibers from the failed matrix, and it is applied using:

$$XT = XT^{*} * FBRT \tag{22}$$

$$XC = YC^{*} * YCFAC \tag{23}$$

where a parameter with an asterisk denotes the pristine value of the input parameter. The FBRT parameter defines the percentage of the pristine fiber strength (XT) that is left following compressive matrix failure; therefore, its value should be in the 0–1 range. The YCFAC parameter uses the pristine matrix strength YC to determine the damaged compressive fiber strength, which means that the upper limit of YCFAC is XC/YC. The input value for the two parameters FBRT and YCFAC cannot be measured experimentally and must be determined by trial and error.

The softening reduction factor (SOFT) parameter is a strength-reduction factor for crush simulations. This parameter reduces the strength of the elements immediately ahead of the crush front to simulate damage propagating from the crush front. The strength degradation is applied to four of the material strengths as follows:

$$\left\{XT, XC, YT, YC\right\} = \left\{XT, XC, YT, YC\right\}^{*} * SOFT \tag{24}$$

where the asterisk indicates the pristine strength value. Reducing material strengths using *SOFT* allows for greater stability to achieve stable crushing by softening the load transition from the active row of elements to the next. The SOFT parameter is active within the 0–1 range, where SOFT = 1 indicates that the elements at the crush front retain their pristine strength and no softening occurs. Because this parameter cannot be measured experimentally, it must be calibrated by trial and error for crush simulations. It has been shown in previous studies [83 and 90] that the SOFT parameter directly influences the average crush loading result of the simulation and must be calibrated to match the experiment. This parameter will be discussed at length in section 10.2 of this report.

The failure criteria described in equations 17–20 provide the maximum stress limit of a ply, and the damage mechanisms described in equations 22–24 reduce the stress limit by a specified value given specific loading conditions. None of these mechanisms, however, cause the ply stress to go to zero. Instead, there are five critical strain values that reduce the ply stresses to zero. These are the strain-to-failure values in the positive fiber direction (tension), DFAILT; in the negative fiber direction (compression), DFAILC; in the matrix direction, DFAILM; in shear, DFAILS; and a non-physical failure strain parameter, effective failure strain (EFS). It is important to note that in the matrix direction, there is only one failure strain value, which is used for both tension and compression.

Four of the failure strains can be measured through coupon-level tests, but if they are not known, LS-DYNA gives the user the option to employ a generic failure strain parameter, EFS. The EFS immediately reduces the ply stresses to zero when the strain in any direction exceeds EFS, which is given by:

$$EFS = \sqrt{\frac{4}{3}\left(\varepsilon_{11}{}^{2} + \varepsilon_{11}\varepsilon_{22} + \varepsilon_{22}{}^{2} + \varepsilon_{12}{}^{2}\right)} \tag{25}$$

A critical EFS value can be calculated for any simulation by determining 1-, 2-, and 12-strains at element failure and using them in equation 25. EFS values below the critical EFS will cause premature element deletion. The default value for EFS is zero, which is interpreted by MAT54 to be numerically infinite, thereby making the EFS parameter ineffective in element deletion.

An element is deleted once the stress in all of the plies has been reduced to zero, as determined by failure strain parameters. Element deletion can also occur when the element becomes highly distorted and requires a very small time step. A minimum time step parameter, TFAIL, removes distorted elements as follows:

$TFAIL \leq 0$: No element deletion by time-step

$0 < TFAIL \leq 0.1$: Element is deleted when its time-step is smaller than $TFAIL$

$TFAIL > 0.1$: Element is deleted when $\dfrac{\text{current time-step}}{\text{original time-step}} < TFAIL$

Defining TFAIL to be very near or greater than the element time step will cause premature element deletion because the element will violate the TFAIL condition in its initial state. If significant element distortion is not a concern, it is recommended that a value that is an order of magnitude smaller than the element time step for TFAIL be chosen. LS-DYNA assigns the element time-step automatically to ensure that the Courant condition [91] is satisfied:

$$\Delta t = \frac{k\Delta h}{c} \tag{26}$$

where Δt is the time step of integration, Δh is the characteristic mesh dimension, k is a stability factor (0.6–0.8), and c is the speed of the sound wave through the material. For a one-dimensional longitudinal wave, the speed of the sound wave is $c = \sqrt{E/\rho}$, where E is the modulus of elasticity and ρ is the density [92–93].

Unlike the strength-based ply failure criteria in equations 17–20, there are no history variables for ply failure caused by maximum strains or element deletion due to TFAIL. For this reason, it is not possible to distinguish the failure mode that causes element deletion from the simulation results.

8. DEVELOPING THE BASELINE SEMICIRCULAR CORRUGATION MODEL

The full description, development, and results from the parametric study conducted for the semicircular corrugation baseline model have been published previously in the FAA report DOT/FAA/AR-11/21 [83]. This previously developed baseline model used the UD variant of the current plain-weave fabric material system under investigation in this report. In this section, the basic definitions and details of the baseline model are presented in addition to the changes made to the model to account for the fabric material system rather than the UD system. The new fabric semicircular corrugation baseline model provides the basis necessary to develop the subsequent new element shape crush models.

The baseline LS-DYNA model developed to model the crush progression of the corrugated coupon is shown in figure 41, which shows the loading plate, the corrugated composite specimen, and the trigger row of elements. The specimen was modeled with a total of 840 elements measuring 0.1″ x 0.1″ (2.54 mm x 2.54 mm). The specimen was kept at rest by constraining all degrees of freedom using a nodal single-point constraint boundary condition on the bottom row of nodes opposite the crush trigger. A large single-shell element perpendicular to the specimen crush front was used to model the loading plate, and was given the material properties of steel using the built-in rigid body material model MAT20.

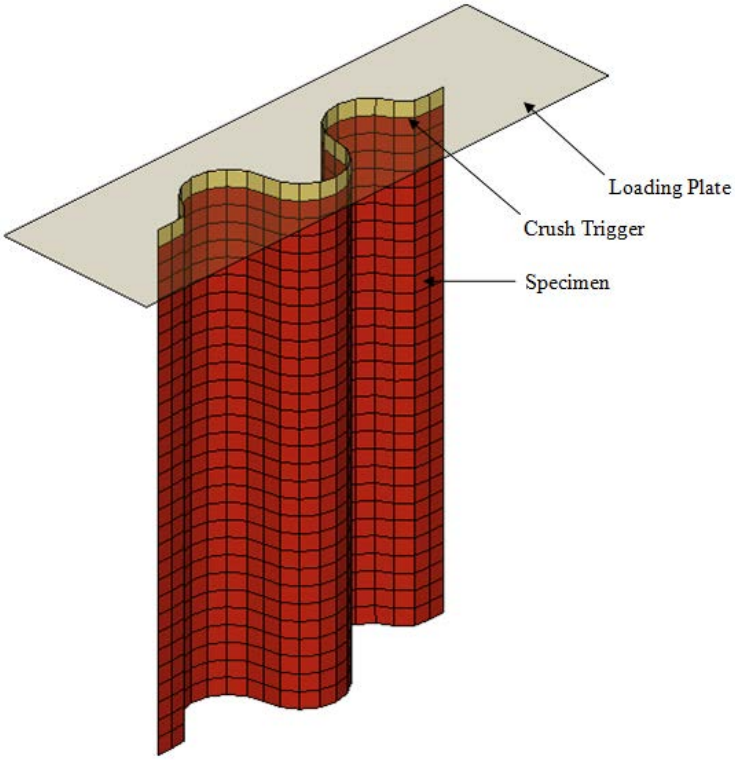

Figure 41. The LS-DYNA model of the corrugated composite crush specimen

The velocity of the loading plate is 150 in/s, and is defined by a linear load curve imposed on the nodes of the loading plate. The effect of using a simulated crush velocity that is much higher than the experimental velocity is discussed in the parametric studies.

A contact definition between the loading plate and the specimen is necessary for the two parts to properly interact. LS-DYNA offers a variety of built-in contact algorithms. For crash analysis, standard penalty formulation contact methods are typically used [50–68], which place springs normal to the surface between all penetrating nodes and the contact surface to facilitate a reaction force upon contact. The user input load-penetration (LP) curve defines the reaction normal force applied to each node as a function of the distance the node has penetrated through the surface that it is contacting. The baseline LP curve is shown in figure 42. The LP curve constitutes the most critical parameter for crush simulation in the contact definition and is discussed further in section 9.3 of this report.

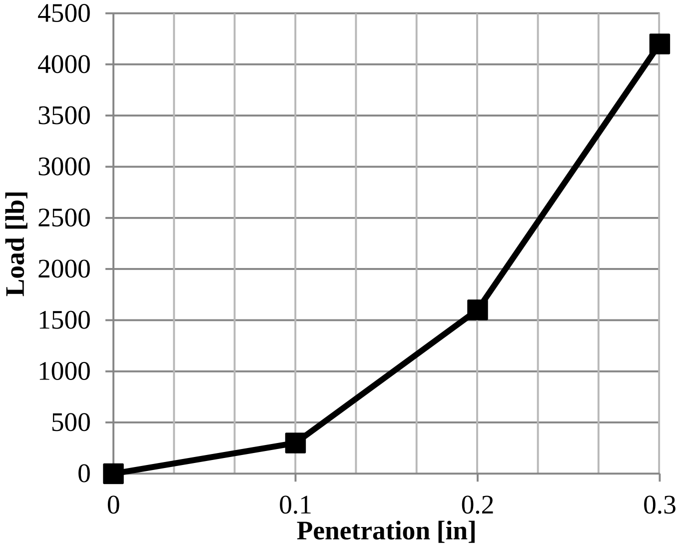

Figure 42. LP contact curve used in the baseline crush simulation

Two standard penalty formulation contact types have been shown to work well for crush simulation using MAT54: the Entity type (which was the baseline contact definition in the UD corrugation model (Feraboli and Wade [83]), and the Rigid Nodes to Rigid Body (RN2RB) type. The contact interface between the loading plate and the crush specimen is defined using the contact type RN2RB for the baseline simulation. Both types will be investigated in this report; however, the focus will be on the RN2RB type, which is generally more stable in crush simulations than Entity [90]. The only significant difference between these two contact types with regard to their influence on crush simulation is that the RN2RB contact is sensitive to changes in the thickness of the trigger row of elements while Entity is not [83–90]. This feature of RN2RB will be discussed further in the parametric study sections of this report.

The baseline MAT54 UD Entity crush model (Feraboli and Wade [83]) is modified to have the material properties and layup of the fabric laminate as given in table 2. The baseline MAT54 input deck for the fabric material model is shown in figure 43. For the 8-ply fabric layup, there are 8 integration points through the thickness of each element. The fabric material elements have a constant thickness of 0.07286″ (1.85 mm), except at the trigger row, which for the Entity models is equal to 0.01″ (0.254 mm), and for the RN2RB models is equal to 0.052″ (1.32 mm).

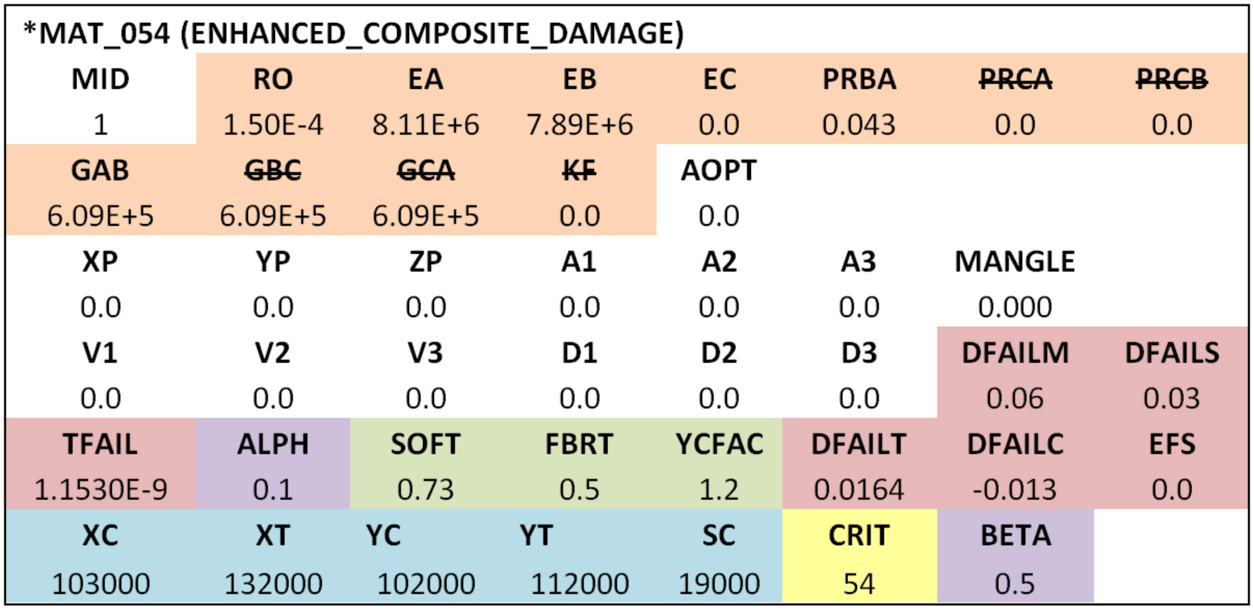

*MAT_054 (ENHANCED_COMPOSITE_DAMAGE)

MID	RO	EA	EB	EC	PRBA	~~PRCA~~	~~PRCB~~
1	1.50E-4	8.11E+6	7.89E+6	0.0	0.043	0.0	0.0
GAB	~~GBC~~	~~GCA~~	~~KF~~	AOPT			
6.09E+5	6.09E+5	6.09E+5	0.0	0.0			
XP	YP	ZP	A1	A2	A3	MANGLE	
0.0	0.0	0.0	0.0	0.0	0.0	0.000	
V1	V2	V3	D1	D2	D3	DFAILM	DFAILS
0.0	0.0	0.0	0.0	0.0	0.0	0.06	0.03
TFAIL	ALPH	SOFT	FBRT	YCFAC	DFAILT	DFAILC	EFS
1.1530E-9	0.1	0.73	0.5	1.2	0.0164	-0.013	0.0
XC	XT	YC	YT	SC	CRIT	BETA	
103000	132000	102000	112000	19000	54	0.5	

Figure 43. Baseline MAT54 input deck for the fabric material model with calibrated DFAILM and SOFT values

By simply changing the material properties and stacking sequence to those of the fabric laminate, an unstable crush curve with a low average crush load is generated, as shown in figure 44. The SEA of the simulated sinusoid crush has an error of -32% from the experiment. The MAT54 SOFT parameter is recalibrated, from 0.57 to 0.72, to increase the crushing load. The resulting crush curve exhibits a higher average crush load, but is very unstable, as shown in figure 45.

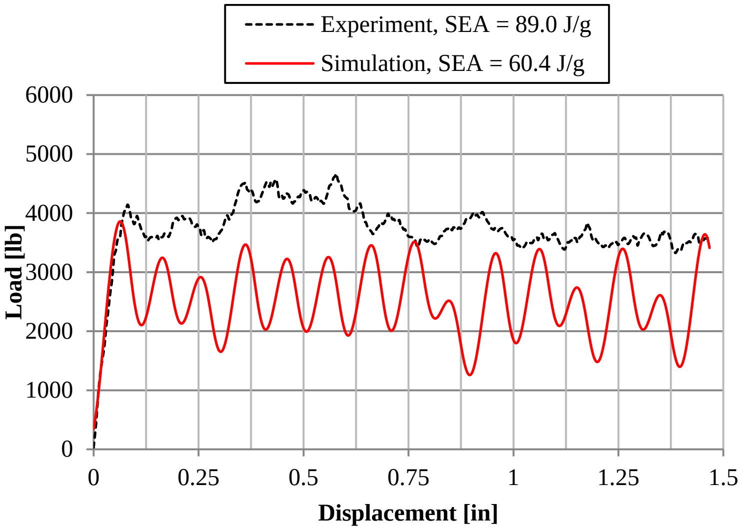

Figure 44. Load-displacement crush curve from replacing the UD material system in the baseline simulation with the fabric material system without further adjustments

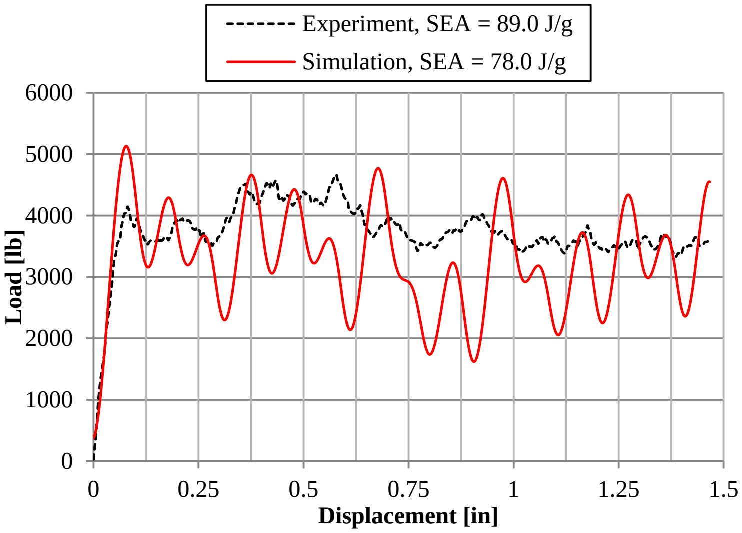

Figure 45. Load-displacement crush curve from calibrating the SOFT parameter in the simulation shown in figure 44

To stabilize the fabric model, DFAILM is raised from 0.0141 in/in to 0.06 in/in. The resulting model is the baseline fabric Entity model, which crushes in a stable manner and simulates the experiment well, except at the initial load peak. Because the Entity contact type is used, no further adjustments to the model can be made to improve the simulation of the initial load peak.

The raw and filtered load-displacement data generated by the baseline model are shown in figure 46(a), while the filtered data are compared against the experimental data in figure 46(b). It is common practice to filter the numeric results using a low-pass digital filter with a channel frequency class (CFC) of 600 Hz during post-processing. The practice of filtering impact data was standardized by the Society of Automotive Engineers in 1974 for experimental testing [94] and is used for all numeric crush simulations submitted for the CMH-17 Crashworthiness Numeric RR [95]. The effect of the filter on the simulation results was previously investigated in Feraboli and Wade [83]. The SEA-displacement plot of the simulation showed a poor match of the initial load peak when compared with the experimental data, shown in figure 46(c), and there is significant error in SEA during the first 0.5″ of displacement. The crushing SEA of the fabric Entity baseline is 90.2 J/g, which has a low error of +0.1% from the experiment. Solution time takes 84 seconds using a workstation with 2.26 GHz dual Quadcore 64-bit computer.

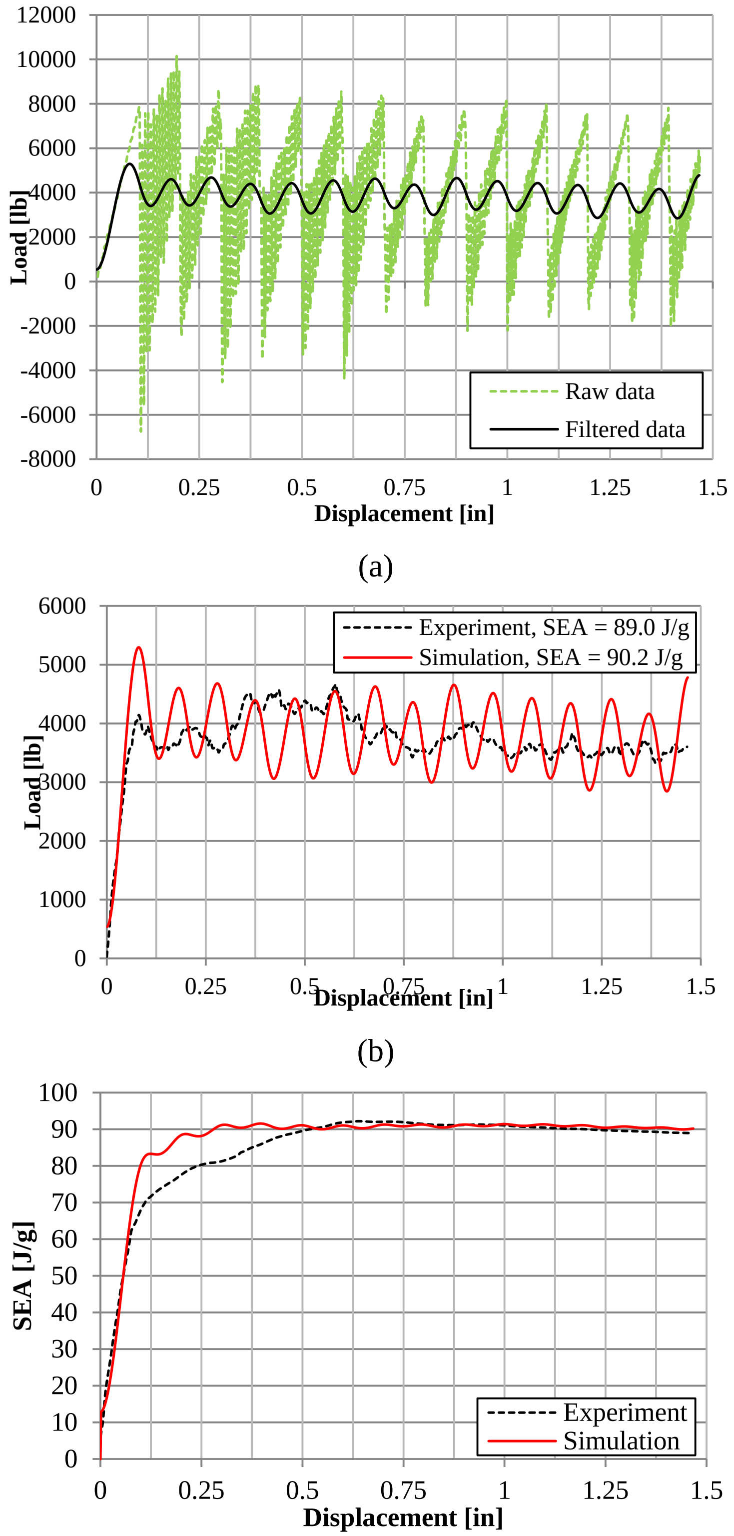

(a)

(b)

(c)

Figure 46. Baseline simulation for the fabric sinusoid crush using entity (a) raw and filtered load-displacement curve, (b) load, and (c) SEA compared with the experiment

The time progression of the baseline simulation, shown in figure 47, also indicates stable crushing. Failure advanced in an even and stable fashion, through element deletion at the crushfront. When the first ply in an element failed, the element remained upright and did not exhibit a different morphology. Once all plies had failed, the element was deleted. Elements across the entire crushfront row were deleted simultaneously.

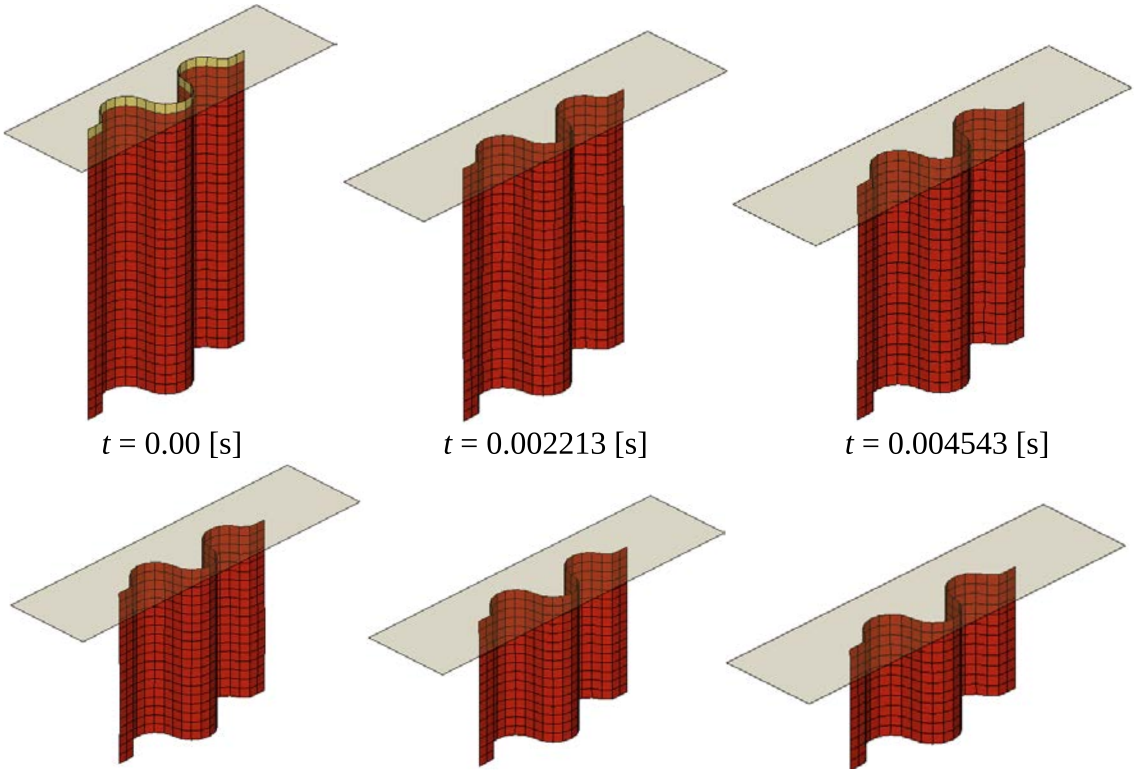

t = 0.00 [s] *t* = 0.002213 [s] *t* = 0.004543 [s]

t = 0.006873 [s] *t* = 0.009203 [s] *t* = 0.01153 [s]

Figure 47. Time progression of the baseline entity crush simulation

To generate the baseline RN2RB fabric sinusoid simulation, only the material properties and layup of the UD RN2RB baseline are changed to simulate the fabric laminate. Note that in the UD RN2RB baseline simulation, the trigger thickness had been calibrated to a value that correctly captured the initial load peak, 0.052″ (1.32 mm). Without changing any other parameters, the resulting simulation captures the initial peak load but has a low average crush load, shown in figure 48. To raise the load, the SOFT is recalibrated from 0.57 to 0.73, which results in an unstable simulation, shown in figure 49. For instance, with the Entity model, DFAILM is raised to 0.06 in/in to stabilize the model, and the resulting simulation is the fabric RN2RB baseline simulation. The raw and filtered load-displacement data generated by the model are shown in figure 50(a). The crush and SEA-displacement curves match the experiment well, as shown in figures 50(b) and 50(c). The SEA of the RN2RB fabric baseline simulation is 88.90 J/g, yielding a low error of -0.1% from the experiment. Solution time for this model takes 75 seconds.

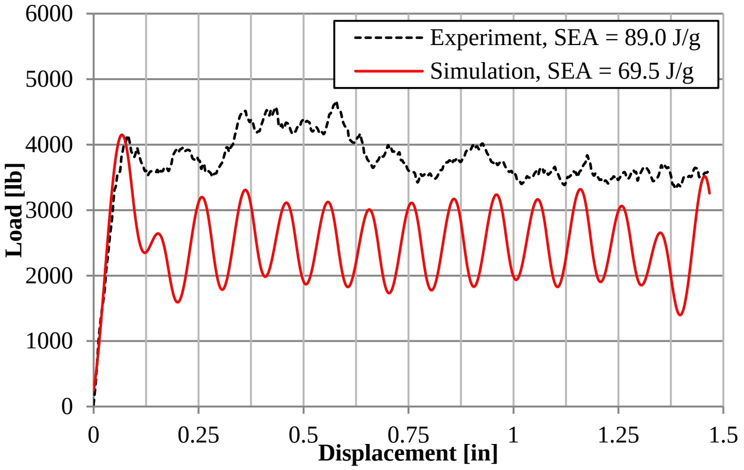

Figure 48. Load-displacement crush curve generated from replacing the UD RN2RB baseline simulation with the fabric material system without further adjustments

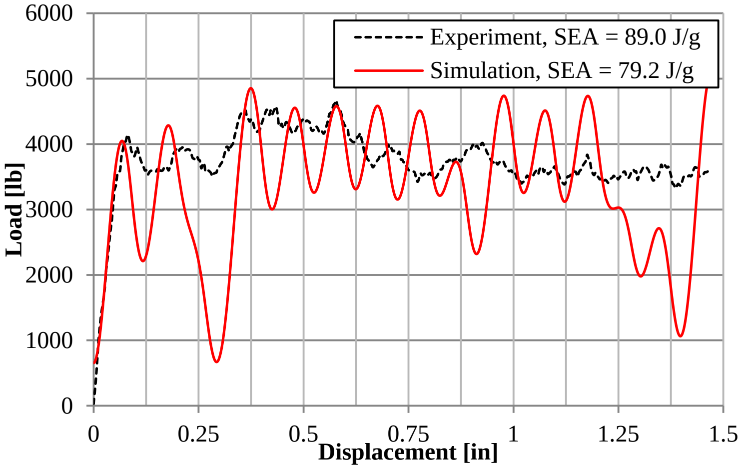

Figure 49. Load-displacement crush curve from calibrating soft parameter in simulation shown in figure 48

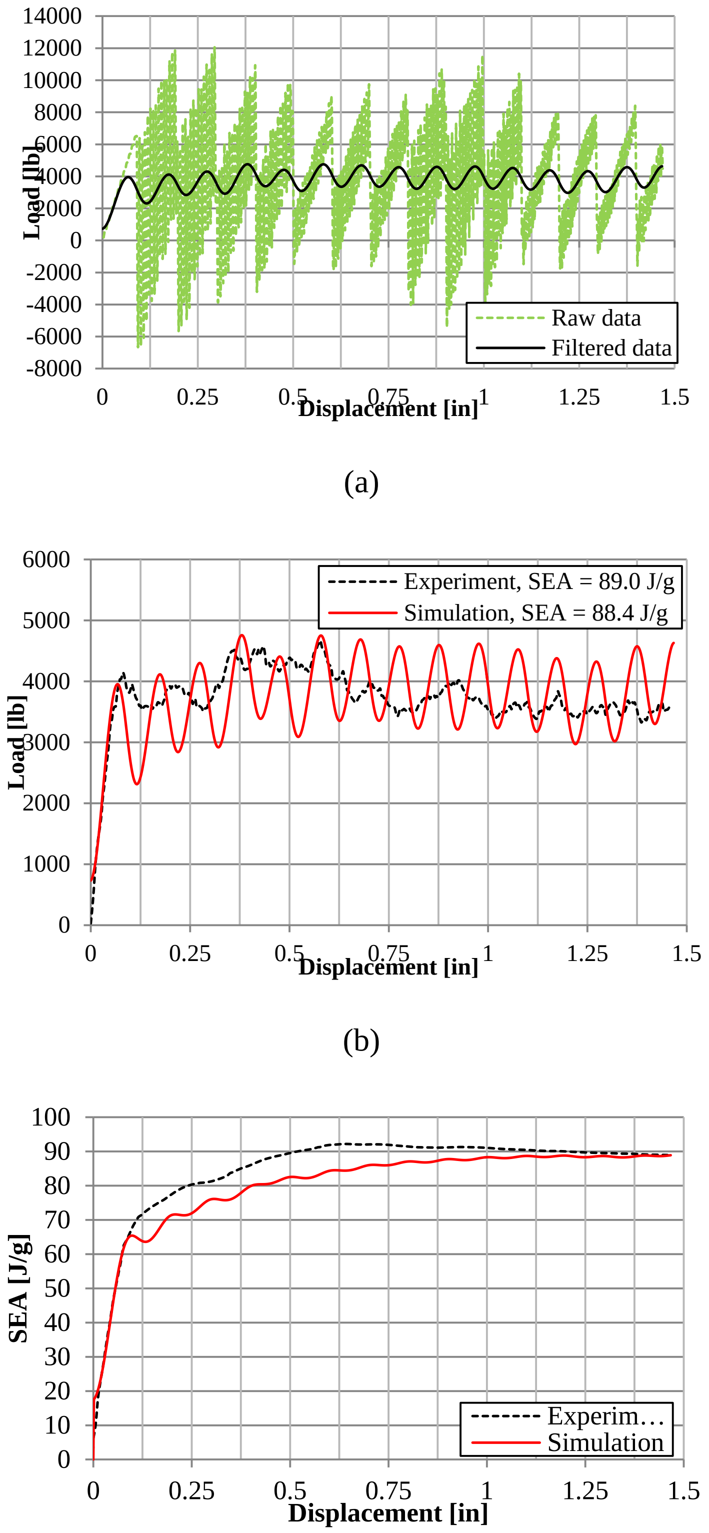

(a)

(b)

(c)

Figure 50. Baseline simulation for the fabric sinusoid crush element using RN2RB: (a) raw and filtered load-displacement curve, (b) load, and (c) SEA compared with the experiment

The transverse failure strain is modified for the fabric material system in simulations using both contact types, so that the experimental transverse material properties shown in figure 15 no longer accurately represent the MAT54 model defined in the baseline simulations. The adjusted material property stress-strain curves used in the baseline fabric MAT54 material model show that the curves in the axial and transverse directions are no longer similar and that the failure strain (and artificial plasticity) in the transverse direction is significantly greater (see figure 51).

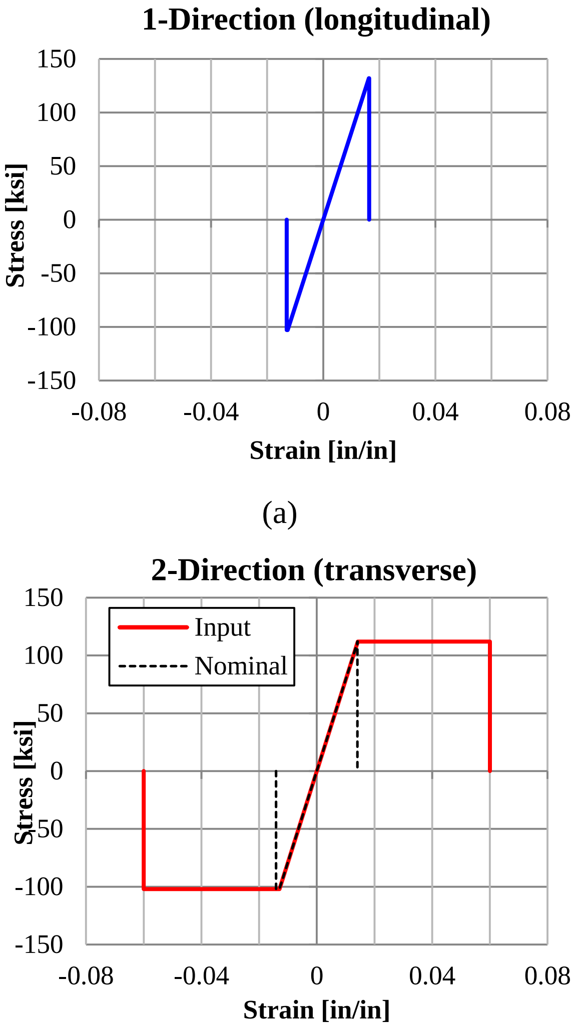

(a)

(b)

Figure 51. Stress-strain curve inputs of the material model MAT54 for the baseline fabric crush models

Two baseline sinusoid crush simulations using MAT54 to model a fabric material system have been successfully generated from existing MAT54 models of a UD material system using two different contact types. Creating the successful fabric baseline crush simulations requires minimal adjustments from the initial UD models for this specific material system. To modify a UD model to simulate a fabric, the SOFT and DFAILM parameters must be recalibrated, both increasing in value for the fabric material system. To change the contact definition from Entity and RN2RB contact types, only the trigger thickness must be recalibrated. The adjustments necessary to simulate the baseline semicircular corrugation crush elements using the AGATE material system are shown in figure 52.

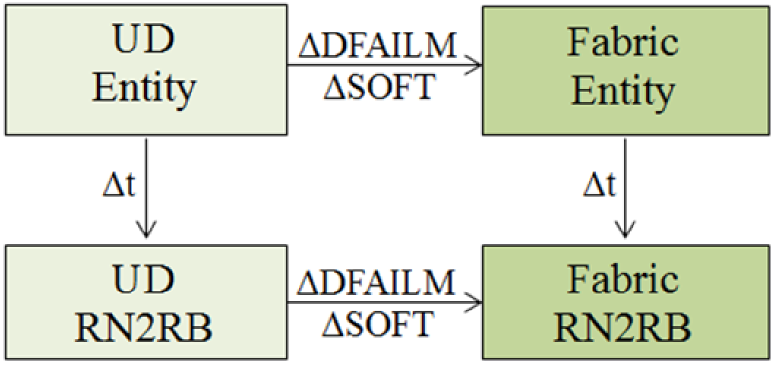

Figure 52. Summary of the parametric changes necessary to model the four UD and fabric sinusoid crush baselines using either the entity or RN2RB contact type

9. BASELINE MODEL PARAMETRIC STUDIES AND RESULTS

An effective material model needs to be sufficiently robust to tolerate small variations in material property input data to accommodate small errors in measured strength and stiffness. However, it should also be sensitive enough to capture different behaviors for different input material properties. The sensitivity of the model to variations in strengths (XT, XC, YT, YC, and SC) and strains-to-failure (DFAILT, DFAILC, DFAILM, and DFAILS) upon the baseline fabric material model used in the crush simulation of the semicircular corrugation shape is discussed in this section. For this sensitivity study, the RN2RB contact formulation is used. A summary of the parametric study performed on the fabric material model is shown in table 8.

Table 8. Summary of the parametric studies performed on the fabric material model (units not shown for clarity)

Parameter	Baseline Value	Parametric Variation	Figure
MAT54: XT	132000	50000, 100000, 2500000	-
MAT54: XC	-103000	-50000, -75000, -90000, -95000, -105000, -150000	Figure 53
MAT54: SC	19000	10000, 12000, 13000, 25000	Figure 54
MAT54: YT	112000	5000, 50000, 75000, 150000	Figure 55
MAT54: YC	-102000	-5000, -30000, -50000, -75000, -90000, -120000, -130000, -140000, -150000, -200000	Figure 56
MAT54: DFAILT	0.0164	0, 0.01, 0.011, 0.02, 0.05	-
MAT54: DFAILC	-0.013	-0.011, -0.012, -0.025, -0.03, -0.05	Figure 57
MAT54: DFAILM	0.06	0, 0.01, 0.014, 0.0141, 0.025, 0.027, 0.028, 0.03, 0.035, 0.038, 0.04, 0.05	Figure 58
MAT54: DFAILS	0.03	0.005, 0.015, 0.02, 0.05	Figure 59
MAT54: ALPH	0.1	0, 1.0E-14, 0.3, 1.0	-
MAT54: BETA	0.5	0, 0.01, 0.05, 0.1, 1.0	Figure 60
MAT54: FBRT	0.5	0, 0.1, 0.95, 1	-
MAT54: YCFAC	1.2	0, 0.25, 0.5, 0.75, 1.0	Figure 61
MAT54: SOFT	0.73	0.3, 0.5, 0.57, 0.6, 0.72, 0.8	Figure 62
Crush Speed	150	1.5, 15, 50	Figure 64
Contact LP Curve	PCWL	PCWL Stiff, PCWL Soft, PCWL Soft 2, Linear	Figure 65 to Figure 66
Mesh Size	0.1	0.05, 0.15, 0.2	Figure 67 to Figure 68
Trigger Thickness	0.052	0.01, 0.03, 0.04, 0.06	Figure 63

PCWL = piecewise linear

9.1 SENSITIVITY OF THE FABRIC MAT54 MODEL TO MATERIAL PROPERTIES

Varying the fiber tensile strength XT above or below the baseline value does not affect the outcome of the simulation, except for cases where XT is particularly low, such as XT ≤ 50 ksi. As was the case in the UD material system sensitivity study [83], the axial tensile strength does not appear to be a primary failure driver for the given specimen geometry-material combination. The axial compressive strength XC directly influences the average crush load for the fabric model, as it did for the UD model. Small increments in XC (making it less negative) significantly lower the average crush load, and slight decreases in XC (making it more negative) significantly raise the average crush load. This is true within an envelope of stable values, beyond which the model became unstable, shown in figure 53. The influence of the shear strength parameter, SC, is not strong. Increasing SC does not affect results, but decreasing it by 32% to 10 ksi causes the model to mildly destabilize, shown in figure 54. Such low values of SC are not realistically within the boundaries of experimental error when measuring shear strength. SC is therefore not considered a sensitive MAT54 parameter for the fabric material, unlike the UD material model for which smaller changes in SC caused great instability. The fabric model appears to be more robust to changes in SC than the UD model.

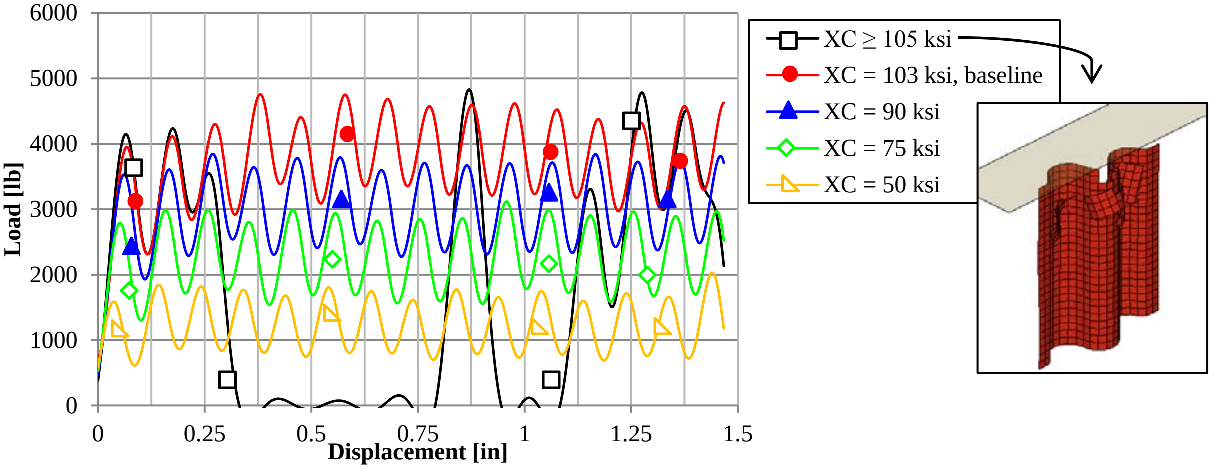

Figure 53. The effect of varying compression strength XC on the baseline model: Small changes in XC give large changes in the simulation

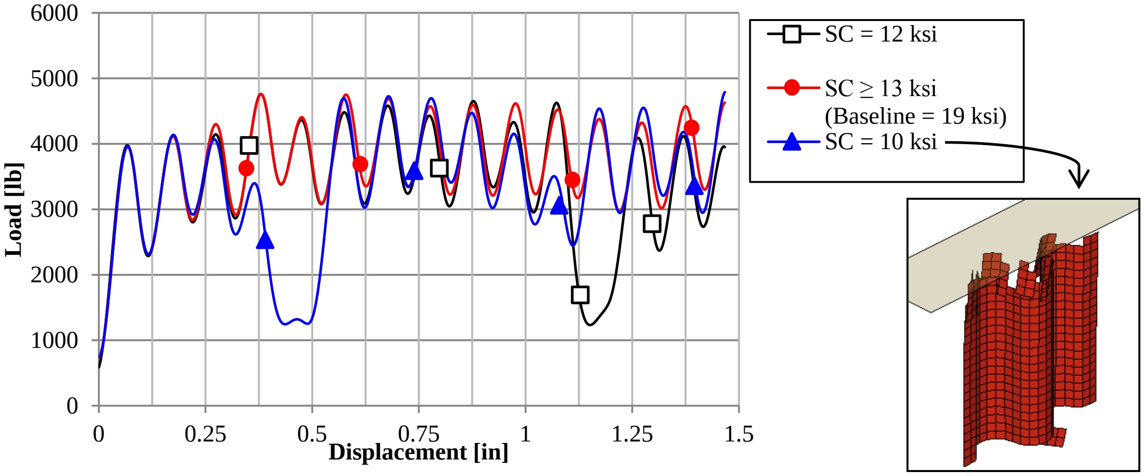

Figure 54. Effect of varying shear strength SC on the baseline model: Particularly small values destabilize the crush curve

Raising the tensile transverse strength parameter YT does not affect the crush model, but low values near 5 ksi cause early failure and a great reduction of load in the crush curve, shown in figure 55. This low magnitude of tensile strength is not feasible for a fabric material, and YT is not a significant parameter for the fabric material model. The compressive transverse strength, however, has a great effect on the stability of the fabric crush model. Only values of YC within a certain range produce stable results, shown in figure 56. The baseline fabric YC value lies within the stable range of 90–130 ksi; however, this stable range is relatively slim. The YC parameter only appears in the compressive matrix failure criterion, equation 20, which is the only failure criterion in MAT54 designed specifically to simulate a matrix material. This failure criterion is not appropriate for a fabric material system, and as such, it is not expected that transverse compressive failure would be properly simulated. For this particular fabric material system, the baseline YC value worked well, but it may have been acceptable to adjust this parameter had it not produced stable results when a fabric material system was being modeled. This cannot be said about the other strength parameters because the other failure criteria, equations 17–19 are appropriate for fiber-dominated laminates, such as the fabric material system.

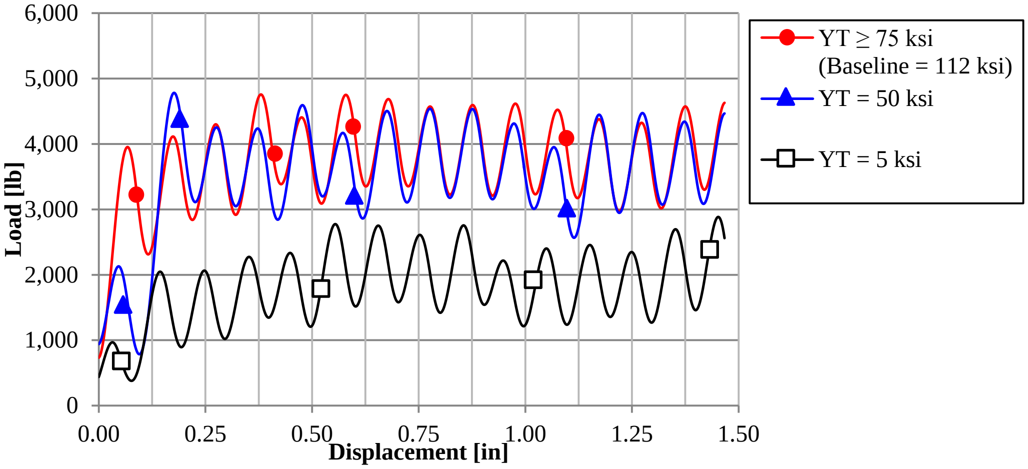

Figure 55. Effect of varying transverse tensile strength YT on the baseline model: Very small values lower the crush curve

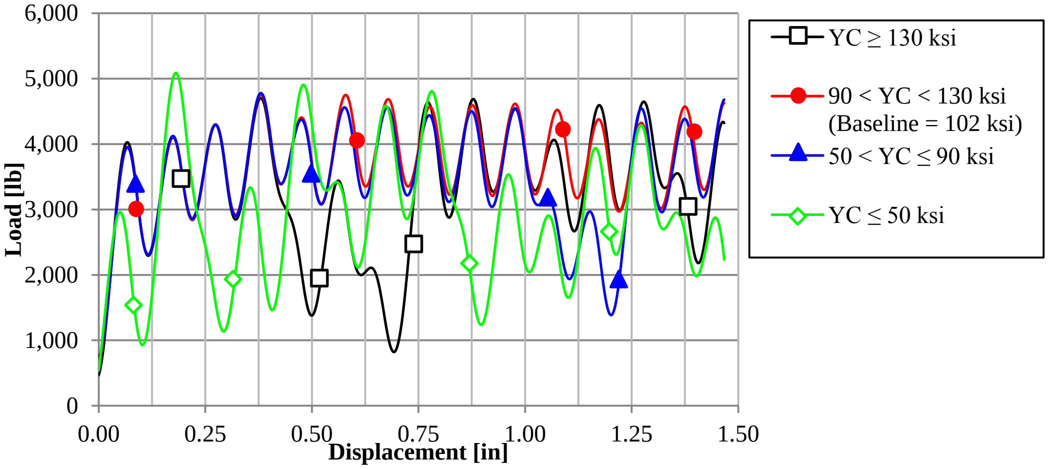

Figure 56. Effect of varying transverse compressive strength YC on the baseline model showing that large changes influence overall stability of the crush curve

Changes of the tensile strain-to-failure in the axial direction, DFAILT, are inconsequential for both the UD and fabric crush simulations, which allow for a virtual plasticity in the positive axial direction that does not affect the simulation. Changes in the compressive strain-to-failure in the axial direction, DFAILC, greatly affect the average crush load, shown in figure 57. The upper bound of DFAILC at which the fabric crush simulation became unstable is only 15% higher than the baseline value, which does not leave sufficient room for experimental error.

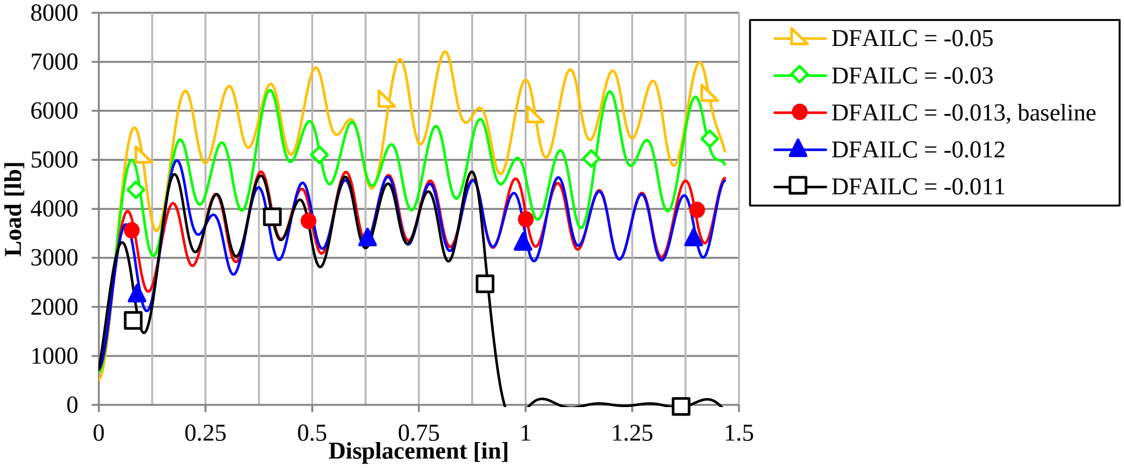

Figure 57. Effect of varying the axial compressive strain-to-failure, DFAILC, on the baseline model: Small changes can lead to greater loads and less stability

Changes to the transverse strain-to-failure, DFAILM, caused instabilities in both the UD and the fabric models. For the fabric, the nominal, experimentally derived DFAILM is too small and caused instabilities, shown in figure 58. The baseline simulation features a much larger DFAILM value and a virtual plasticity in the transverse direction, which was necessary for stability. Lower values of DFAILM allow for stable results, as low as 0.028 in/in; however, the model is only conditionally stable and often destabilizes with other parametric changes. For this reason, a large amount of virtual plasticity is added to the baseline simulation to ensure robust stability.

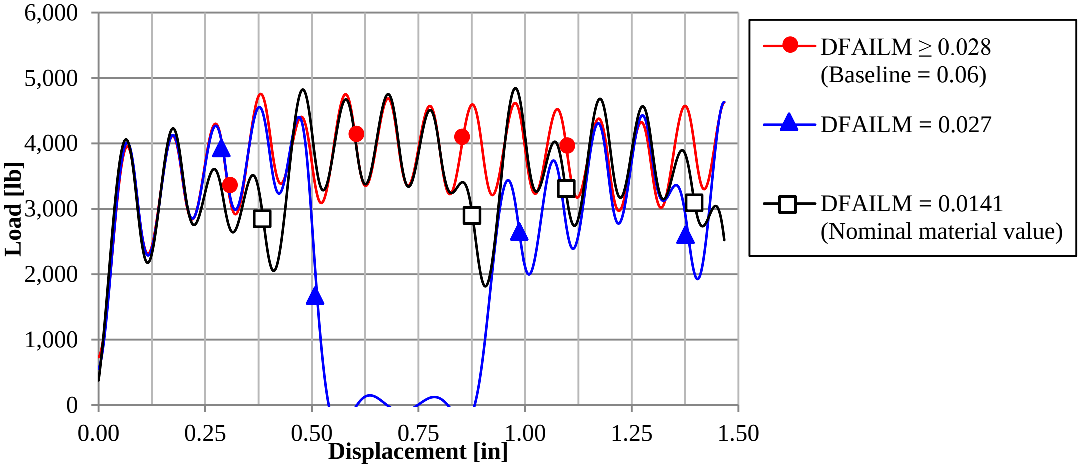

Figure 58. Effect of varying the transverse strain-to-failure, DFAILM, on the baseline model: An enlarged value is necessary for stability

The shear strain-to-failure, DFAILS, is one parameter that exhibited very different behaviors between the UD and the fabric crush simulations. While varying DFAILS by any amount in the UD material model had no effect on the results, lowering DFAILS by more than 30% destabilizes the fabric crush model, shown in figure 59. The low DFAILS values that destabilize the model are not physically significant; however, it is often recommended to assume a shear failure strain value of 3–5% for a carbon fiber-epoxy composite material model [1 and 81].

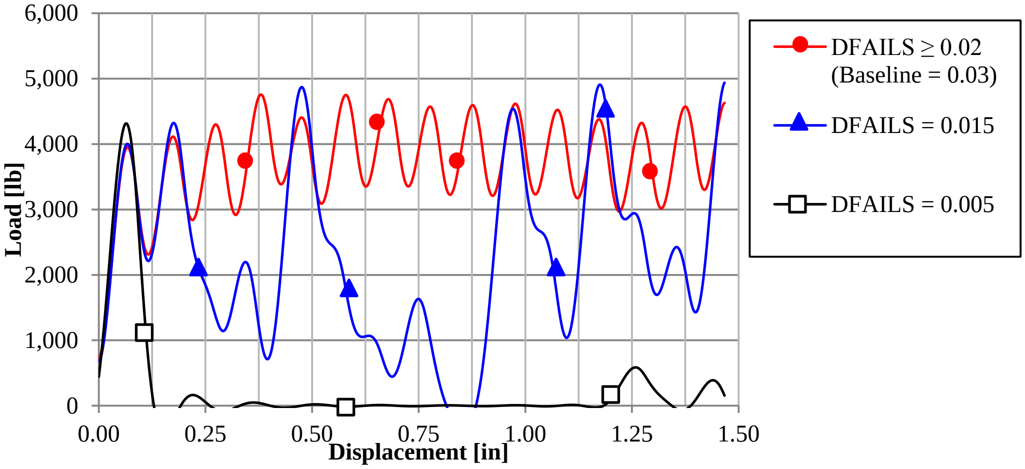

Figure 59. Effect of varying the shear strain-to-failure DFAILS on the baseline model: Significant influence on the stability of the model

9.2 SENSITIVITY OF THE FABRIC MAT54 MODEL TO OTHER MODEL-SPECIFIC PARAMETERS

This section focuses on the effect of modeling parameters that are specific to the MAT54 material model, and that are necessary for the simulation to run. These parameters either have no immediate physical significance or cannot be measured experimentally and therefore have to be calibrated by trial and error. These quantities include the ALPH, BETA, FBRT, YCFAC, and SOFT parameters.

Parametric changes to the shear stress weighing factors, ALPH and BETA, did not influence the results of either the UD or fabric material models, except for very low values of BETA. The fabric material is successfully modeled using any value of BETA above 0.05, shown in figure 60. This indicates that the maximum stress failure criterion (BETA = 0) for the tensile axial mode, equation 17, cannot be used and that at least some shear stress is necessary to prevent the axial tensile failure from being the dominant mode when modeling the fabric material system.

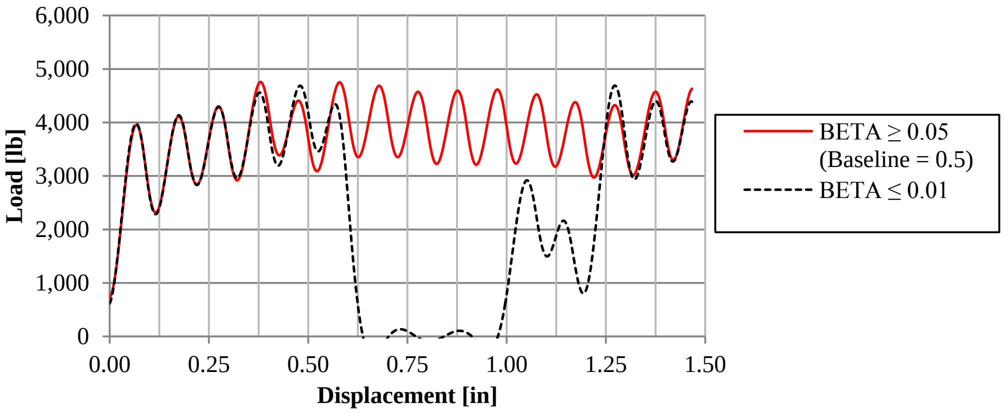

Figure 60. Effect of using very low values of beta on the baseline model

Both the FBRT and YCFAC terms are fiber strength reduction factors (for XT and XC respectively) used to degrade the fiber strength properties of the element following a transverse matrix failure. Parametric changes of the FBRT parameter do not affect the simulation results for both the UD and fabric material models. While the YCFAC parameter was not an influence for the UD material system, YCFAC can be important for the crushing stability of the fabric model, shown in figure 61. This suggests that there is transverse damage, occurring in the fabric elements, which activates YCFAC to reduce the effective compressive fiber strength, XC. Greater reductions in XC following damage (i.e., lower values of YCFAC) cause instabilities as crush front elements are deleted at a lower stress threshold.

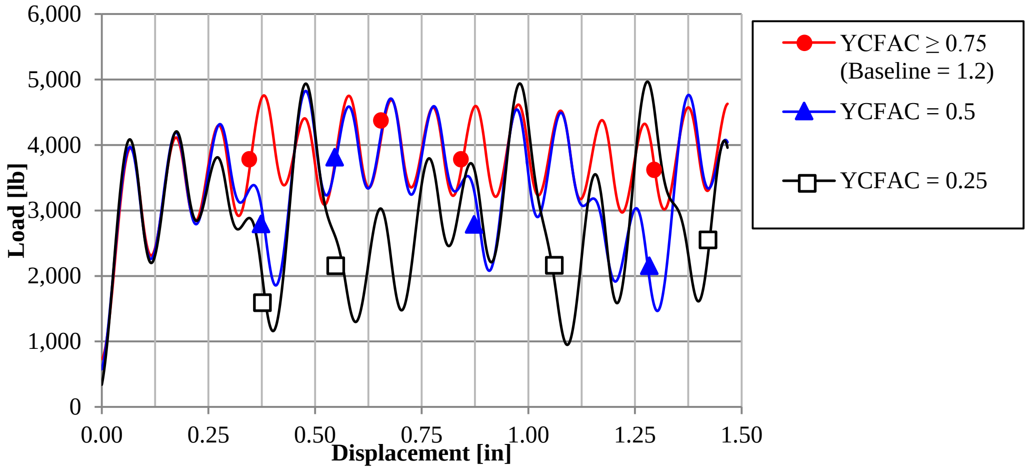

Figure 61. Effect of varying the transverse compressive strength damage factor, YCFAC, on the baseline model: Influences stability

The UD parametric study found the SOFT parameter to be the most influential MAT54 parameter for crush simulations [83]. The purpose of the SOFT parameter is to artificially reduce the strength of the elements immediately ahead of an active crush front. In the physical world, one could interpret the SOFT parameter as a damage zone (comprised of delaminations and cracks) ahead of the crush front that reduces the strength of the material. By itself, the SOFT is capable of dictating whether the simulation is stable or unstable. It can also shift the average crush load above or below the baseline by at least 40% from the baseline value of 88.90 J/g (for SOFT = 0.72), as shown in figure 62. The SOFT value cannot be increased much larger than the baseline value without resulting in instability, and for SOFT = 0.8, the simulated corrugation shape buckled during crushing. Lowering the SOFT parameter has the effect of lowering the average crush load and SEA value of the simulation. For SOFT = 0.5, SEA = 51.77 J/g (-42%), and SEA is reduced even further for lower values of SOFT. Determining the correct value of the SOFT parameter is a challenging task because it cannot be measured experimentally. It must be calibrated by trial and error until the load–displacement curve of the simulation matches the experimental result. Unless the right value of the SOFT parameter is found and used, it is not possible to obtain a successful simulation. The most important consequence of this observation is that the MAT54 material model is not a true predictive tool because the SOFT parameter needs to be calibrated to the experiment.

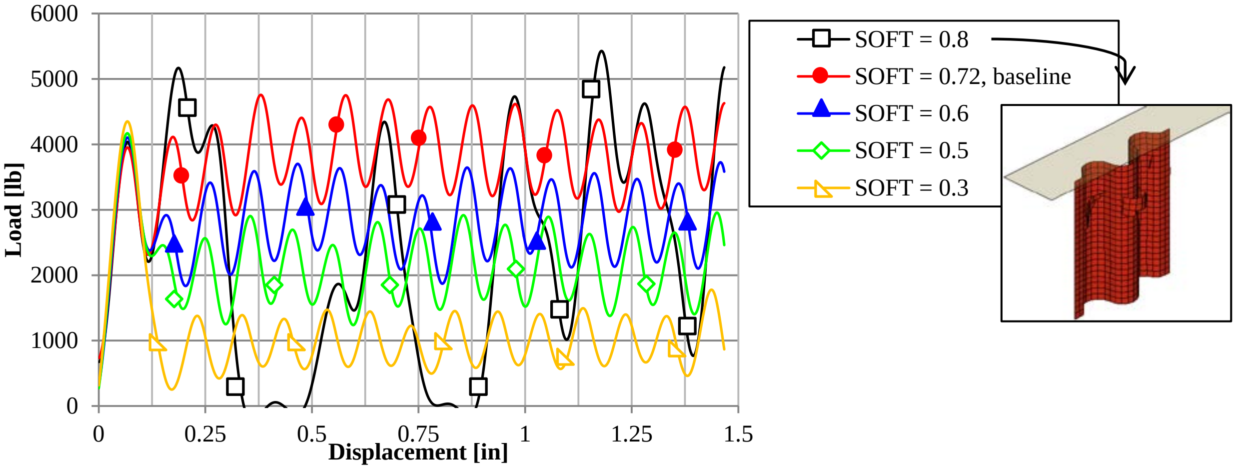

Figure 62. Effect of varying the SOFT crush-front parameter on the baseline model: Strong influence on the results of the crush curve

9.3 SENSITIVITY OF THE FABRIC MAT54 MATERIAL MODEL TO OTHER MODEL PARAMETERS

In this section, the influence of parameters that are not specific to the material model itself but are particularly influential for the execution of the simulation is discussed. These include crush velocity, the LP curve of the contact definition, the mesh size, and the trigger element thickness. The direct effect of the trigger thickness on the initial peak load of the semicircular corrugation crush model using the RN2RB contact type is shown in figure 63. In the case of the Entity contact, the trigger thickness did not significantly affect the simulation, as demonstrated in the UD model.

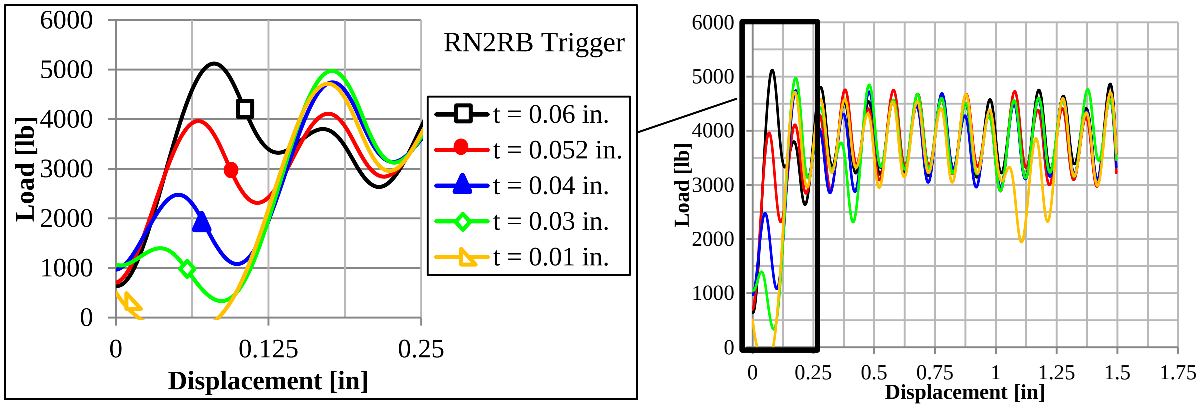

Figure 63. Effect of changing the trigger thickness on the initial load peak of the baseline crush curve when using the RN2RB contact type

Although the true experimental crush loading rate was 1.0 in/min (25.4 mm/min), simulations were performed using a crush velocity of 150 in/s (3,810 mm/s) because of computational limitations. Because all material properties are measured with quasistatic tests, no strain-rate-dependent material properties were defined in the material deck; therefore, the material model cannot assume strain-rate behavior. Nonetheless, inertial effects may occur, which could lead to different global response for the specimen. To verify the validity of the assumption, three simulations are carried out at simulation speeds of 50 in/s (1270 mm/s), 15 in/s (381 mm/s), and 1.5 in/s (38 mm/s), which are well below any dynamic threshold reported in the literature [15, 16, and 95]. These simulations have runtimes of 230 seconds, 29 minutes, and 4 hour 48 minutes, respectively, and are less practical to use with the available computational power, especially when considering that these simulations are of structural elements that ideally would be scaled up and used in the full structural model. Reducing the crush velocity does not significantly change the results from the baseline simulation, except at the initial load peak, shown in figure 64. The trigger thickness can be recalibrated to achieve better matching results at initiation.

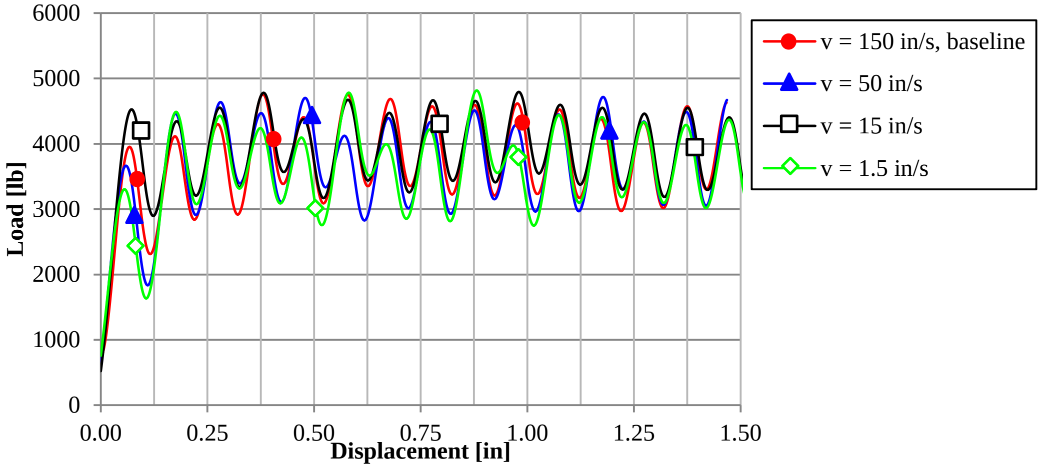

Figure 64. Effect of varying loading velocity on the baseline model

The LP curve defines the reaction forces at the contact interface for both the Entity and RN2RB contact types. Such a curve is necessary in the contact definition when using the MAT54 material model. Varying the LP curve has an important effect on the stability of the model, yet there is no way of knowing a priori or determining experimentally the correct shape this curve needs to have for the specific material/geometry/loading combination. Four LP curves that differ from the baseline PCWL curve are used to study the effect of the LP curve, as shown in figure 65(a). The baseline LP curve introduces the load in a gradual fashion into the coupon, the stiff LP curve introduces the load into the coupon more suddenly, and the two soft LP curves introduce the load more gradually. The fourth LP curve is linear and introduces the load into the specimen quickly. Without changing any other parameters, many of the alternative LP curves introduce instabilities and cause global buckling of the corrugated element, as shown in figure 65(b). In some cases, buckling results from the greater forces acting at the contact, such as the stiff and linear LP curves, while in the case of the SOFT 2 LP curve, the forces at the contact surface are not introduced quickly enough, and the contact interface is allowed to fully pass through the element in contact, preventing stable crushing from proper initiation. As done in the parametric study of LP curves in the UD corrugated crush element [83], the SOFT parameter is recalibrated for unstable simulations to enable stability, and the stabilized LP parametric results agree with those discovered in the UD study, as shown in figure 66.

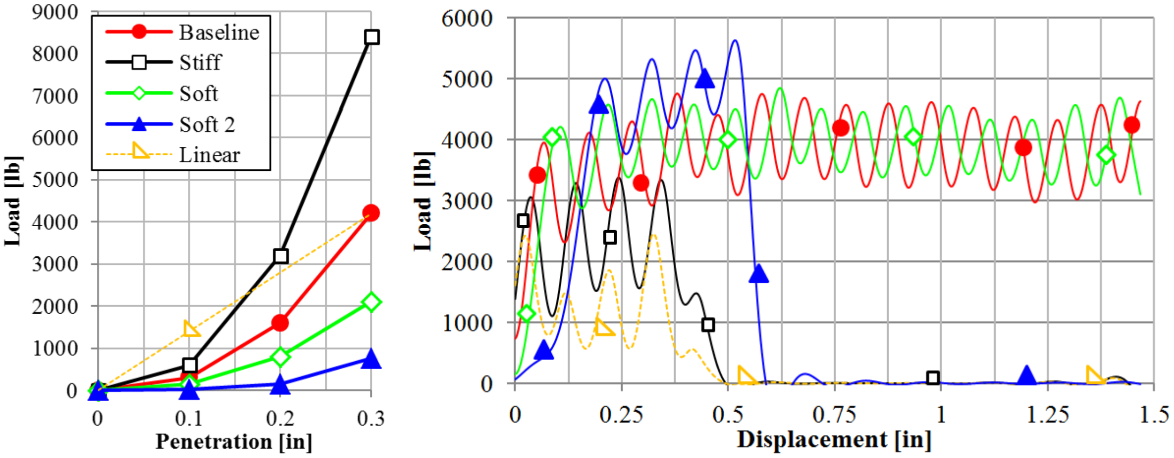

(a) (b)

Figure 65. (a) Five different LP curves investigated in the contact definition and (b) their influence on the baseline model crush curves

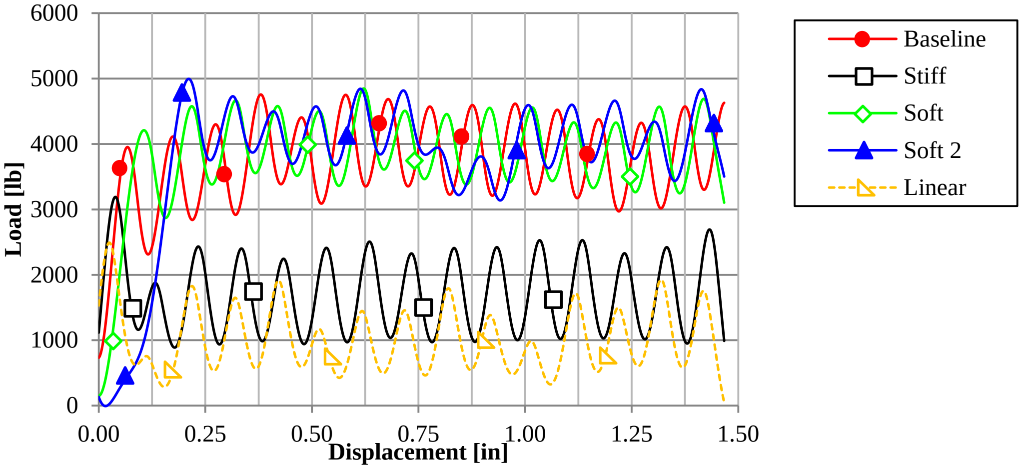

Figure 66. Effect on the baseline model crush curve using various LP curves and recalibrating the soft parameter to provide stability

Explicit FEA codes are particularly mesh-sensitive, and although it is usually desirable to use a finer mesh size, computational costs become demanding. The curved features of the corrugated geometry used in this crush study are incompatible with mesh sizes larger than the baseline size of 0.1″ (2.54 mm), which cannot model the curvature of the semicircular cross section. The mesh size is, therefore, only varied by reducing it to 0.05″ (1.27 mm) for the parametric study. The run time for the finer mesh is 17 minutes, 42 seconds. The finer mesh produces a load-displacement curve with two oscillations before global buckling (see figure 67 [black]). To address this, the SOFT is recalibrated (from 0.73 to 0.60) to stabilize the smaller elements from the load pulses. Stable crushing initiates, but global buckling still occurs (see figure 67 [blue]). The fine mesh requires further stabilization, which is accomplished by increasing DFAILC (from 0.013 to 0.02 in/in). This is a MAT54 parameter that has a baseline value at the edge of its stability threshold for the fabric material system, shown in figure 57. The resulting simulation demonstrates stable crushing behavior and matches the baseline simulation well (see figure 68). This fabric material crush model is mesh sensitive, but it is possible to make empirical adjustments to the material deck to stabilize it using a different mesh size.

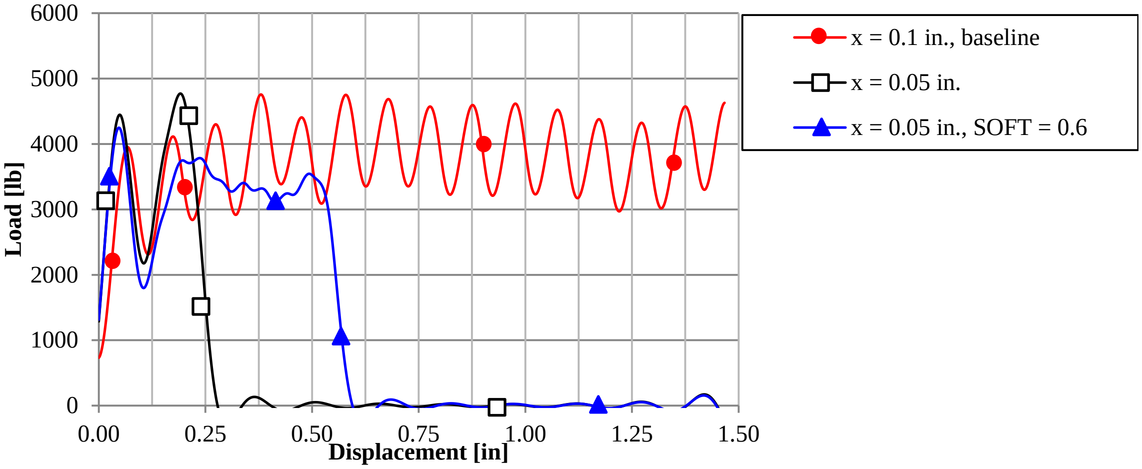

Figure 67. Effect of using a smaller mesh size without changing any parameters (black) and after recalibration of the SOFT (blue), which shows unstable behavior for both

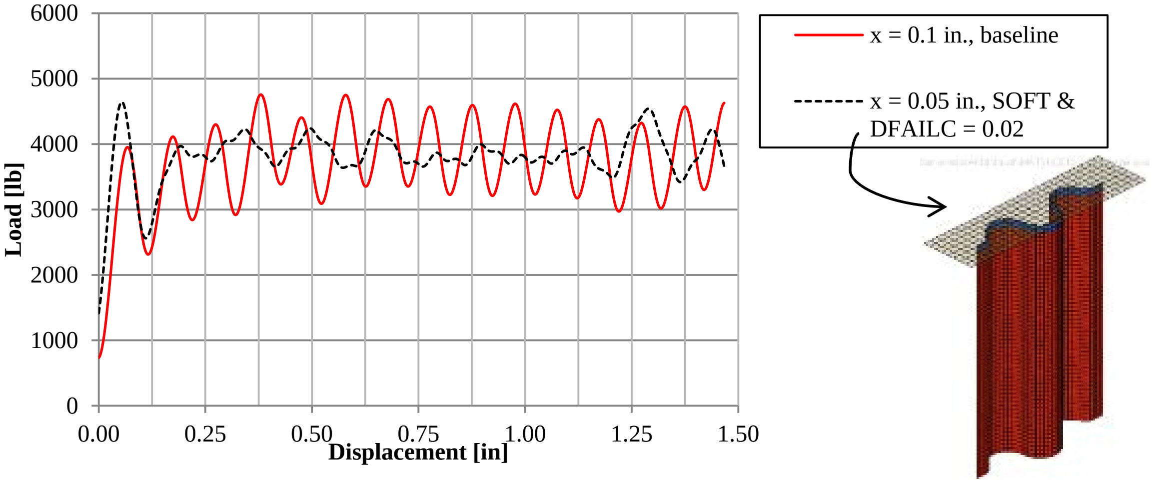

Figure 68. Load-displacement crush curves from using two different mesh sizes in the baseline model, and recalibrating SOFT and DFAILC parameters for the smaller mesh

9.4 COMPARISON OF MAT54 PARAMETRIC TRENDS OF THE FABRIC AND UD MODELS

Many of the parametric trends observed for the crush simulation of the UD material system modeled using MAT54 are also observed for the fabric. The critical MAT54 parameters, which most affected the stability and SEA of the UD crush simulation, XC, DFAILC, and SOFT, also greatly influence the crush simulations modeling the fabric composite. The fabric material model, however, is also strongly influenced by transverse compressive parameters YC (and consequently YCFAC) and DFAILM, which was not observed during the parametric study of the UD system. The compressive transverse mode is not suitable to simulate a fabric material system because of the Hashin failure criterion implemented by MAT54. Given this, it is sensible that the transverse compressive strength parameter, YC, could be an empirical parameter for a fabric material system. Similarly, the transverse failure strain, DFAILM, is meant to model matrix materials, which have a higher strain-to-failure value than fibers.

One of the biggest differences between the two material models is that the true material properties of the UD yield stable results that match the experiment, while the fabric material model must use artificial plasticity in the transverse direction to achieve stable results. Furthermore, there are parameters, such as XC and DFAILC, which have material property values that are 2% and 15% away from causing instability in the fabric model. The fabric MAT54 model appears to be not as robust as the UD model, and sensitive material parameters may require adjustment when other simulation features, such as mesh size and velocity, are changed.

9.5 CONCLUSIONS

The LS-DYNA material model MAT54 has been successfully shown to model a fabric material system based on a modeling approach developed to simulate a UD material system in the simulation of a sinusoidal specimen undergoing axial crushing. The performance of the UD and fabric models within the crush simulation share many similar trends, such as the sensitivity of the model to the fiber compression strength XC and strain-to-failure DFAILC parameters. Regardless of the material system modeled, these parameters are the primary material parameters that ultimately determine energy absorption in a crush simulation by determining element failure and deletion. The SOFT parameter is the single most influential MAT54 input parameter for energy absorption and determining the success of the crush simulation. Using a systematic calibration against the crush experiment, the appropriate value for the SOFT parameter can be identified. Some differences between the UD and fabric material systems were identified, such as the influence of the transverse tensile strength YC and strain-to-failure DFAILM, which both significantly influence the stability of the fabric model, but not the UD model. Both of these parameters are measured from experiment, and while the experimental value of the YC parameter yielded a stable simulation, DFAILM required artificial increase for a stable simulation. This increase provides transverse plasticity in the model following failure, a feature noted in impact simulations to be necessary for composite modeling [68]. This has also been noted to be similar to the stress unloading following failure featured in simulations of composite materials involving stress concentrations and linear elastic fracture [96]. If a stable crush simulation of a MAT54 UD material model has already been defined, a change of material properties followed by a calibration of the DFAILM and SOFT parameters has been shown to achieve a successful crush simulation. This modeling approach is not yet considered to be predictive for this level of structural complexity and instead is classified as a calibration of the model using experimental data within the scope of the building-block approach, building towards a full-scale crash simulation.

10. SIMULATION OF OTHER CRUSH ELEMENT SHAPES

10.1 MODEL DEVELOPMENT

Building upon the baseline semicircular corrugation crush element model, several new crush element shapes are simulated using the same modeling strategy as the baseline model. The new crush element shapes are comprised of the seven geometries, five channel variants, and two additional corrugated shapes, for which experimental crush test results were presented in section 4.1 of this report. The eight geometry models (including the baseline semicircular corrugation) are shown in figure 69. The modeling strategy developed for the fabric semicircular corrugation crush element—including mesh size, contact definition, boundary conditions, and material card—is used as a template to model the seven new geometries. The nominal dimensions for the sinusoidal and channel specimens are shown in figures 16 and 19, respectively.

The experimental investigation of the different crush elements revealed that the cross-sectional geometry of the crush element greatly influences its energy-absorbing capability, indicating that SEA is not a constant of the material system. The difference in SEA is attributed to the various failure mechanisms exhibited by each crush element. In particular, elements with more curvature exhibited greater delamination suppression, which encourages material fragmentation, a highly energy-absorbent failure mechanism. The variation in SEA measured from the different crush elements is directly dependent upon the different failure mechanisms experienced, and it is the goal of this numerical investigation to determine the best way to represent such changes in the simulated crush models.

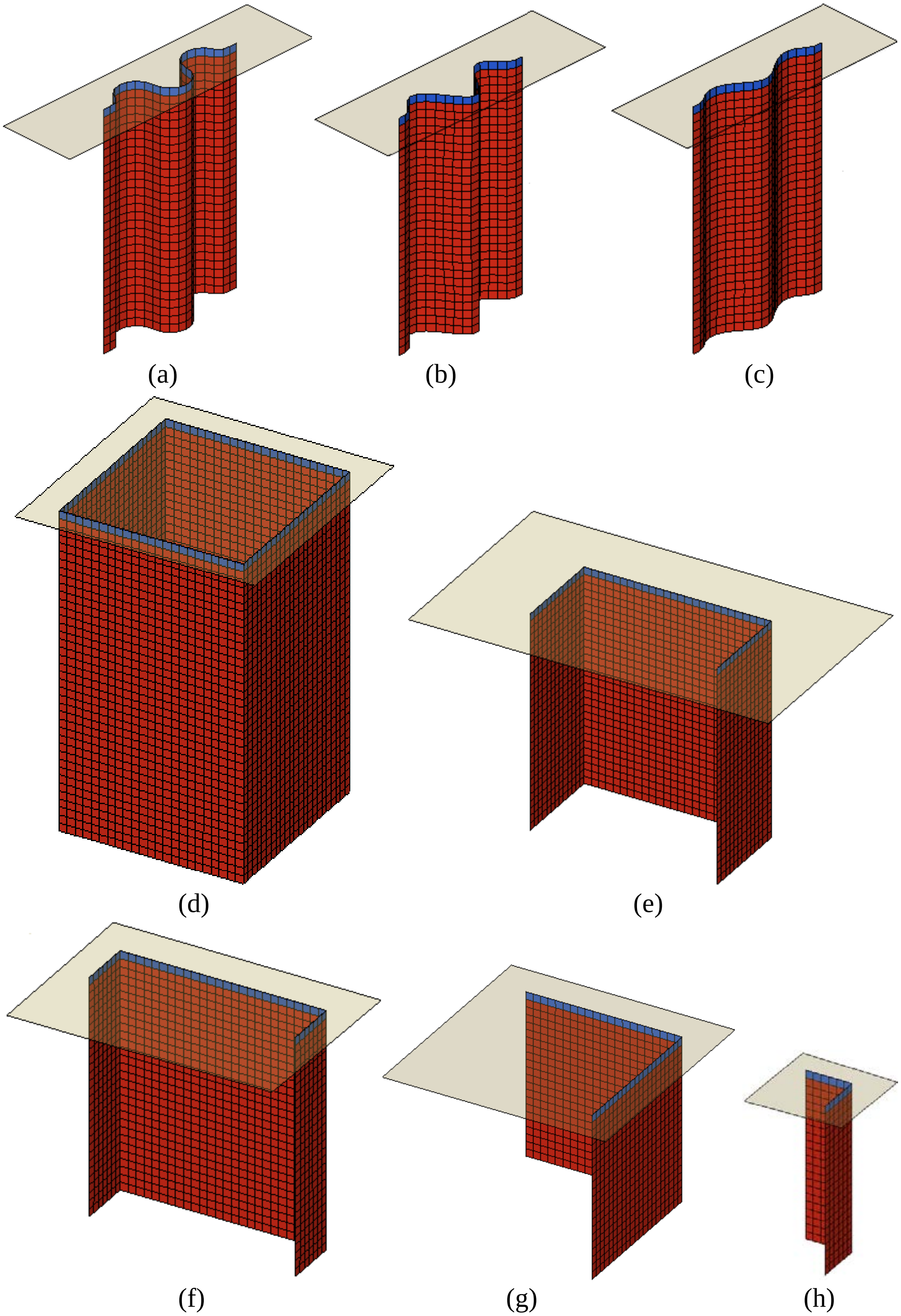

Figure 69. Eight LS-DYNA crush specimen models with different geometries: (a) semicircular sinusoid, (b) high sinusoid, (c) low sinusoid, (d) tube, (e) large C-channel, (f) small C-channel, (g) large corner, and (h) small corner

Unfortunately, the failure mechanisms that differentiate the energy-absorbing capability of the different crush elements (e.g. delamination) cannot be directly simulated using the single shell element approach developed for the sinusoid crush simulations. Without the capability to simulate delamination, it is expected that simulating different geometries requires changes in the material model itself, even though the material remains constant throughout this investigation. This investigation will determine what changes are necessary in the model to simulate the crush elements with various geometries that were previously crush tested.

The baseline MAT54 input deck for the fabric material model is shown in figure 43. The baseline MAT54 parameter values were derived from the material properties of the fabric material system shown in table 2, with the exception of the DFAILM parameter, which was artificially increased for stability of the corrugated crush model. From the corrugated crush model, all modeling definitions remain the same, and only the geometry is changed. For the square tube element, the change of geometry causes a failure at crush initiation where several elements erode away from the crush front at very high loads, which directly leads to global buckling, shown in figure 70. Similar results are obtained from modeling each of the other seven geometries directly from the baseline corrugated model. By simply changing the geometry, the crush simulations of the new shapes are not successful; however, this result is not unexpected because the different energy-absorbing failure mechanisms cannot be individually modeled using the current approach. The continued systematic investigation is focused to discover the best method to simulate the change in SEA because of the change in geometry using the modeling parameters that most influence stability and SEA, as discovered in the parametric studies of the crush model.

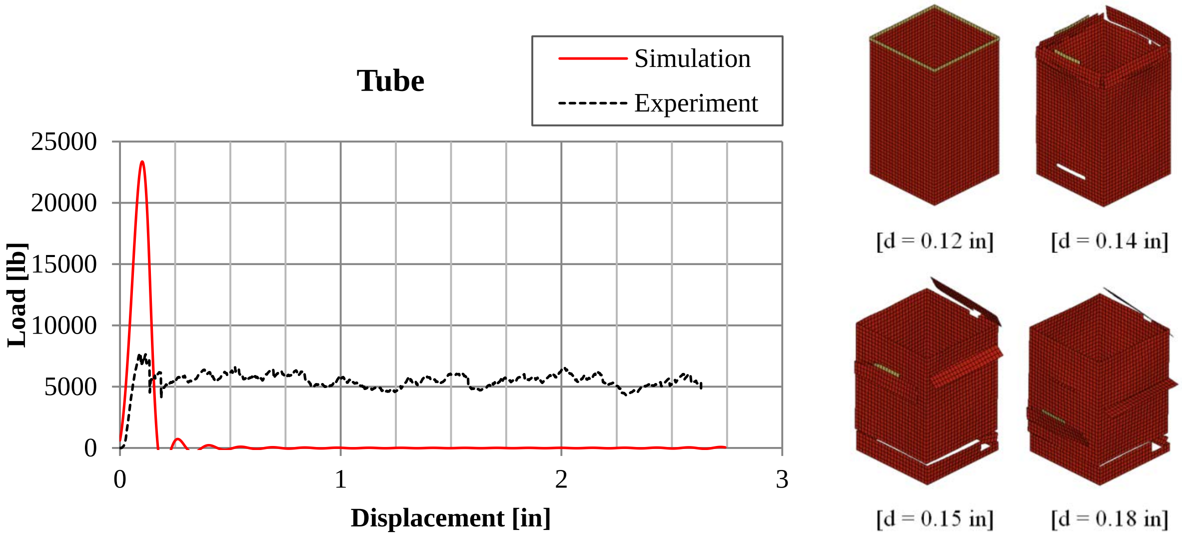

Figure 70. Simulated load-displacement crush curve and simulation morphology from changing only the specimen geometry from the sinusoid baseline to that of the tube element

First, the modeling parameters that influence SEA are investigated to discover if the crushing loads can be reduced enough to achieve stability and the correct simulated SEA. With the intent to reduce the crush loads, the MAT54 parameters SOFT, DFAILC, and XC are reduced without acceptable success. It is observed that the crush models of all the tubular, channel, and corner geometries are too unstable to appropriately alter the crushing load without experiencing global failures, such as those shown in figure 70. Next, parameters that influence stability are investigated with the goal of reducing variability and promoting stability so the changes can be made to lower the crushing load. To promote stability, DFAILS, SC, and YCFAC are raised in conjunction with lowering the SEA-influencing parameters DFAILC, XC, and SOFT. All such efforts, which only make changes within the MAT54 card, are unable to provide a significant improvement in the model stability.

Considering parameters outside of the material card, the LP curve at the contact is altered to promote stability. A softer contact LP curve, shown in figure 71, is used to soften the introduction of the reaction forces transmitted into the crush specimens. This is the same LP curve featured in the fabric sinusoid crush parametric study, labeled PCWL Soft 2 in figure 66.

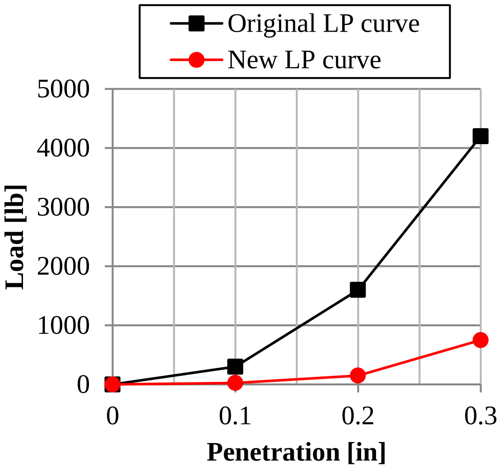

Figure 71. Original and new LP curves defined in the contact deck

Implementing only this change in the contact definition LP curve and applying the baseline sinusoid material model to the seven geometries did not yield immediate success, as shown in figure 72.

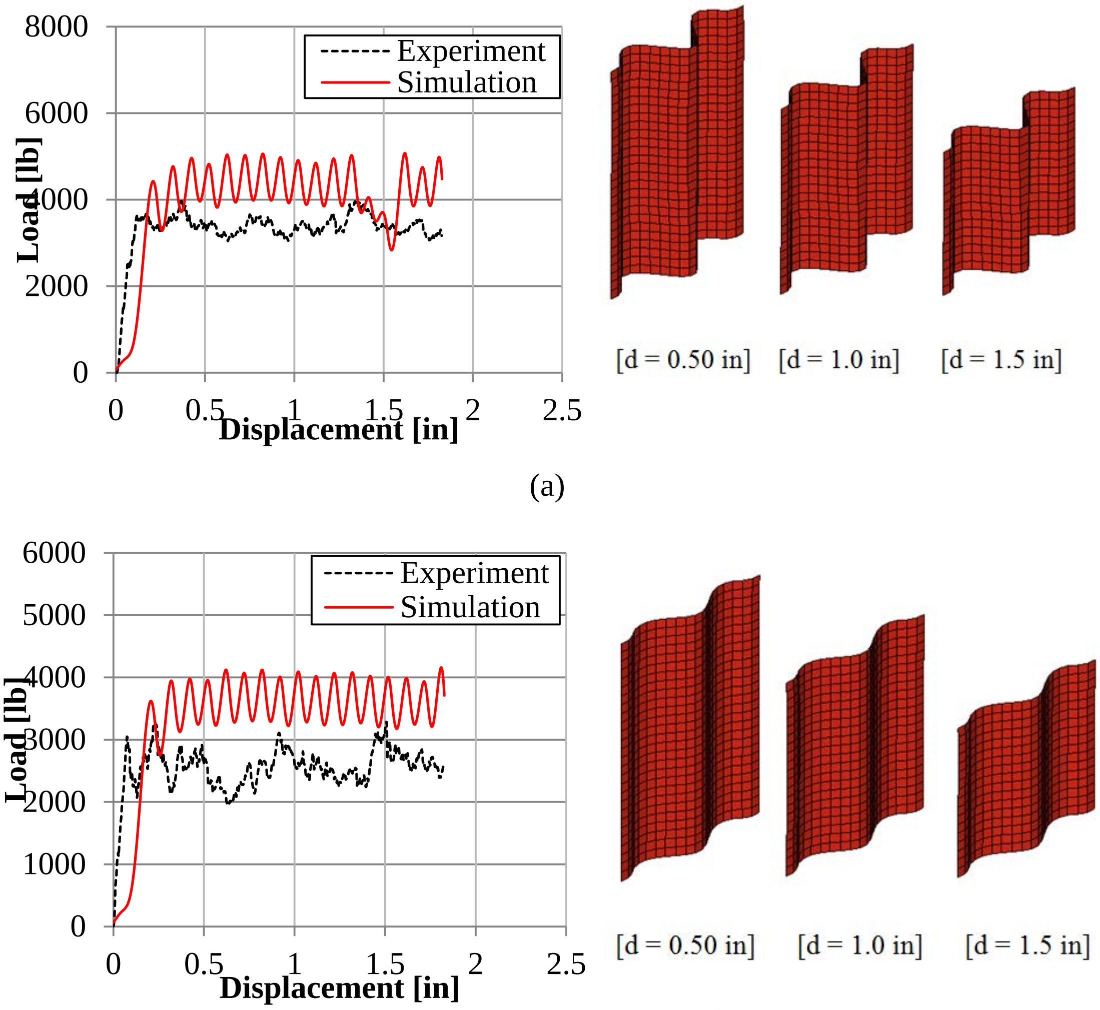

(a)

(b)

Figure 72. Undesired crush simulation results compared against the experimental curve when only the geometry is changed from the semicircular corrugation baseline model: (a) high sinusoid, (b) low sinusoid, (c) square tube, (d) large C-channel, (e) small C-channel, (f) large corner, and (g) small corner elements

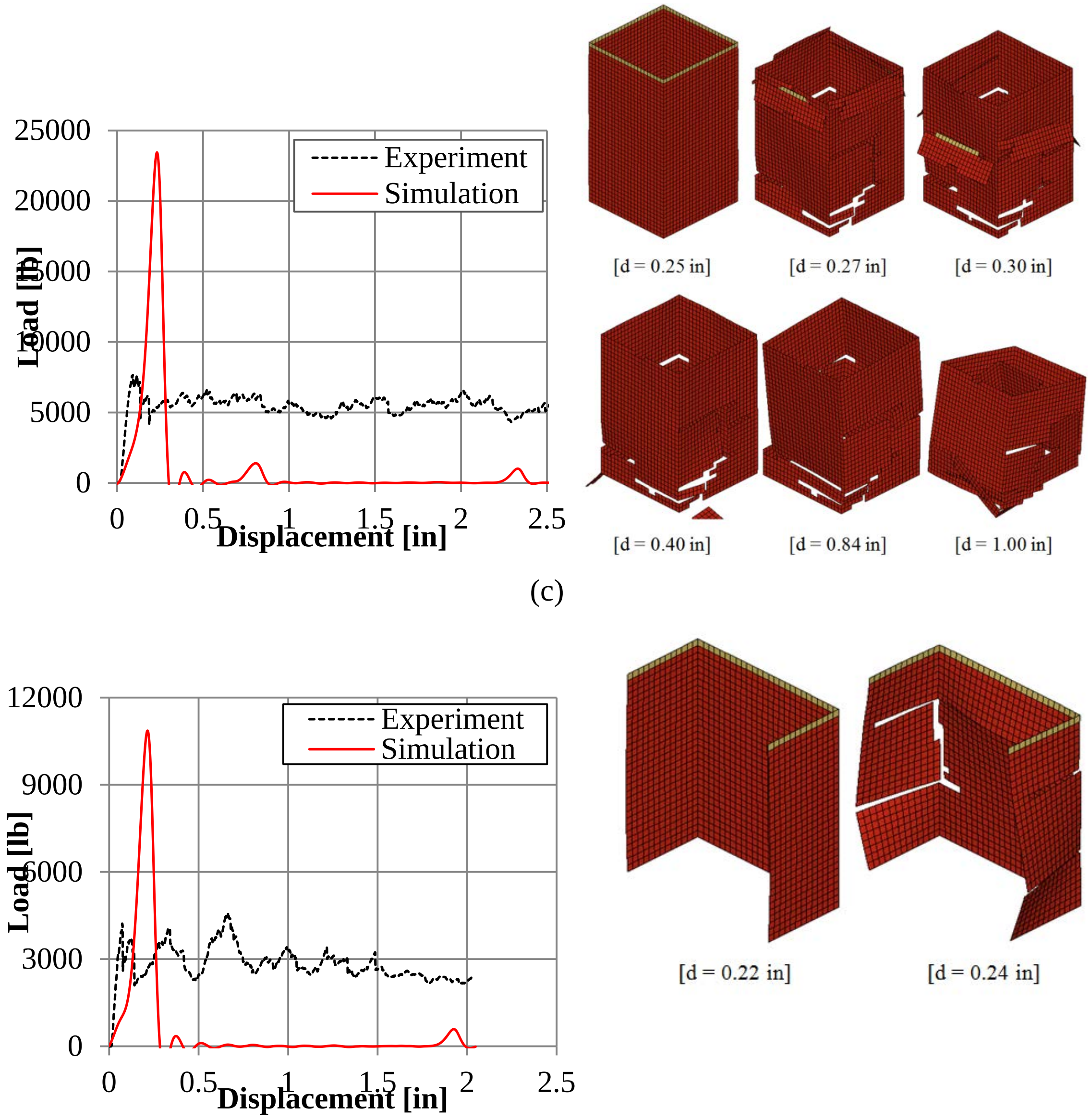

(c)

(d)

Figure 72. Undesired crush simulation results compared against the experimental curve when only the geometry is changed from the semicircular corrugation baseline model: (a) high sinusoid, (b) low sinusoid, (c) square tube, (d) large C-channel, (e) small C-channel, (f) large corner, and (g) small corner elements (continued)

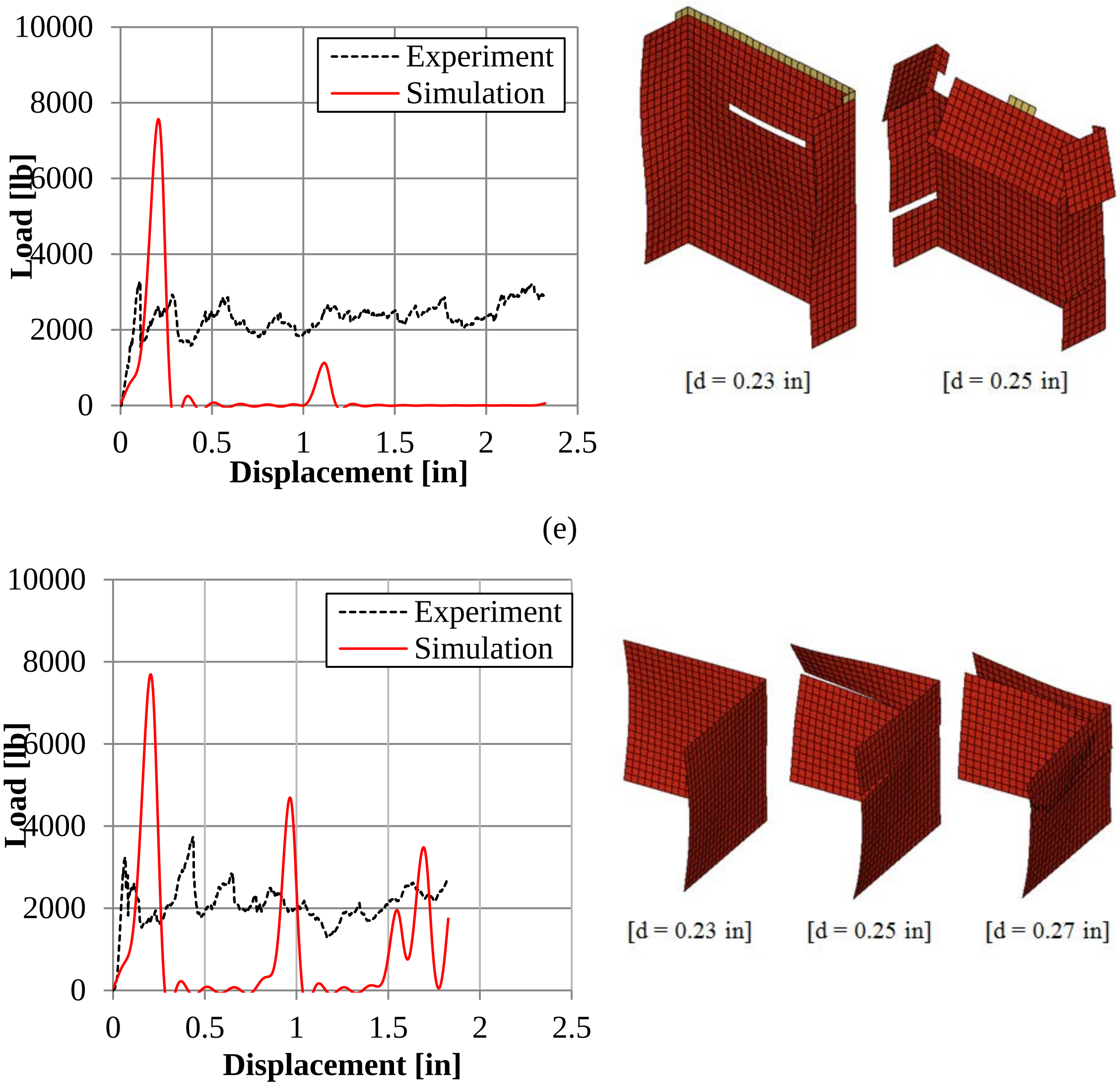

(e)

(f)

Figure 72. Undesired crush simulation results compared against the experimental curve when only the geometry is changed from the semicircular corrugation baseline model: (a) high sinusoid, (b) low sinusoid, (c) square tube, (d) large C-channel, (e) small C-channel, (f) large corner, and (g) small corner elements (continued)

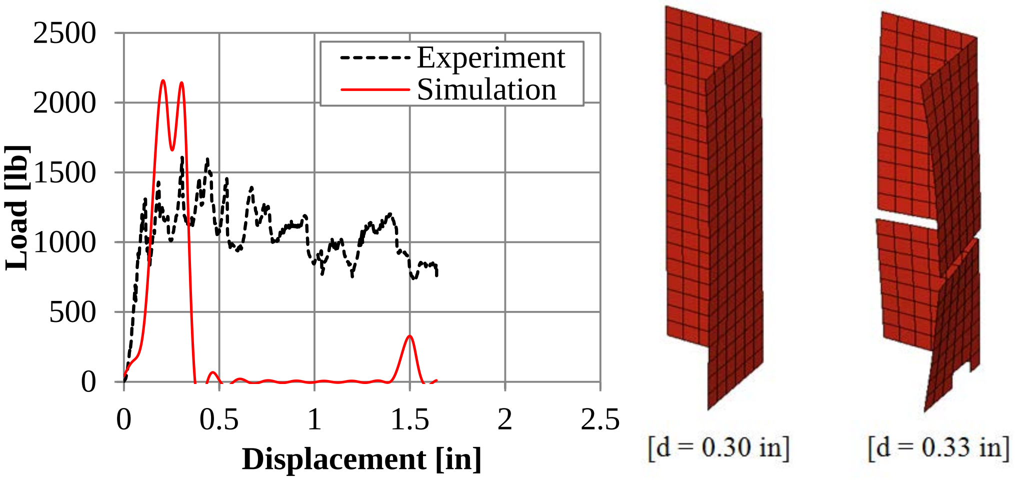

(g)

Figure 72. Undesired crush simulation results compared against the experimental curve when only the geometry is changed from the semicircular corrugation baseline model: (a) high sinusoid, (b) low sinusoid, (c) square tube, (d) large C-channel, (e) small C-channel, (f) large corner, and (g) small corner elements (continued)

Although the initial results shown in figure 72 are unstable, changes to the SOFT parameter and the trigger thickness in combination with the new LP curve generated positive results. First, noting from figure 70(c) that failure of the square tube occurs at the initial load peak, the trigger thickness in this simulation is reduced to 0.011″ (0.28 mm) to prevent early failure and enable crush initiation. With a softer LP curve and a lower trigger thickness, the SOFT parameter was calibrated to a value of 0.145 such that the average crush load matched that of the experiment, shown in figure 73. Next, the trigger thickness is then recalibrated to a value of 0.015″ (0.38 mm) to match the initial load peak of the experimental curve, as shown in figure 74. The shape of the resulting load-displacement curve, initial peak load value, crush load value, and SEA value well matches the experimental results of the tube crush baseline simulation, as shown in figure 75. The crush progression, shown in figure 76, is smooth as elements are deleted simultaneously, row by row, at the crush front. Several steps were taken to develop a calibrated tube crush specimen simulation.

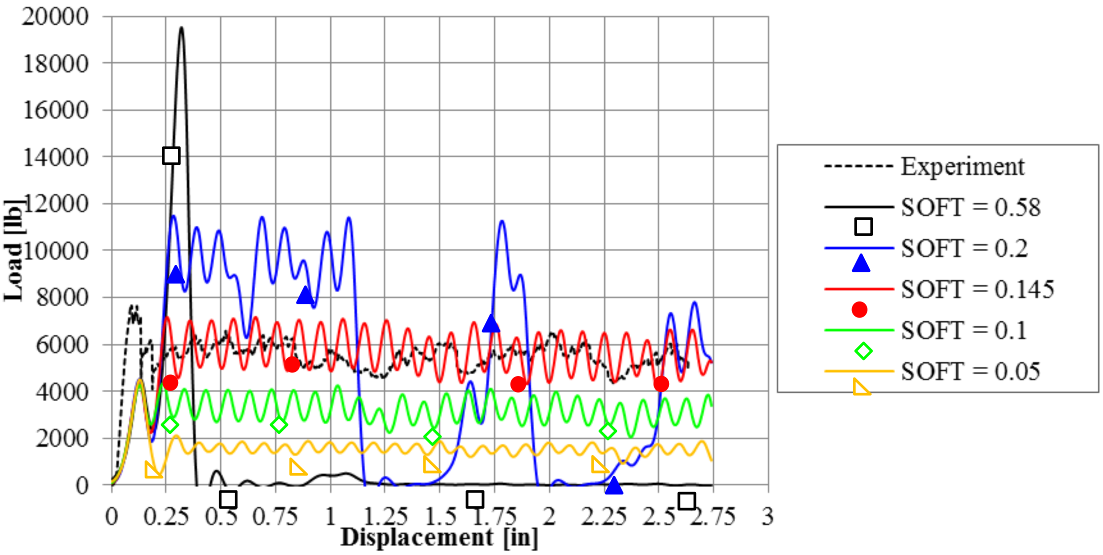

Figure 73. SOFT parameter calibration of the tube simulation using new contact LP curve

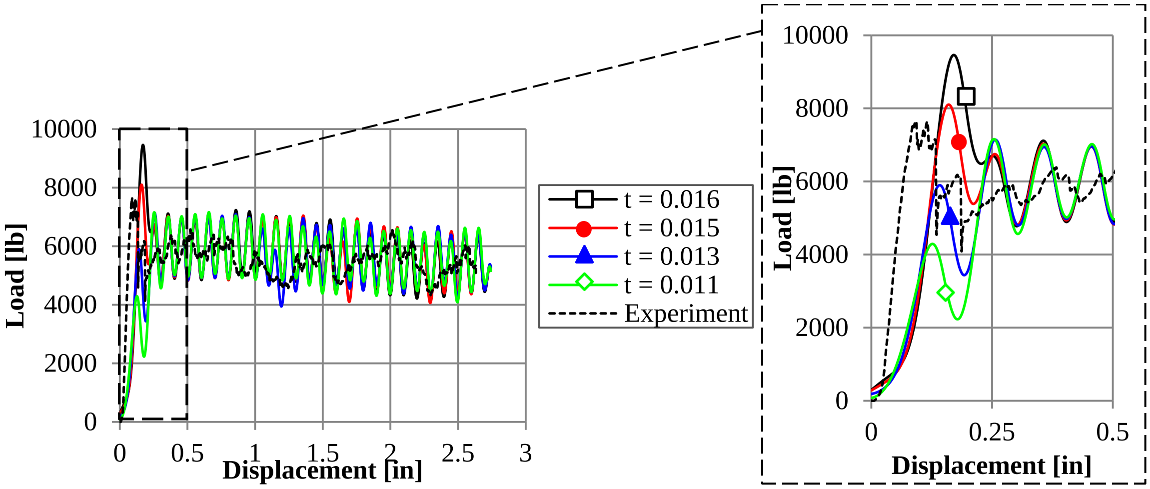

Figure 74. Trigger thickness calibration of the tube simulation using new contact LP curve

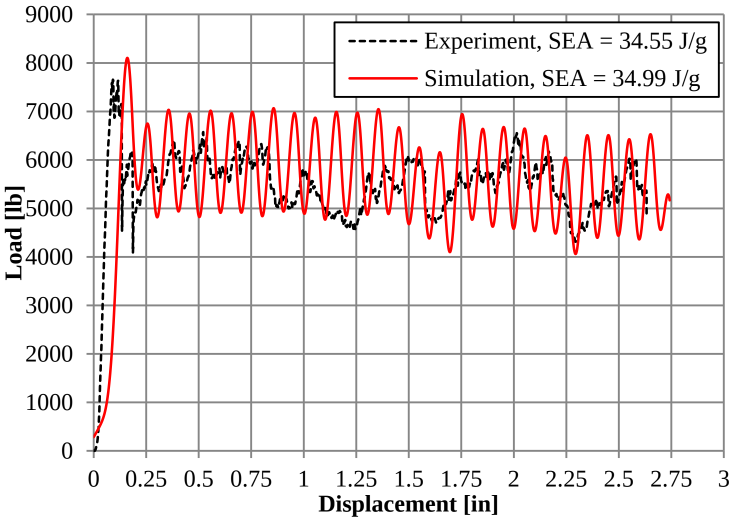

Figure 75. Load-displacement curves from simulation and experiment of the calibrated tube crush specimen

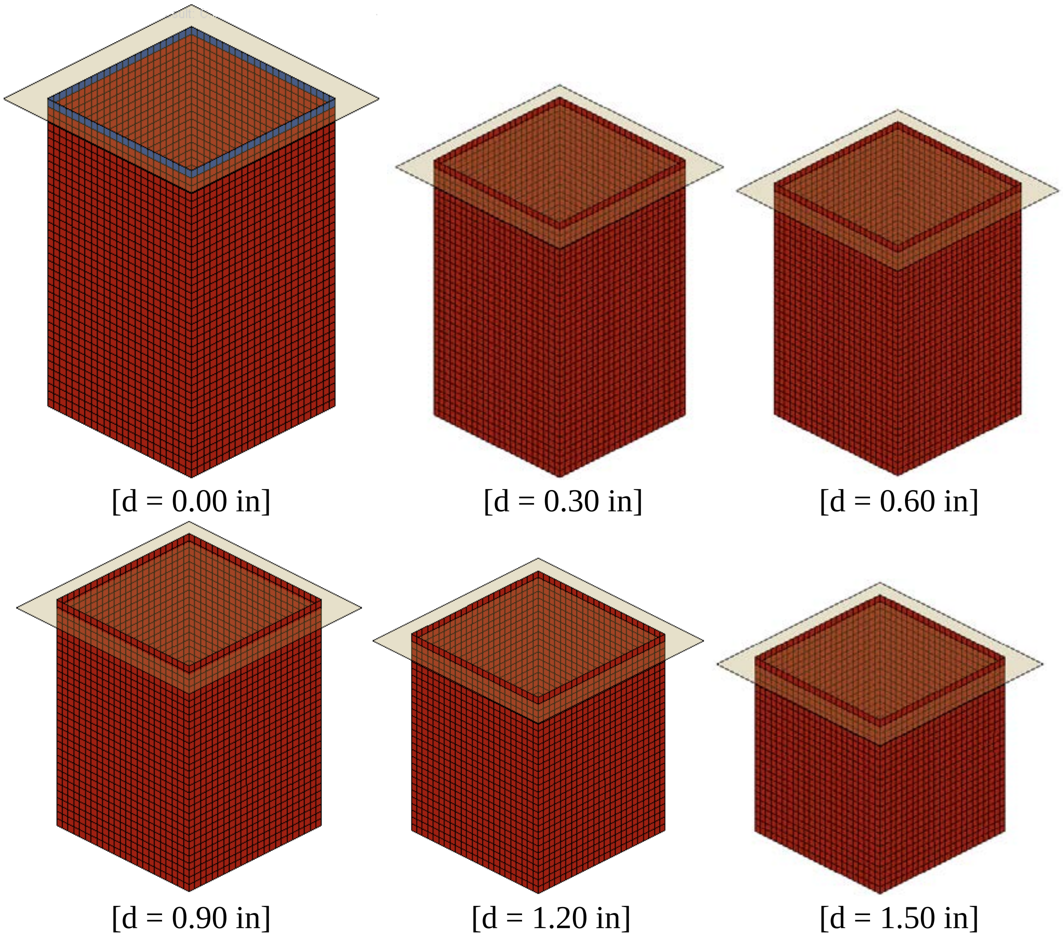

Figure 76. Time progression of the crushing simulation of the square tube baseline (d = displacement)

From the development and calibration process of the square tube crush simulation, three parameters required adjustment when changing the geometry of the crush specimen from the corrugation to the tube: the LP curve for stability, the SOFT value to calibrate the crush load and SEA, and the trigger thickness to calibrate the initial load peak value. Rather than calibrate the LP curve for each new geometry, the new soft LP curve is used for all the crush simulations, including the original baseline semicircular corrugation crush model, which is retroactively updated to have the new LP curve. In this way, only two parameters, SOFT and trigger thickness, are necessary to calibrate when changing the geometry of the crush specimen.

The successful tube crush simulation is modified to simulate each of the remaining seven geometries. After inserting these specimens into the crush simulation, the SOFT parameter and trigger thickness are each calibrated to match the experimental crush curve. By making only these two changes, all geometries were successfully simulated in crush. Crush curves of the LS-DYNA simulations calibrated to match the experimental load-displacement curves of the seven new geometries (excluding the square tube) are shown in figure 77. The calibrated SOFT and trigger thickness parameters used in all eight cases are shown in table 9, along with the simulated SEA results.

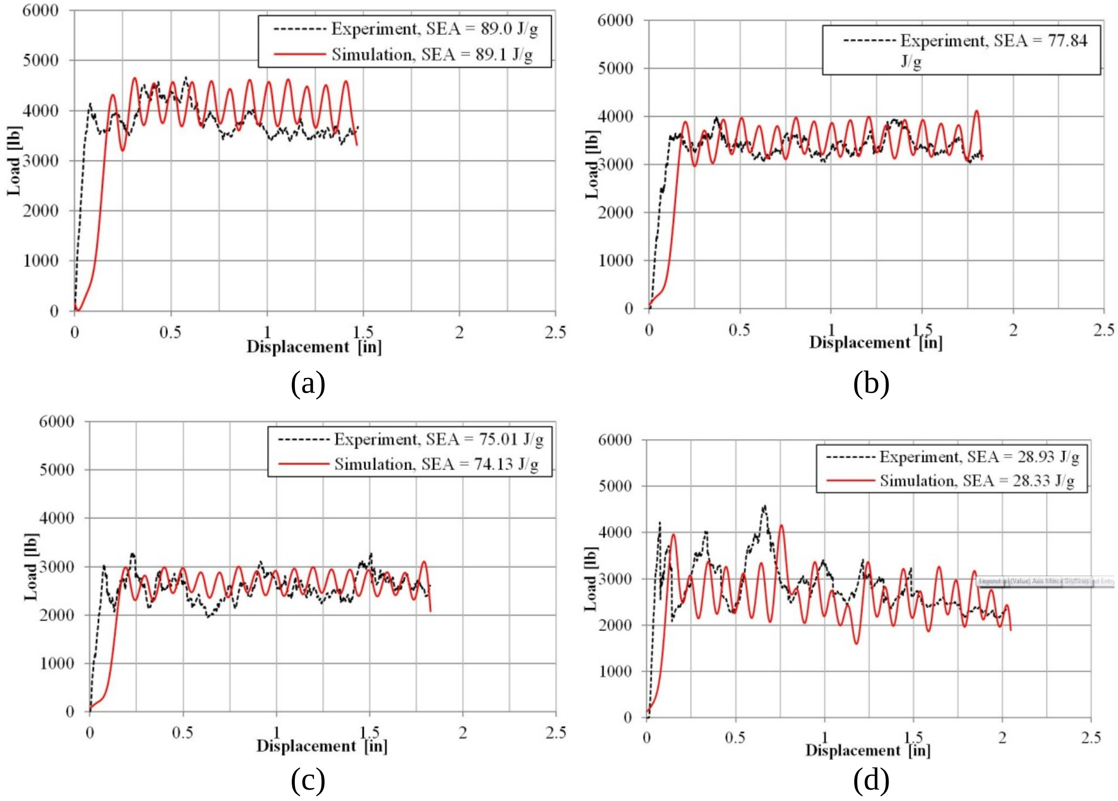

(a) (b)

(c) (d)

Figure 77. Load-displacement crush curve results comparing simulation with experiment for seven crush specimen geometries: (a) semicircular sinusoid, (b) high sinusoid, (c) low sinusoid, (d) large C-channel, (e) small C-channel, (f) large corner, and (g) small corner

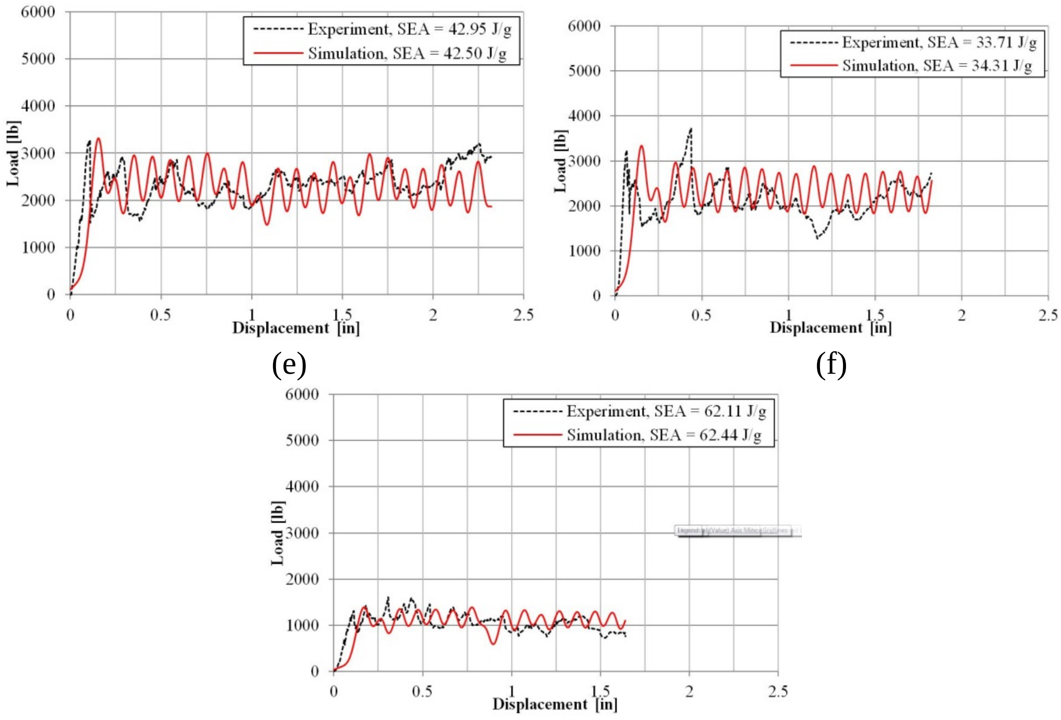

(e) (f)

(g)

Figure 77. Load-displacement crush curve results comparing simulation with experiment for seven crush specimen geometries: (a) semicircular sinusoid, (b) high sinusoid, (c) low sinusoid, (d) large C-channel, (e) small C-channel, (f) large corner, and (g) small corner (continued)

Table 9. Summary of the modeling parameters necessary to change each crush element geometry to match the experimental results, and the resulting error between simulation and experiment

Geometry	Trigger Thickness [in]	SOFT	Single Test SEA [J/g]	Numeric SEA [J/g]	Error
SC Sinusoid	0.044	0.580	88.98	89.08	0.1%
High Sinusoid	0.045	0.540	77.84	77.28	-0.7%
Low Sinusoid	0.040	0.450	75.01	74.13	-1.2%
Tube	0.015	0.145	34.55	34.99	1.3%
Large Channel	0.021	0.215	28.93	28.33	-2.1%
Small Channel	0.023	0.220	42.49	42.49	0.0%
Large Corner	0.022	0.205	33.71	33.43	-0.8%
Small Corner	0.030	0.310	62.11	62.44	0.5%

10.2 DISCUSSION OF RESULTS

As a result of this investigation, it is possible to generate relations between experimental data and modeling parameters that would allow crush modeling of various geometries from an initial calibrated crush model. First, the linear relation between the calibrated SOFT parameter and the experimentally measured SEA is revealed in their plot, shown in figure 78. The SOFT parameter can be interpreted as a utility to account for the virtual damage that has propagated beyond the crush front. Figure 78 shows that greater values of SOFT yield higher SEA in the simulation. The micrographic analysis of crushed specimens from sections with varying SEA capability, shown in figure 38, indicates that the greater the damaged area, the smaller the SEA. This provides a new interpretation of the SOFT parameter as the degree of damage and delamination suppression provided by the geometry, thickness, layup, and material system. Because the thickness, layup, and material system remained constant, in this study the SOFT parameter is perceived as the degree of damage suppression provided by the geometry of the crush specimen. The higher the SOFT value is, the higher the crush damage suppression and SEA will be. This relationship provides a link between an experimental measurement (SEA) and the most important modeling parameter that requires calibration when the SEA changes (SOFT).

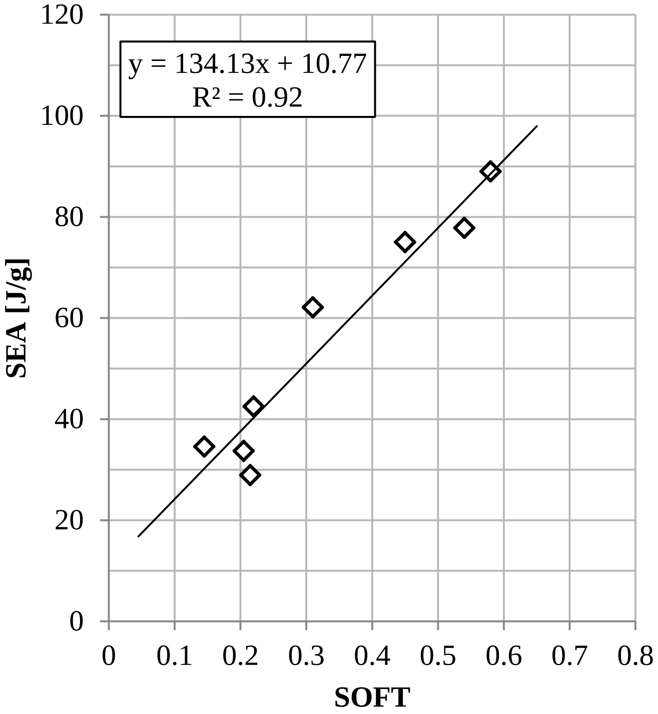

Figure 78. Linear trend between calibrated MAT54 SOFT parameter and the experimental SEA

The only other modeling parameter that requires calibration when the geometry of the crush element changes is the trigger thickness. The thickness of the trigger elements is reduced to facilitate crush initiation, and the reduced cross section of the trigger elements ensures these elements fail at a lower applied force than the full-thickness elements. In this way, the trigger thickness is a strength knockdown factor for the initial row of elements, which are not subject to the SOFT knockdown because the crush front is established only after failure of the initial element row. It would therefore seem logical that the strength knock-down provided by the reduction in thickness for the trigger elements should be equal to the strength knock-down provided by SOFT for the rest of the elements. To verify this, the calibrated SOFT is plotted against the ratio of the reduced trigger thickness to the total element thickness, which generates the linear relationship shown in figure 79. The fact that this linear relationship is nearly 1:1 suggests that the trigger row of elements has nearly the same strength knockdown, by virtue of reducing the cross-sectional area, as that applied by SOFT to the rest of the elements. The correct trigger thickness value can therefore be determined from the calibrated SOFT parameter. Changing the geometry of the crush element is dependent only on a single variable (SOFT).

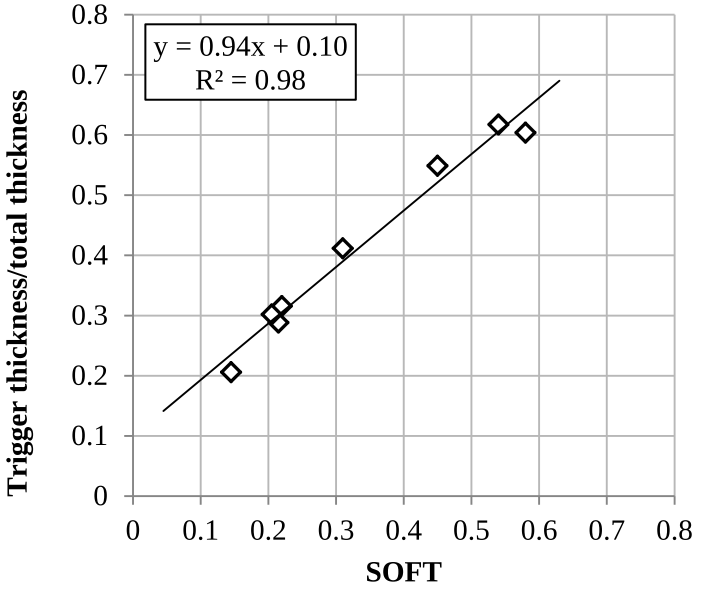

Figure 79. Linear trend between the calibrated SOFT parameter and the ratio of trigger thickness to original thickness

For this fabric material system, the calibrated values of the numerical SOFT and trigger thickness can be estimated from the experimentally measured SEA using the plots in figures 78 and 79, which will produce a good crush simulation. This approach is not predictive, but uses experimental data at the element level to guide model calibration.

10.3 ANALYTICAL CONCLUSIONS

Using the existing MAT54 material model developed for the corrugated element shape, several simulations of crush elements with various cross-sectional geometries have been successfully calibrated to match the experimental results well. In this MAT54 crush modeling approach, it is not possible to simulate different specimen geometries without making changes to the material model because specific damage and failure mechanisms (such as delamination) cannot be modeled individually. From this investigation, sensitivity studies have established important MAT54 and other modeling parameters, which influence these crush simulations the most. Finally, some relationships have been established that link experimental parameters (SEA) to important modeling parameters (SOFT, trigger thickness), making the calibration of the crush simulation more focused by reducing the scope of the trial and error calibration process. Ultimately, this modeling approach requires a comprehensive set of experimental element-level crush data, which fully characterizes the energy-absorbing capability of the composite material system so that trial-and-error calibration of the SOFT parameter can be executed to develop a good crush model. The next goal in this body of work is to modify the MAT54 material model to investigate if a better composite material model for crush simulation can be developed and successfully implemented for these element-level crush specimens.

11. PART III—MODIFIED MATERIAL MODEL MAT54

A modified version of the MAT54 material model has been developed by changing an isolated portion of the source code of the LS-DYNA program. Specific details of the MAT54 source code and modifications made to the code are outlined in appendix A. This section will present the results of the modified model as it was used in the single-element and crush simulations.

The modification efforts of MAT54 are best understood when the composite failure model is generalized as the simulation of three phases: 1) the elastic response, 2) failure determination, and 3) post-failure degradation. These three phases are summarized in the basic stress-strain curve generated by MAT54, shown in figure 80. In each of these three phases, modifications were made to attempt to improve the original material model.

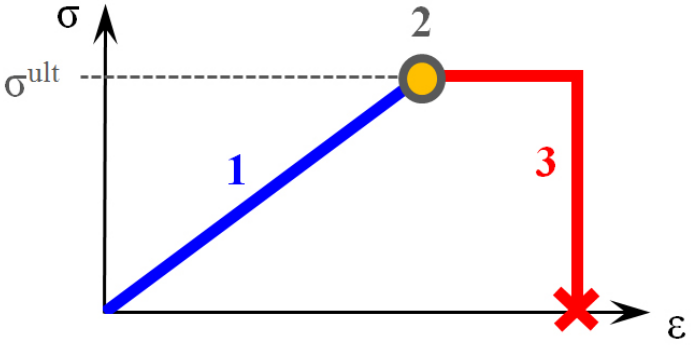

Figure 80. Material stress-strain curve outlining three of the basic MAT54 composite failure regions: (1) elastic, (2) failure, and (3) post-failure degradation

12. MODIFIED ELASTIC RESPONSE

12.1 MODEL DEFINITION

During the MAT54 single element investigation, it was determined that the elastic response of a UD composite material could not be modeled as it behaves physically because of the limited constitutive property input parameters available from MAT54. Missing constitutive parameters include the compressive modulus in both the axial and transverse directions, and a strain-to-failure value for compression in the transverse direction. These three missing constants are added as new user input parameters, and the single-element and crush simulations, which model both the UD and fabric composite material systems, reveal the effect of these added parameters. The compressive properties input into the modified model are taken from published AGATE data, as shown in table 2.

12.2 SINGLE-ELEMENT RESULTS

The improvement in the elastic definition of the UD material is immediately apparent because the modified MAT54 is capable of exactly modeling the material as it is defined by its material properties. This is shown by the stress-strain curves in figure 81. There is noticeable improvement in the simulation of the compressive stiffness and, for the transverse case, the failure strain. The characteristic perfectly plastic region of MAT54 is no longer present in the modified model. The modified single-element model of the UD cross-ply laminate also produces improved results, as shown in figure 82. For this case, the simulations are compared against experimental data, resulting in a larger error, mainly because of the error of the CLT calculations used to predict the laminate behavior from the lamina properties against the experimental laminate data. For this case, it is more useful to compare the improvement of the modified model over the original MAT54.

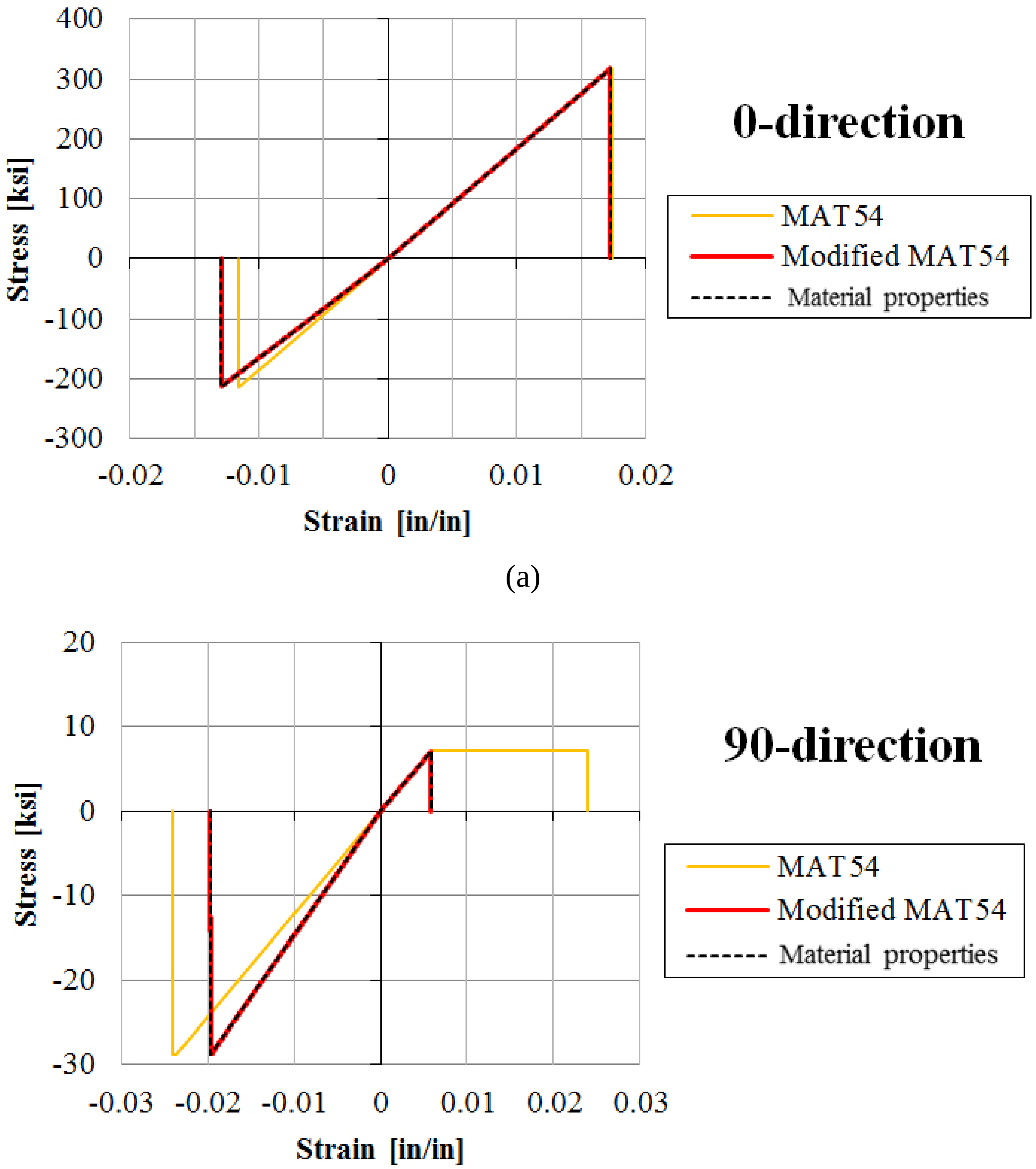

(a)

(b)

Figure 81. Results of modified elastic response on the UD single-element model in the (a) axial, 0-direction and (b) transverse, 90-direction

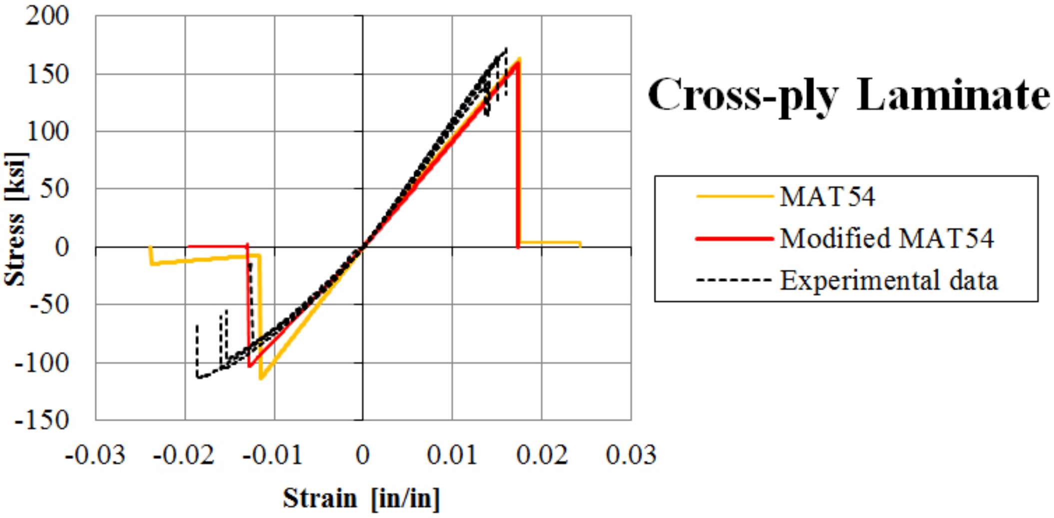

Figure 82. Results of modified elastic response on the UD cross-ply laminate single-element model as compared against experimental coupon data

12.3 CRUSH SIMULATION RESULTS

The semicircular sinusoid crush simulation is run using the modified UD material model, and the resulting crush curve is just as stable as the original model, shown in figure 83. It should be noted that, because the compressive modulus was updated to reflect the true compressive modulus of the material, the DFAILC strain-to-failure value was also changed to maintain a material behavior that is perfectly linear elastic until failure. Recall that changes in DFAILC result in changes in the average crush load of the load-displacement curve in MAT54 crush simulations. As expected, raising DFAILC did raise the average crush load of the simulation, so a slight decrease of SOFT was necessary to match the experiment for the modified model. All of these MAT54 parameter changes that were made for the sinusoid crush simulation of the UD material are shown in table 10.

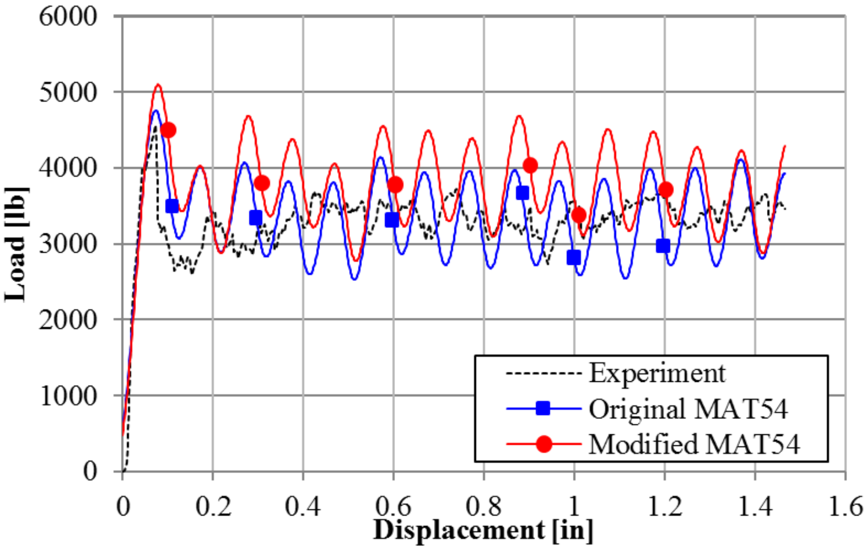

(a)

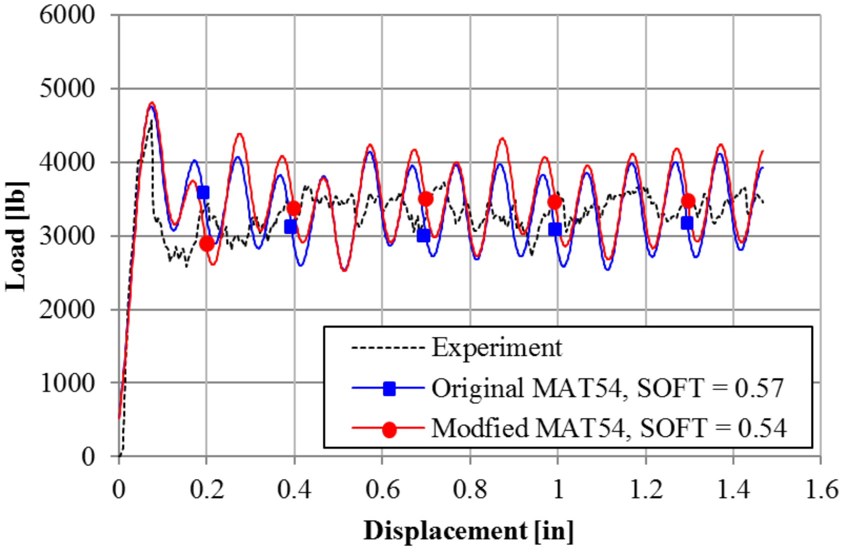

(b)

Figure 83. Crush curve results of modified elastic response on the UD sinusoid crush simulation as compared against the original MAT54 and the experimental data (a) before SOFT adjustment and (b) after SOFT adjustment

Table 10. Original and modified material input parameters used for the UD material definition

	MAT54	Modified MAT54
EA	18.4 Msi	18.4 Msi
EAC	18.4 Msi	16.5 Msi
EB	1.22 Msi	1.22 Msi
EBC	1.22 Msi	1.47 Msi
DFAILM	0.024	0.0058
DFAIL2M	0.024	0.0196
DFAILC	-0.0116	-0.0129
SOFT	0.57	0.54

For the model of the fabric material, there is no improvement gained by utilizing the modified model, as shown in the single-element results in figure 84. This is largely because there is a smaller difference in compressive and tensile properties of the fabric material system, and for this reason there was little error in the original MAT54 material model of the fabric. Also, for the fabric material, only the axial data is of interest because all the elements are given a 0-degree orientation in the composite part definition of the fabric material, so the addition of the DFAIL2M parameter is not evident in this single-element simulation. For these reasons, no improvement is apparent using the modified material model for the fabric material system.

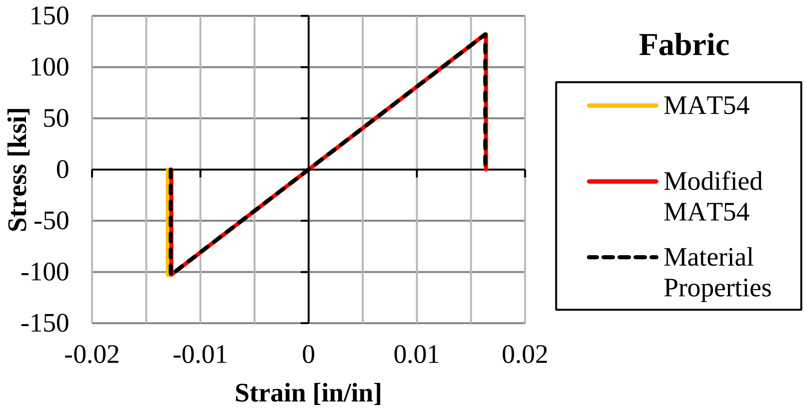

Figure 84. Results of modified elastic response on the fabric single-element model

Implementing the modified material model to simulate the fabric material for use in the crush element simulations also does not provide improvement, and in fact destabilizes some crush elements. First, the effect of using the additional compressive moduli, EAC and EBC, is investigated. When comparing the crush simulation results using the original MAT54 against those using the modified MAT54 with compressive moduli, some simulations are undisturbed, such as the simulation of the small C-channel crush element shown in figure 85(a), while others are slightly disrupted by the modified model, such as the small corner crush element shown in figure 85(b). In general, the disruptions caused by the added compressive moduli are relatively minor and tend to only slightly change the resulting crush curve while crushing remains stable and progressive.

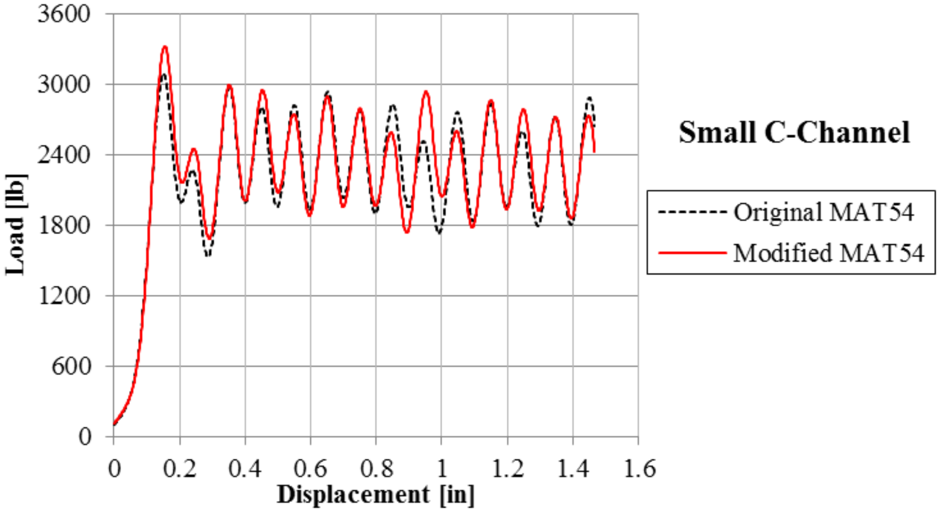

(a)

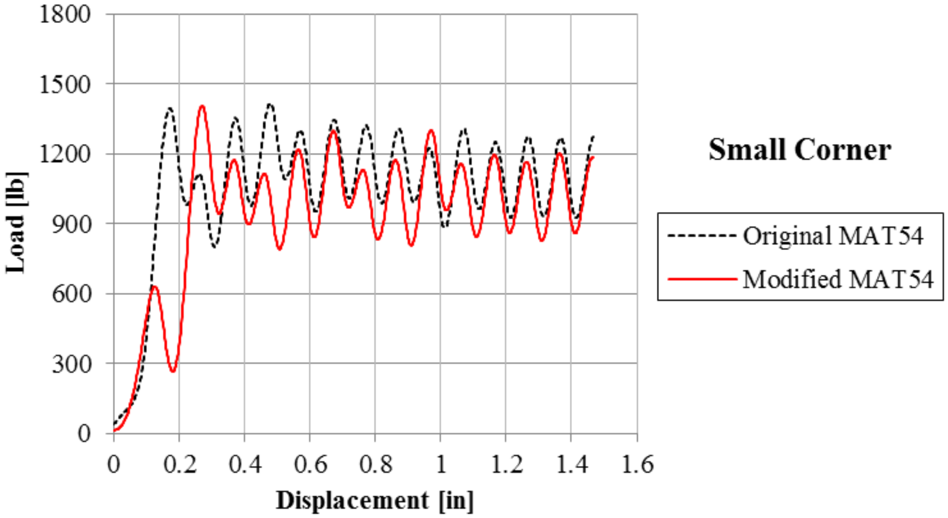

(b)

Figure 85. Crush simulation results, the original MAT54 compared against a modified version that has compressive moduli, on the (a) small C-channel and (b) small corner crush elements

The addition of the DFAIL2M parameter in the modified MAT54 model allows for an investigation of the transverse plasticity required by the original MAT54 crush element models. Recall that when using the original MAT54, the transverse strain-to-failure parameter, DFAILM, had to be greatly increased from its measured experimental value to stabilize the fabric material model crush-element simulations, effectively inducing artificial plasticity in the transverse direction in both tension and compression. While not all of the fabric crush elements required the increased DFAILM for stability, each of the simulations featured transverse plasticity to maintain a consistent material input deck.

With the modified model, it is possible to consider the transverse load cases separately and determine if plasticity is necessary in tension, compression, or both for the fabric crush element models. Each crush element was investigated using various DFAILM and DFAIL2M, and it was determined that only two of the crush elements required plasticity for stability, while the rest could use the experimental strain-to-failure values for both DFAILM and DFAIL2M. One such example is shown in figure 86, in which results of the small C-channel element are shown to be stable and mostly unchanged with and without transverse plasticity.

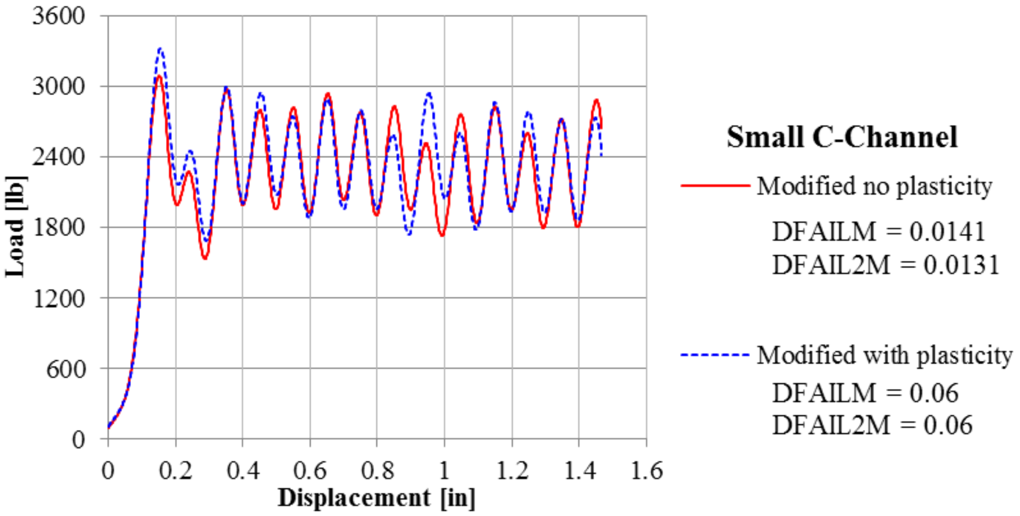

Figure 86. Stable crush simulation results of the small C-channel element using the modified material model with and without transverse plasticity

The two crush elements that required transverse plasticity were the small corner and large C-channel elements. For both cases, plasticity was required in both the tension and compression transverse load cases to achieve stable and progressive crushing throughout the simulation. Results from using the modified model on the large C-channel element, shown in figure 87, show that without the plasticity in both DFAILM and DFAIL2M, the crush element is completely destabilized and experiences global buckling. In the case for which only the tensile load case is given plasticity (DFAILM = 0.06; DFAIL2M = 0.0131), buckling occurs near the end of the simulation. This result indicates that the addition of the DFAIL2M parameter provides no real benefit for the simulation of the fabric material.

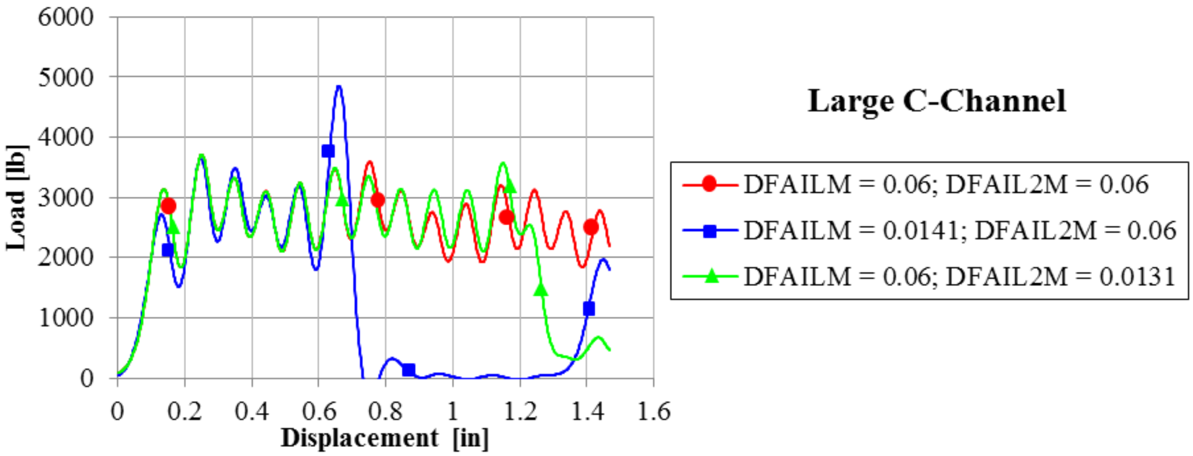

Figure 87. Crush curve results showing the destabilizing effect of changing the two transverse strain-to-failure parameters, DFAILM and DFAIL2M, in the modified model of the large C-channel crush element

The modifications made to the MAT54 source code to improve the elastic response of the composite material model provided benefits only for the model of the UD material. These benefits were clearly evident in the single-element simulations, where the true material behavior was exactly modeled—an accomplishment not possible without the modifications. The model of the fabric material was not improved using the modified model for elastic behavior; in fact, these modifications provided disruptions to the stability of the fabric crush element simulations. Overall, the modifications made for the elastic response are recommended only for the model of the UD material and will not be used in any further models of the fabric material presented in this report.

13. MODIFIED FAILURE DETERMINATION

13.1 MODEL DEFINITION

Different failure criteria are implemented to investigate the effectiveness of the Hashin failure criteria used in MAT54 and to determine if other failure criteria can provide better results for crush simulation. Three new sets of failure criteria are investigated: a set of criteria meant for fabric materials, a maximum crush stress criterion for crush front elements, and a strain-energy-based criterion. It should also be noted that LS-DYNA allows for the Tsai-Wu failure criterion to be implemented in place of the Hashin criteria by selecting a value of 55 for the CRIT input parameter in MAT54, effectively making it the material model MAT55. This model is not appropriate for simulations that require modeling beyond failure, such as crash, because there is no post-failure model included with MAT55. For this reason, the Tsai-Wu option of MAT54/55 is not explored in this research as a viable alternative for crash modeling.

13.1.1 Fabric Failure Criteria

The Hashin failure criteria used by MAT54 are meant to simulate the failure of a UD material, for which failure is driven by fiber breakage in the axial direction and matrix cracking in the transverse direction. For this reason, the axial and transverse failure modes are referred to as fiber and matrix modes, respectively. The matrix modes are specifically prescribed to predict matrix cracking, and, in particular, the compressive matrix failure mode is unique to the compressive fiber mode, as evidenced by comparing the compressive criteria in equations 28 and 30. For the model of the fabric material system, it would be more appropriate to apply the fiber failure criteria in both axial and transverse directions. It is proposed that the following failure criteria are used for the fabric material model:

Tensile Fiber Mode

$$\left(\frac{\sigma_{11}}{F_1^{tu}}\right)^2+\beta\left(\frac{\sigma_{12}}{F_{12}{}^{u}}\right)^2=1 \qquad \text{for } \sigma_{11}>0 \tag{27}$$

Compressive Fiber Mode

$$\left(\frac{\sigma_{11}}{F_1^{cu}}\right)^2=1 \qquad \text{for } \sigma_{11}<0 \tag{28}$$

Tensile Matrix Mode

$$\left(\frac{\sigma_{22}}{F_2^{tu}}\right)^2+\beta\left(\frac{\sigma_{12}}{F_{12}{}^{u}}\right)^2=1 \qquad \text{for } \sigma_{22}>0 \tag{29}$$

Compressive Matrix Mode

$$\left(\frac{\sigma_{22}}{F_2^{cu}}\right)^2=1 \qquad \text{for } \sigma_{22}<0 \tag{30}$$

13.1.2 Crush Stress Criterion

It is desired that an experimentally derived parameter be used as a simulation input to make material failure for crush simulation predictive for different crush element geometries, and not dependent on the trial and error calibration of the SOFT parameter. The crush stress criterion uses the average crush stress as measured from crush experiment as an input parameter to the simulation in place of the arbitrary material softening caused by SOFT. A new maximum stress criterion is applied to crush front elements only, using the crush stress as the limiting parameter rather than reducing the crush front element strengths by the SOFT parameter. The crush stress criterion is therefore:

$$\frac{\sigma_1}{\sigma_{crush}} = 1 \tag{31}$$

Note that, for this investigation, the crush stress criterion is in effect only in the axial direction of the element; thus, the criterion utilizes the one-direction stress component. This criterion is effective along with the existing Hashin criteria, which remain to account for any other failure modes the material may experience.

13.1.3 Wolfe Strain Energy Criterion

Another experimentally derived input parameter that could potentially replace the need for the empirically derived SOFT is strain energy. Wolfe's failure criterion utilizes axial, transverse, and shear strain energy components measured from coupon-level material testing to determine material failure in equation 11.

To implement this failure criterion into the modified MAT54 material model, several new user input parameters are required to define the ultimate strain energy values of the material, as measured by material coupon experiment and by the three shape functions M1, M2, and M6. Altogether, eight new user inputs are implemented, as shown in table 11.

Table 11. New modified MAT54 user input parameters added for Wolfe's strain energy failure criterion

SEFT	Ultimate axial (fiber) tensile strain energy component
SEFC	Ultimate axial (fiber) compressive strain energy component
SEMT	Ultimate transverse (matrix) tensile strain energy component
SEMC	Ultimate transverse (matrix) compressive strain energy component
SES	Ultimate shear strain energy component
M1	Shape function value for the axial strain energy component
M2	Shape function value for the transverse strain energy component
M6	Shape function value for the shear strain energy component

13.2 SINGLE-ELEMENT RESULTS

13.2.1 Fabric Failure Criteria

The effect of the fabric failure criteria upon the single-element and crush-element simulations was investigated. For the fabric single-element, no changes were observed and the result was identical to those using the Hashin failure criteria. This was expected because the single element was given basic tensile and compressive loading conditions that are shear free. Without shear terms, the original Hashin failure criteria reduce to the fabric criteria, so the two single-element simulations were expected to be identical.

13.2.2 Wolfe Strain Energy Criterion

The Wolfe failure criterion is first enacted along with the existing Hashin failure criteria so that either may cause element failure. Single-element simulations were run using the modified material model for both the UD and fabric material models. The ultimate strain energy values input into the modified model were measured from the experiment. The shape function parameters M1, M2, and M6 were initially given default values of 1.0, as suggested by Wolfe [61]. Results from both the UD and fabric material models indicate that the Wolfe failure criterion prematurely predicts element failure, as shown in the stress-strain curves of figure 88. This result is not unexpected, as the results published by Wolfe when implementing this strain energy failure criterion also under-predicted failure for several different composite material systems undergoing biaxial loading conditions.

Adjustments can be made to the new strain energy and shape function input parameters to reduce the error between simulation and experiment, as shown in figure 88(c); however, doing so makes the implementation of the Wolfe criterion an exercise of trial and error for several new parameters.

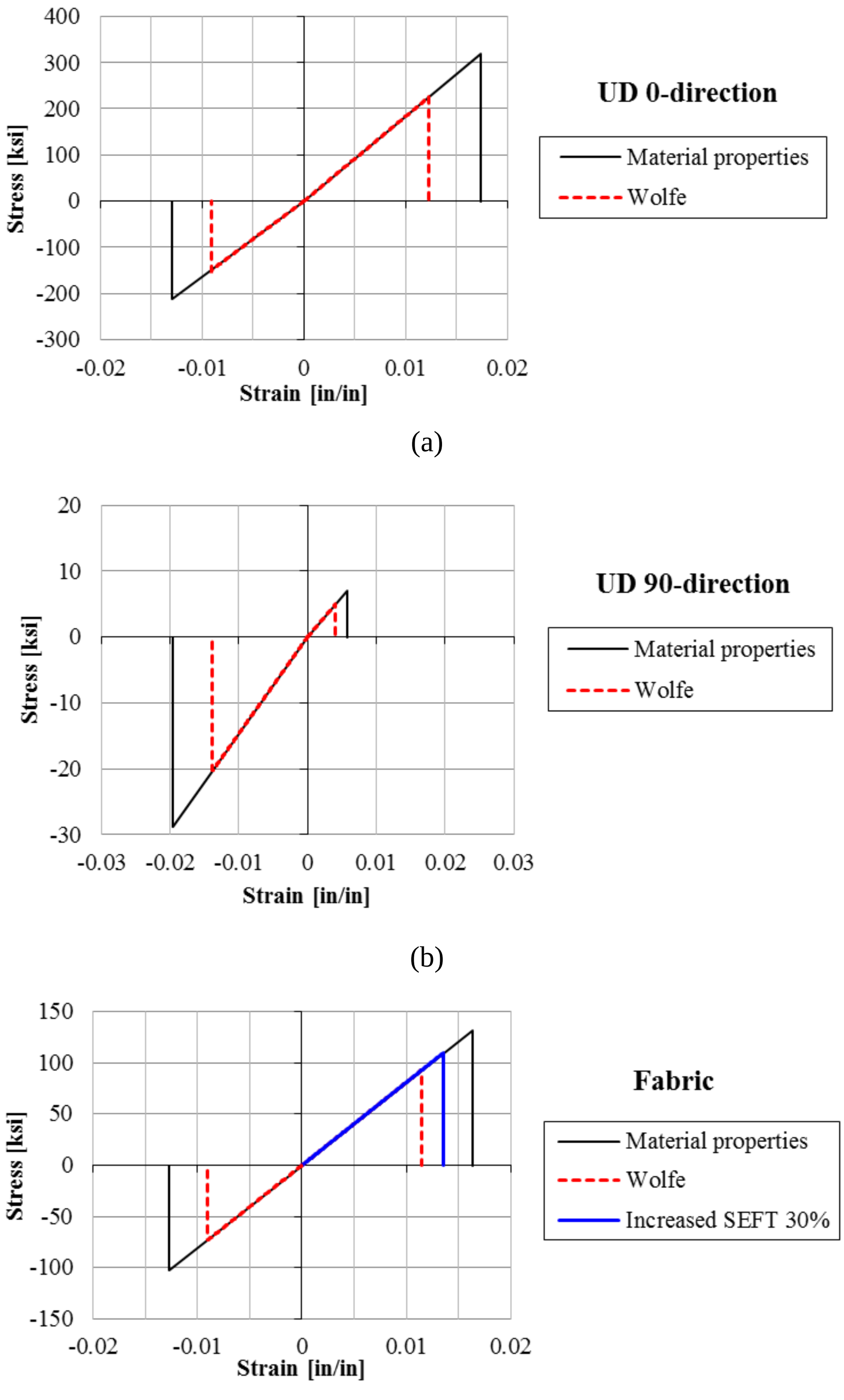

(a)

(b)

(c)

Figure 88. Single-element stress-strain curves that show the result of using the Wolfe failure criterion against the material properties for the UD material in the (a) axial and (b) transverse, and for the (c) fabric material system

13.3 CRUSH SIMULATION RESULTS

13.3.1 Fabric Failure Criteria

The use of the fabric failure criteria has very little influence on the results of the crush element simulations as well. For most of the crush elements, the resulting crush curve is indistinguishable from the original MAT54 results, such as for the large corner element, as shown in figure 89(a). Only the large C-channel and small corner elements experience some instability, as shown in figure 89(b). These are also the only two elements that experienced instabilities due to the modified transverse strain-to-failure values, and in general seem to be more easily destabilized by changes in the model than any of the other elements. In general, it can be concluded that these fabric failure criteria provide no real benefit for crush modeling.

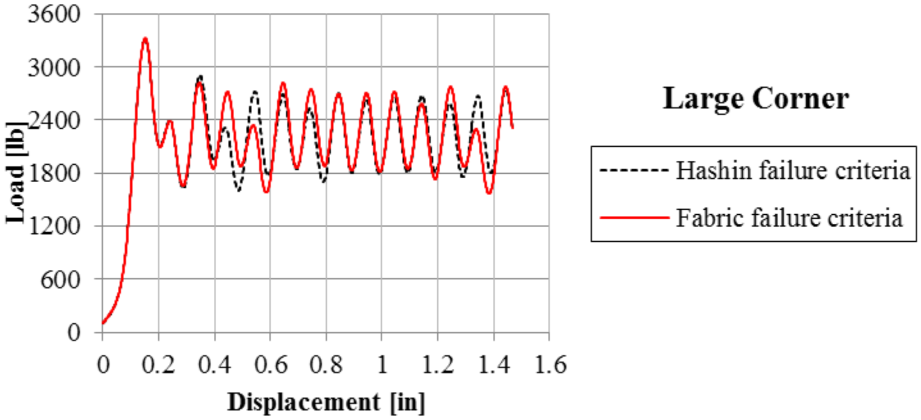

(a)

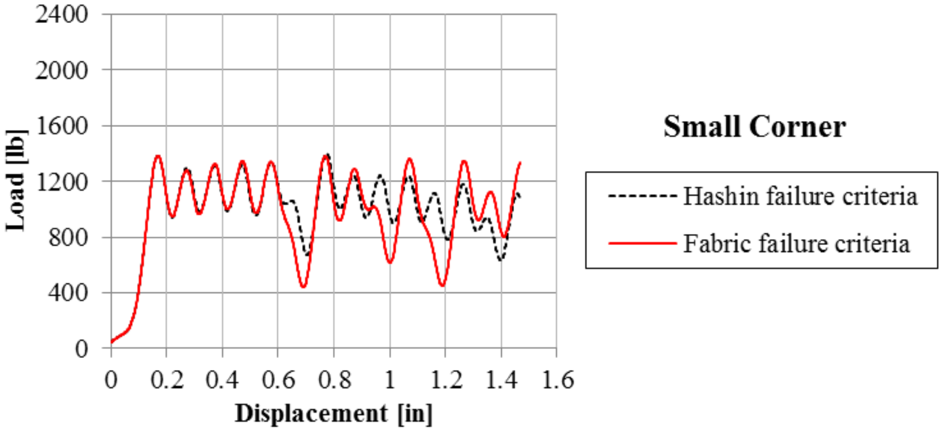

(b)

Figure 89. Effect upon the crush simulation results of changing the failure criteria from Hashin to the fabric criteria for the (a) large corner element and (b) small corner element

13.3.2 Crush Stress Criterion

The new crush stress criterion is used in simulations of the semicircular sinusoid crush element using both the UD and fabric material models. The average crush loads measured from the experiment of the UD and fabric sinusoid crush elements are 3360 lbs and 3800 lbs, respectively [90]. Given the cross-sectional area of the semicircular sinusoid element, the average crush stresses measured from the experiment are 15 ksi for the UD element and 20 ksi for the fabric element. These values are used for the new SIGCR user input parameter, and SOFT is set to 1.0 to prevent material softening, instead allowing for the crush stress criterion to remove elements at the crush-front. Note that the SIGCR parameter is input as a negative value because it is a compressive stress.

The resulting sinusoid crush simulation using the UD material model with the experimentally measured crush stress input, SIGCR = -15 ksi, yields a simulated crush curve with a crush load much lower than expected, as shown in figure 90. Increasing the maximum crush stress parameter value delays crush front element deletion and increases the crush load much in the same way that SOFT affects crush front element deletion and the resulting average crush load. A SIGCR value of 130 ksi yields results that match the experiment well, which is nearly nine times the experimentally measured value of crush stress.

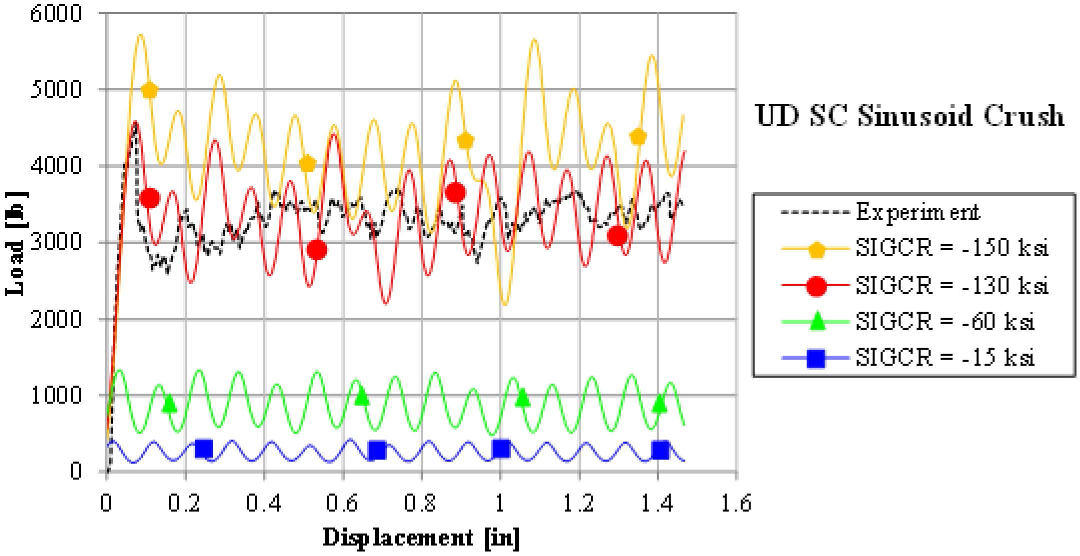

Figure 90. Effect of changing the SIGCR maximum crush stress parameter on the crush results of the semicircular sinusoid using the UD modified material model

The same trend is observed for the sinusoid crush simulation using the fabric material model, where a SIGCR value of 60 ksi, nearly three times the experimentally measured value of crush stress, simulates the crush experiment well, shown in figure 91. For the fabric material simulation, the initial load peak is not affected by the crush stress criterion because the crush front is not established until after the initial row of elements is deleted. The initial load peak is instead determined by the trigger thickness, which has not changed and continues to match the experiment well. This is different from the UD model because it uses a different contact definition for which the initial load peak represents the deletion of the first crush front row of elements, not the trigger. These contact definitions were discussed in section 8 during the development of the two baseline sinusoid crush models.

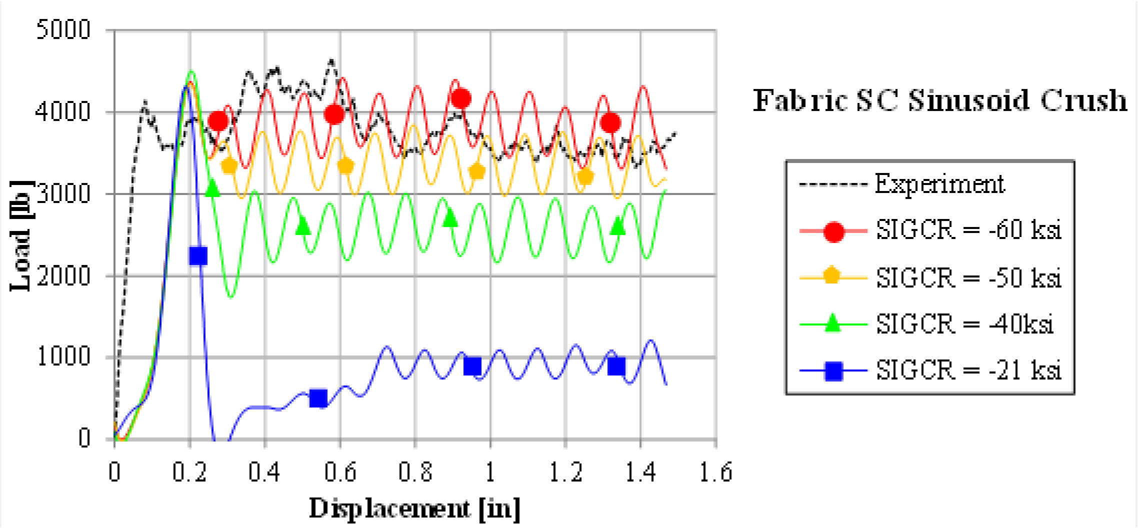

Figure 91. Effect of changing the SIGCR maximum crush stress parameter on the crush results of the semicircular sinusoid using the fabric modified material model

While it was expected that the experimentally measured crush stress value would be an appropriate limiting stress value for the crush front elements, these values have been shown to be too low. This is suspected to be due to the contact definition, and in particular the LP curve, which prescribes the load applied to the elements at the contact surface. This curve effectively alters the loads at the contact surface, causing elements to experience different stresses than they would at a purely rigid contact. Unfortunately, such a contact is required by MAT54, and contact definitions without LP curves have been shown to be ineffective with MAT54 elements [90]. For this reason, the SIGCR value that best matches the crush experiment is not the average crush stress as measured by the experiment, and its appropriate input value can only be determined by trial and error. In this way, the SIGCR parameter and the crush stress criterion have the same benefit to the MAT54 crush model as the SOFT parameter and the crush front material softening. Either parameter and crush front element deletion method can yield successful simulation results, but only after being calibrated against the crush element experiment.

13.3.3 Wolfe Strain Energy Criterion

Experimentally derived values are preferred and are used in the crush simulation of the semicircular sinusoid element. The result is that several elements are deleted prematurely from the crush front, and stable crushing is not achieved for either material system, shown in figure 92.

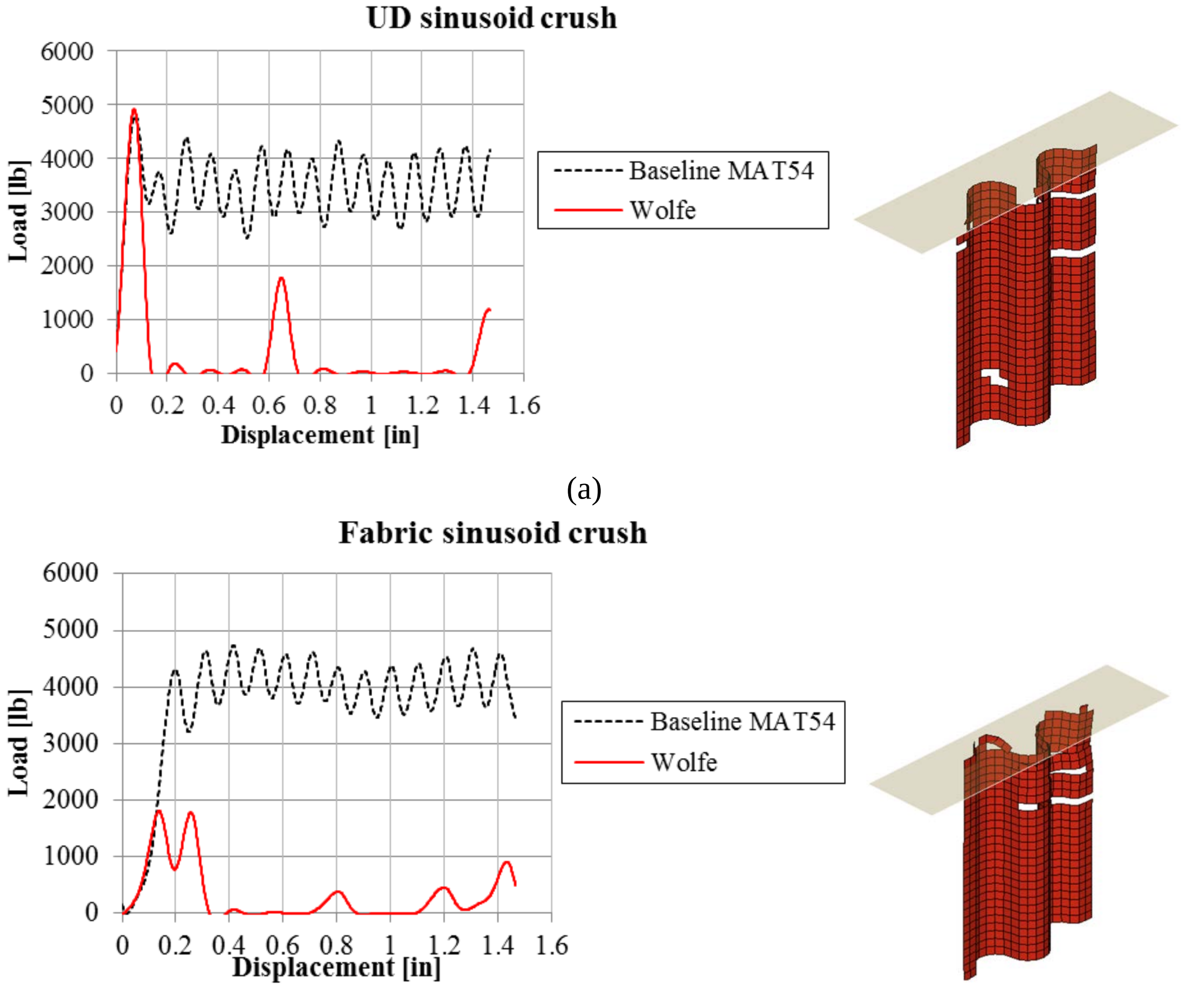

(a)

(b)

Figure 92. Unstable crush simulation results from using the Wolfe failure criterion in addition to the Hashin failure criteria on the sinusoidal crush element for the (a) UD and (b) fabric material models as compared against results from the baseline MAT54 models

Implementing the strain-energy-based Wolfe failure criterion in addition to the existing Hashin criteria causes element failure predictions to be worse in situations where the Hashin criteria had successfully predicted failure (i.e., in simple loading conditions and away from the crush front). In these situations, no improvement of failure prediction is necessary; instead it is the goal to improve failure prediction at the crush front without having to rely on an empirical parameter such as SOFT. In light of this, the Wolfe failure criterion is changed so it is only active at the crush front where premature failure predictions may be beneficial to the material model.

Simulations of the sinusoid crush element were rerun, employing the Wolfe criterion only at the crush front, while setting SOFT to a value of 0.999 to prevent material softening at the crush front. The simulation results of the sinusoid crush element were greatly improved from using Wolfe on all elements (see figure 93), and the crush front Wolfe failure criterion produced a similar but less stable result than the baseline MAT54 simulations, which used the calibrated SOFT parameter for the crush front elements.

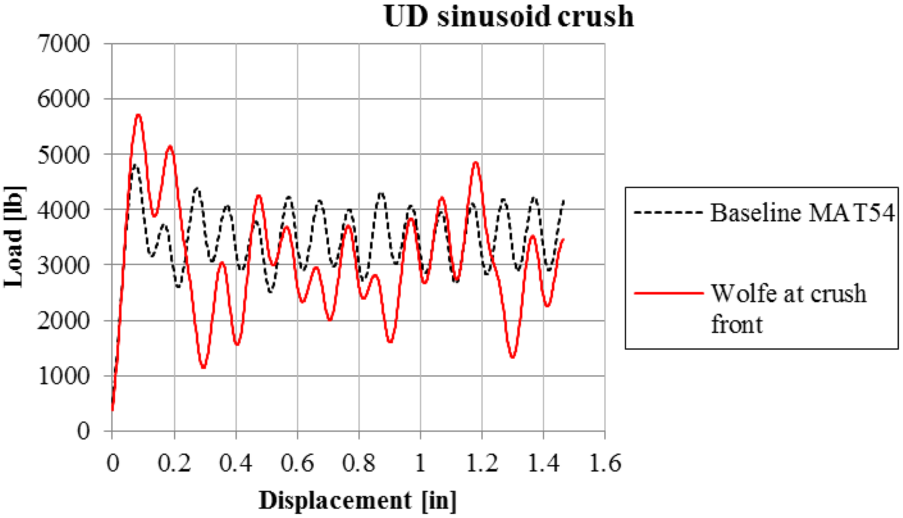

(a)

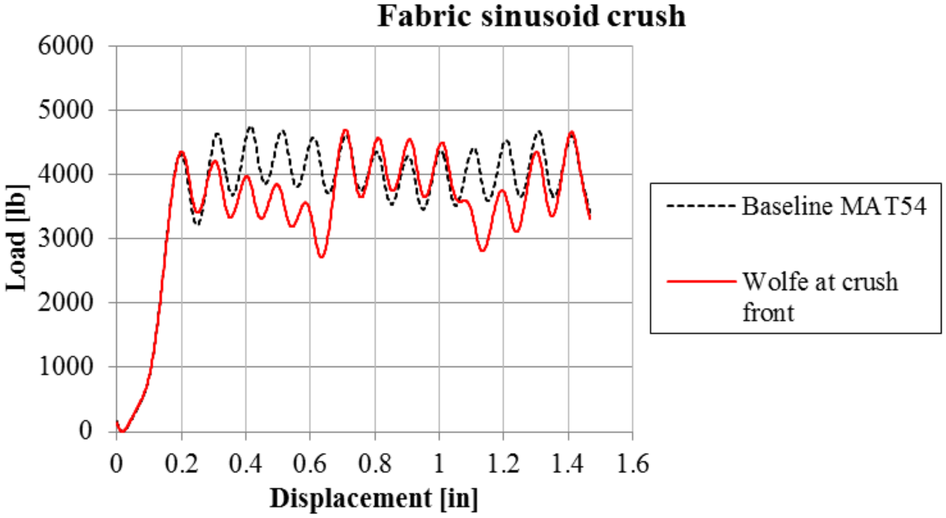

(b)

Figure 93. Crush simulation results from using the Wolfe failure criterion for the crush front elements in place of the SOFT parameter for the sinusoidal crush element using the (a) UD and (b) fabric material models as compared against results from the baseline MAT54 models

While the simulation result of the sinusoid elements shows promise, simulations of the other crush elements reveal that the Wolfe criterion cannot predict the crushing response well. For example, figure 94 shows that the crush simulation of the small C-channel element using the crush front Wolfe criterion produces a result where the load peak is more than double that of the baseline simulation, which causes failures beyond the crush front and ultimately global buckling of the crush element. By reducing all the strain energy input parameters artificially by 80%, a good match to the baseline MAT54 crush simulation can be achieved; however, this property reduction is entirely arbitrary and, like the SOFT parameter, cannot be determined without having the experimental results against which to calibrate the simulation. Trials in which only the shape function input parameters were adjusted did not produce improved crush simulation results.

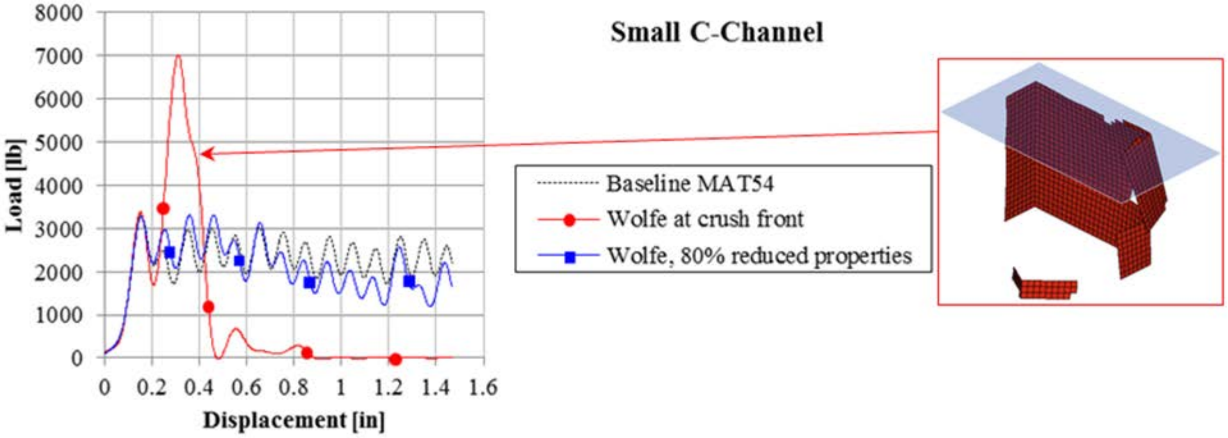

Figure 94. Crush simulation of the small C-channel element using the Wolfe criterion on the crush front elements with measured material properties, and artificially reduced properties, compared against the baseline MAT54 crush simulation

While all of the Wolfe criterion strain energy input parameters are derived from coupon-level experiments, these baseline values do not produce good crush simulation results and, ultimately, arbitrary calibration is necessary when using the crush front Wolfe criterion. For this reason, the Wolfe failure criterion does not provide improvement in failure predictions against the baseline MAT54 method of using the SOFT crush front reduction parameter with the Hashin criteria for failure prediction. At best, the crush front Wolfe criterion can be made to produce similar results to the baseline MAT54 simulations by calibrating several of its strain energy input parameters. This approach is not preferable to the baseline MAT54 strategy in which only a single input parameter requires calibration.

14. MODIFIED POST-FAILURE DEGRADATION

14.1 MODEL DEFINITION

The post-failure property degradation scheme in MAT54 produces an elastic-perfectly plastic stress-strain response of the material. This can be avoided by defining the strain-to-failure parameters to be coincident with failure, thereby creating a perfectly elastic-until-brittle failure behavior. However, some strain-to-failure parameters in MAT54 must be artificially increased to produce stable crush simulation results for some material systems. For this reason, the perfectly plastic curve following failure cannot be ignored, and several alternative post-failure property degradation schemes are investigated to determine if improvements can be made for crush simulations. A detailed description can be found in reference [97].

Four new approaches to model material behavior following failure are investigated: 1) reducing stress immediately to zero as a brittle material coupon behaves, 2) linearly reducing stress to zero similar to a CDM model, 3) linearly reducing stress to a specified constant value until the strain-to-failure is achieved, and 4) reducing stress by 1% each time-step until the strain-to-failure is achieved. These approaches investigated are shown in an idealized stress-strain curve in figure 95.

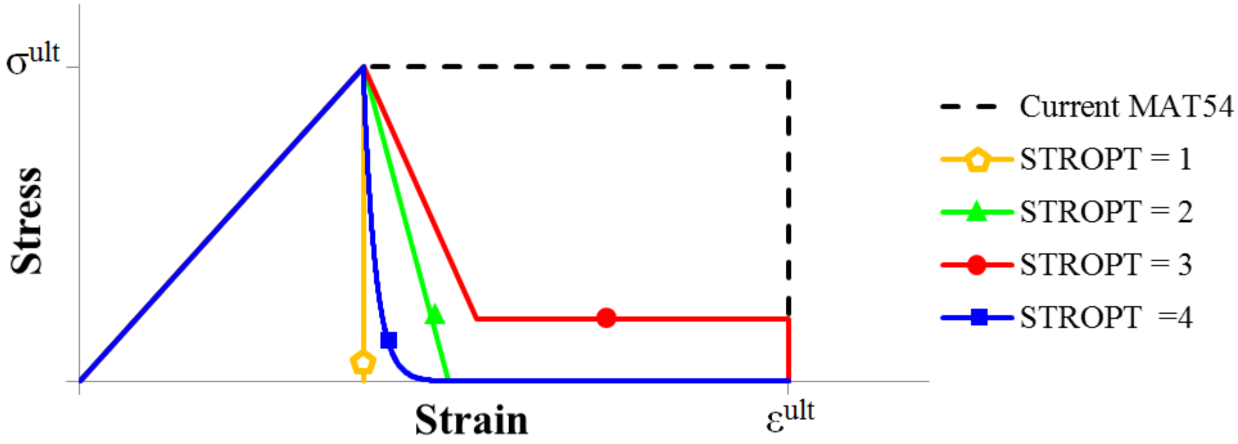

Figure 95. Idealized material stress-strain curves demonstrating four alternative post-failure property degradation schemes are investigated

Alternative versions of the modified post-failure model are also developed specifically to address crush simulation. Recall that for crash and impact simulations, the MAT54 transverse strain-to-failure parameter DFAILM must be increased to provide stability. If DFAILM is not increased, then the material behavior is linear elastic until a perfectly brittle failure upon which the stress goes to zero. In this scenario, the post-failure behavior cannot be employed and is therefore not relevant, but because DFAILM is increased, the post-failure behavior in the transverse direction of the element becomes important. It is unknown if the artificial increase in DFAILM serves to stabilize the elements at the crush-front as they experience failure or those beyond the crush-front to prevent premature deletion. By isolating the degradation scheme to be applicable only for the crush-front elements or the rest of the elements, it can be determined for which elements the artificial plasticity is effective and necessary for providing stability. The alternative versions of the modified post-failure model isolate the application of the stress degradation schemes to the crush-front elements or the rest of the elements, as shown in figure 96. In addition to separating the behaviors of the crush-front and all other elements, the degradation schemes have the option to be applied in only the transverse direction, which is the direction in which the artificially increased DFAILM allows for the degradation scheme to be applicable. These alternative versions of the modified post-failure stress degradation code are only used in crush element simulations in which crush-front elements are active.

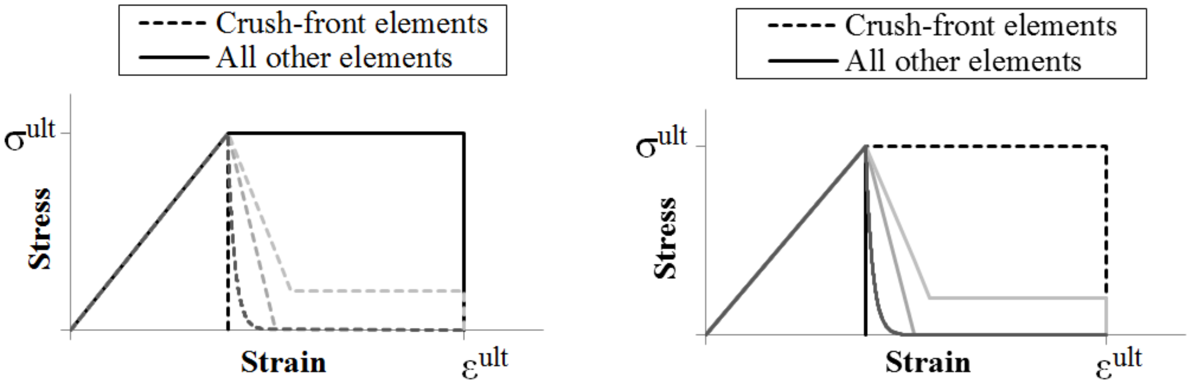

(a) (b)

Figure 96. Idealized material stress-strain curves demonstrating the two alternate versions of the modified code in which stress degradation options presented in figure 97 are applied to (a) crush-front elements only and (b) to all other elements only

14.2 SINGLE-ELEMENT RESULTS

The new post-failure stress degradation options are first tested using a single element under simple loading conditions to confirm that these new post-failure behavior schemes work as intended. The UD material model is used for this exercise; but to demonstrate the new behaviors after failure, the strain-to-failure parameters are modified so the element is not deleted prior to the observation of the new post-failure behaviors. All the failure strain parameters are extended to the arbitrary value of ±0.024 in/in. When the baseline failure strain values are used, the single elements behave exactly the same as the unmodified MAT54 material model. Each of the four post-failure stress degradation options are used with both the zero-degree and 90-degree UD single elements in tension and compression, using arbitrary baseline values of NDGRAD = 1,000 and SIGLIM = 0.2. The stress-strain results of the zero-degree element are shown in figure 97 and the stress-strain results from the 90-degree element are shown in figure 98.

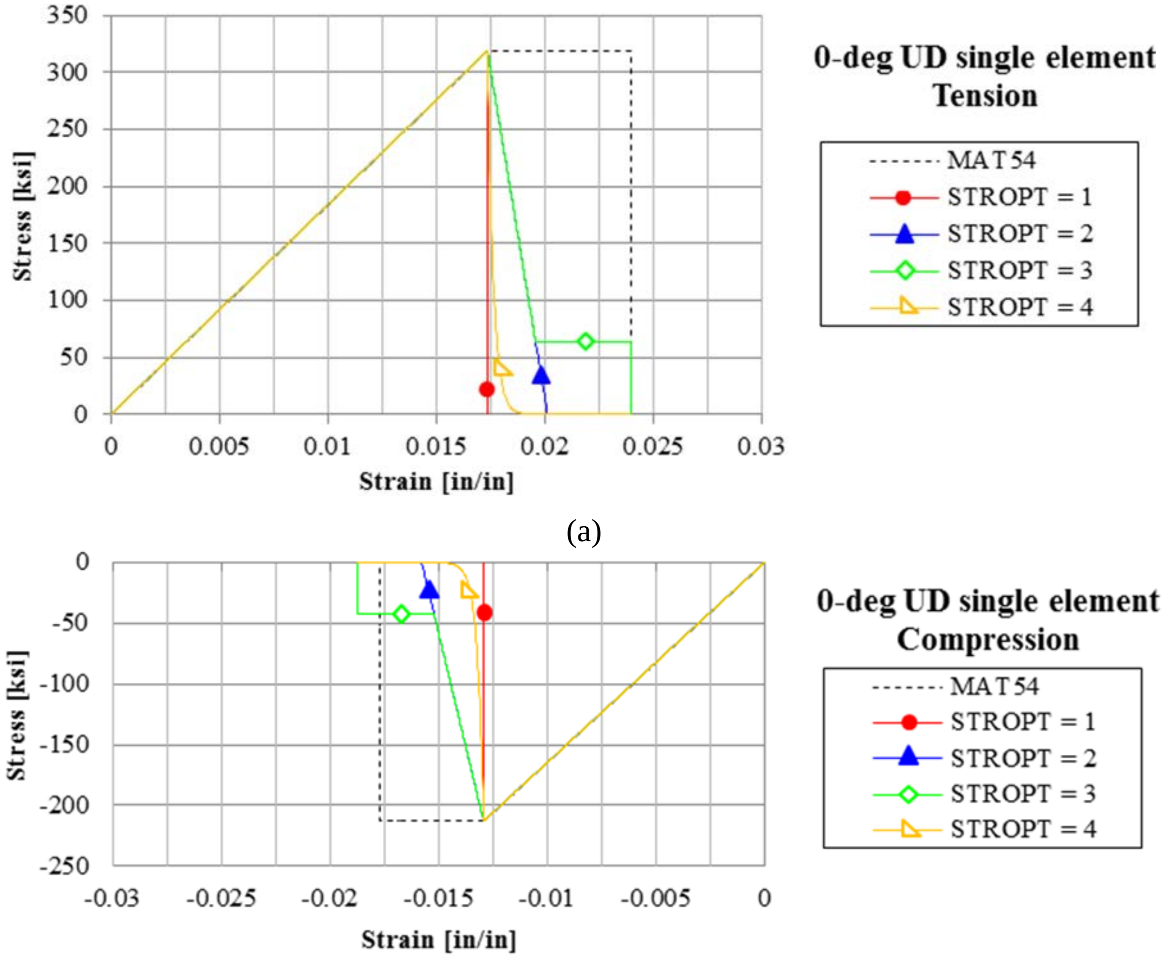

(a)

(b)

Figure 97. Stress-strain results of the zero-degree UD single element implementing four new post-failure stress degradation options under (a) tensile and (b) compressive loading conditions

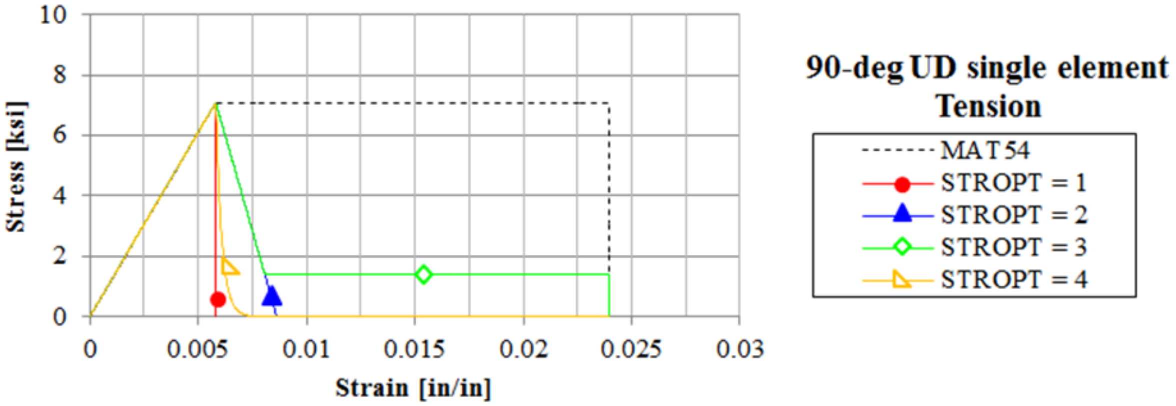

(a)

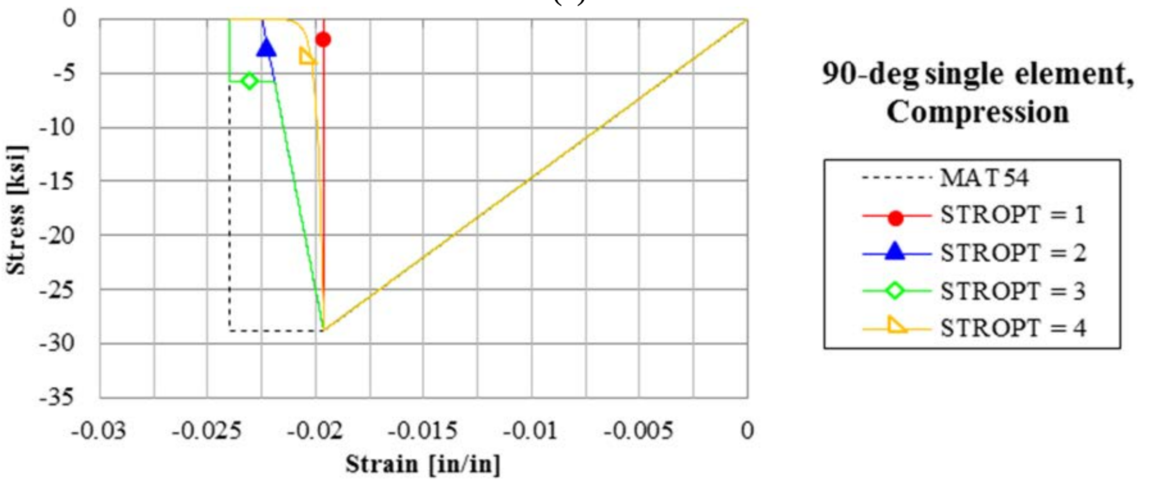

(b)

Figure 98. Stress-strain results of the 90-degree UD single-element implementing four new post-failure stress degradation options under (a) tensile and (b) compressive loading conditions

It is important to test all four load cases to make sure that all four failure modes are followed by the correct stress degradation option. From the results of the single-element simulations, it is clear that the post-failure degradation schemes are working as intended and the implementation of the modified code is a success. For STROPT = 1, the element is deleted as soon as failure occurs for all load cases. The slope of the linear degradation in all four load cases, and for both STROPT = 2 and 3, is the same as NDGRAD remains constant. The plastic stress level for STROPT = 3 is 20% of the failure stress in all four load cases, and a logarithmic-like decay is observed in all load cases when STROPT = 4.

A parametric study is conducted on the two new user input parameters, NDGRAD and SIGLIM, to observe their influence on the zero-degree UD single-element simulation under tensile loading. The NDGRAD parameter is varied using values of 100, 500, 1000, and 2000 iterations, while the SIGLIM parameter is varied using values of 5%, 20%, and 40%. Figure 99 demonstrates that the modified model works as intended, and the NDGRAD parameter directly influences the degradation slope while the SIGLIM parameter directly influences the plastic stress level. These single-element simulations and short parametric study have confirmed that the new modified post-failure degradation schemes are all working as intended.

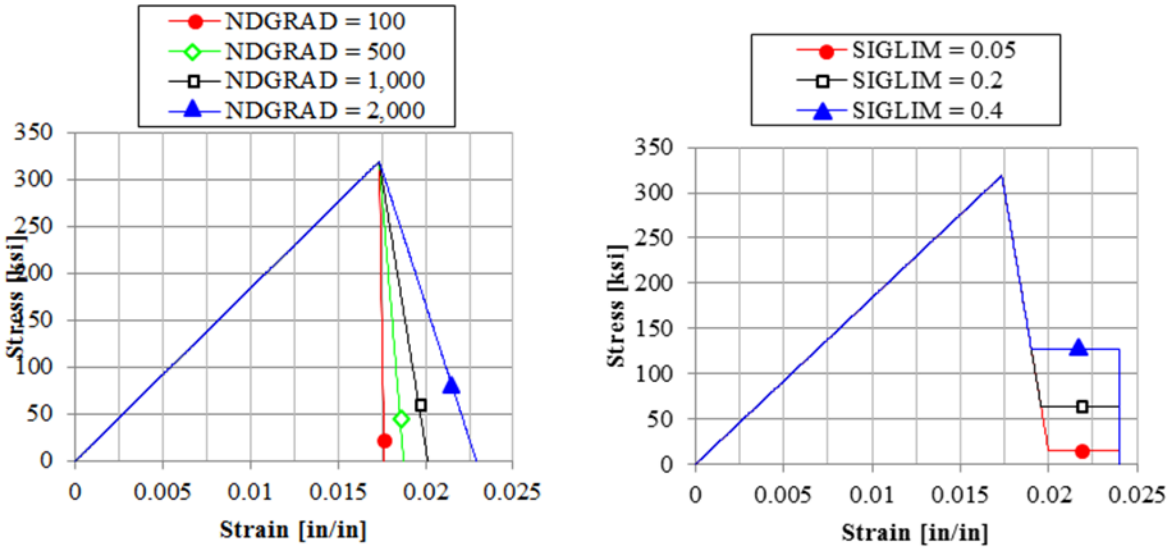

(a) (b)

Figure 99. Influence of the new (a) NDGRAD (STROPT = 2) and (b) SIGLIM (STROPT = 3) parameters on the post-failure stress degradation schemes in zero-degree single-element simulation under tensile loading

14.3 CRUSH SIMULATION RESULTS

The new post-degradation options are implemented with the fabric sinusoid crush element model. For the crush simulations, there are two additional variables to consider for stress degradation in the simulation test matrix. First, there are three options regarding which elements experience degradation following failure: all elements, only crush-front elements, or all except crush-front elements. Second, there are also three options regarding which stress components experience degradation: axial stresses, transverse and shear stresses, or all stresses. For each combination of these two variables, the four new post-failure stress degradation schemes are investigated. The resulting idealized material stress-strain curves are different for each case, depending on the given variables. Figure 100 shows a table of the idealized material stress-strain curves in terms of the two variables: elements degraded and stresses degraded. In this visualization of the test matrix, the default MAT54 plastic behavior following failure is represented as STROPT = 0. The test matrix presented in this way identifies nine general cases for which all STROPT options are investigated in the crush simulations. The simulated load-displacement curves from this investigation, using baseline values for NDGRAD and SIGLIM, are presented in the same format as the test matrix for ease of interpretation, as shown in figure 101. In general, the result for most cases is highly unstable. In all cases in which the crush-front elements are subjected to stress degradation following failure, as presented in the first two columns of figure 101, every simulation is destabilized and, in several cases, severely so. The crush-front elements in particular require plasticity within their material stress-strain definition for stability.

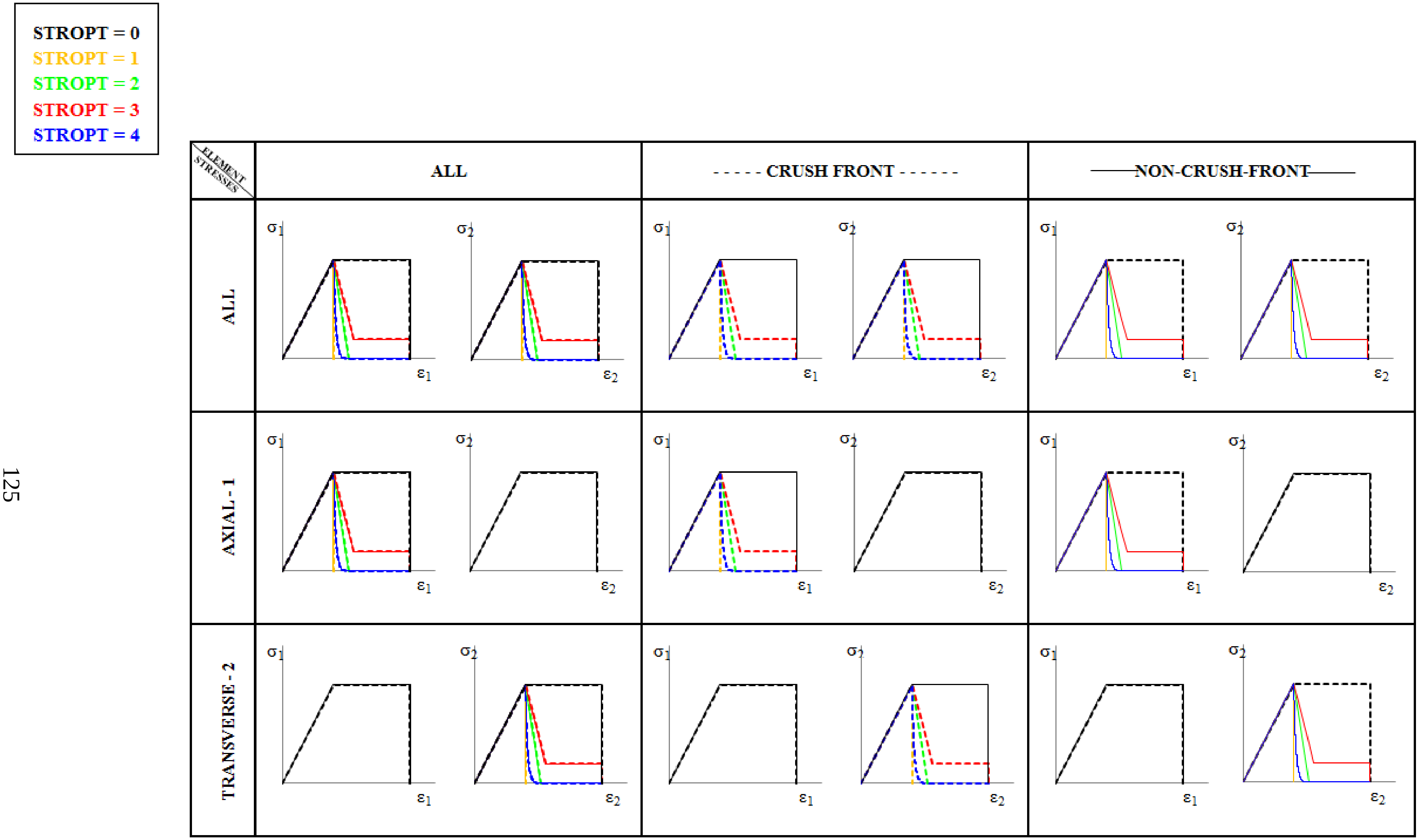

(Note that the axial curves are greatly exaggerated in the amount of plasticity to showcase the degradation options, although in the baseline fabric material deck there is no significant amount of plasticity.)

Figure 100. Idealized material stress-strain curves implemented in the test matrix of the five different post-failure degradation schemes applied to different elements: crush front (dashed) and non-crush-front (solid); and applied to different stress components: (1) axial and (2) transverse.

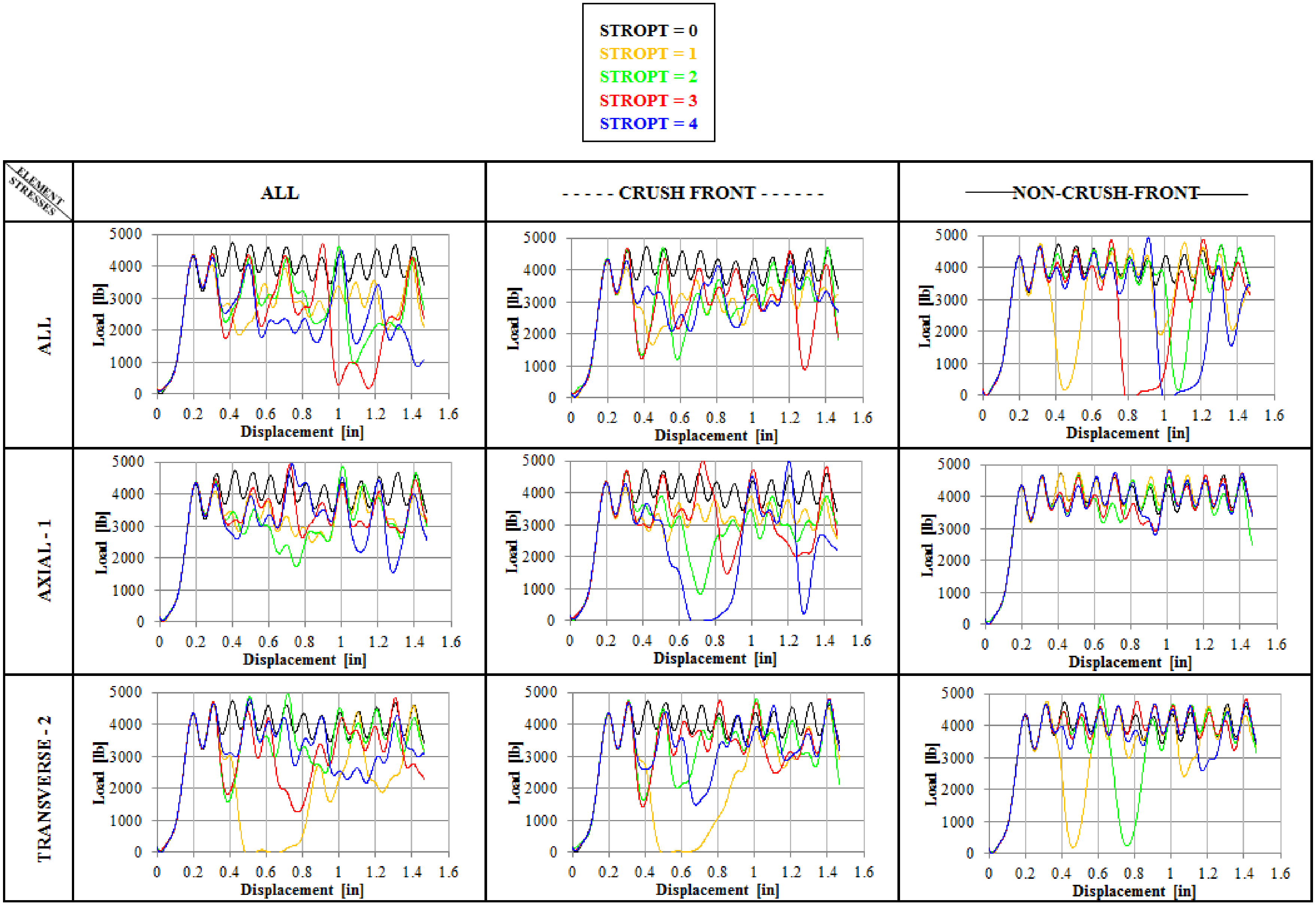

Figure 101. Simulated load-displacement crush curve results of the fabric sinusoid element subjected to the test matrix of different post-failure degradation options outlined in figure 100

In the cases for which only the non-crush-front elements are subjected to the stress degradation schemes, presented in the third column of figure 101, it is possible to achieve stability. In particular, when only the axial stresses are degraded and the transverse stresses are allowed to plastically deform after failure, all of the stress degradation options produce stable crush results. When the transverse stresses are not allowed to plastically deform, however, two of the degradation schemes are destabilized in the middle of seemingly stable crushing.

From these initial results, it seems as though crush-front elements must always be allowed to plastically deform, and perhaps transverse stresses must also be allowed plastic deformation following failure. A parametric study of the NDGRAD and SIGLIM parameters is performed to study their effect on the crush simulation results, both to determine if variations of these parameters can stabilize the unstable simulations and to determine the effect upon an already stable crush simulation. Changes of these two parameters are effective only for STROPT = 2 and 3. For cases in which crush-front elements are degraded (columns one and two from the test matrix in figure 100), several parametric trials using a variety of NDGRAD and SIGLIM values were consistently unable to stabilize the crush simulation. Parametric results of NDGRAD and SIGLIM are shown for the case in which all stresses are degraded in all elements following failure in figure 102. This result confirms that these parameters alone are not influential enough to stabilize an unsuccessful simulation, and that implementing new post-failure degradation schemes for crush-front elements worsens the crush simulation performance of MAT54. Crush-front elements must always be allowed to plastically deform for crush simulation.

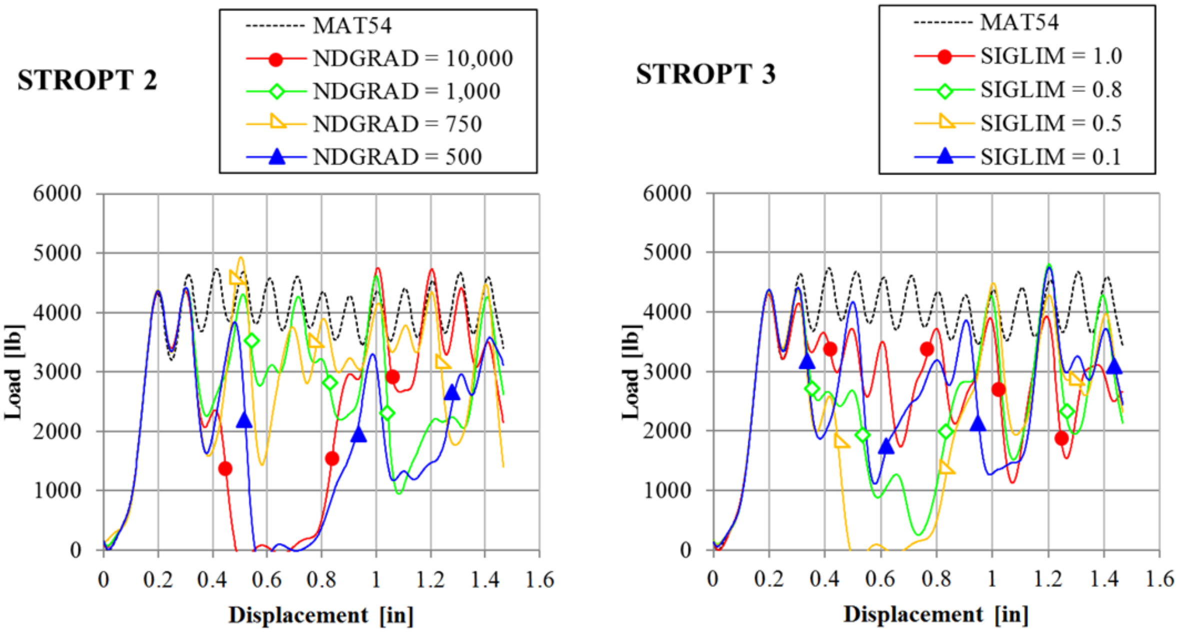

(a) (b)

Figure 102. Changing the (a) NDGRAD and (b) SIGLIM modified MAT54 parameters when degradation is applied to all stresses in all elements does not stabilize the simulation of the sinusoid crush element

The NDGRAD and SIGLIM parameters are varied for crush simulations for cases where only the non-crush-front elements are degraded, shown in column three from the test matrix in figure 100. For the case where only axial stresses are degraded, shown in the second row in figure 100, there is little room for improvement of the already stable results, and these new parameters are investigated to see if they have a negative impact on the simulation results. Low values of NDGRAD and SIGLIM cause small destabilizations in the simulation, while values near the baseline and higher remain stable, as shown in figure 103. Considering the shape of the material stress-strain curve, higher values of NDGRAD cause a lower degradation slope that is closer in shape to the perfectly plastic default MAT54 behavior. The same is true with higher values of SIGLIM, which is perhaps why higher values of both parameters promote stability.

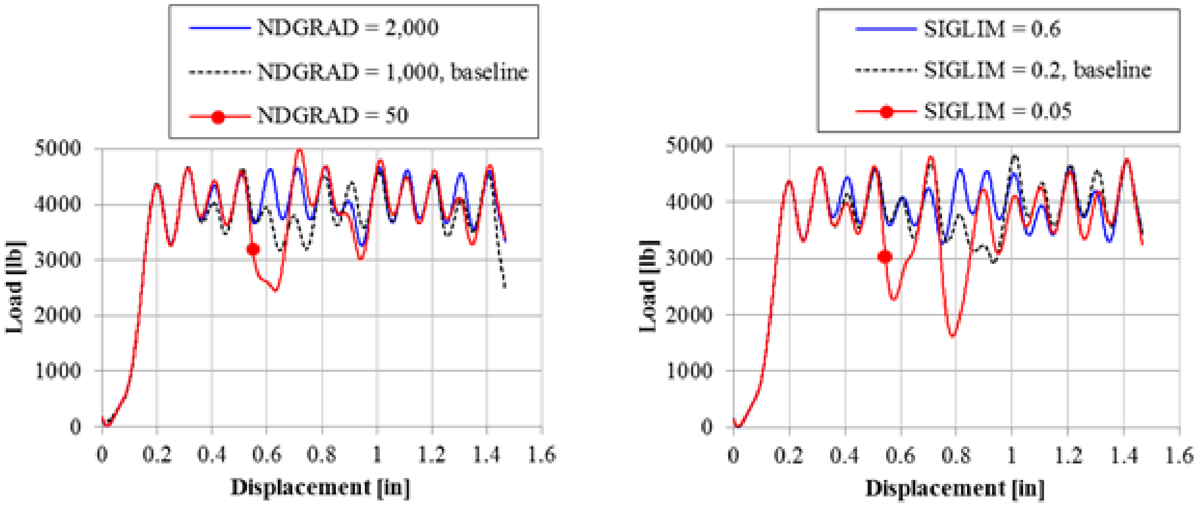

(a) (b)

Figure 103. Effect of changing the (a) NDGRAD and (b) SIGLIM modified MAT54 parameters when degradation is applied to axial stresses only in non-crush-front elements

The new post-failure material behavior models do not provide improvement over the default MAT54 perfectly plastic behavior. Furthermore, the new user input parameters, which control the shape of the material stress-strain curve following failure, do not significantly influence the result of the simulation enough to warrant further investigation. While a stable result can be obtained, it requires application of the degradation scheme to specific elements and specific stresses, and this strategy does not offer improvement over the default MAT54 model. In addition to the sinusoid crush element, other crush element geometries were investigated using the modified post-failure model with similar unsatisfactory results. For example, select results from the small C-channel crush element implementing the modified post-failure model are shown in figure 104.

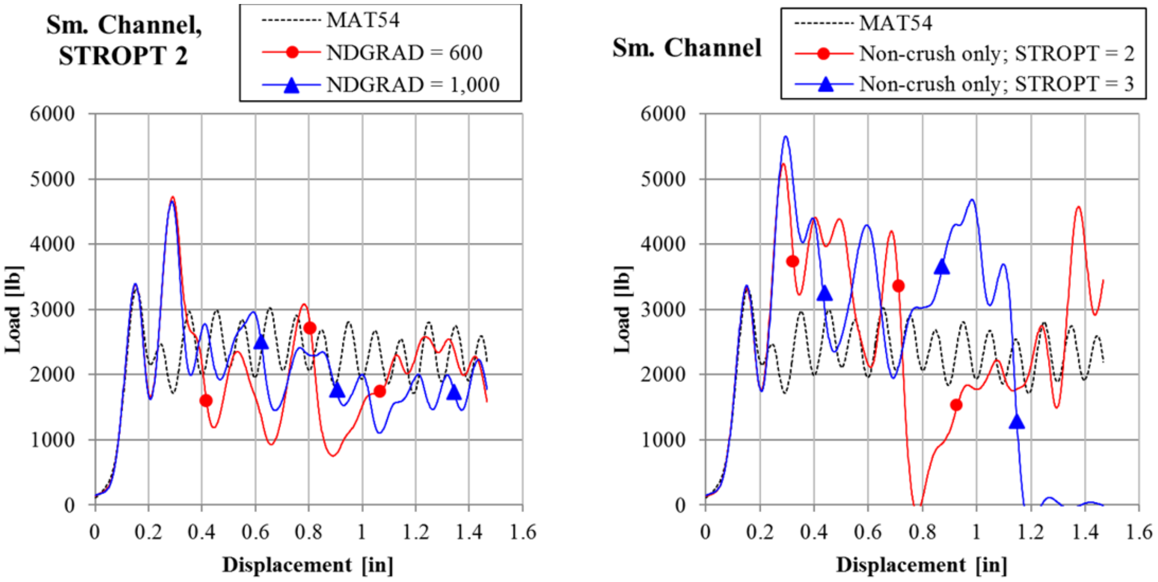

(a) (b)

Figure 104. Simulation results from using the modified post-failure stress degradation model on the small C-channel crush element (a) applied to all elements using STROPT = 2 and varying NDGRAD values and (b) applied to non-crush-elements only, using different STROPT options

15. MODIFIED MATERIAL MODEL CONCLUSIONS

Access to the Fortran source code for MAT54 allowed for both a better understanding of this material model as well as the capability to modify and implement a modified composite damage material model in LS-DYNA simulations. The modification strategy of this research for MAT54 has resulted in a composite material model with a better capability to simulate the elastic behavior of an anisotropic UD composite material, has validated the selection of the built-in Hashin failure criteria to determine lamina failure, and has presented several alternatives to the post-failure model of the material. The modified model features the addition of compressive constitutive material properties, which has expanded the capability of MAT54 such that it may more accurately model the composite material response to complex multi-axial loading conditions. This is an important addition because composite material systems often have significantly different moduli in tension and compression. This particular modification improved MAT54 such that it simulated the elastic behavior exactly as the experimental material coupon tests for the UD material system.

Three other sets of failure criteria options were added in place of (or in some trials, in addition to) the default Hashin criteria. These other criteria each demonstrated an equal or worse capability to predict initial material failure, and this study has strongly validated the use of Hashin to predict the onset of initial material failure. The default approach for modeling the crush-front elements by reducing their strength using the SOFT parameter proved to be most effective for crush modeling, although an alternative method developed as a part of the modification strategy was shown to work just as well. An equivalent simulation result can be obtained by using a crush stress criterion that evaluates crush-front elements using a user-defined lower material ultimate strength. The input maximum crush stress parameter must be calibrated using experimental crush curves in the same way SOFT is calibrated.

Finally, modifications made to implement a variety of different post-failure material behaviors proved to demonstrate the particular sensitivity of crush simulations to the post-failure stress profile of the material. Four different post-failure material behaviors were implemented, each with user-controlled variable stress profiles. These post-failure stress profiles varied from dropping the stress to zero, as would happen in a material coupon test, to a linear stress degradation down to a constant stress level, similar to that found in CDM composite models. Of the many different degradation methods applied to different elements and the stress components produced, the resulting crush simulations did not outperform the strategy to use pure material plasticity following failure. The requirement for a high degree of material plasticity following the onset of failure in crush simulation was clearly demonstrated in the modification strategy.

16. GUIDELINE FOR USING MAT54

This section provides guidelines for using the LS-DYNA built-in composite damage material model MAT54 in simulations of composite structures subjected to crush loading. Much of the information provided here comes from performing a thorough investigation on MAT54 for use in crush and impact simulations, as well as some information collected from materials distributed by LSTC to its customers [11, 98–101], and specified journal articles. This document focuses particularly on MAT54 and other portions of the FEA model development that affect or are affected by MAT54. For a more comprehensive review of other aspects of composite crash modeling, a NASA technical report from Fasanella and Jackson [50] entitled, “Best Practices for Crash Modeling and Simulation” is recommended. The Fasanella and Jackson report contains detailed information pertaining to many aspects of crash modeling, which will not be discussed in this report, such as the development of the geometry CAD model, dummy models, lumped mass approximations, and complex initial conditions. The purpose of this section is to outline the modeling strategy developed for using MAT54 for crush analysis, and most of the discussion will be relevant to the material model and aspects of the simulation that influence the material model.

The use of MAT54 for crush simulation relies on the BBA, shown in figure 11. A method has been developed by the author for the calibration of the MAT54 material model using a specified set of experimental crush data at the element level of the BBA, which allows for the material model to be used in higher levels of the BBA with little or no further adjustment. These guidelines will first describe the necessary set of experimental crush data necessary for the analysis calibration. Following this, recommendations are made for the initial development of the element level crush models, including the full definition of the MAT54 material input deck, as well as other model features, such as control decks, damping, element type, contact definition, etc. Finally, an example exercise of the MAT54 calibration for crush simulation will be summarized, which refers to the extensive work done during the in-depth investigation of MAT54 and development of various MAT54 crush models.

16.1 REQUIRED EXPERIMENTAL DATA FOR THE MATERIAL MODEL

The material deck MAT_ENHANCED_COMPOSITE_DAMAGE (MAT54), shown in figure 39, found in the LS-DYNA keyword input file contains the entire material definition for the composite model. A detailed discussion of the governing equations and fundamental behaviors of the MAT54 material model is found in section 7 of this report, as well as published in [89–90].

As shown in table 7, the constitutive properties, material strengths, and most deletion parameters are measured from standardized tension, compression, and shear material property experiments performed using material coupons (i.e., data from the coupon level of the BBA). The material model uses the material properties of the lamina, and the layup of the composite laminate is defined by the element. To ensure stability in impact and crush simulations, the *DFAILM* parameter requires an increase from its experimentally measured value, which can be done during calibration.

To use MAT54 for crush simulation, a set of element-level crush experiments must be performed, which characterize the energy absorption capability of the material system so the MAT54 SOFT parameter can be calibrated. The energy absorption of a composite material system is dependent on both the layup and the specimen geometry. The method developed for the crashworthiness research proposed here relates the energy absorption of a composite laminate directly to the geometric feature of the crush specimen referred to as the degree of curvature. This means that while the other MAT54 input parameters can be defined by lamina properties, the SOFT parameter is a laminate property that is adjusted depending on the degree of curvature of the element shape it is modeling. The degree of curvature is defined to the length of curved segments over the total length of the geometry, or a percentage of the geometry that is curved.

The SEA of a composite material system increases as does the degree of curvature, to the limit that a flat crush coupon will exhibit the minimum SEA, and a corrugated crush element will exhibit the maximum SEA of the material system. It is recommended that three crush element tests, which represent low, medium, and high curvature specimens, be tested—for example a flat coupon, a square tube or C-channel, and a corrugated specimen. Three element-level crush tests with significantly different degrees of curvature are sufficient to define the range of the energy absorption capability of the laminate needed for MAT54 calibration.

If the same geometric features crush tested are those used in the simulation, then the experimental load-displacement curve is itself used as the metric against which the simulation results are directly compared to calibrate the material model. Otherwise, an empirical relationship between the measured SEA and the degree of curvature of the crush specimen must be developed for the laminate from the element-level experiments. In this case, the SEA becomes the evaluation metric for the simulation, and the simulation is calibrated such that simulated SEA matches that expected from the laminate.

16.2 RECOMMENDED FEA MODEL DEVELOPMENT

16.2.1 MAT54 Material Input Parameter Definitions

There are numerous other MAT54 input parameters aside from those that are experimentally derived. The local material axes parameters (group 2 in figure 39) are defined using the AOPT parameter, equation 32, and in figure 105.

$$AOPT \begin{cases} = 0.0, & Locally\ orthotropic\ with\ material\ axes\ determined\ by \\ & element\ nodes\ 1, 2, and\ 4 \\ = 2.0, & Globally\ orthotropic\ with\ material\ axes\ determined\ by \\ & vector\ \boldsymbol{a} \\ & Locally\ orthotropic\ material\ axes\ determined\ by \\ = 3.0, & rotating\ the\ cross\ product\ of\ the\ vector\ \boldsymbol{V}\ with\ the \\ & element\ normal\ \boldsymbol{n}\ by\ the\ angle\ MANGLE \\ < 0.0, & The\ absolute\ value\ of\ AOPT\ is\ a\ coordinate\ system\ ID \end{cases} \tag{32}$$

The material density, RO, requires special attention when using English units. Densities are often reported in terms of lbf/in^3, which is a measure of weight per unit volume. To maintain a consistent set of units, FE codes require density to be in terms of lbm/in^3 that is a measure of mass per unit volume. The difference between weight and mass is the gravitational constant, g = 386.4 in/s^2, which must be divided from the weight to get the mass, and density with the unit lbf-s^2/in^4, which is the correct unit.

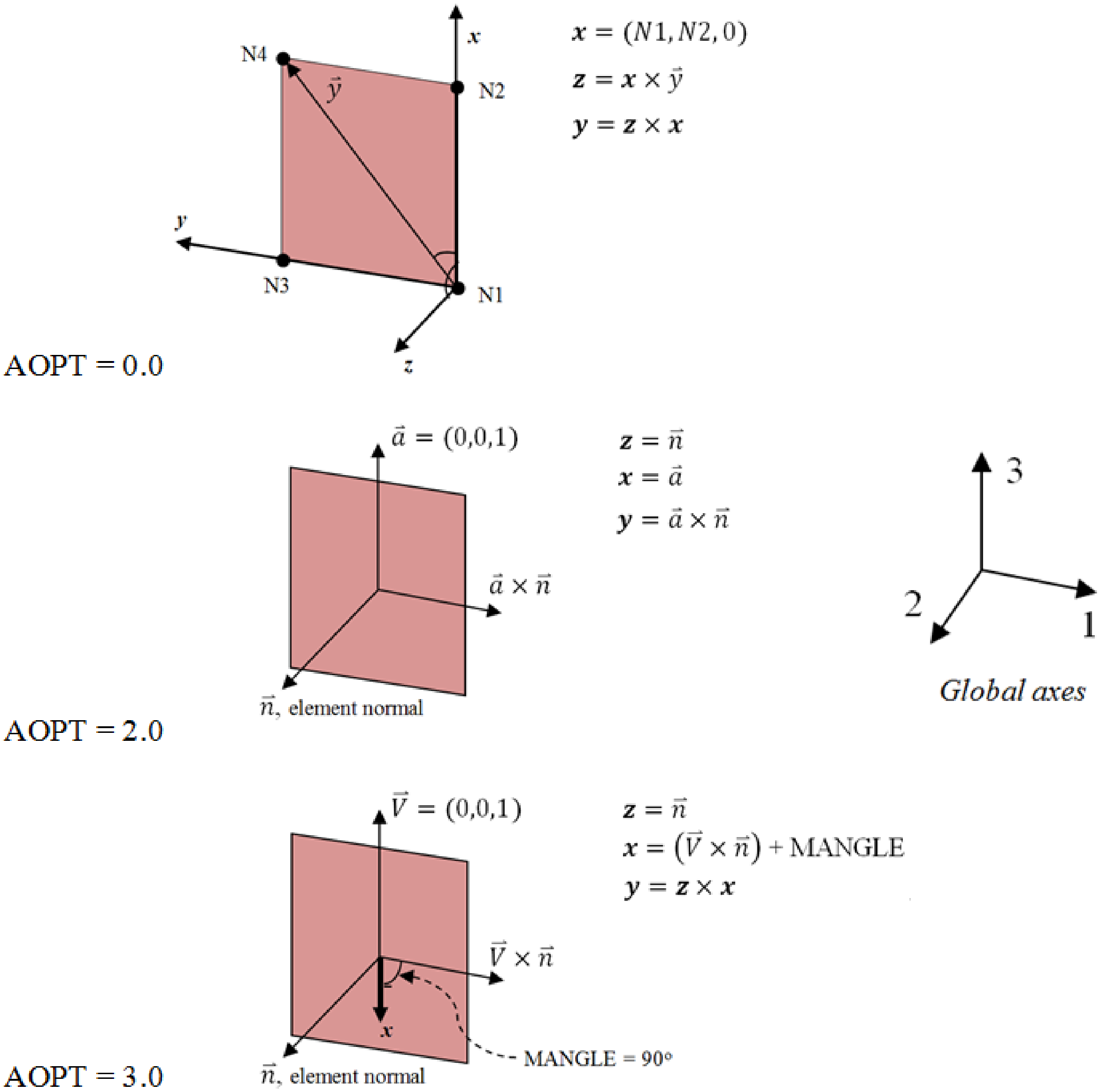

Figure 105. Three local material axes definition options for MAT54 as determined by the AOPT parameter

Among the deletion parameters, TFAIL is the only one not derived from the experimental data and is instead given a value of at least half of the critical time-step, as determined by the Courant condition (see equation 26). The EFS input value can be determined from critical values of experimental failure strains, as given by equation 25, or not be used at all but assigned a value of 0 (recommended).

Of the shear and damage factors, the default values given in table 7 are recommended to avoid possible instabilities, with the exception of the SOFT parameter. This parameter requires calibration against the element-level crush experiments, a process that will be discussed at length in section 16.3 of this report.

The computational parameter CRIT simply specifies whether to use MAT54 or MAT55 by assigning a value of 54 or 55, respectively. MAT55 should not be used for crash simulation because this material model does not contain element erosion/deletion criteria or a post-failure damage model. Although this is not mentioned in the LS-DYNA User's or Theory Manuals, this trait of MAT55 was discovered while investigating the modified material model presented in this report.

16.2.2 Other LS-DYNA Keyword Input File Definitions

In addition to the MAT54 material input deck, a number of other LS-DYNA keyword input parameters are important to discuss when using MAT54 for crush simulation. For reference, the baseline fabric sinusoid LS-DYNA keyword input file, with the element and nodal coordinate and set definition decks removed for the sake of brevity, is given in appendix B.

In the CONTROL_SHELL deck, the parameter ISTUPD controls thickness changes for highly distorted and deformed shell elements. Although no significant influence was noted in this investigation, LSTC [98] strongly recommends that this parameter be turned off for composite materials for numeric stability. Also in the CONTROL_SHELL deck, the parameter LAMSHT variable controls the use of Laminated Shell Theory in the calculation of the laminate stiffness through the thickness, which is otherwise assumed to be constant. This is especially important for sandwich composites, which have great stiffness variation through the thickness, but it is not required that LAMSHT be active for a thin composite laminate undergoing crushing.

The CONTROL_TIMESTEP deck is used to manually adjust the time-step of the simulation. The variable TSSFAC is the time-step scale factor, which scales down the time-step from its critical value as determined by the Courant condition [91]. The default value of TSSFAC is 0.9, which makes the time-step 90% of the critical time-step value. It was found in several of the single-element simulations for which elements became highly distorted that the time-step needed to be reduced to 50% of the critical value. Reducing the time-step greatly increased the computational cost of the simulation; however, it was necessary for stability when significant element distortion was simulated, an example of which is shown in figure 106. The sensitivity of MAT54 to the time-step is a feature that may require revisiting during the calibration stage of the material model.

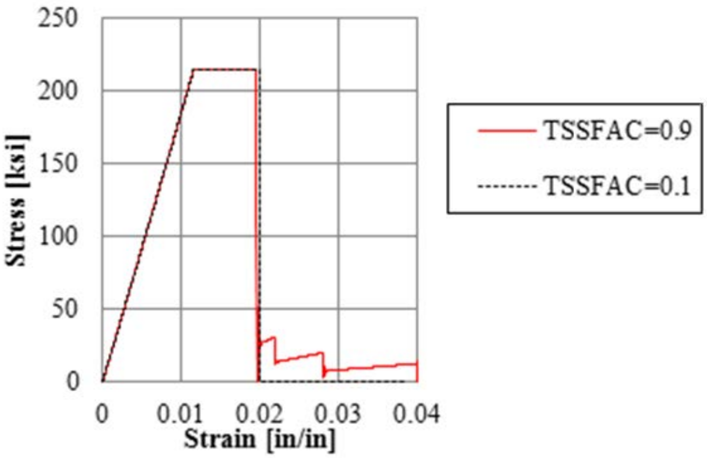

Figure 106. The reduction of the time-step factor TSSFAC improves stability in a single-element simulation in which the element is highly distorted at the point of deletion

One other control deck that can be of use for crush simulations in particular is the CONTROL_ACCURACY deck, in which invariant node numbering (INN) can be turned on for shell elements. INN prevents the local coordinate system definition from being erroneously assigned in highly distorted elements and makes element forces independent of node sequencing. An example of INN comes from LSTC, shown in figure 107 [97].

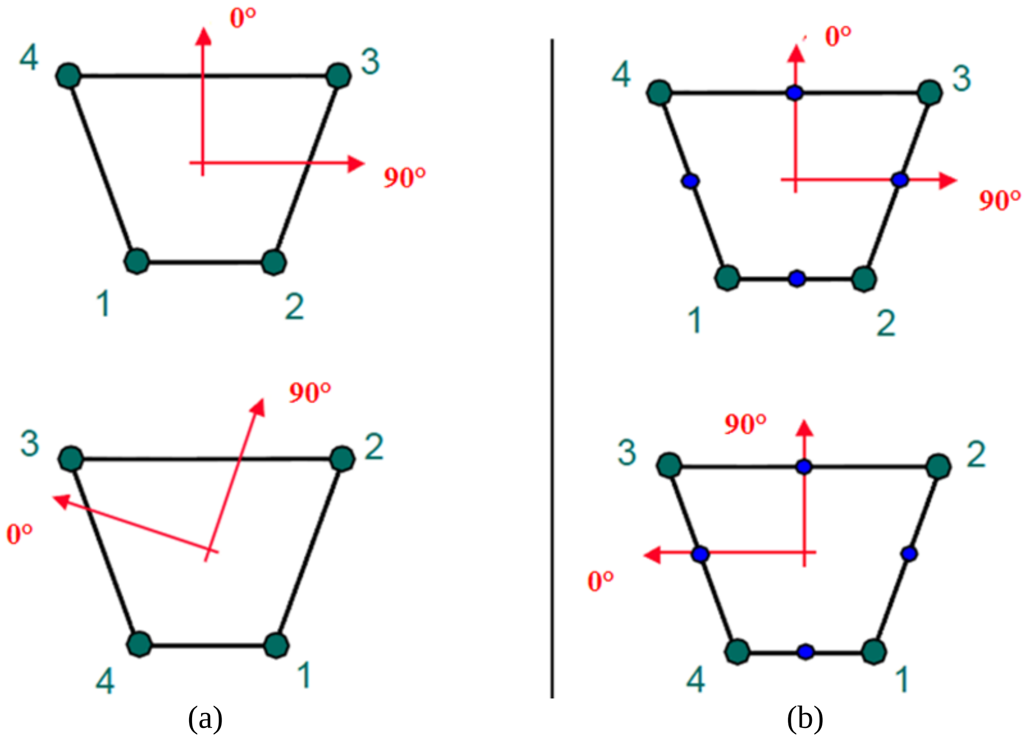

Figure 107. Example given by LSTC on the effect of INN on the definition of a local material coordinate system on a deformed element showing (a) incorrect local definition when INN is turned off and (b) correct local definition when INN is turned on [97]

The DATABASE decks define the output data saved and the output files generated. The DATABASE_EXTENT_BINARY deck has two important variables relevant to MAT54 models: the number of extra history variables (NEIPS) and the number of integration points through the thickness, MAXINT. To record the failure mode history variables for MAT54 as defined by equations 17–20, NEIPS must be set to at least 6. In these studies, it was set to 12 to record additional MAT54 history variables, which proved to be unnecessary for this particular exercise. Also, to record all of the ply data generated at each integration point, the MAXINT must be set equal to the number of plies.

Part damping is recommended to represent the inherent damping that exists within real structures. Without part damping, an FE code will vibrate continuously, and especially in nonlinear dynamic models, these oscillations can have high amplitudes and distort data [50]. This is primarily an issue with larger models, and while damping was not observed to have a significant effect in the crush element models, it is still recommended to be included. In LS-DYNA, generic part damping is achieved by using the DAMPING_PART_STIFFNESS cards; a damping coefficient equal to 0.05 was used in this study.

16.2.3 Element Selection

MAT54 requires shell elements, and the type used in this study is the four-node Type 16 fully integrated quadrilateral element. This type allows for a local coordinate system to be defined and has been specially formulated to be a computationally inexpensive fully integrated element. It has two integration points through the thickness by default—one at the top of the shell thickness and one at the bottom. However, additional integration points are added, which each simulate a ply of a laminated composite material. The number of integration points, which should equal the number of plies, must be defined in the SECTION_SHELL deck variable NIP. If the PART_COMPOSITE deck is used in place of SECTION_SHELL, this variable does not require definition.

16.2.4 Precision Solver

Although most finite element (FE) codes offer both a single and a double precision solver, it is becoming standard that the double precision solver is used by default for codes such as Abaqus and RADIOSS. LS-DYNA still gives the user the equal option to use either single or double precision. Because explicit formulations are very computationally expensive, it may be desirable to use a single precision solver for improved utilization of memory and disk space; however, problems have been identified in this study when using the single precision solver with MAT54. Specifically, in the single-element study, when large deformations were imposed on the MAT54 element, the single-precision solver often produced inexplicably unstable results (see figure 108). By simply changing the solver to the double precision version, these instabilities went away, and the single element deformed as expected. For this reason, it is always recommended to use the double-precision solver when using MAT54.

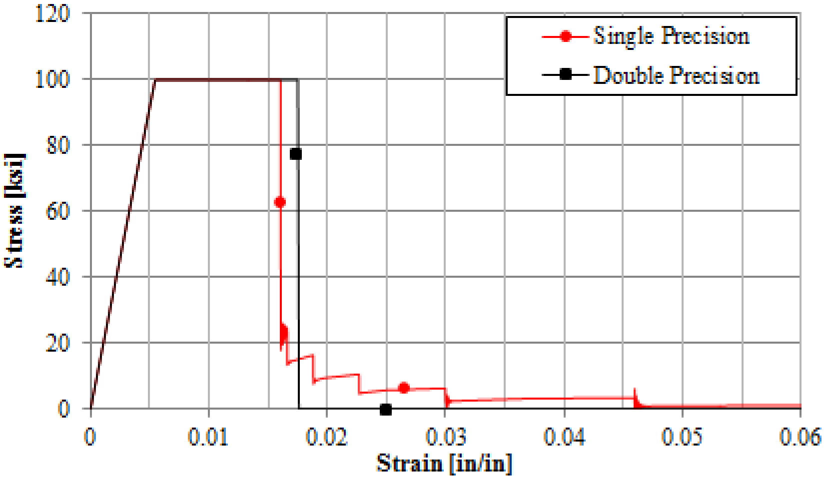

Figure 108. Example from the single-element investigation of the MAT54: basic stress-strain material response is unstable using a single precision solver vs. stable using a double precision solver

16.2.5 Contact Definition

The contact between the loading plate and the crush element is defined by the CONTACT_RIGID_NODES_TO_RIGID_BODY contact deck. MAT54 requires a contact type that employs an LP curve, and automatic or eroding contact types do not work [83]. The definition of the LP curve will severely impact the stability of the crush simulation using MAT54, and is certainly the most important variable in the contact deck (the load curve identification parameter LCID in CONTACT_RIGID_NODES_TO_RIGID_BODY). A piecewise-linear curve that increases in stiffness at greater penetration values is the recommended shape of the LP curve. It was found that for stable crush geometries with high curvature, such as the sinusoid, an aggressive and stiff LP curve best modeled the experimental crush results (see figure 66), however, was not capable of modeling other geometries. Applying the aggressive LP curve to the tubular geometries did not facilitate stable crushing, and a softer LP curve was required. Because it is undesirable to tailor different LP curves to different composite parts, a conservatively soft piecewise-linear LP curve is recommended for best universal results in a crush simulation using MAT54. This compromises the accuracy of the initial stiffness of the crush curve for most crush geometries (see figure 77), but without this concession, the stability of the crash model is jeopardized. The LP curve is an important parameter, which may require revisiting if the MAT54 crush model is found to be unstable during initial development.

16.2.6 Experiment-Analysis Correlation

The simulation load-displacement results should be recorded at a location in the model that is representative of the experimental load data collection location. In the example exercise, data collection occurs across all of the nodes along the fixed boundary condition at the opposite end as the loading plate, as this is similar to the location of the load cell used in the crush experiments. The load data is filtered using a low-pass CFC 600 Hz filter, as is recommended practice for crash simulations [50].

16.2.7 Mesh Size

The CAD models for each crush geometry must be developed and meshed at a mesh size appropriate for scaling up to higher levels of the BBA, which require up to full-scale structural models. The mesh size must also be small enough to capture important geometric features, such as the curvature of the structural crush elements. A mesh size was chosen for this exercise to be 0.01″ (2.54 mm) because this was small enough to capture the curvature of the sinusoid crush element, but large enough to allow for scaling up to larger structures. The MAT54 material model alone is not mesh sensitive because it does not include any strain-rate dependent parameters or model any strain-rate dependent behaviors in its governing equations. The mesh insensitivity of MAT54 has been demonstrated at the element-level in the simulation of the sinusoid crush element [83].

16.3 MAT54 MODEL CALIBRATION

The element-level crush experimental data used in this exercise included a flat crush coupon and eight different crush elements of tubular (see figure 24) and corrugated (see figure 28) variants. From these crush tests, the energy-absorption capability of the T700/2510 carbon fiber/epoxy plain-weave fabric $[(0/90)]_{8f}$ laminate was characterized. After performing all of the crush tests, a relationship between SEA and the geometric degree of curvature was empirically derived (see figure 109). From this relationship, the expected SEA of any crush element for this laminate can be determined and used to calibrate the simulation.

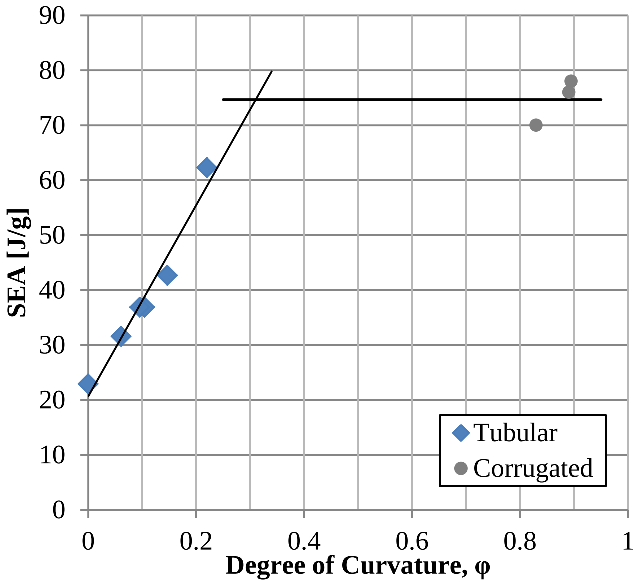

Figure 109. SEA vs. φ for nine different crush geometries of the same laminate

The simulation of the semicircular corrugated element is chosen for the initial model development. Recommendations from the first part of the guidelines are followed to create the baseline input file given in appendix B. This model uses a mesh size of 0.1 in (2.54 mm), and the RIGID_NODES_TO_RIGID_BODY contact type with a shallow and conservative LP curve (see *DEFINE_CURVE "For Contact," LCID = 82 in appendix B). Although more accurate results can be obtained from using a more aggressive LP curve, the stability of the analysis is compromised by doing so. It is recommended that the initial trigger thickness value be set to a very low value, such as 10% of the total thickness, for stability and crush initiation for the initial calibration.

The trigger thickness is defined in the section definition for the trigger elements, *SECTION_SHELL "Trigger," using the parameters T1, T2, T3, and T4, to define the thicknesses at each node (see appendix B). The initial MAT54 SOFT value should be an intermediate value, such as 0.5. Both this value and the trigger thickness values will change during calibration. The DFAILM parameter is preemptively increased from its experimentally measured value of 0.012 in/in to 0.06 in/in to ensure stability of the crush simulations. It has been shown earlier that low values of DFAILM can severely inhibit stability of the crush simulation, whereas increasing DFAILM well beyond a value that results in a stable model has no adverse effect on the crush simulation (see figure 110). The large increase of DFAILM ensures that the transverse strain limitation will not cause premature element erosion; instead other failure strains (such as the compressive fiber strain, DFAILC) will cause element erosion prior to DFAILM, as desired.

The experimental load-displacement crush curve is compared against the load-displacement curve of the simulation generated from the sum of the forces across the bottom row of nodes. Initial results prior to calibration are expected to be either entirely unstable (i.e., erratic and uneven element erosion) or stable (i.e., even row-by-row element erosion), but with incorrect simulated load values. In the case of complete instability, the SOFT parameter should be lowered. For geometric features with low degrees of curvature, the SOFT may need to be reduced below 0.1 for stability. If stable crushing cannot be obtained from simply lowering SOFT, then the MAT54 parameter DFAILM should be further increased. Changing DFAILM is a calibration that only needs to be made once for the material model of the entire laminate.

Once simulated crush stability is obtained, the SOFT parameter should be finely adjusted to directly calibrate the average crushing load value (and subsequently, the SEA) until it matches the experiment. An example of the effect that SOFT has on the average crush load and stability of the square tube crush simulation is shown in figure 73. In this case, high values of SOFT, such as 0.58, destabilized the model completely and caused global buckling. SOFT was then lowered to a value of 0.2, which only semi-stabilized the model. Fine adjustments of SOFT were made around the value of 0.15 to calibrate the simulation to the experiment.

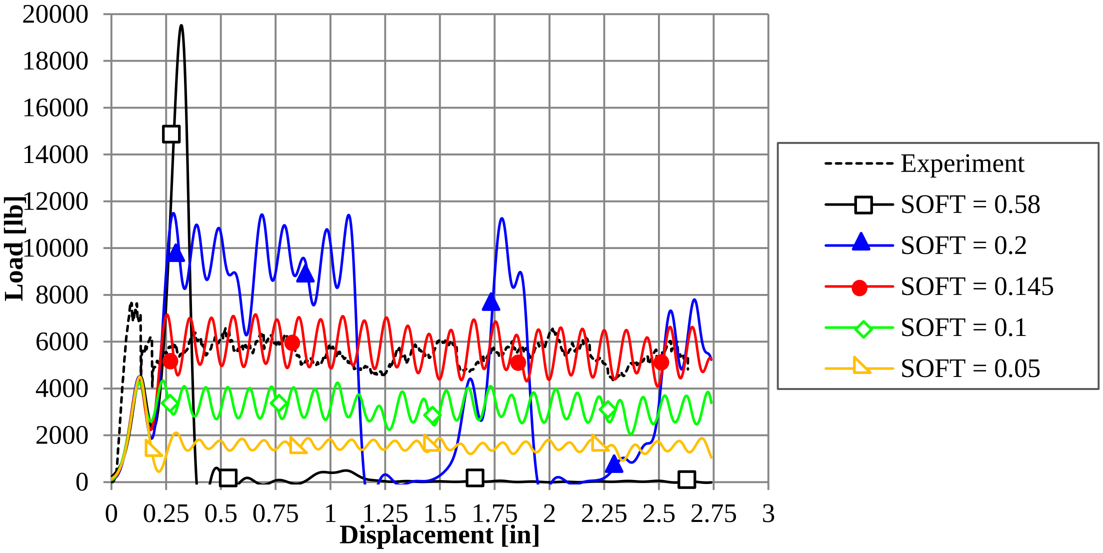

Figure 110. Step one: SOFT parameter calibration of the tube simulation using new contact LP curve

After calibrating the SOFT, the initial peak load can be calibrated so it also matches the experiment by adjusting the trigger thickness. An example of the effect of the trigger thickness on the square tube crush simulation is shown in figure 111.

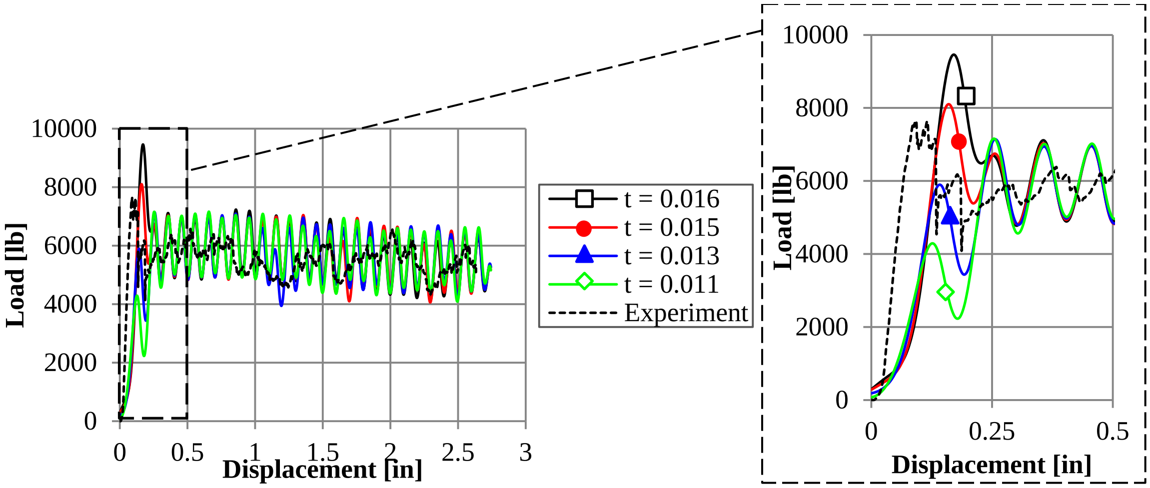

Figure 111. Step two: Trigger thickness calibration of the tube simulation using new contact LP curve

Following the development of the baseline crush model, more crush element geometries can be simulated using the same basic model definition. The change in geometry will destabilize the model, and the modeler must determine the reason for the destabilization and evaluate if it is to be expected or if it is a greater problem. If the initial development has produced a stable and robust model, then only the SOFT and trigger thickness parameters require calibration to produce successful element-level crush simulations of different geometries. If changing only the SOFT parameter does not work, then changes in other parameters, such as DFAILM, must be explored. Other parameters known to affect stability include the failure strains DFAILS and DFAILT. In some cases, the transverse and shear material strength parameters, YT and SC, have been shown to cause instability; however, this is often when given unrealistic values. If none of the parameters known to affect stability fix the problem, then changes in larger modeling definitions must be explored, such as the time-step or LP curve in the contact definition.

Given a stable baseline model, only two changes are necessary in the model definition for each simulated geometry: 1) SOFT, to capture the average crush load, and 2) trigger thickness, to capture the initial load peak. It is expected that these two parameters must be calibrated for all MAT54 crush simulations. The DFAILM parameter remained at the increased value determined during the baseline sinusoid model development for all of the element-level simulations of this particular composite material system. From the element-level material model calibration, two important empirical relationships were developed for the composite material system modeled in this example: one that relates the experimentally measured SEA to the numerically calibrated SOFT parameter shown in figure 112(a) and one that relates the calibrated SEA and trigger thickness values shown in figure 112(b). The first linear trend relates SOFT to SEA and allows for the calibration of the numeric SOFT parameter using the experimentally measured SEA. Similarly, the second linear trend relates SOFT to the trigger thickness, allowing for the calibration of the trigger thickness following the calibration of SOFT without the need for an experimental load-displacement curve for calibration. These two relations are very important in the scenario in which only three element geometries are crush tested to generate the relationship between SEA and degree of curvature. In this case, the MAT54 model must be calibrated using inferred SEA values without the experimental load-displacement curve. These two trends effectively prevent a blind trial-and-error process of defining the material model, and instead provide a guided calibration process that effectively generates a material model capable of simulating composites in crush failure.

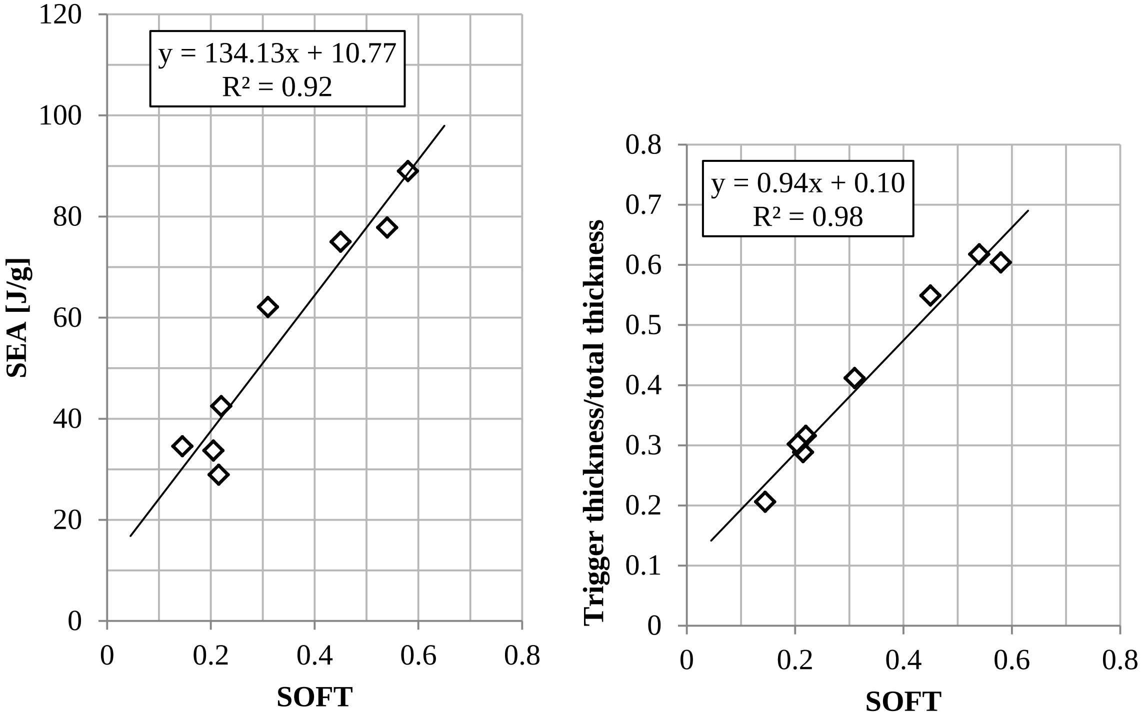

(a) (b)

Figure 112. (a) Linear trend between the calibrated MAT54 SOFT parameter and the experimental SEA and the (b) linear trend between the calibrated SOFT parameter and the ratio of trigger thickness to original thickness.

For the composite material system used in this study, an experimental relationship between SEA and degree of curvature was generated so that, given a new geometry for a crush element, the SEA can be estimated based on the calculation of the crush element's degree of curvature. This means that if a new crush element were to be introduced at the subcomponent level, it would be possible to estimate the appropriate SOFT value without conducting further crush element tests. The best approach, however, is to identify in advance all of the geometric crush elements in the structure and treat each geometry as a necessary element to crush test during the BBA to calibrate the numeric model so the approximations are minimized. Following the successful calibration of the MAT54 material model for simulating crush at the element level, the material model can be validated at the next level of the BBA—the subcomponent level.

17. CONCLUSION

The behavior of composite materials under crush conditions poses particular challenges for engineering analysis because it requires modeling beyond the elastic region and into failure initiation and propagation. Crushing is the result of a combination of several failure mechanisms, such as matrix cracking and splitting, delamination, fiber tensile fracture and compressive kinking, frond formation and bending, and friction. With today's computational power, it is not possible to capture each of the failure mechanisms; therefore, great simplifications are required. Macro-mechanical models based on lamina-level properties have been used, notwithstanding the well-accepted limitations for composite failure criteria in predicting the onset of damage within laminate codes. This report investigates the ability of a commercially available, mainstream industry analytical tool to predictively simulate composites under crush conditions.

In the first part of this report, the complex energy-absorbing mechanisms of a composite material system subjected to crush loading were investigated, and some key findings were made. First, SEA is not a material property of a composite material system and SEA measurements vary significantly according to the geometry of the crush test element, as different geometries favor different failure mechanisms that, in turn, provide varying levels of energy absorption. This means that no single crush test can fully characterize the SEA of a composite. Instead, the characterization of the energy absorption capability of a composite material system requires a set of crush element experiments that are each representative of geometric features of the structure in consideration. In doing so, a curve can be developed that describes the SEA in terms of structural geometry. For the composite material system investigated, an empirical relationship between the SEA and the degree of curvature of the crush element was developed. This relationship can be extrapolated and applied to additional crush geometries that were not tested to provide approximate predictions for SEA.

The relationship between SEA and the degree of curvature is explained by the failure modes observed during crush testing. These failure modes are divided into two extremes—delamination/splaying and fragmentation. Crush failure is a combination of varying degrees of both. During delamination, little energy is absorbed in splitting the material along an interlaminar crack front, and the resulting SEA measurement is low. Flat segments of crush elements do not provide delamination suppression and are prone to this low-SEA failure mode. Fragmentation failure is a destructive mode that leaves little material intact and expends a lot of energy to completely break up the material, resulting in high SEA. Curved geometries suppress delamination fronts and fragmentation occurs, causing great energy absorption.

In the second part of this report, an advanced simulation method using the LS-DYNA material model MAT54 to simulate crush failure has been investigated, and a modified version of the composite material model, which simulates failure and post-failure behaviors, has been developed. This composite damage material model was thoroughly investigated using single-element models and several crush models to provide a comprehensive overview of its theory, parameters, and parametric sensitivities with regard to crush modeling, details of which were all previously unavailable. MAT54 has been successfully used to capture the behavior of a fabric material system for the simulation of specimens undergoing axial crushing. It was found that the SOFT crush front parameter is the single most influential parameter for determining the success of the crush simulation. Through a careful calibration by trial-and-error, the right value for the SOFT parameter can be identified, but there is no way of determining it a priori or measuring it experimentally.

Following the development of the stable crush simulation of a sinusoid crush element using MAT54, several simulations of crush elements with various cross-sectional geometries were calibrated using SOFT to match the experimental results well. It is not possible to simulate different specimen geometries without making changes to the material model because specific and individual damage and failure mechanisms (such as delamination versus fragmentation) cannot be modeled using MAT54. Empirical curves have been established that relate experimental parameters (e.g., specific energy absorption) to important modeling parameters (e.g., SOFT and trigger thickness), making the calibration of the crush simulation more focused by reducing the scope of the trial-and-error calibration process. Ultimately, this modeling approach requires experimental element-level crush data so that trial-and-error calibration of the SOFT parameter can be executed to develop a good crush model. Therefore, consistent with other findings of the Composite Materials Handbook (CMH-17) Crashworthiness Working Group Numerical Round Robin, it cannot be said that LS-DYNA MAT54 can be a predictive tool for simulating simple shapes, such as tubes or stiffeners.

Finally, the MAT54 source code was edited so a modified composite damage material model composite was implemented in single-element and crush simulations. The modified model has an improved capability to simulate the elastic behavior. Several alternative failure criteria were investigated in the modified model, each demonstrating an equal or worse capability to predict initial failure than MAT54, thus validating its use of the Hashin criteria to determine lamina failure. The default approach for modeling the crush elements by reducing their strength using the SOFT parameter proved to be most effective for crush modeling as well. While several modifications were made in the post-failure material behavior, none produced favorable crush results, thereby reinforcing the importance of the plasticity used by MAT54 for crush stability. Overall, although the modified model improved some aspects of MAT54, it primarily served to confirm that regardless of the scientific details of the approach chosen to approximate the post-failure behavior, it is more important to capture the macroscopic engineering behavior.

18. REFERENCES

1. Composite Materials Handbook (CMH-17), Rev. G., Vol. 3, Chapter 16.

2. Nailadi, C.,“A Summary of the ACC Tube Testing Program,” in *Proceedings of the 49th MIL-HDBK-17 Coordination Meeting*, Santa Monica, California, December 2005.

3. Browne, A., Johnson, N., and Botkin, M., “Dynamic Crush Response of Composite Crash Boxes: Effects of Impact Angle and Bumper Attachment,” in *Proceedings of the ASC 27th Technical Conference*, Dayton, Ohio, September 2010.

4. Bisagni, C. “Experimental Investigation of the Collapse Modes and Energy Absorption Characteristics of Composite Tubes,” *International Journal of Crashworthiness*, Vol. 14, No. 4, 2009, pp. 365–378.

5. Jeryan, R. “Energy Management Working Group Activities,” in *Proceedings of the 48th MIL-HDBK-17 Coordination Meeting—Crashworthiness Working Group*, Charlotte, North Carolina, March 2005.

6. Jackson, K. and Fasanella, E. “Development of an LS-DYNA Model of an ATR42-300 Aircraft for Crash Simulation,” in *Proceedings of the 8th International LS-DYNA User's Conference*, Detroit, Michigan, May 2004.

7. Wiggenraad, J. “Crashworthiness Research at NLR: 1990–2003,” NLR TP-2003-217, June 2003.

8. McCarthy, M., Harte, G., Wiggenraad, J., et al., “Finite Element Modeling of Crash Response of Composite Aerospace Sub-Floor Structures,” *Computational Mechanics,* Vol. 26, 2000, pp. 250–258.

9. Hull, D. “A Unified Approach to Progressive Crushing of Fibre-Reinforced Composite Tubes,” *Composite Science & Technology*, Vol. 40, No. 4, 1991, pp. 377–421.

10. Pickett, A., Pyttel, T., Payen, F., et al., “Failure Prediction for Advanced Crashworthiness of Transportation Vehicles,” *International Journal of Impact Engineering*, Vol. 30, 2004, pp. 853–872.

11. Du Bois, P., “Crashworthiness Engineering With LS-DYNA,” in *FEA Information International News for the World-Wide Engineering Community*, December 2001.

12. Feraboli, P., “Development of a Modified Flat Plate Test and Fixture Specimen for Composite Materials Crush Energy Absorption,” *Journal of Composite Materials*, Vol. 43, No. 19, 2009, pp. 1967–1990.

13. Lestari, W., Thuis, H., and Wiggenraad, J., “Development of a Trigger Mechanism to Reduce Peak Forces in Crash Loaded Composite Sine-Wave Spars,” in *20th European Rotorcraft Forum*, Amsterdam, The Netherlands, October 1994.

14. Farley, G. and Jones, R.,“Energy-Absorption Capability of Composite Tubes and Beams,” NASA TM 101634, Hampton, Virginia, 1989.

15. Farley, G. and Jones, R., “Crushing Characteristics of Continuous Fiber-Reinforced Composite Tubes,” *Journal of Composite Materials*, Vol. 26, No. 1, 1992, pp. 37–50.

16. Carruthers, J., Kettle, A., and Robinson, A., “Energy Absorption Capability and Crashworthiness of Composite Material Structures: A Review,” *Applied Mechanics Reviews*, No. 51, pp. 635–649, 1998.

17. Hamada, H., Coppola, J., Hull, D., et al., “Comparison of Energy Absorption of Carbon/Epoxy and Carbon/PEEK Composite Tubes,” *Composites*, Vol. 23, 1992, pp. 245–252.

18. Adams, D., “Crashworthiness Test Methods,” in *Proceedings of the 57th CMH-17 Coordination Meeting—Crashworthiness Working Group*, Atlanta, Georgia, November 2009.

19. Lavoie, J. and Morton, J., “Design and Application of a Quasi-Static Crush Test Fixture for Investigating Scale Effects in Energy Absorbing Composite Plates,” NASA CR 4526, July 1993.

20. Johnson, A. and Kohlgruber, D., “Design and Performance of Energy Absorbing Subfloor Structures in Aerospace Applications,” in *IMechE Seminar S672*, London, England, May 2000.

21. Jacob, G., Fellers, J., Starbuck, J., and Simunovic, S., “Crashworthiness of Automotive Composite Material Systems,” *Journal of Applied Polymer Science*, Vol. 92, 2004, pp. 3218–3225.

22. Feindler, N., Döll, J., and Drechsler, K., “Test Method to Analyse the Energy Absorption of Composite Material Using Flat Coupon Testing,” in *5th International Conference on Composites Testing and Model Simulation*, Lausanne, Switzerland, February 2011.

23. Thornton, P., “Energy Absorption in Composite Structures,” *Journal of Composite Materials*, July 1979, pp. 248–262.

24. Mamalis, A., Robinson, M., Manolakos, D., et al., “Review: Crashworthy Capability of Composite Material Structures,” *Composite Structures*, Vol. 37, 1997, pp. 109–134.

25. Jacob, G., Fellers, J., Simunovic, S., and Starbuck, J., “Energy Absorption in Polymer Composites for Automotive Crashworthiness,” *Journal of Composite Materials*, Vol. 36, 2002, pp. 813–850.

26. Farley, G., “Energy Absorption of Composite Materials,” *Journal of Composite Materials*, Vol. 17, 1983, pp. 267–279.

27. Schmueser, D., and Wickcliffe, L., “Impact Energy Absorption of Constinuous Fiber Composite Tubes,” *Journal of Engineering Material and Technology*, Vol. 109, 1987, pp. 72–77.

28. Hamada, H., Ramakrishna, S., and Satoh, H., “Crushing Mechanism of Carbon Fibre/PEEK Composite Tubes,” *Composites: Part A*, Vol. 26, 1995, pp. 749–755.

29. Tao, W., Robertson, R., and Thornton, P., “Effects of Material Properties and Crush Conditions on the Crush Energy Absorption of Fiber Compsoite Rods,” *Composites Science and Technology*, Vol. 47, 1993, pp. 405–418.

30. Kindervater, C., “Energy Absorption of Composites as an Asepct of Aircraft Structural Crash-Resistance,” in *Developments in the Science and Technology of Composite Materials*, Stuttgart, Germany, Elsevier Applied Science Publishers, 1990, pp. 643–651.

31. Farley, G., “Effect of Specimen Geometry on the Energy Absorption Capability of Composite Materials,” *Journal of Composite Materials*, Vol. 20, pp. 390–400, 1986.

32. Mamalis, A., Manolakos, D., Viegelahn, G., et al., “On the Axial Crumpling of Fiber-Reinforced Composite Thin-Walled Conical Shells,” *International Journal of Vehicle Design*, Vol. 12, 1991, pp. 450–467.

33. Farley, G. and Jones, R., “Crushing Characteristics of Composite Tubes With 'Near Elliptical' Cross Sections,” *Journal of Composite Materials*, Vol. 26, 1992, pp. 1741–1751.

34. Hanagud, S., Craig, I., Sriram, P., and Zhou, W., “Energy Absorption Behavior of Graphite Epoxy Composite Sine Webs,” *Journal of Composite Materials*, Vol. 23, No. 5, 1989, pp. 448–459.

35. McCarthy, M. and Wiggenraad, J., “Numerical Investigation of a Crash Test of a Composite Helicopter Subfloor Structure,” *Composite Structures*, Vol. 51, 2001, pp. 345–359.

36. San Vicente, J., Beltran, F., and Martinez, F., “Simulation of Impact on Composite Fuselage Structures,” in *European Conference on Computational Methods in Applied Sciences and Engineering*, *ECCOMAS*, Barcelona, Spain, September 2000.

37. Jackson, A., Dutton, S., Gunnion, A., and Kelly, D., “Investigation Into Laminate Designe of Open Carbon-Fibre/Epoxy Sections by Quasi-Static and Dynamic Crushing,” *Composite Structures*, Vol. 93, 2011, pp. 2646–2654.

38. Hurley, T. and Vandenburg, J., “Small Airplane Crashworthiness Design Guide,” Simulia Technologies TR-98099; AGATE Integrated Design and Manufacturing AGATE-WP3.4-034043-036, Phoenix, Arizona, 2002.

39. Farley, G. and Jones, R., “Prediction of the Energy-Absorption Capability of Composite Tubes,” *Journal of Composite Materials*, Vol. 26, No. 3, 1992, pp. 388–404.

40. Hamada, H. and Ramakrishna, S., “A FEM Method for Prediction of Energy Absorption Capability of Crashworthy Polymer Composite Materials,” *Journal of Reinforced Plastics and Composites*, Vol. 16, 1997, pp. 226–242.

41. Tabiei, A. and Chen, Q.,“Micromechanics Based Composite Material Model for Impact and Crashworthiness Explicit Finite Element Simulation,” in *6th International LS-DYNA Conference*, Detroit, Michigan, April 2000.

42. Morthorst, M. and Horst, P., “Failure Model for Composite Materials Under Quasi-Static Crushing Conditions,” *Journal of Strain Analysis for Engineering Design*, Vol. 39, 2004, pp. 411–421.

43. McGregor, C., Vaziri, R., Poursartip, A., et al., “Simulation of Progressive Damage Developement in Braided Composite Tubes Undergoing Dynamic Axial Crushing,” in *9th International LS-DYNA Conference*, Detroit, Michigan, June 2006.

44. Fouinneteau, M. and Pickett, A., “Shear Mechanism Modelling of Heavy Tow Braided Composites Using a Meso-Mechanical Damage Model,” *Composites: Part A*, Vol. 38, 2007, pp. 2294–2306.

45. Greve, L., Pickett, A., and Payen, F., “Experimental Testing and Phenomenological Modelling of the Fragmentation Process of Braided Carbon/Epoxy Composite Tubes Under Axial and Oblique Impact,” *Composites: Part B*, Vol. 39, 2008, pp. 1221–1232.

46. Najafi, A, Huang, D., Rais-Rohani, M., et al., “Simulation of Crushing Process in Composite Tubes,” in *51st AIAA/ASME/ASCE/AHA/ASC Structures, Structural Dynamics, and Materials Conference*, Orlando, Florida, April 2010.

47. Fasanella, E., Jackson, K., and Lyle, K.,“Finite Element Simulation of a Full-Scale Crash Test of a Composite Helicopter,” in *American Helicopter Society 56th Annual Forum*, Virginia Beach, Virginia, May 2000.

48. Johnson, A. and Pickett, A., “Impact and Crash Modeling of Composite Structures: A Challenge for Damage Mechanics,” in *Proceedings of ECCM'99 Conference*, Munich, Germany, September 1999.

49. Li, X., Ferrie, C., Nottorf, E., et al., “A Building Block Method for Damage Tolerance Evaluation of Impacted Composite Stringer Panel,” in *American Helicopter Society 61st Annual Forum*, Grapevine, Texas, June 2005.

50. Fasanella, E. and Jackson, K., “Best Practices for Crash Modeling Simulation,” National Aeronautics and Space Administration and Langley Research Center (U.S.), Hampton, Virginia, October 2002.

51. Sandhu, R., “A Survey of Failure Theories of Isotropic and Anisotropic Materials,” No. AFFDL-TR-72-71. Air Force Flight Dynamics Laboratory, Wright-Patternson Air Force Base, Ohio, 1972.

52. Soni, S., "A Comparative Study of Failure Envelopes in Composite Laminates," *Journal of Reinforced Plastic Composites*, Vol. 2, 1983, pp. 34–42.

53. Tsai, S., "A Survey of Macroscopic Failure Criteria for Composite Materials," *Journal of Reinforced Plastic Composites*, Vol. 3, 1984, pp. 40–62.

54. M. Nahas, "Survey of Failure and Post-Failure Theories of Laminated Fibre Reinforced Composites," *Journal of Composites, Technology, & Research*, Vol. 8, 1986, pp. 138–153.

55. Soden, P., Kaddour, A., and Hinton, M. "Recommendations for Designers and Researchers Resulting From the World-Wide Failure Exercise," *Composite Science & Technology*, No. 64, 2004, pp. 589–604.

56. Orifici, A., Herszberg, I., and Thomson, R., "Review of Methodologies for Composite Material Modelling Incorporating Failure," *Compsite Structures*, Vol. 86, 2008, pp. 194–210.

57. Hashin, Z., "Failure Criteria for Unidirectional Fiber Composites," *Journal of Applied Mechanics*, Vol. 47, 1980, pp. 329–334.

58. Chang, F. and Chang, K., "A Progressive Damage Model for Laminated Composites Containing Stress Concentrations," *Journal of Composite Materials*, Vol. 21, 1987, pp. 834–855.

59. Puck, A. and Schurmann, H., "Failure Analysis of FRP Laminates by Means of Physically Based Phenomenological Models," *Composites Science & Technology*, Vol. 58, 1998, pp. 1045–1067.

60. Hinton, M., Kaddour, A., and Soden, P., "A Comparison of the Predictive Capabilities of Current Failure Theories for Composite Lamiates, Judged Against Experimental Evidence," *Composites Science & Technology*, Vol. 62, 2002, pp. 1725–1797.

61. Wolfe, W. and Butalia, T., "A Strain-Energy Based Failure Criterion for Non-Linear Analysis of Composite Laminates Subjected to Biaxial Loading," *Composites Sciences and Technology,* Vol. 58, 1998, pp. 1107–1124.

62. Butalia, T. and Wolfe, W., "A Strain-Energy-Based Non-Linear Failure Criterion: Comparison of Numerical Predictions and Experimental Observations for Symmetric Composite Laminates," *Composites Science and Technology*, Vol. 62, 2002, pp. 1697–1710.

63. Talreja, R., "Modeling of Damage Development in Composites Using Internal Variable Concepts," in *Damage Mechanics in Composites*, A. Wang and G. Haritos, Eds., ASME AD-Vol. 12, 1987, pp. 11–16.

64. Johnson, A., Pickett, A., and Rozycki, P., "Computational Methods for Predicting Impact Damage in Composite Structures," *Composites Science and Technology*, Vol. 61, 2001, pp. 2183–2192.

65. Sokolinsky, V., Indermuehle, K., and Hurtado, J., "Numerical Simulation of the Crushing Process of a Corrugated Composite Plate," *Composites: Part A*, Vol. 42, 2011, pp. 1119–1126.

66. Feraboli, P., "Composite Materials Strength Determination Within the Current Certification Methodology for Aircraft Structures," *Journal of Aircraft*, Vol. 46, No. 4, 2009, pp. 1365–1374.

67. Rassaian, M. and Davis, K., "Use of Nonlinear Analysis for Crashworthiness Certification," in *Aerospace Structural Impact Dynamics International Conference*, Wichita, Kansas, November 2012.

68. Feraboli, P., Deleo, F., Wade, B., et al., "Predictive Modeling of an Energy-Absorbing Sandwich Structural Concept Using the Building Block Approach," *Composites: Part A*, Vol. 41, 2010, pp. 774–786.

69. Heimbs, S., Hoffman, M., Waimer, M., et al., "Dynamic Testing and Modelling of Composite Fuselage Frames and Fasteners for Aircraft Crash Simulations," *International Journal of Crashworthiness*, Vol. 18, 2013, pp. 406–422.

70. Jackson, K., Fasanella, E., Boitnott, R., and Lyle, K., "Full-Scale Crash Test and Finite Element Simulation of a Composite Prototype Helicopter," NASA TP-2003-212641, ARL-TR-2824, Hampton, Virginia, 2003.

71. Stockwell, A., "Simulation of an Impact Test of the All-Composite Lear Fan Aircraft," NASA CR-2002-211458, Hampton, Virginia, 2002.

72. Terry, J., Hooper, S., and Nicholson, M., "Design and Test of an Improved Crashworthiness Small Composite Airframe," NASA CR-2002-211774, Hampton, Virginia, 2002.

73. Delsart, D., Joly, D., Mahe, M., and Winkelmuller, G., "Evaluation of Finite Element Modelling Methodologies for the Design of Crashworthy Composite Commercial Aircraft Fuselage," in *24th International Congress of the Aeronautical Sciences*, Yokohama, Japan, September 2004.

74. Jackson, K., "Impact Testing and Simulation of a Crashworthy Composite Fuselage Concept," *International Journal of Crashworthiness*, Vol. 6, 2001, pp. 107–122.

75. Maia, L. and de Oliveira, P., "A Review of Finite Element Simulation of Aircraft Crashworthiness," SAE Technical Paper 2005-01-4012, 2005.

76. Sokolinksy, V., Indermuehle, K., and Hurtado, J., “Numerical Simulation of the Crushing Process of a Corrugated Composite Plate,” *Composites: Part A*, Vol. 42, 2011, pp. 1119–1126.

77. Fleming, D., “Delamination Modeling of Composites for Improved Crash Analysis,” *Journal of Composite Materials*, Vol. 35, 2001, pp. 1777–1792.

78. Rassaian, M. and Wade, B., “Numerical Round Robin Action Items,” in *9th CMH-17 Crashworthiness Working Group Meeting*, Costa Mesa, California, July 2010.

79. Byar, A., “A Crashworthiness Study of a Boeing 737 Fuselage Section,” Drexel University Doctoral Dissertation, 2004, Philadelphia, Pennsylvania.

80. Gabrys, J., Schatz, J., Carney, K., et al., “The Use of LS-DYNA in the Columbia Accident Investigation and Return to Flight Activities,” in *Proceedings of the 8th International LS-DYNA User's Conference*, Detroit, Michigan, May 2004.

81. Tomblin, J., Sherraden, J., Seneviratne, W., and Raju, K., “A-Basis and B-Basis Design Allowables for Epoxy-Based Prepreg: Toray T700SC-12k-50C/#2510 Plain Weave Fabric (AGATE-WP3.3-033051-134),” National Institute for Aviation Research, Wichita, Kansas, October 2002.

82. Feraboli, P., “Development of a Corrugated Test Specimen for Composite Materials Energy Absorption,” *Journal of Composite Materials*, Vol. 42, 2008, pp. 229–256.

83. Feraboli, P. and Wade, B., “Crushing Behavior of a Composite Corrugated Specimen Representative of an Aircraft Subfloor: Experiment and Simulation,” FAA Technical Report, DOT/FAA/AR-11/21, September 2013.

84. Feraboli, P., Wade, B., Deleo, F., et al., “LS-DYNA MAT54 Modeling of the Axial Crushing of a Composite Tape Sinusoidal Specimen,” *Composites: Part A*, Vol. 42, 2011, pp. 1809–1825.

85. Lavoie, J. and Kellas, S., “Dynamic Crush Tests of Energy-Absorbing Laminated Composite Plates,” *Composites Part A*, Vol. 27, No. 6, , 1996, pp. 467–475.

86. Bolukbasi, A. and Laananen, D., “Energy Absorption in Composite Stiffeners,” *Composites*, Vol. 26, No. 4, 1995, pp. 291–301.

87. Bolukbasi, A., Baxter, T., Nguyen, T., et al., “Energy Absorbing Structure for Aircraft,” United States Patent 8376275.

88. Jackson, K., Morton, J., Lavoie, J., and Boitnott, R., “Scaling of Energy Absorbing Composite Plates,” *Journal of American Helicopter Society*, Vol. 39, No. 1, 1994, pp. 17–23.

89. Wade, B., Feraboli, P., Osborne, M., and Rassaian, M. “Simulating Laminated Composite Materials Using LS-DYNA Material Model MAT54: Single Element Investigation,” FAA Technical Report, DOT/FAA/TC-14/19, May 2014.

90. Wade, B., “Capturing the Energy Absorbing Mechanisms of Composite Structures Under Crash Loading,” (Doctoral disseration), University of Washington, Seattle, Washington, 2014.

91. Courant, R., Friedrichs K., and Lewy, H., “Über Die Partiellen Differentialgleichungen der Mathematischen Physik,” *Mathematische Annelen*, Vol. 100, 1928, pp. 32–74.

92. Paz, M., *Structural Dynamics Theory and Computation*, 3rd ed., New York, New York: Van Nostrand Reinhold, 1991.

93. Zukas, J., Nicholas, T., Swift, H., et al., *Impact Dynamics*, 1st ed., John Wiley & Sons, 1982.

94. S.A.E. Recommended Practice J211b, “Instrumentation for Impact Tests,” Society of Automotive Engineers, Warrendale, Pennslyvania, 1974.

95. Feraboli, P. and Rassaian, M., “Proceedings of the CMH-17 (MIL-HDBK-17) Crashworthiness Working Group Numerical Round Robin,” Costa Mesa, California, July 2010.

96. Mabson, G., Weckner, O., and Ramnath, M., “Finite Element Based Decohesive Failure Simulation Sensitivity Studies,” in *53rd AIAA/ASME/ASCE/AHS/ASC Structures, Structural Dynamics and Materials Conference*, Honolulu, Hawaii, April 2012.

97. Wade, B., “Capturing the Energy Absorbing Mechanisms of Composite Structures under Crash Loading,” Dissertation - Need to look this up Thesis at the University of Washington 2014

98. Bala, S. and Day, J., “General Guidelines for Crash Analysis in LS-DYNA,” Livermore Software Technology Corporation, [Online]. Available at http://blog2.d3view.com/general-guidelines-for-crash-analysis-in-ls-dyna. [Accessed 2010].

99. Day, J., “Modeling of Composites in LS-DYNA,” Livermore Software Technology Corporation, [Online]. Available at awg.lstc.com/tiki/tiki-download_file.php?fileId=19. [Accessed 2010].

100. Bala, S., “Contact Modeling in LS-DYNA—Some Recommendations,” *FEA Information International News*, August 2001.

101. Bala, S., “Initial Penetrations in Contact Interfaces,” Livermore Software Technology Corporation, 2006. [Online]. Available at http://blog2.d3view.com/initial-penetrations-in-contact-interfaces. [Accessed 2010].

APPENDIX A—MAT54 SOURCE CODE & MODIFICATIONS

The Fortran source code of MAT54 was provided by Livermore Software Technology Corporation (LSTC). LSTC also provides resources for its licensed users to implement user-defined material models [A-1]; however these models follow an incompatible format against the built-in models such as MAT54, so a different approach for compiling the existing code and implementing the modified model in an LS-DYNA executable was necessary. Appendix A discusses the method in which code compilation was achieved, an interpretation of the MAT54 source code, and the modifications made to the code to alter its material modeling capability.

A.1. COMPILATION OF THE FORTRAN CODE

LSTC provides a usermat package to implement user-defined interfaces, such as user-defined material models (UMATs), contact definitions, friction formulations, etc. Most of the files contained in this package are library files, which cannot be read or edited because they are made up of 99.5% of the LS-DYNA source code, which is not necessary for implementing user-defined interfaces. The other files in this package are the dyn21.F, dyn21b.F Fortran files, and a makefile command for compilation. The two Fortran files contain all of the necessary code to define user interfaces, and the makefile file contains the commands that direct the compilation of the two Fortran files into the rest of the code to create an LS-DYNA executable with user-defined content. Each usermat package is unique to the LS-DYNA version, operating system, precision (single or double), and processor (multi- or single). The compiler necessary to create new LS-DYNA executable files must be the exact same compiler as used by LSTC when creating the original executable for that version, operating system, precision, and processor type. For the usermat package used in this research, the LS-DYNA version 971 R5.1.1 on 64-bit Windows was used, with double precision and a single processor (rendering the file name ls971_d_R5.1.1_winx64_p_lib). For this particular setup, LSTC prescribes to use the “Intel Visual Fortran Compiler for applications running on Intel 64, Version 10.1.034,” and it must be emphasized that using any version other than this exact one does not work.

With the usermat package, users can only modify and implement user-defined interfaces as allowed by LSTC in the dyn21.F and dyn21b.F files, and existing models, such as MAT54, are not visible and cannot be modified. The MAT54 subroutine made available by LSTC for this research was contained in its own external Fortran file. Initial trials to compile the MAT54 subroutine Fortran file into the usermat package did not work because the original code for MAT54 subroutine contained in the unavailable library files overwrites any external definition, thereby, overwriting any modifications made in the separate Fortran file. Given this, attempts were made to create a UMAT, which replicated MAT54, then modify this UMAT.

It was determined that making MAT54 into a UMAT was not feasible because the fundamental structure of the MAT54 subroutine code varied significantly from that of the UMAT models. For instance, the manner in which common variables are passed in blocks between the material subroutine and the main routine is different in the UMAT. It appeared that many of the common blocks referenced by the UMAT were organized and named differently than those used by MAT54. MAT54 declares 16 common blocks that contain 166 common Fortran variables necessary for the code, and simply declaring these 16 blocks in the UMAT caused grave errors due to naming mismatches and other unknown problems. These errors could not be explored further without greater access to the LS-DYNA source code. Similarly, the Fortran variables passed directly from the main routine to the material subroutine during the subroutine call were inconsistent between the UMAT and MAT54. This meant that the UMAT could not be called in the same fashion as MAT54, and the appropriate variables necessary for MAT54 could not be passed correctly. Furthermore, the input parameters specified by the user in the keyword file are organized in a particular way in the UMAT, which differs from MAT54, and could not be easily remedied. Without access to the main LS-DYNA source code to decipher these discrepancies, it was virtually impossible to define MAT54 as a UMAT.

With the further cooperation of LSTC, the development team provided a slightly modified usermat package, which had the original MAT54 subroutine removed from the main code so that an external subroutine would not be overwritten and could be compiled in with the rest of the code. This allowed for the MAT54 source code originally provided by LSTC to be externally modified and compiled into a new LS-DYNA executable that used the modified material model. For the compilation, the makefile file was modified to include commands to compile the MAT54 Fortran file (shl54s.F) by adding similar lines of code that already existed for the dyn21.F and dyn21b.F, as shown in the highlighted portions of figure A-1.

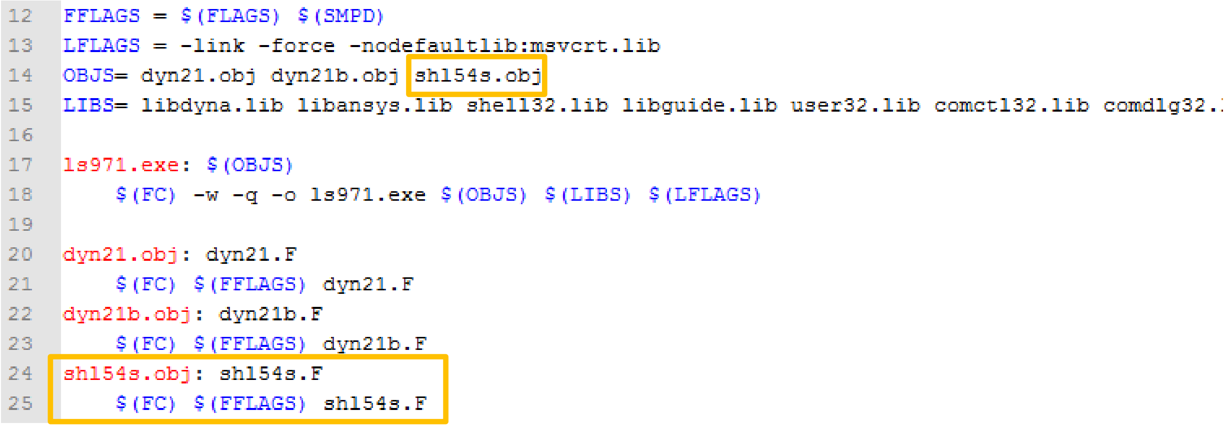

```
FFLAGS = $(FLAGS) $(SMPD)
LFLAGS = -link -force -nodefaultlib:msvcrt.lib
OBJS= dyn21.obj dyn21b.obj shl54s.obj
LIBS= libdyna.lib libansys.lib shell32.lib libguide.lib user32.lib comctl32.lib comdlg32.

ls971.exe: $(OBJS)
    $(FC) -w -q -o ls971.exe $(OBJS) $(LIBS) $(LFLAGS)

dyn21.obj: dyn21.F
    $(FC) $(FFLAGS) dyn21.F
dyn21b.obj: dyn21b.F
    $(FC) $(FFLAGS) dyn21b.F
shl54s.obj: shl54s.F
    $(FC) $(FFLAGS) shl54s.F
```

Figure A-1. Additional makefile commands to include the modified MAT54 Fortran file in the compilation of the LS-DYNA executable

Given the unique usermat package from LSTC, the correct compiler for that package, and the changes made to the makefile routine, the MAT54 Fortran source code was a standalone file that could be independently edited to implement the desired modifications of the material model calculations and behaviors. To verify that this compilation process was working, the MAT54 subroutine was compiled without any modifications, and the baseline semicircular sinusoid crush simulation was run. The results from this simulation were compared against those obtained using the same keyword input file in the standard LS-DYNA executable, and their crush curves are shown in figure A-2. The very slight differences between the two results are similar to those that have been shown to occur when using different computers, operating systems, versions of LS-DYNA, 32- versus 64-bit, etc.

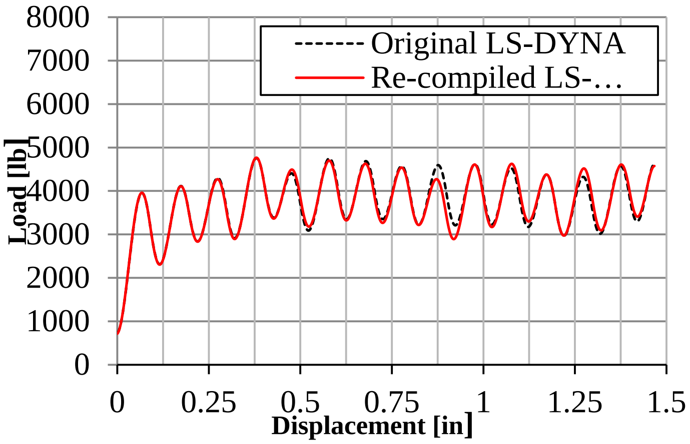

Figure A-2. Filtered crush simulation results of the original and recompiled LS-DYNA MAT54, which verify the compilation process of the new MAT54 subroutine

A.2. INTERPRETATION OF THE MAT54 SOURCE CODE

The entirety of the MAT54 Fortran source code was provided for the purpose of this research by LSTC. In general, this code is not made available to the public and for this reason irrelevant portions of the code are omitted from this report. For instance, the code, which calls and initializes the common and user-defined variables from the main LS-DYNA code, is not included because it is not relevant to the actual function of the MAT54 material model; however, variables that are relevant will be defined as they appear in the code. The code replicated here represents approximately 75% of the original MAT54 source code along with a thorough explanation of the code. The line numbering is unique to this publication of the code and used solely for the purpose of referencing specific portions of the code in this document.

The MAT54 material model is a vectorized model, which means that it performs its operations upon groups of elements, rather than one element at a time, to achieve better efficiency. For a composite material model, operations are performed in each element on a user-specified number of integration points through the thickness, which are representative of the composite material plies, and each has its own material orientation angle (also user specified). Although these are important definitions for the material model, they are defined in the shell element model code and are, therefore, not present in the MAT54 source code. Instead, by the time stresses and strains are passed to the material model subroutine, the operations are performed across a vector of integration points, which has a length of *nlq*. The length *nlq* is determined by the number of elements in a vectorized material model computation cycle and the number of integration points per element as specified by the user. A vectorized material model contains variables (such as stresses, strains, etc.) that are vectors with length *nlq*, which hold the variable value at each integration point in the cycle. Every operation of these variables occurs within “do” loops, which cycle through the variable *i* from the variable *lft* to the variable *llt*, which are the first and last integration points considered in the cycle.

The MAT54 Fortran code presented here can be summarized into several sections, which perform its major operations. These sections are shown in a flow chart in figure A-3, and the corresponding code attributed to each section is listed in table A-1.

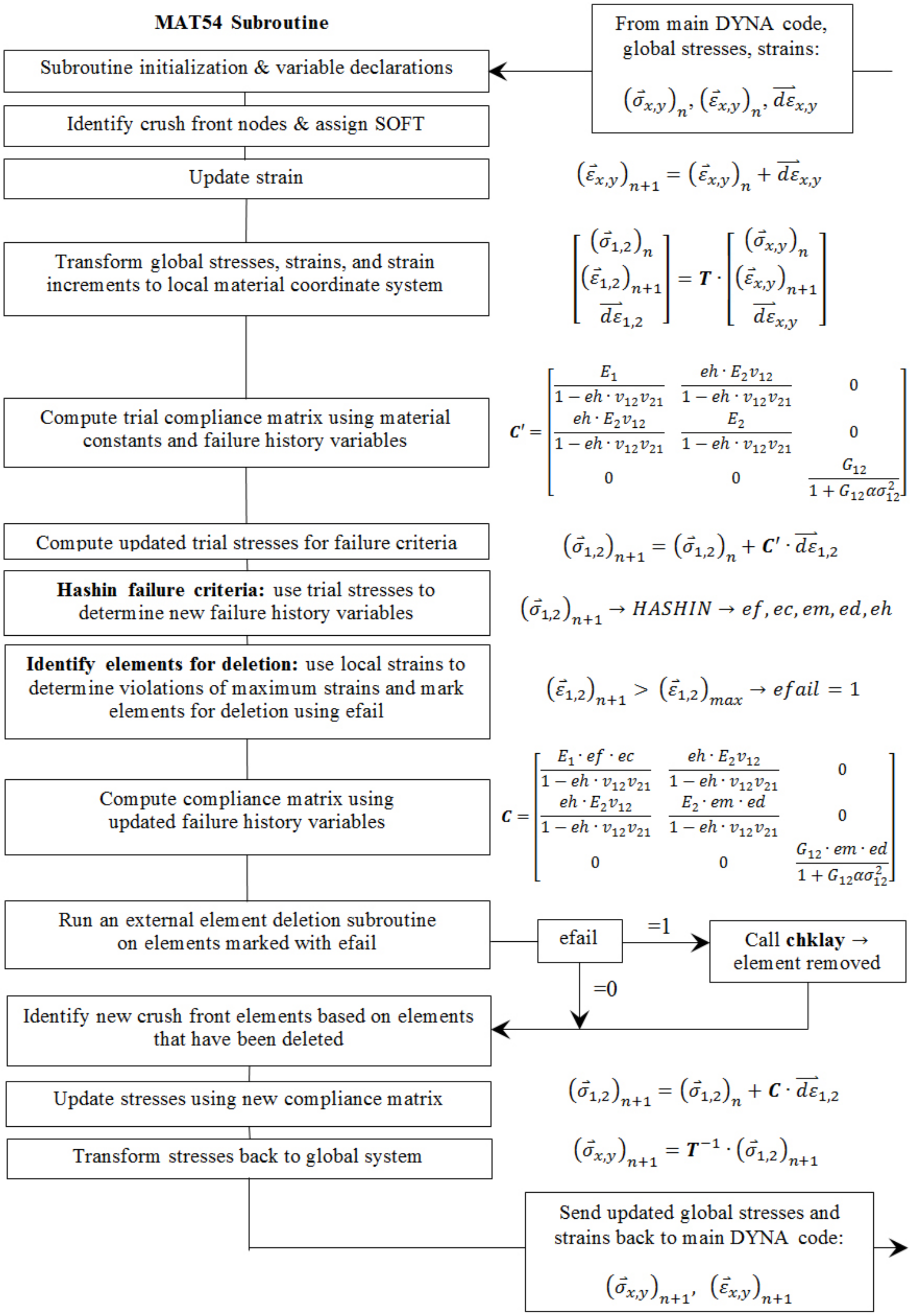

Figure A-3. Simplified flow chart of MAT54 source code operations

Table A-1. Contents of major operations performed in MAT54

Lines 001–039	Initialization and variable declaration, basic constant operations
Lines 040–052	Crush front initialization and material softening definition
Lines 053–067	Global to local transformation of stresses
Lines 068–072	Update strain
Lines 073–093	Global to local transformation of strains and strain increments
Lines 094–107	Compliance matrix computation for trial stresses
Lines 108–114	Trial stress computation
Lines 115–142	Failure criteria
Lines 143–170	Elements marked for deletion
Lines 171–203	New compliance matrix computation, which takes failure into account
Lines 204–248	Element deletion and new crush front elements flagged
Lines 249–255	Update stresses
Lines 256–271	Transform stresses back to global system

The line-by-line presentation and explanation of the code begins with the subroutine declaration of the MAT54 subroutine, called shl54s. This name needed to remain unchanged as it is referred to within the main LS-DYNA source code.

```
001   subroutine shl54s (cm,capa,nnm1,nshbwp,tfail,lft,llt,
002  . ncrshf,ipt,nip,ipt_thk,eosp)
003c
004c*****************************************************************
005c| Livermore Software Technology Corporation (LSTC)      |
006c| ------------------------------------------------------------ |
007c| Copyright 1987-2008 Livermore Software Tech. Corp      |
008c| All rights reserved                              |
009c*****************************************************************
```

Following the subroutine declaration, the common variables from the main LS-DYNA code are initialized, for example, the declaration of the global stresses, sig1, sig2, sig3, sig4, sig5, sig6, and sig7 from common block aux14loc, as shown below. As stated previously, most of this section of the source code has been omitted from this publication.

```
010   common/aux14loc/
011  &sig1(nlq),sig2(nlq),sig3(nlq),sig4(nlq),
012  &sig5(nlq),sig6(nlq),sig7(nlq),
```

This is followed by the declaration of the constants defined by the user in the keyword simulation input file, which are passed into the MAT54 subroutine in the vector cm. The code specifies the location within the cm vector using a constant mx, which accounts for an offset that is necessary as a result of being a vectorized material model. An example follows:

```
ymx =cm(mx+1)
ymy =cm(mx+2)
nuy =cm(mx+4)
nux =nuy*ymx/ymy
```

The location of the user-defined parameters in the cm vector is not the same as their location in the keyword input file, and it is useful to make this distinction to understand how and where to add new user input parameters when modifying the code. The MAT54 keyword input deck is shown in figure A-4, where each parameter is shown in terms of its keyword name (in bold), cm vector location (in terms of mx+n) and the name of the variable, as found in the MAT54 source code, which is often different than the keyword name.

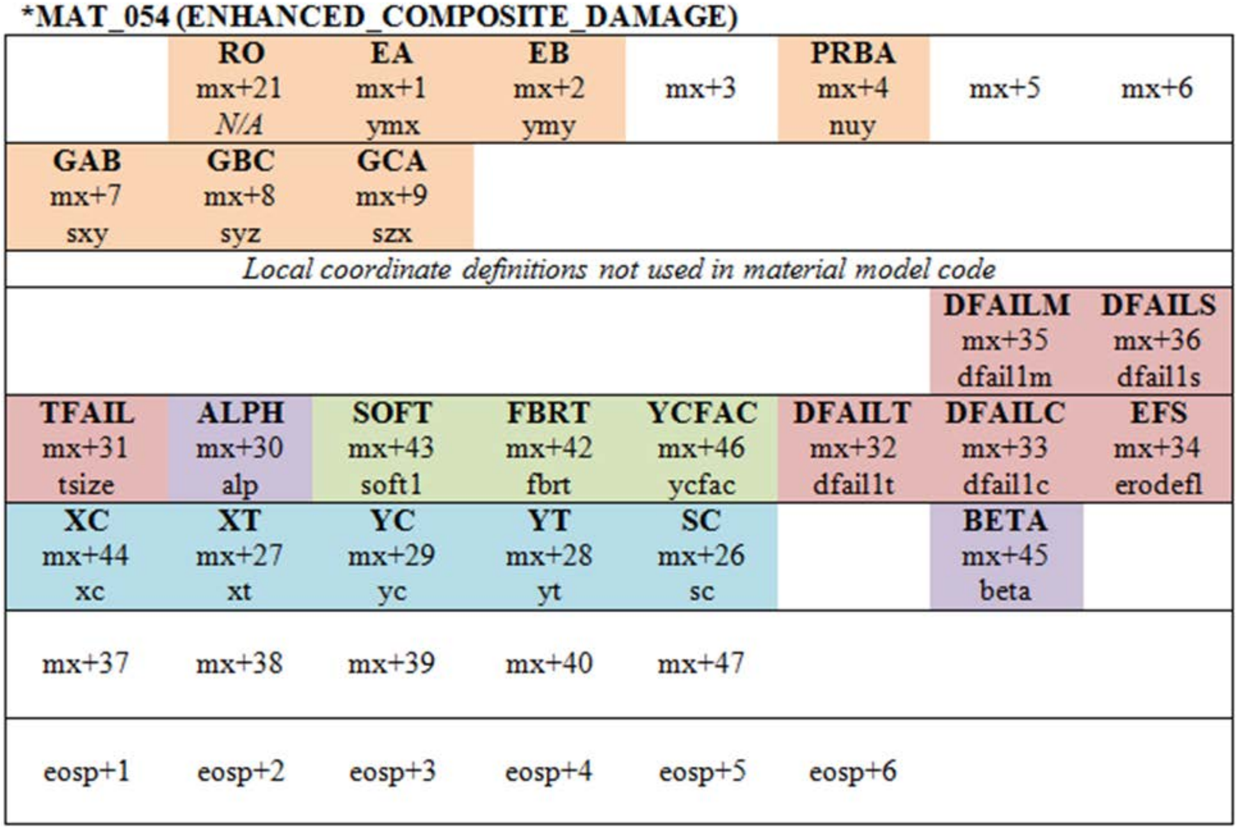

***MAT_054 (ENHANCED_COMPOSITE_DAMAGE)**

	RO mx+21 *N/A*	**EA** mx+1 ymx	**EB** mx+2 ymy	mx+3	**PRBA** mx+4 nuy	mx+5	mx+6
GAB mx+7 sxy	**GBC** mx+8 syz	**GCA** mx+9 szx					
Local coordinate definitions not used in material model code							
						DFAILM mx+35 dfail1m	**DFAILS** mx+36 dfail1s
TFAIL mx+31 tsize	**ALPH** mx+30 alp	**SOFT** mx+43 soft1	**FBRT** mx+42 fbrt	**YCFAC** mx+46 ycfac	**DFAILT** mx+32 dfail1t	**DFAILC** mx+33 dfail1c	**EFS** mx+34 erodefl
XC mx+44 xc	**XT** mx+27 xt	**YC** mx+29 yc	**YT** mx+28 yt	**SC** mx+26 sc		**BETA** mx+45 beta	
mx+37	mx+38	mx+39	mx+40	mx+47			
eosp+1	eosp+2	eosp+3	eosp+4	eosp+5	eosp+6		

Figure A-4. User-defined input parameters for MAT54 in terms of their keyword name, cm vector location, and source code variable name

The additional two cards, which contain spaces (mx+37-mx+47) and a new user input vector (eosp+1-eosp+6) are optional cards in MAT54, which contain variables that are not used in this report. Instead, these two cards provided user input vector locations for new user inputs to be defined during modification of the material model.

For many of the user input parameters, their introduction is immediately followed by an operation to address the case of a zero value. For many, the solution is to set the variable to a numerically infinite value (1E+16). For others the variable is given a default value, such as YCFAC = 2. These operations are:

```
if (ycfac.le.0.) ycfac=2.
if (dfail1m.eq.0.0) dfail1m=1.e+16
if (dfail1s.eq.0.0) dfail1s=1.e+16
if (erodefl.eq.0.0) erodefl=1.e+16
if (sc.eq.0.0) sc=1.e+08
if (xc.eq.0.0) xc=1.e+16
if (yt.eq.0.0) yt=1.e+16
if (yc.eq.0.0) yc=1.e+16
```

Other operations are performed to alter the user input variable values to a form that is more useful to use in later calculations. For instance, “mlt1” is a constant multiplier used to compute nonlinear shear terms in the failure criteria, and “mlt2” is a constant multiplier used in the compressive matrix failure criterion. These operations and their resulting new variables are:

```
xt2 =1./(xt*xt)
if(fbrt.gt.0.) then
 xt2fbrt=xt2/(fbrt*fbrt)
else
 xt2fbrt=xt2
endif
```

$$\text{xt2fbrt} = \begin{cases} \left(\frac{1}{XT}\right)^2 & if\ FBRT = 0 \\ \left(\frac{1}{XT*FBRT}\right)^2 & else \end{cases} \tag{A-1}$$

```
yt2 =1./(yt*yt)
```

$$\text{yt2} = \left(\frac{1}{YT}\right)^2 \tag{A-2}$$

```
sc2 =sc*sc
sd2 =.25/sc2
```

$$\text{sd2} = \left(\frac{1}{2SC}\right)^2 \tag{A-3}$$

```
ap3 =3.0*alp
ap34=.75*alp
od2g=.5/sxy
mlt1=1./(sc2*(od2g+ap34*sc2))
mlt2=(yc*yc*sd2-1.)/yc
```

$$\text{mlt1} = \frac{1}{SC^2\left(\frac{1}{2G_{12}}+\frac{3}{4}\alpha SC^2\right)} \tag{A-4}$$

$$\text{mlt2} = \left(\left(\frac{YC}{2SC}\right)^2 - 1\right)\frac{1}{YC} \tag{A-5}$$

The variable icrash_loc is a logical parameter that is true when the user defines an active SOFT value less than 1. This parameter enables crash-front elements to be determined.

```
icrash_loc = soft1.lt.0.9999
```

Next, the crash-front nodes are identified and material softening using the SOFT parameter is prepared within the do loop numbered 5 (lines 041–047). This is preceded by an “if” statement, which checks the value of the logical icrash_loc to determine if material softening due to the crash front is in use. Note that the crash-front elements are determined at the end of the subroutine after failure is determined; therefore, no crash-front nodes are identified in the first several cycles until after initial failure occurs. Crash-front nodes are identified by flagging the variable ncrshf to a value of 1. At each integration point in an element, there are four ncrshf values, one for each node denoted (ix1) through (ix4). The initial value of the crash-front flag at each node is zero and none of the following softening code is executed until after one of the nodes is flagged, as indicated by the second IF statement:

```
040      if(icrash_loc) then
041      do 5 i=lft,llt
042      if (max(ncrshf(ix1(i)),ncrshf(ix2(i)),
043     .    ncrshf(ix3(i)),ncrshf(ix4(i))).eq.1) then
```

If any of the nodes in the element are flagged, then two values are initialized in the crush front element—dam and soft. A second do loop, numbered 7 (lines 049–052) calculates the multipliers qq1 and qq2, which are directly used in the failure criteria to perform material softening. The qq1 variable acts as a flag within the Fortran code for crush-front elements.

```
044        dam(i)=1.e-08
045        soft=soft1
046        endif
047     5  continue
048      endif
049      do 7 i=lft,llt
050       qq1(i)=1.0-(1.0-soft)*(0.5+sign(0.5,dam(i)))
051       qq2(i)=1./(qq1(i)*qq1(i))
052     7 continue
```

$$qq1 = \begin{cases} SOFT, & \textit{crush front element} \\ 1.0, & \textit{all other elements} \end{cases} \tag{A-6}$$

$$qq2 = \begin{cases} \left(\frac{1}{SOFT^2}\right), & \textit{crush front element} \\ 1.0, & \textit{all other elements} \end{cases} \tag{A-7}$$

Next, the stresses are transformed from the global system to the material system in the do loop numbered 20 (lines 053–067). Before the stresses are transformed, the strain energy at the integration point, einc(i), is calculated by summing the product of the global stresses components sig1(i)–sig6(i) and the global strain components e1(i)–e6(i). The component numbering follows the common scheme adopted for composite materials:

$$\begin{bmatrix}\sigma_{11}\\ \sigma_{22}\\ \sigma_{33}\\ \sigma_{12}\\ \sigma_{23}\\ \sigma_{13}\end{bmatrix}=\begin{bmatrix}\sigma_{1}\\ \sigma_{2}\\ \sigma_{3}\\ \sigma_{4}\\ \sigma_{5}\\ \sigma_{6}\end{bmatrix}=\begin{bmatrix}\mathrm{sig1}\\ \mathrm{sig2}\\ \mathrm{sig3}\\ \mathrm{sig4}\\ \mathrm{sig5}\\ \mathrm{sig6}\end{bmatrix} \tag{A-8}$$

```
  do 20 i=lft,llt
  einc(i)=e1(i)*sig1(i)+e2(i)*sig2(i)+e4(i)*sig4(i)+
 1    e5(i)*sig5(i)+e6(i)*sig6(i)
```

The transformation occurs in two steps, first defining an intermediary matrix a in terms of the sine (q2(i)) and cosine (q1(i)) of the material multiplied against the stresses. The a matrix is defined as follows:

$$\begin{bmatrix}a_{11}\\ a_{12}\\ a_{21}\\ a_{22}\end{bmatrix}=\begin{bmatrix}\cos\theta & 0 & -\sin\theta\\ \sin\theta & 0 & \cos\theta\\ 0 & -\sin\theta & \cos\theta\\ 0 & \cos\theta & \sin\theta\end{bmatrix}\begin{bmatrix}\mathrm{sig1}\\ \mathrm{sig2}\\ \mathrm{sig4}\end{bmatrix} \tag{A-9}$$

```
  stg5(i)=sig5(i)
  stg6(i)=sig6(i)
  a11(i) =q1(i)*sig1(i)-q2(i)*sig4(i)
  a12(i) =q2(i)*sig1(i)+q1(i)*sig4(i)
  a21(i) =q1(i)*sig4(i)-q2(i)*sig2(i)
  a22(i) =q2(i)*sig4(i)+q1(i)*sig2(i)
```

The a matrix is then multiplied against more sine and cosine terms to achieve the desired transformation. For the stress variables, the transformed local stress vector takes the place of the original global stress vector sig1(i)–sig6(i):

$$\begin{bmatrix}\mathrm{sig1}\\ \mathrm{sig2}\\ \mathrm{sig4}\\ \mathrm{sig5}\\ \mathrm{sig6}\end{bmatrix}=\begin{bmatrix}\cos^2\theta & \sin^2\theta & -2\cos\theta\sin\theta & 0 & 0\\ \sin^2\theta & \cos^2\theta & 2\cos\theta\sin\theta & 0 & 0\\ \cos\theta\sin\theta & -\cos\theta\sin\theta & \cos^2\theta-\sin^2\theta & 0 & 0\\ 0 & 0 & 0 & \cos\theta & \sin\theta\\ 0 & 0 & 0 & -\sin\theta & \cos\theta\end{bmatrix}\begin{bmatrix}\mathrm{sig1}\\ \mathrm{sig2}\\ \mathrm{sig4}\\ \mathrm{sig5}\\ \mathrm{sig6}\end{bmatrix} \tag{A-10}$$

```
  sig1(i)=q1(i)*a11(i)-q2(i)*a21(i)
  sig2(i)=q2(i)*a12(i)+q1(i)*a22(i)
  sig4(i)=q1(i)*a12(i)-q2(i)*a22(i)
  sig5(i)=q2(i)*stg6(i)+q1(i)*stg5(i)
  sig6(i)=q1(i)*stg6(i)-q2(i)*stg5(i)
20 continue
```

Next, the global strains are updated, the strain and strain increments are transformed from the global system to the material system, and the effective plastic strain is computed in the do loop numbered 30 (lines 068–093). First, the strains are updated by summing the strain plus the new strain increment. Note that the shear strain increment (e4(i)) is multiplied by 0.5 to resolve the difference between engineering and tensor strains:

```
068   do 30 i=lft,llt
069   d4(i) =.5*e4(i)
070   eps1(i)=eps1(i)+e1(i)
071   eps2(i)=eps2(i)+e2(i)
072   eps4(i)=eps4(i)+d4(i)
```

Then the strain increment transformation occurs in two steps in the same fashion as the stress transformation. First, the intermediary matrix a is redefined for the strain increment transformation:

$$\begin{bmatrix} a_{11} \\ a_{12} \\ a_{21} \\ a_{22} \end{bmatrix} = \begin{bmatrix} \cos\theta & 0 & -\sin\theta \\ \sin\theta & 0 & \cos\theta \\ 0 & -\sin\theta & \cos\theta \\ 0 & \cos\theta & \sin\theta \end{bmatrix} \begin{bmatrix} \mathrm{e1} \\ \mathrm{e2} \\ \mathrm{d4} \end{bmatrix} \tag{A-11}$$

```
073   a11(i) =q1(i)*e1(i)-q2(i)*d4(i)
074   a12(i) =q2(i)*e1(i)+q1(i)*d4(i)
075   a21(i) =q1(i)*d4(i)-q2(i)*e2(i)
076   a22(i) =q2(i)*d4(i)+q1(i)*e2(i)
```

The a matrix is then multiplied against more sine and cosine terms to achieve the desired transformation. The transformed local strain vector d1(i)–d6(i) is given a separate vector from the original global strain increment vector e1(i)–e6(i):

$$\begin{bmatrix} \mathrm{d1} \\ \mathrm{d2} \\ \mathrm{d4} \\ \mathrm{d5} \\ \mathrm{d6} \end{bmatrix} = \begin{bmatrix} \cos^2\theta & \sin^2\theta & -2\cos\theta\sin\theta & 0 & 0 \\ \sin^2\theta & \cos^2\theta & 2\cos\theta\sin\theta & 0 & 0 \\ 2\cos\theta\sin\theta & -2\cos\theta\sin\theta & 2(\cos^2\theta - \sin^2\theta) & 0 & 0 \\ 0 & 0 & 0 & \cos\theta & \sin\theta \\ 0 & 0 & 0 & -\sin\theta & \cos\theta \end{bmatrix} \begin{bmatrix} \mathrm{e1} \\ \mathrm{e2} \\ \mathrm{d4} \\ \mathrm{e5} \\ \mathrm{e6} \end{bmatrix} \tag{A-12}$$

```
077   d1(i) =q1(i)*a11(i)-q2(i)*a21(i)
078   d2(i) =q2(i)*a12(i)+q1(i)*a22(i)
079   d4(i) =2.*(q1(i)*a12(i)-q2(i)*a22(i))
080   d5(i) =q2(i)*e6(i)+q1(i)*e5(i)
081   d6(i) =q1(i)*e6(i)-q2(i)*e5(i)
```

This is followed by the total strain transformation and the intermediary matrix a is redefined for the total strain transformation:

$$\begin{bmatrix} a_{11} \\ a_{12} \\ a_{21} \\ a_{22} \end{bmatrix} = \begin{bmatrix} \cos\theta & 0 & -\sin\theta \\ \sin\theta & 0 & \cos\theta \\ 0 & -\sin\theta & \cos\theta \\ 0 & \cos\theta & \sin\theta \end{bmatrix} \begin{bmatrix} \mathrm{eps1} \\ \mathrm{eps2} \\ \mathrm{eps4} \end{bmatrix} \tag{A-13}$$

```
082   a11(i) =q1(i)*eps1(i)-q2(i)*eps4(i)
083   a21(i) =q1(i)*eps4(i)-q2(i)*eps2(i)
084   a12(i) =q2(i)*eps1(i)+q1(i)*eps4(i)
085   a22(i) =q2(i)*eps4(i)+q1(i)*eps2(i)
```

The a matrix is then multiplied against more sine and cosine terms to achieve the desired transformation. The transformed total strain vector strn1(i)-strn4(i) is given a separate vector from the original global total strain vector eps1(i)-eps4(i):

$$\begin{bmatrix} \mathrm{strn1} \\ \mathrm{strn2} \\ \mathrm{strn4} \end{bmatrix} = \begin{bmatrix} \cos^2\theta & \sin^2\theta & -2\cos\theta\sin\theta \\ \sin^2\theta & \cos^2\theta & 2\cos\theta\sin\theta \\ \cos\theta\sin\theta & -\cos\theta\sin\theta & \cos^2\theta - \sin^2\theta \end{bmatrix} \begin{bmatrix} \mathrm{eps1} \\ \mathrm{eps2} \\ \mathrm{eps4} \end{bmatrix} \tag{A-14}$$

```
086   strn1(i)=q1(i)*a11(i) -q2(i)*a21(i)
087   strn2(i)=q2(i)*a12(i)+q1(i)*a22(i)
088   strn4(i)=q1(i)*a12(i)-q2(i)*a22(i)
```

Finally, the effective plastic strain is calculated using the global strains, as given by:

$$effstn = \sqrt{(eps1 + eps2)^2 + \frac{1}{3}(eps1 - eps2)^2 + \frac{3}{4}eps4^2} \tag{A-15}$$

```
089   sa=0.5*(eps1(i)+eps2(i))
090   sb=0.5*(eps1(i)-eps2(i))
091   scc=  sb**2+eps4(i)**2
092   effstn(i)=1.1547*sqrt(3.0*sa**2+scc)
093 30 continue
```

Next, the compliance matrix is calculated so that the trial stresses for failure determination can be calculated. The compliance matrix is determined in the do loop numbered 40 (lines 094–107) and uses several of the user-defined constitutive parameters. The variables em(i), ef(i), and ed(i) are failure flags that assume a value of 0 if the ply has failed in matrix tension, fiber tension, and r matrix compression modes, respectively. These get grouped into the failure flag eh(i), which is then multiplied into the compliance matrix to reduce the constitutive properties (and thereby stiffness) of failed elements to zero. The shear modulus gxy(i) is assured a nonzero value by adding an infinitesimally small non-zero value 1E-17.

```
094   do 40 i=lft,llt
095   eg(i) =em(i)*ef(i)
096   eh(i) =eg(i)*ed(i)
097   ex(i) =ymx
098   ey(i) =ymy
099   prx(i)=eh(i)*nux
100   pry(i)=eh(i)*nuy
101   gxy(i)=1.e-17+sxy
102   pxy(i)=1.0/(1.-prx(i)*pry(i))
```

Following the initialization of all of the necessary parameters, the compliance matrix is calculated as follows:

$$\boldsymbol{C} = \begin{bmatrix} \frac{E_1}{1-eh\cdot v_{12}v_{21}} & \frac{eh\cdot E_2 v_{12}}{1-eh\cdot v_{12}v_{21}} & 0 \\ \frac{eh\cdot E_2 v_{12}}{1-eh\cdot v_{12}v_{21}} & \frac{E_2}{1-eh\cdot v_{12}v_{21}} & 0 \\ 0 & 0 & \frac{G_{12}}{1+G_{12}\alpha\sigma_{12}^2} \end{bmatrix} \tag{A-16}$$

```
103   c11(i)=pxy(i)*ex(i)
104   c12(i)=pxy(i)*prx(i)*ey(i)
105   c22(i)=pxy(i)*ey(i)
106   c44(i)=gxy(i)/(1.+gxy(i)*ap3*sig4(i)*sig4(i))
107 40 continue
```

Next, the trial stresses are calculated in an unnumbered do loop (lines 108–114) so that failure determination can be made. The trial stresses are calculated by taking the sum of the stress from the previous cycle (sig1(i)–sig4(i)) and the product of the strain increment (d1(i)–d4(i)) with the compliance matrix (c11(i)–c44(i)) as follows:

$$\vec{\sigma}_n = \vec{\sigma}_{n-1} + \boldsymbol{C}\overrightarrow{d\varepsilon} \tag{A-17}$$

```
108   do i=lft,llt
109   stg1(i)=sig1(i)+c11(i)*d1(i)+c12(i)*d2(i)
110   stg2(i)=sig2(i)+c12(i)*d1(i)+c22(i)*d2(i)
111   stg4(i)=sig4(i)+c44(i)*d4(i)
```

Further operations are performed on the shear stress, which are of use during the failure criteria calculations. After these operations, the non-linear fiber-matrix shearing term that augments each damage mode is calculated, as defined in the LS-DYNA Theory Manual (see Material Model 22). This term, sg44(i), is simply a non-linear shear stress term divided by its equivalent nonlinear shear strength term:

$$\mathrm{sg44} = \frac{\frac{{\tau_{12}}^2}{2G_{12}}+\frac{3}{4}\alpha{\tau_{12}}^4}{\frac{SC^2}{2G_{12}}+\frac{3}{4}\alpha SC^4} \tag{A-18}$$

```
112   sg42(i)=stg4(i)*stg4(i)
113   sg44(i)=mlt1*sg42(i)*(od2g+ap34*sg42(i))*qq2(i)
114   enddo
```

Next, the four failure criteria are calculated and failure flags are defined in the do loop numbered 50 (lines 115–142). Failure modes are determined by considering the sign of the one- and two-direction local stresses, stg1(i) and stg2(i), respectively. For each mode, the criterion is calculated and saved to a variable. It is then checked to see if its value exceeds 0, which is an indication of failure. Most of the terms used in the failure criteria calculations have already been calculated earlier in the code.

First, the tensile fiber mode uses the variable ef2(i) and calculates the criterion when the one-direction stress is greater than zero (tension). For the case of ec2(i), the compressive fiber variable is assigned a value of -1 because the element cannot fail in this mode while undergoing tensile stresses. Some earlier calculations are useful to recall when interpreting the fiber failure criteria:

- $\mathrm{qq2} = \begin{cases} \left(\frac{1}{SOFT^2}\right), & crush\ front\ element \\ 1.0, & all\ other\ elements \end{cases}$
- $\mathrm{xt2fbrt} = \frac{1}{XT^2 \cdot FBRT^2}$
- $\mathrm{xt2} = \frac{1}{XT^2}$
- $\mathrm{ed} = \begin{cases} 1.0, & no\ matrix\ failure \\ 0, & matrix\ failure \end{cases}$
- $\mathrm{xc2} = \frac{1}{XC^2}$ where $\mathrm{XC} = \begin{cases} XC, & no\ matrix\ failure \\ YC * YCFAC, & matrix\ failure \end{cases}$

```
115   do 50 i=lft,llt
116   if (stg1(i).gt.0.) then
117    ef2(i)=qq2(i)*(xt2fbrt+(xt2-xt2fbrt)*ed(i))*
118  .     max(0.0,stg1(i))**2+beta*sg44(i)-1.0
119    ec2(i)=-1.
```

Thus, the fiber tension failure criterion becomes:

$$\mathrm{ef2} = \begin{bmatrix} \left(\frac{1}{SOFT^2}\right) \\ or \\ 1.0 \end{bmatrix} * \begin{bmatrix} \left(\frac{1}{FBRT^2}\right) \\ or \\ 1.0 \end{bmatrix} * \left(\frac{\sigma_{11}}{XT}\right)^2 + \beta * \left(\frac{\frac{\tau_{12}{}^2}{2G_{12}} + \frac{3}{4}\alpha\tau_{12}{}^4}{\frac{SC^2}{2G_{12}} + \frac{3}{4}\alpha SC^4}\right) * \begin{bmatrix} \left(\frac{1}{SOFT^2}\right) \\ or \\ 1.0 \end{bmatrix} - 1 \qquad \text{(A-19)}$$

The compressive fiber mode is calculated if the circumstance of the previous IF statement for a positive one-direction stress is false, as indicated by the else statement. This mode uses the variable ec2(i) and the tensile fiber variable ef2(i) is assigned a value of -1. The compressive fiber failure criterion becomes:

$$\mathrm{ec2} = \begin{bmatrix} \left(\frac{1}{SOFT^2}\right) \\ or \\ 1.0 \end{bmatrix} * \begin{bmatrix} \left(\frac{1}{XC^2}\right) \\ or \\ \left(\frac{1}{YC*YCFAC^2}\right) \end{bmatrix} * \sigma_{11}{}^2 - 1 \qquad \text{(A-20)}$$

```
else
 ef2(i)=-1.
 xc2(i) = ed(i)*xc + (1.0-ed(i))*ycfac*yc
 xc2(i) = 1/(xc2(i)*xc2(i))
 ec2(i)= qq2(i)*xc2(i)* min(0.0,stg1(i))**2-1.0
endif
```

Next, the tensile matrix mode is calculated using the variable em2(i) for the case that the two-direction stress is greater than zero. For this case ed2(i), the compressive matrix variable is assigned a value of -1 because the element cannot fail in this mode while undergoing tensile stresses. Some earlier calculations are useful to recall when interpreting the matrix failure criteria:

- $\mathrm{yt2} = \frac{1}{YT^2}$
- $\mathrm{sd2} = \frac{1}{4SC^2}$
- $\mathrm{mlt2} = \frac{1}{YC}\left(\frac{YC^2}{4SC^2} - 1\right)$
- $\mathrm{qq1} = \begin{cases} SOFT, & crashfront\ element \\ 1.0, & all\ other\ elements \end{cases}$

```
if (stg2(i).gt.0.) then
 em2(i)=qq2(i)*yt2* max(0.0,stg2(i))**2+sg44(i)-1.0
 ed2(i)=-1.
```

Thus, the matrix tension failure criterion becomes:

$$\mathrm{em2} = \begin{bmatrix} \left(\frac{1}{SOFT^2}\right) \\ or \\ 1.0 \end{bmatrix} * \left(\frac{\sigma_{11}}{YT}\right)^2 + \left(\frac{\frac{\tau_{12}{}^2}{2G_{12}} + \frac{3}{4}\alpha\tau_{12}{}^4}{\frac{SC^2}{2G_{12}} + \frac{3}{4}\alpha SC^4}\right) * \begin{bmatrix} \left(\frac{1}{SOFT^2}\right) \\ or \\ 1.0 \end{bmatrix} - 1 \qquad \text{(A-21)}$$

The compressive matrix mode is calculated if the circumstance of the previous IF statement for a positive two-direction stress is false, as indicated by the else statement. This mode uses the variable ed2(i) and the tensile matrix variable em2(i) is assigned a value of -1. The compressive matrix failure criterion becomes:

$$\text{ed2} = \begin{bmatrix} \left(\frac{1}{SOFT^2}\right) \\ or \\ 1.0 \end{bmatrix} * \frac{{\sigma_{22}}^2}{4SC^2} + \begin{bmatrix} SOFT \\ or \\ 1.0 \end{bmatrix} * \frac{\sigma_{22}}{YC}\left(\frac{YC^2}{4SC^2} - 1\right) + \left(\frac{\frac{{\tau_{12}}^2}{2G_{12}}+\frac{3}{4}\alpha{\tau_{12}}^4}{\frac{SC^2}{2G_{12}}+\frac{3}{4}\alpha SC^4}\right) * \begin{bmatrix} \left(\frac{1}{SOFT^2}\right) \\ or \\ 1.0 \end{bmatrix} - 1 \qquad \text{(A-22)}$$

```
129   else
130    em2(i)=-1.
131    ed2(i)=qq2(i)*sd2* min(0.0,stg2(i))**2+
132  1    mlt2*stg2(i)/qq1(i)+sg44(i)-1.0
133   endif
```

Flags for each failure mode are assigned, followed by history variable assignment. The history variables, ef(i), ec(i), em(i), and ed(i) are used during the calculation of the compliance matrix to reduce constitutive properties to zero following failure. The Fortran sign command used to determine the history variable values takes the magnitude of the first argument, and the sign of the second argument to produce a number. In this way, when failure is present and the ef2(i), ec2(i), em2(i), or ed2(i) value is greater than zero, the history variables take on a value of 0. Otherwise, when there is no failure, the history variables take on a value of 1.

```
134   if(ed2(i).gt.0.) iflagd=1
135   if(em2(i).gt.0.) iflagm=1
136   if(ef2(i).gt.0.) iflagf=1
137   if(ec2(i).gt.0.) iflagc=1
138   ef(i) =ef(i)*(.5-sign(.5,ef2(i)))
139   ec(i) =ec(i)*(.5-sign(.5,ec2(i)))
140   em(i) =em(i)*(.5-sign(.5,em2(i)))
141   ed(i) =ed(i)*(.5-sign(.5,ed2(i)))
142 50 continue
```

Plies are marked for deletion using the efail(i) variable, which is given a value of 0 to indicate deletion. This occurs because of maximum strain violations in the do loop numbered 55 (lines 144–169). First, the code addresses the case in which maximum strain parameters are not defined by setting DFAILM and DFAILS to numerically infinite values (earlier in the code), initializing the parameter efmin to a zero or near-zero value, and beginning the do loop with an IF statement checking if DFAILT is nonzero, and initializing efail(i) to a value of 1:

```
143   efmin=(.5+sign(.5,fbrt-1.e-15))*1.0e-05
144   do 55 i=lft,llt
145   if(dfail1t.gt.0.0) then
146    efail(i)=1.0
```

For the case in which maximum strain parameters are defined, the local strain components strn(i), strn2(i), and strn4(i) are compared against the corresponding maximum strain parameter values and, if violated, efail(i) is set to zero, indicating ply deletion:

```
   if (dfail1t-strn1(i).lt.0.) then
     efail(i)=0.0
   endif
   if (strn1(i)-dfail1c.lt.0.) then
     efail(i)=0.0
   endif
   if (dfail1m-strn2(i).lt.0.) then
     efail(i)=0.0
   endif
   if (strn2(i)+dfail1m.lt.0.) then
     efail(i)=0.0
   endif
   if (dfail1s-abs(strn4(i)).lt.0.) then
     efail(i)=0.0
   endif
```

For the case in which maximum strain parameters are not defined, efail(i) is degraded following fiber tensile failure, at which point the history variable ef(i) changes from a value of 1 to 0. In each time-step following fiber tensile failure, 0.01 is subtracted from efail(i), and after 100 time-steps, efail(i) is 0, which marks the ply for deletion. To avoid a negative value of efail(i), the efmin constant acts as a limiting maximum:

```
  else
   efail(i)=efail(i)-.01*(1.-ef(i))
   efail(i)= max(efmin,efail(i))
  endif
```

Ply deletion can also occur from violating the effective failure strain parameter, erodefl (EFS in the MAT54 user input deck):

```
  if (effstn(i).gt.erodefl) then
  efail(i)=0.0
  endif
```

The variable fail(i) is a secondary parameter, which keeps track of deletion, and is determined from the value of efail(i). The initialized value of fail(i) is zero, so given that efail(i) is not given a zero value, fail(i) will take a value of 1.

```
  fail(i) = max(fail(i),(.5+sign(.5,efail(i)-.01)))
55 continue
```

The compliance matrix is calculated again, taking any new failures into account. First, constitutive properties are redefined by using the newly defined history variables in an unnumbered do loop (lines 171–181):

```
171   do i=lft,llt
172   eg(i) =em(i)*ef(i)
173   eh(i) =eg(i)*ed(i)
174   ex(i) =ymx
175   ey(i) =ymy
176   prx(i)=eh(i)*nux
177   pry(i)=eh(i)*nuy
178   gxy(i)=sxy
179   pxy(i)=1.0/(1.-prx(i)*pry(i))
180   c12(i)=eh(i)*pxy(i)*prx(i)*ey(i)
181   enddo
```

The compliance matrix is then calculated within the do loop numbered 60 (lines 182–203) while taking into consideration the sign of the products of local stresses (stg1(i), stg2(i), and stg4(i)) and strain increments (d1(i), d2(i), and d4(i)). The resulting compliance matrix is:

$$\boldsymbol{C} = \begin{bmatrix} \frac{E_1 \cdot ef \cdot ec}{1 - eh \cdot v_{12} v_{21}} & \frac{eh \cdot E_2 v_{12}}{1 - eh \cdot v_{12} v_{21}} & 0 \\ \frac{eh \cdot E_2 v_{12}}{1 - eh \cdot v_{12} v_{21}} & \frac{E_2 \cdot em \cdot ed}{1 - eh \cdot v_{12} v_{21}} & 0 \\ 0 & 0 & \frac{G_{12} \cdot em \cdot ed}{1 + G_{12} \alpha \sigma_{12}^2} \end{bmatrix} \tag{A-23}$$

```
182       do 60 i=lft,llt
183       if( stg1(i)*d1(i).gt.0.) then
184        c11(i)=(.5-sign(.5,ec2(i)))*
185      1    (.5-sign(.5,ef2(i)))*pxy(i)*ex(i)
186       else
187        c11(i)=pxy(i)*ex(i)
188       endif
189       if( stg2(i)*d2(i).gt.0.) then
190        c22(i)=(.5-sign(.5,em2(i)))*
191      1    (.5-sign(.5,ed2(i)))*
192      2    (.5+sign(.5,efail(i)))*pxy(i)*ey(i)
193       else
194        c22(i)=pxy(i)*ey(i)
195       endif
196       if( stg4(i)*d4(i).gt.0.) then
197        c44(i)=(.5-sign(.5,em2(i)))*
198      1    (.5-sign(.5,ed2(i)))/
199      2    (1.0/gxy(i)+0.0*sig4(i)*sig4(i))
200       else
201        c44(i)=1.0/(1.0/gxy(i)+0.0*sig4(i)*sig4(i))
202       endif
203    60 continue
```

If a minimum time-step limit (tsize, called TFAIL in the keyword input file) is defined by the user, elements whose time-steps violate this limit are marked for deletion in the do loops numbered 70–72 (lines 205–214). First, the time-step of the element, dt(i) is determined based on the material density, mesh size, and speed of sound parameters calculated in the main LS-DYNA code.

```
204       if(tsize.ne.0.0) then
205        do 70 i=lft,llt
206         dt(i)=sarea(i)/(sqrt(diagm(i))*cx)
207    70 continue
```

The value of dtfail(i), which will be used to determine time-step violation, is determined based on the user input TFAIL (tsize). The TFAIL input parameter can be used in two different ways, depending on its magnitude, as specified in the LS-DYNA User's Manual [91]:

$$TFAIL = \begin{cases} \leq 0 & \text{No element deletion by } TFAIL. \\ 0 < TFAIL \leq 0.1 & \text{Element is deleted when its time-step is smaller than the given value.} \\ > 0.1 & \begin{array}{c}\text{Element is deleted when the quotient of the time-step} \\ \text{and the original time-step drops below the given value.}\end{array} \end{cases}$$

Given this definition of TFAIL, an IF statement divides the definition of dtfail(i) according to whether tsize is greater than 0.1:

```
   if(ncycle.eq.0) then
   if(tsize.gt.0.1) then
    do 71 i=lft,llt
71   dtfail(i)=dt(i)*tsize
   else
    do 72 i=lft,llt
72   dtfail(i)=tsize
   endif
   endif
```

Elements are marked for deletion if their time-step is less than dtfail(i) by setting efail(i) to 0, along with all of the stresses. Note that the fail(i) parameter is an additional failure parameter, which was given a value according to the value of efail(i) following the strain-based ply deletions.

```
   do 75 i=lft,llt
    if( dt(i).lt.dtfail(i) .or. fail(i).lt.0.1 ) then
     sig1(i)=0.0
     sig2(i)=0.0
     sig3(i)=0.0
     sig4(i)=0.0
     sig5(i)=0.0
     sig6(i)=0.0
     efail(i)=0.0
    endif
```

Elements deletion occurs using a separate subroutine, chklay. The parameter “nplane” is the number of integration points in the plane of the element (nodes), and the following IF statement ensures that the element is a fully integrated shell element with four nodes. If efail(i) of the element is less than zero, the chklay subroutine is run and deletes the element.

```
     if (nplane.eq.4) then
      if (efail(i).lt.0.01) then
      call chklay(faillay(i,id_plane),ipt_thk,isnyf)
      endif
    endif
75 continue
```

After deletion is established, the new crush front elements are identified. This operation is only done once per element, so first an IF statement is put in place to check if the integration point number ipt is equal to the number of integration points, nip, which occur only four times per element because there are four integration points in the plane (nodes). Then, the counter jf and the increment jinc are used only to apply the do loop numbered 74 (lines 235–249) one time per element as it cycles through all of the integration points . The do loop first checks for element deletion:

```
233    if (ipt.eq.nip) then
234     jinc =4
235     do 74 i=lft,llt
236      if((dt(i).lt.dtfail(i) .or. fail(i).lt.0.1)) then
```

Recall that the ncrshf parameter identifies a node as being at the crush front by assuming a value of 1. If the deleted element was not at the crush front (i.e., the sum of all of its node ncrshf values is not 4), the jf counter adds 4 to move to the next element:

```
237       if (ncrshf(ix1(i)+numnp)+ncrshf(ix2(i)+numnp)+
238  .     ncrshf(ix3(i)+numnp)+ncrshf(ix4(i)+numnp).ne.4)then
239        jf =jf+jinc
240       endif
```

Otherwise, if the deleted element was at the crush front, then the new crush front elements are established by moving onto the next element:

```
241       ncrshf(ix1(i)+numnp)=1
242       ncrshf(ix2(i)+numnp)=1
243       ncrshf(ix3(i)+numnp)=1
244       ncrshf(ix4(i)+numnp)=1
245      endif
246 74   continue
247    endif
248   endif
```

The last task in the material model is to update the stresses and transform them back to the element system. The strains are not transformed back because the transformed strain and strain increment values occupied their own vectors and did not overwrite the global coordinate system strain and strain increments. These operations are performed in the do loop numbered 80 (lines 249–269). First, the local stresses are updated by summing the old stresses (sig1(i)–sig6(i)) with the new stress increment, as calculated using the strain increments (d1(i)–d4(i)) and compliance matrix (c11(i)–c44(i)), as follows:

$$\begin{bmatrix} \sigma_1 \\ \sigma_2 \\ \sigma_3 \\ \sigma_4 \\ \sigma_5 \\ \sigma_6 \end{bmatrix}_n = \begin{bmatrix} \sigma_1 \\ \sigma_2 \\ 0 \\ \sigma_4 \\ \sigma_5 \\ \sigma_6 \end{bmatrix}_{n-1} + \begin{bmatrix} c_{11} & c_{12} & 0 & 0 & 0 \\ c_{12} & c_{22} & 0 & 0 & 0 \\ 0 & 0 & 0 & 0 & 0 \\ 0 & 0 & 0 & c_{44} & 0 \\ 0 & 0 & 0 & 0 & 0 \\ 0 & 0 & 0 & 0 & 0 \end{bmatrix} \begin{bmatrix} d_1 \\ d_2 \\ 0 \\ d_4 \\ 0 \\ 0 \end{bmatrix}$$

$$\vec{\sigma}_n = \vec{\sigma}_{n-1} + \boldsymbol{C}\Delta\vec{\varepsilon} \tag{A-24}$$

```
249   do 80 i=lft,llt
250   sig1(i)=sig1(i)+c11(i)*d1(i)+c12(i)*d2(i)
251   sig2(i)=sig2(i)+c12(i)*d1(i)+c22(i)*d2(i)
252   sig3(i)=0.0
253   sig4(i)=sig4(i)+c44(i)*d4(i)
254   stg5(i)=sig5(i)
255   stg6(i)=sig6(i)
```

The stress transformation back to the global system occurs in two steps in the same fashion as the first transformations occurred. First, the intermediary matrix a is redefined:

$$\begin{bmatrix} a_{11} \\ a_{12} \\ a_{21} \\ a_{22} \end{bmatrix} = \begin{bmatrix} cos\theta & 0 & sin\theta \\ -sin\theta & 0 & cos\theta \\ 0 & sin\theta & cos\theta \\ 0 & cos\theta & -sin\theta \end{bmatrix} \begin{bmatrix} \text{sig1} \\ \text{sig2} \\ \text{sig4} \end{bmatrix} \tag{A-25}$$

```
256   a11(i) = sig1(i)*q1(i)+sig4(i)*q2(i)
257   a12(i) =-sig1(i)*q2(i)+sig4(i)*q1(i)
258   a21(i) = sig4(i)*q1(i)+sig2(i)*q2(i)
259   a22(i) =-sig4(i)*q2(i)+sig2(i)*q1(i)
```

An extra measure is taken to ensure that the stresses of deleted elements are zero by making the q1(i) and q2(i) values zero if deletion has occurred. Otherwise, the qq1(i) and qq2(i) variables take on the cosine and sine of the ply angle, as before:

```
  qq1(i)=efail(i)*q1(i)
  qq2(i)=efail(i)*q2(i)
```

Finally, the transformation of stresses back to the global system is completed by multiplying the a matrix by another set of sines and cosines, resulting in the complete transformation matrix:

$$\begin{bmatrix} \mathrm{sig1} \\ \mathrm{sig2} \\ \mathrm{sig4} \\ \mathrm{sig5} \\ \mathrm{sig6} \end{bmatrix} = \begin{bmatrix} cos^2\theta & sin^2\theta & 2cos\theta sin\theta & 0 & 0 \\ sin^2\theta & cos^2\theta & -2cos\theta sin\theta & 0 & 0 \\ -cos\theta sin\theta & cos\theta sin\theta & cos^2\theta - sin^2\theta & 0 & 0 \\ 0 & 0 & 0 & cos\theta & -sin\theta \\ 0 & 0 & 0 & sin\theta & cos\theta \end{bmatrix} \begin{bmatrix} \mathrm{sig1} \\ \mathrm{sig2} \\ \mathrm{sig4} \\ \mathrm{sig5} \\ \mathrm{sig6} \end{bmatrix} \tag{A-26}$$

```
  sig1(i)= qq1(i)*a11(i)+qq2(i)*a21(i)
  sig2(i)=-qq2(i)*a12(i)+qq1(i)*a22(i)
  sig4(i)= qq1(i)*a12(i)+qq2(i)*a22(i)
  sig5(i)=-qq2(i)*stg6(i)+qq1(i)*stg5(i)
  sig6(i)= qq1(i)*stg6(i)+qq2(i)*stg5(i)
```

The new strain energy of the plies are calculated using the components of stress and strain in the global coordinate system, and the material model code is completed and returns to the main LS-DYNA code:

```
  einc(i)=e1(i)*sig1(i)+e2(i)*sig2(i)+e4(i)*sig4(i)+
 1    e5(i)*sig5(i)+e6(i)*sig6(i)+einc(i)
80 continue
  return
  end
```

A.3. MODIFICATIONS MADE TO SOURCE CODE

A.3.1 ELASTIC RESPONSE

MAT54 does not allow for the definition of the compressive modulus in the axial and transverse directions, or the compressive strain-to-failure value in the transverse direction. These three material properties are added to the modified model as new user input parameters, and the material model code is changed so the appropriate property is used based on the stress state of the element.

New user input parameters are added by including the following lines of code during the variable declarations at the beginning of the code:

```
ymxc =cm(mx+37)
ymyc =cm(mx+38)
dfail2m =cm(mx+39)
```

Note that the locations of these three parameters in the cm vector correspond to a new line of the keyword input file, as shown in figure A-4. Initial attempts at adding the new user input parameter DFAIL2M used the unused cm vector locations (mx+3), (mx+5), and (mx+6) as well as a hard-coded value in the subroutine. Each case produced different results in the baseline sinusoid crush simulation, in one case completely destabilizing the model and causing global buckling, as shown by the load-displacement curve behavior in figure A-5. It is speculated that these cm vector locations, although inactive in MAT54, may be referenced elsewhere in the LS-DYNA code. Results using the hard-coded DFAIL2M value on the baseline sinusoid crush were the same as when the "cm" vector locations after (mx+37) were used, thereby verifying that these locations are valid to use for new parameters.

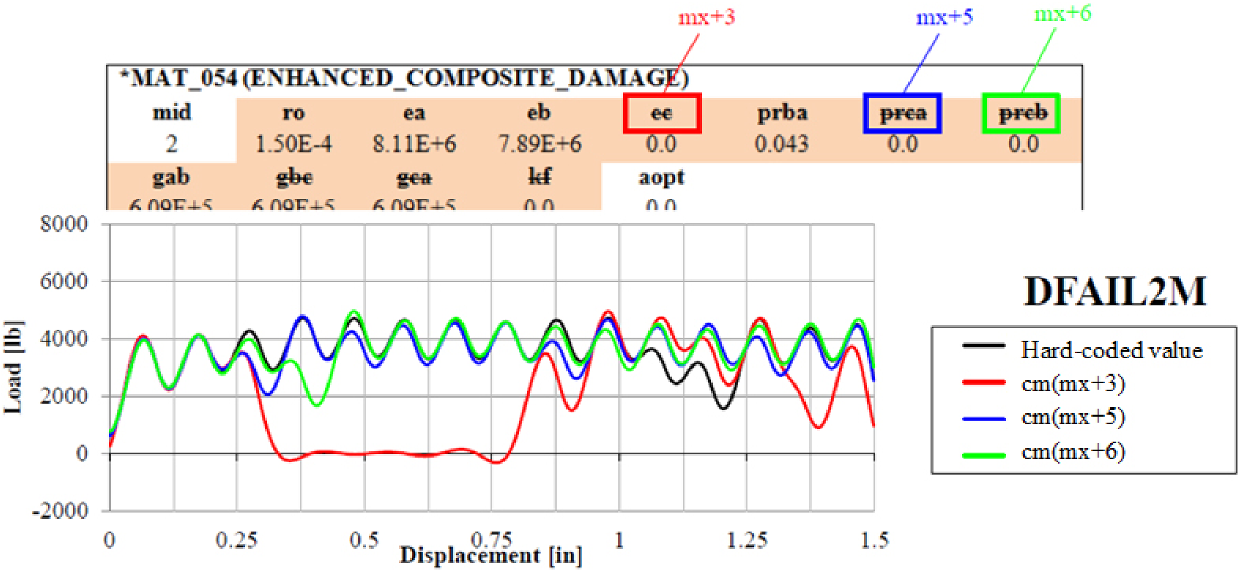

*MAT_054 (ENHANCED_COMPOSITE_DAMAGE)

mid	ro	ea	eb	~~ee~~	prba	~~prea~~	~~preb~~
2	1.50E-4	8.11E+6	7.89E+6	0.0	0.043	0.0	0.0
gab	~~gbe~~	~~gea~~	~~kf~~	aopt			
6.09E+5	6.09E+5	6.09E+5	0.0	0.0			

Figure A-5. Baseline sinusoid crush simulation results from using different "cm" vector locations for the DFAIL2M parameter in the modified material model

The code that implements the new compressive moduli replaces code during the two computations of the compliance matrix, both before and after failure is determined. For these computations in the original code, the axial and transverse moduli are defined in lines 097–098 and 174–175. These lines are replaced by an IF statement that determines the value of ex(i) and ey(i) for the compliance matrix calculations based on the sign of the stresses as follows:

```
if (sig1(i).gt.0.) then
 ex(i) =ymx
else
 ex(i)=ymxc
endif
if (sig2(i).gt.0.) then
 ey(i) =ymy
else
 ey(i)=ymyc
endif
```

In a similar fashion, the new compressive strain-to-failure parameter in the transverse direction is implemented during the determination of element deletion in the transverse compression case (lines 156–158). The original dfail1m parameter is replaced with the new DFAIL2M parameter as follows:

```
if (strn2(i)+dfail2m.lt.0.) then
  efail(i)=0.0
endif
```

With these simple changes, the elastic definition of MAT54 is modified.

A-3.2 FAILURE DETERMINATION

Three new sets of failure criteria are added as options to use in the modified MAT54 model: a set of criteria meant for fabric materials, a maximum crush stress criterion for crush front elements, and a strain-energy-based criterion.

A-3.2.1 Fabric Failure Criteria

The MAT54 code is modified to implement the fabric failure criteria by removing the matrix damage terms FBRT and YCFAC, which appear in the fiber failure modes (lines 116–125), and changing the matrix failure modes to those prescribed by equation 19. The code for the axial failure criteria of the fabric, which replaces lines 116–125, is as follows:

```
do 50 i=lft,llt
if (stg1(i).gt.0.) then
 ef2(i)=qq2(i)*xt2* max(0.0,stg1(i))**2+beta*sg44(i)-1.0
 ec2(i)=-1.
else
 ef2(i)=-1.
 xc2(i)= 1/(xc*xc)
 ec2(i)= qq2(i)*xc2(i)* min(0.0,stg1(i))**2-1.0
endif
```

The new code for the transverse failure criteria of the fabric, which replaces lines 126–133, is as follows:

```
if (stg2(i).gt.0.) then
 em2(i)=qq2(i)*yt2* max(0.0,stg2(i))**2+beta*sg44(i)-1.0
 ed2(i)=-1.
else
 em2(i)=-1.
 yc2(i)= 1/(yc*yc)
 ed2(i)= qq2(i)*yc2(i)* min(0.0,stg2(i))**2-1.0
endif
```

A.3.2.2 Crush Stress Criterion

To implement the crush stress criterion, a new user input parameter for the crush stress, SIGCR, is introduced in the (mx+47) position of the user input vector as follows:

```
sigcr =cm(mx+47)
```

This cm vector location corresponds to the fifth location on the seventh card of the MAT54 keyword file input deck (see figure A-4).

The code for the crush stress failure criterion is inserted following the Hashin failure criteria. First, an IF statement determines if the element is at the crush front by using the qq1 variable. Recall that this variable equals 1.0 unless the element is at the crush front (equation 40). If the element is at the crush front, then the maximum crush stress criterion is implemented as follows:

```
if (qq1(i).ne.1.0) then
   ecr(i)=stg1(i)/sigcr
else
   ecr(i)=0.0
endif
```

If the element is not at the crush front, then the failure flag ecr is given a zero value. When this failure flag achieves a value greater than or equal to 1.0, the crush stress failure criterion is violated, and the efail variable takes on a zero value to indicate deletion as follows:

```
if (ecr(i).eq.1.0 .or. ecr(i).gt.1.0 ) then
   efail=0.0
endif
```

A.3.2.3 Wolfe Strain Energy Criterion

Wolfe’s failure criterion utilizes axial, transverse, and shear strain energy components measured from coupon-level material testing to determine material failure in equation A-27. This equation has been reproduced from equation 11 in the main document:

$$\left(\frac{\int_{\varepsilon_1}\sigma_1 d\varepsilon_1}{\int_{\varepsilon_1^u}\sigma_1 d\varepsilon_1}\right)^{m_1}+\left(\frac{\int_{\varepsilon_2}\sigma_2 d\varepsilon_2}{\int_{\varepsilon_2^u}\sigma_2 d\varepsilon_2}\right)^{m_2}+\left(\frac{\int_{\varepsilon_6}\sigma_6 d\varepsilon_6}{\int_{\varepsilon_6^u}\sigma_6 d\varepsilon_6}\right)^{m_6}=1 \qquad \text{(A-27)}$$

To implement this failure criterion into the modified MAT54 material model, several new user input parameters are required to define the ultimate strain energy values of the material, as measured by material coupon experiment, as well as the three shape functions—m_1, m_2, and m_6. Altogether, eight new user inputs are implemented, as listed in table A-2.

Table A-2. New modified MAT54 user input parameters added for Wolfe's strain energy failure criterion

SEFT	Ultimate axial (fiber) tensile strain energy component
SEFC	Ultimate axial (fiber) compressive strain energy component
SEMT	Ultimate transverse (matrix) tensile strain energy component
SEMC	Ultimate transverse (matrix) compressive strain energy component
SES	Ultimate shear strain energy component
M1	Shape function value for the axial strain energy component
M2	Shape function value for the transverse strain energy component
M6	Shape function value for the shear strain energy component

For the strain energy failure criterion, code is added into MAT54, which computes the updated strain energy components of the element using the updated strain components and trial stresses, as follows:

```
einc1(i)=(strn1(i)+d1(i))*stg1(i)
einc2(i)=(strn2(i)+d2(i))*stg2(i)
einc4(i)=(strn4(i)+d4(i))*stg4(i)
```

This operation is performed after the trial stresses stg1(i), stg2(i), and stg4(i) have been computed (lines 109–111). Because both tensile and compressive ultimate strain energies are defined, the Wolfe failure criterion is dependent on the sign of the element stresses. During the computation of the Hashin failure criteria (lines 116–133), IF statements segregate operations depending on the sign of the element stresses to treat tensile and compressive failure modes individually. This existing code is used to assign the appropriate ultimate strain energy values as tensile or compressive, which are later used in the Wolfe criterion. In the following code from the Hashin failure criteria, new lines of code (identified by ADD) create the variable sef(i), which holds the value of the one-direction ultimate strain energy, and sem(i), which holds the value of the two-direction ultimate strain energy, as follows:

```
116   if (stg1(i).gt.0.) then
117    ef2(i)=qq2(i)*(xt2fbrt+(xt2-xt2fbrt)*ed(i))*
118  .      max(0.0,stg1(i))**2+beta*sg44(i)-1.0
119    ec2(i)=-1.
ADD    sef(i)=seft
120   else
121    ef2(i)=-1.
122    xc2(i) = ed(i)*xc + (1.0-ed(i))*ycfac*yc
123    xc2(i) = 1/(xc2(i)*xc2(i))
124    ec2(i)= qq2(i)*xc2(i)* min(0.0,stg1(i))**2-1.0
ADD    sef(i)=sefc
125   endif
126   if (stg2(i).gt.0.) then
127    em2(i)=qq2(i)*yt2* max(0.0,stg2(i))**2+sg44(i)-1.0
128    ed2(i)=-1.
ADD    sem(i)=semt
129   else
130    em2(i)=-1.
131    ed2(i)=qq2(i)*sd2* min(0.0,stg2(i))**2+
132  1    mlt2*stg2(i)/qq1(i)+sg44(i)-1.0
ADD    sem(i)=semc
133   endif
```

This added code allows for the computation of the Wolfe failure criterion after the Hashin failure criteria, as follows:

```
      ew(i)=(einc1(i)/sef(i))**m1+(einc2(i)/sem(i))**m2+
     1    (einc4(i)/ses)**m6
```

In this code, the ew(i) term acts as a history variable, which stores the value of the calculated Wolfe criterion. If this variable exceeds a value of 1, the element is marked for deletion using efail(i) as follows:

```
if (ew(i).eq.1. .or. ew(i).gt.1.) then
  efail(i)=0.0
endif
```

With this additional code, the Wolfe failure criterion is enacted along with the existing Hashin failure criteria. Alternatively, the Wolfe failure criterion is also implemented so that it is only active at the crush front where premature failure predictions may be beneficial to the material model. An IF statement is added to the source code calculation of the Wolfe criterion so it is only active for the crush front elements as follows:

```
if (qq1(i).ne.1.0) then
  ew(i)=(einc1(i)/sef(i))**m1+(einc2(i)/sem(i))**m2+
1    (einc4(i)/ses)**m6
else
  ew(i)=0.0
endif
```

Recall that the qq1(i) parameter acts as a flag for crush front elements. Simulations of the sinusoid crush element are rerun employing the Wolfe criterion only at the crush front, while setting SOFT to a value of 0.999 to prevent material softening at the crush front.

A.3.3 Post-Failure Degradation

Three new user input parameters are defined to implement the post-failure degradation modifications (see table A-3). The STROPT parameter is simply for convenience so the user may choose which post-failure degradation option to implement while the NDGRAD and SIGLIM parameters influence the shape of the stress degradation curve for options 2 and 3.

Table A-3. Summary of new user input parameters introduced for the post-failure degradation options in the modified MAT54

STROPT	Specifies which stress degradation option to use: 0: Regular MAT54 behavior (no modification) 1: Zero stress after failure 2: Linear stress degradation after failure 3: Linear degradation followed by constant stress 4: Logarithmic stress decay after failure
NDGRAD	Number of degradation iterations following failure for STROPT = 2, 3; determines the slope of the linear decay
SIGLIM	Percentage of maximum stress allowed during plastic deformation for STROPT = 3

The approach adopted to implement the first stress degradation option is to delete an element if any of its four failure criteria are violated. This achieves the zero stress state result desired for STROPT = 1. Element deletion is governed by the efail(i) variable, and new code is added following the initial assignment of this variable (lines 145–168). The new code is bounded by an IF statement so that it is only implemented if STROPT is set by the user to a value of 1. Subsequent IF statements within this first statement use the failure criteria history variables ef(i), ec(i), em(i), and ed(i) to set efail(i) to a value of zero in case any of the failure criteria have been violated. This is the only additional code necessary to implement the first stress degradation option as follows:

```
if (stropt.eq.1.) then
 if (ef(i).lt.1.e-8) efail(i)= 0.0
 if (ec(i).lt.1.e-8) efail(i)= 0.0
 if (em(i).lt.1.e-8) efail(i)= 0.0
 if (ed(i).lt.1.e-8) efail(i)= 0.0
endif
```

The remaining stress degradation options require significantly more code to be added to implement different types of stress decays following failure. First, several new Fortran variables need to be defined and assigned values before the stress degradation code can be implemented. For stress degradation options, STROPT = 2 and 3, and the slope of the linear stress decay is governed by the user input parameter NDGRAD, which defines the number of iterations during which the decay should occur. The degradation therefore requires that the maximum stress experienced at failure must be a known value. The maximum stress at failure is known only when failure occurs, and must be saved at this instance before it is overwritten during the next iteration. The following code is added to save the failure stresses immediately following the calculation of the failure criteria (lines 116–133) and before the assignment of failure flags iflagf, iflagc, iflagm, and iflagd (lines 134–137).

```
if (iflagf.ne.1 .and. ef2(i).gt.0) then
  sigff(i)=stg1(i)
endif
if (iflagc.ne.1 .and. ec2(i).gt.0) then
  sigfc(i)=stg1(i)
endif
if (iflagm.ne.1 .and. em2(i).gt.0) then
  sigfm(i)=stg2(i)
endif
if (iflagd.ne.1 .and. ed2(i).gt.0) then
  sigfd(i)=stg2(i)
endif
```

These if statements are valid only during the iteration that failure has occurred, between when failure is determined (ef2(i), ec2(i), em2(i), or ed2(i) is greater than zero) and when the failure flag is marked (iflagf, iflagc, iflagm, or iflagd equals 1). The failure stress variables sigff(i), sigfc(i), sigfm(i), and sigfd(i) can therefore only be written once to be equal to the one-direction or two-direction stress of the element, as dictated by the failure mode.

The amount by which the stress is degraded per iteration is 1/NDGRAD, defined in the code to be the new variable "dndg," multiplied by the maximum stress experienced at failure. A counter variable is used so stress degradation continues only for the indicated number of iterations, NDGRAD, before allowing the stress to go to zero via element deletion. There are two such counter variables, dmgkf(i) and dmgkm(i), which are unique for the fiber and matrix failure modes so stress degradation may occur independently in the one- and two-directions. For each iteration, the counter is raised by the discrete value dndg such that when the counter reaches the final value of 1, the stress is zero. For STROPT = 2, a degradation iteration limit variable "dlim" is defined to be the value of the counter one iteration prior to reaching a value of one. For example, if the number of iterations were to be 1,000, the dndg would equal 0.001, and dlim would take the value of 0.999. For STROPT = 3, the iteration limit variable "dlim2" is defined in a slightly different manner so that the degradation iterations are limited when the stress has been degraded to the user-specified plastic deformation stress. If NDGRAD were to be 1,000 and SIGLIM were 0.2 (20% of maximum stress), then dlim2 would be calculated to be 0.799. The code that adds these new Fortran variables is defined during the initial variable declarations and basic constant operations (lines 31–38) as follows:

```
dndg=1./ndgrad
dlim=1.0-dndg
dlim2=dlim-siglim
```

The bulk of the new code is inserted in place of the stress component updates at the end of the MAT54 subroutine (lines 249–253). For the STROPT = 0 and 1 options, the default MAT54 stress update code is unchanged. For the STROPT = 2, 3, and 4 options, the stress is degraded if there is failure, or updated using the normal MAT54 stress update code if there is no failure. Stress degradation depends on the failure mode experienced, as only the failed stress components are degraded. In the case of fiber failure, the one-direction stress sig1(i) is degraded, while in the case of matrix failure, both the two-direction and shear stresses, sig2(i) and sig4(i), are degraded. A flow chart outlining the Fortran code added to the stress update routine for the stress degradation options is shown in figure A-6. Each junction in figure A-6 represents an if statement within the Fortran code. For instance, the first if statement runs the normal MAT54 stress update code (lines 251–253) in the cases where STROPT = 0 or 1, as follows:

```
ADD   if (stropt.eq.0. .or. stropt.eq.1.) then
251    sig1(i)=sig1(i)+c11(i)*d1(i)+c12(i)*d2(i)
252    sig2(i)=sig2(i)+c12(i)*d1(i)+c22(i)*d2(i)
253    sig4(i)=sig4(i)+c44(i)*d4(i)
ADD   endif
```

Subsequent if statements at the initial level of the flow chart separate each of the remaining stress degradation options: STROPT = 2, 3, and 4.

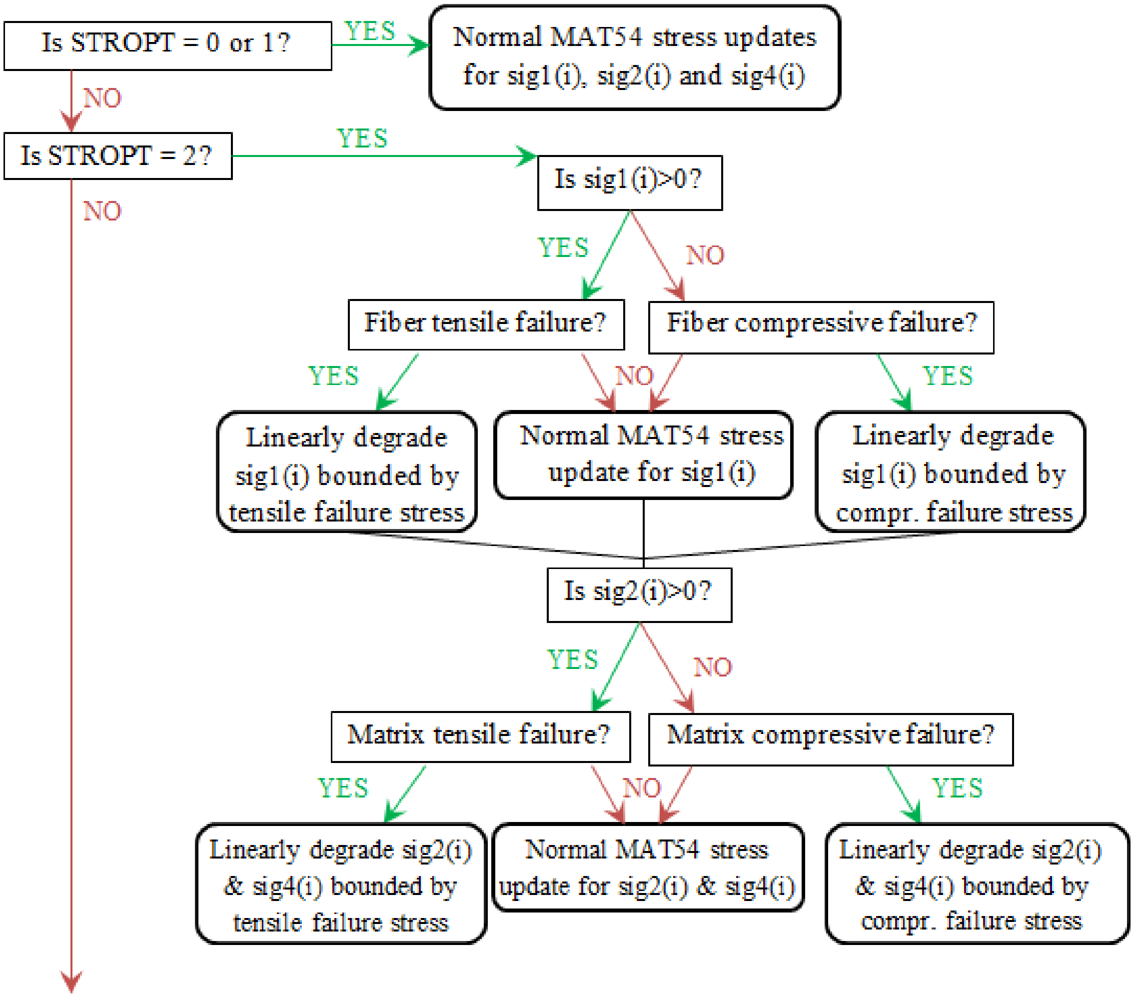

Continued on next page...

Figure A-6. Flow chart outlining Fortran code written for post-failure stress degradation options, added to the MAT54 source code during stress updates at the end of the subroutine

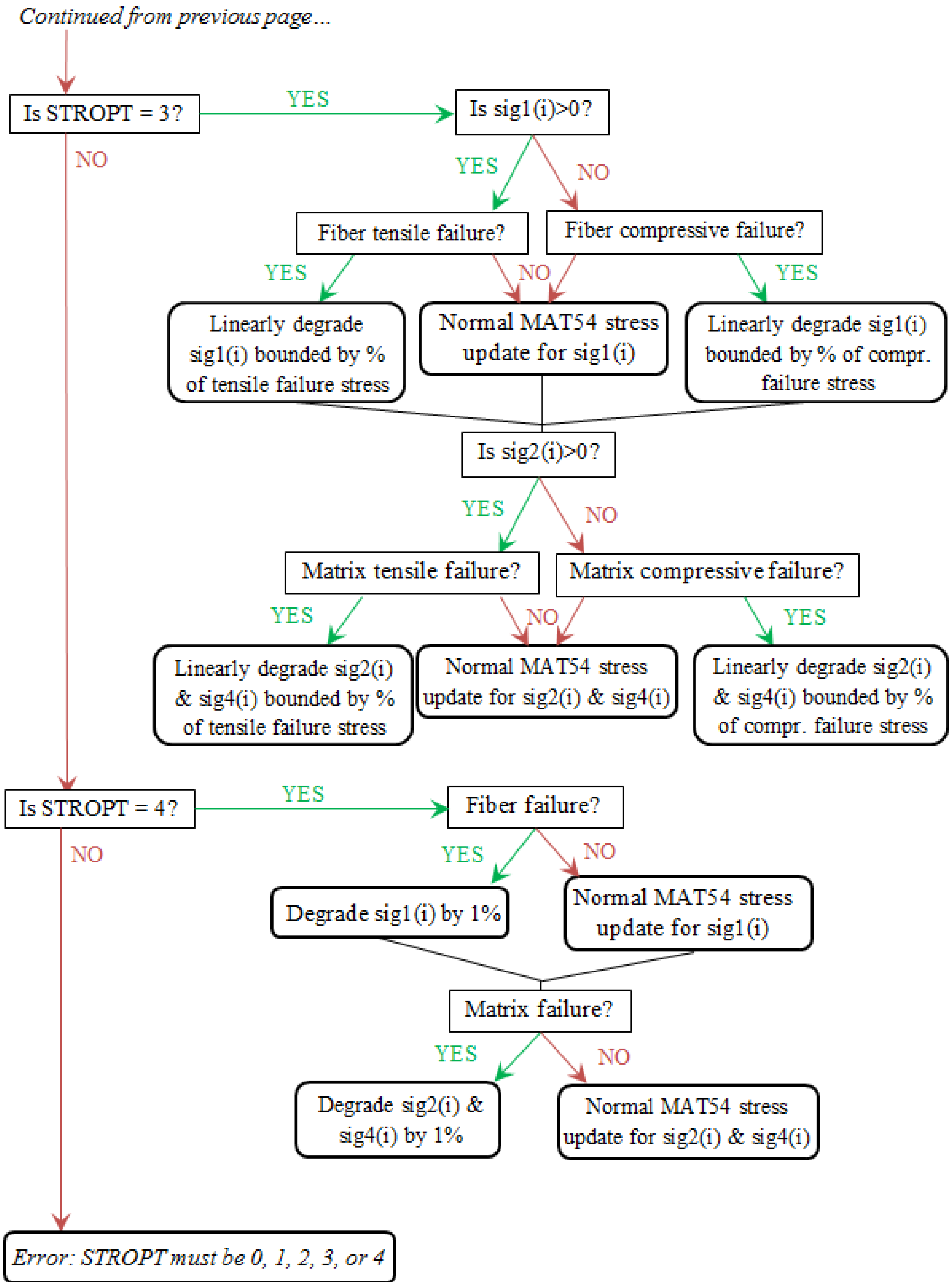

Figure A-6. Flow chart outlining Fortran code written for post-failure stress degradation options, added to the MAT54 source code during stress updates at the end of the subroutine (continued)

After line 253, the code for the STROPT = 2 tensile fiber failure mode stress degradation is added in the stress update section of the MAT54 subroutine, as shown below. The first IF statement establishes the user input parameter STROPT and has a value of 2; the second IF statement establishes that the one-direction component of the element stress is in the tensile mode. There is an ELSE statement at the end of this bundle of code that addresses the compressive mode of the one-direction stress. The third IF statement checks for tensile fiber mode failure, in which case the stress degradation is performed.

```
if (stropt.eq.2.) then
  if (sig1(i).gt.0.) then
  if (ef(i).lt.1.e-8) then
   if (dmgkf(i).lt.dlim) then
    sig1(i)=sig1(i)-(dndg*sigff(i))
    dmgkf(i)=dmgkf(i)+dndg
   else
    sig1(i)= 0.0
    sig2(i)= 0.0
    sig4(i)= 0.0
   endif
  else
   sig1(i)=sig1(i)+c11(i)*d1(i)+c12(i)*d2(i)
   dmgkf(i)= 0.0
  endif
 else
```

In the first run of the code, it is assumed that no failure occurs. When no fiber tensile failure has occurred, the ELSE condition of the third IF statement is valid, and the one-direction stress is updated by the normal MAT54 code (see line 250). The counter variable dmgkf(i) is initialized to a zero value. When failure occurs, the third IF statement is valid, and the fourth IF statement, which immediately follows, checks that the counter variable dmgkf(i) has not surpassed the iteration limit dlim. The one-direction stress is degraded by an amount specified by dndg*sigff(i), and the counter is increased by a value of dndg. Once the counter achieves its limiting value dlim, the 1-, 2-, and 4-components of stress are set to zero. The element cannot be deleted here (efail(i) = 0) because the element deletion subroutine has already been run earlier in the code. Instead, additional code is added following the initial assignment of efail(i) (lines 145–168) so that the element is deleted on the next iteration. In this way, the stresses are set to zero one iteration prior to the full amount specified by the user input parameter NDGRAD, such that the element is deleted upon the following iteration as specified by the user. The element deletion code added for STROPT = 2 is as follows:

```
 if (stropt.eq.2.) then
  if (ef(i).lt.1.e-8) then
    if (sig1(i).lt.dndg*sigff(i)) efail(i)= 0.0
  endif
  if (ec(i).lt.1.e-8) then
    if (sig1(i).gt.dndg*sigfc(i)) efail(i)= 0.0
  endif
  if (em(i).lt.1.e-8) then
    if (sig2(i).lt.dndg*sigfm(i)) efail(i)= 0.0
  endif
  if (ed(i).lt.1.e-8) then
    if (sig2(i).gt.dndg*sigfd(i)) efail(i)= 0.0
  endif
 endif
```

The meaning of this code is that if any of the modes of failure are violated, and the relevant component of stress is less than the degraded stress interval (as defined by dndg multiplied by the failure stress), the element is marked for deletion.

The added code for the STROPT = 2 compressive fiber stress degradation mode is in essence the same as the tensile fiber mode, as follows:

```
  else
   if (ec(i).lt.1.e-8) then
    if (dmgkf(i).lt.dlim) then
     sig1(i)=sig1(i)-(dndg*sigfc(i))
     dmgkf(i)=dmgkf(i)+dndg
    else
     sig1(i)= 0.0
     sig2(i)= 0.0
     sig4(i)= 0.0
    endif
   else
    sig1(i)=sig1(i)+c11(i)*d1(i)+c12(i)*d2(i)
    dmgkf(i)= 0.0
   endif
  endif
```

Similarly, the added code for the STROPT = 2 tensile and compressive matrix degradation modes are the same as the fiber modes, except that the shear stress component of the element is also degraded or updated as follows in the matrix tensile mode portion of the code:

```
 if (sig2(i).gt.0.) then
  if (em(i).lt.1.e-8) then
   if (dmgkm(i).lt.dlim) then
    sig2(i)=sig2(i)-(dndg*sigfm(i))
    sig4(i)=sig4(i)-(dndg*sigfs(i))
    dmgkm(i)=dmgkm(i)+dndg
   else
    sig1(i)= 0.0
    sig2(i)= 0.0
    sig4(i)= 0.0
   endif
  else
   sig2(i)=sig2(i)+c12(i)*d1(i)+c22(i)*d2(i)
   sig4(i)=sig4(i)+c44(i)*d4(i)
   dmgkm(i)= 0.0
  endif
else
```

The added code for STROPT = 3 is very similar to that added for STROPT = 2, with a few exceptions. First, the iteration limit parameter used is dlim2 rather than dlim, and the stresses are not set to zero once this limit is achieved. Instead, if the limit is achieved, then the stress is forced to remain at the limiting value, as defined by SIGLIM multiplied by the failure stress. For the sake of brevity, only the tensile fiber mode code is given below:

```
if (stropt.eq.3.) then
 if (sig1(i).gt.0.) then
  if (ef(i).lt.1.e-8) then
   if (dmgkf(i).lt.dlim2) then
    sig1(i)=sig1(i)-(dndg*sigff(i))
    dmgkf(i)=dmgkf(i)+dndg
   else
    sig1(i)=siglim*sigff(i)
    dmgkf(i)= 1.0
   endif
  else
   sig1(i)=sig1(i)+c11(i)*d1(i)+c12(i)*d2(i)
   dmgkf(i)= 0.0
  endif
 else
```

For the STROPT = 3 stress degradation option, the element is not deleted because of the degradation; rather it is deleted when the element achieves the maximum strain limits just as the normal deletion mechanism of the default MAT54 material model. Therefore, no additional code is necessary to address element deletion for this stress-degradation option.

Finally, for the STROPT = 4 stress-degradation option, the stress update code is modified so the appropriate stress components are degraded by 1% of their current value, each iteration to achieve a logarithmic-like degradation after failure. While the linear stress degradation options relied upon the value of the maximum stress saved at the specific failure mode experienced, this degradation option does not require this value and, therefore, is not dependent on tensile or compressive modes of failure. Only the fiber and matrix modes are considered separately to degrade the appropriate stress components for this stress degradation option, as follows:

```
 if (stropt.eq.4.) then
  if (ef(i).lt.1.e-8 .or. ec(i).lt.1.e-8) then
   sig1(i)= 0.99 *sig1(i)
  else
   sig1(i)=sig1(i)+c11(i)*d1(i)+c12(i)*d2(i)
  endif
  if (em(i).lt.1.e-8 .or. ed(i).lt.1.e-8) then
   sig2(i)= 0.99 *sig2(i)
   sig4(i)= 0.99 *sig4(i)
  else
   sig2(i)=sig2(i)+c12(i)*d1(i)+c22(i)*d2(i)
   sig4(i)=sig4(i)+c44(i)*d4(i)
  endif
endif
```

To isolate the post-failure stress degradation schemes and make them applicable for crush-front only (figure 96(a) of the main document) or all other elements only (figure 96(b) of the main document), IF statements are added that make use of the crush-front flag Fortran variable qq1 (equation 40). The code added to implement the STROPT = 1 option is bounded by a new IF statement, which reads:

```
if (qq1.ne.1.) then
```

in the case of crush-front only degradation (figure 96(a) of the main document), and

```
if (qq1.eq.1.) then
```

in the case of all other elements only (figure 96(b) of the main document). These statements apply the STROPT = 1 stress degradation scheme to elements based on their qq1 value, which equals 1 only for all elements except those at the crush-front.

Similar treatment is given to the bundle of code, which implements the STROPT = 2, 3, and 4 degradation options. A single IF condition is added prior to this bundle of code, which for the case of crush-front only degradation (figure 96(a) of the main document) is:

```
if (qq1.eq.1.) then
  sig1(i)=sig1(i)+c11(i)*d1(i)+c12(i)*d2(i)
  sig2(i)=sig2(i)+c12(i)*d1(i)+c22(i)*d2(i)
  sig4(i)=sig4(i)+c44(i)*d4(i)
else
```

and for the case of the degradation of all other elements only (figure 96(b) of the main document) is:

```
if (qq1.ne.1.) then
  sig1(i)=sig1(i)+c11(i)*d1(i)+c12(i)*d2(i)
  sig2(i)=sig2(i)+c12(i)*d1(i)+c22(i)*d2(i)
  sig4(i)=sig4(i)+c44(i)*d4(i)
else
```

These statements impose the regular MAT54 stress updates to elements based on their qq1 value, but regardless of their failure state, like the default MAT54. This causes the perfectly plastic behavior for the specified elements. Following this IF statement is the else condition of the qq1 value, which contains all the new code for implementing the stress degradations based on the failure state of the element. For the transverse-only degradation version, the one-direction stress degradation code based on the ef(i) and ec(i) failure states is simply commented out such that the sig1(i) value is plastically deformed as in the case of the default MAT54. This concludes the new code added for the implementation of the four new post-failure stress degradation options in the modified MAT54.

A.1 REFERENCE

A-1 Erhart, T., “An Overview of User Defined Interfaces in LS-DYNA,” in 8th European LS-DYNA Conference, Strasburg, Germany, May 2011.

APPENDIX B—KEYWORD INPUT FILE FOR FABRIC CORRUGATED CRUSH

```
*KEYWORD
$---+----1----+----2----+----3----+----4----+----5----+----6----+----7----+----8
*TITLE
Fabric sinusoid crush
$---+----1----+----2----+----3----+----4----+----5----+----6----+----7----+----8
*CONTROL_SHELL
$ wrpang  esort  irnxx  istupd  theory   bwc  miter   proj
   0.0    0    -1    0    2    2    1    0
$ rotascl  intgrd  lamsht  cstyp6  tshell  nfail1  nfail4 psnfail
   0.0    1    0    1
$ psstupd  irquad

*CONTROL_TERMINATION
$ endtim  endcyc  dtmin  endeng  endmas
  0.010
*CONTROL_TIMESTEP
$  dtint  tssfac
   0.0   0.9
$---+----1----+----2----+----3----+----4----+----5----+----6----+----7----+----8
*DATABASE_SPCFORC
$   dt  binary   lcur  ioopt
 .10000E-4    1    0    0
*DATABASE_BINARY_D3PLOT
$ dt/cycl   lcdt   beam  npltc
 .1000E-2    0    0   100
$  ioopt
    0
*DATABASE_EXTENT_BINARY
$  neiph  neips  maxint  strflg  sigflg  epsflg  rltflg  engflg
    0    16    8    1    1    1    1    1
$ cmpflg  ieverp  beamip  dcomp   shge  stssz  n3thdt ialemat
    1
$ nintsld pkp_sen   sclp  blank  msscl  therm

$---+----1----+----2----+----3----+----4----+----5----+----6----+----7----+----8
*PART
Loading Plate
$   pid  secid   mid  eosid   hgid   grav  adpopt   tmid
    19    9    9
*PART
Sinusoid
    1    1    1
*PART
Trigger
    2    2    1
$---+----1----+----2----+----3----+----4----+----5----+----6----+----7----+----8
*SECTION_SHELL_TITLE
Loading Plate
$  secid  elform   shrf   nip  propt qr/irid  icomp  setyp
    9    2  1.000  2.000   0.0   0.0    0    1
$   t1    t2    t3    t4   nloc  marea   idof  edgset
 0.30000 0.30000 0.30000 0.30000    -1
*SECTION_SHELL_TITLE
```

```
Sinusoid
$  secid  elform   shrf   nip  propt qr/irid  icomp  setyp
    1    16  1.000  8.000   0.0   0.0    1    1
$   t1    t2    t3    t4   nloc  marea   idof  edgset
 0.07286 0.07286 0.07286 0.07286    0
$   b1    b2    b3    b4    b5    b6    b7    b8
    0    0    0    0    0    0    0    0
*SECTION_SHELL_TITLE
Trigger
$  secid  elform   shrf   nip  propt qr/irid  icomp  setyp
    2    16  1.000  8.000   0.0   0.0    1    1
$   t1    t2    t3    t4   nloc  marea   idof  edgset
 0.05200 0.05200 0.05200 0.05200    0
$   b1    b2    b3    b4    b5    b6    b7    b8
    0    0    0    0    0    0    0    0
$---+----1----+----2----+----3----+----4----+----5----+----6----+----7----+----8
*MAT_RIGID_TITLE
Loading plate
$   mid    ro    e    pr    n  couple    m  alias
    9  21.180 .3000E+8 0.33000   0.0   0.0   0.0   0.0
$   cmo   con1   con2
  1.000    4    7
$   lco
   0.0
*MAT_ENHANCED_COMPOSITE_DAMAGE_TITLE
Composite
$   mid    ro     eb    ec   prba   prca   prcb
    1 .1500E-3 8110000. 7890000. 1000000. 0.04300   0.0   0.0
$   gab   gbc   gca    kf   aopt
 609000.0 609000.0 609000.0   0.0  3.000
$   xp    yp    zp    a1    a2    a3  mangle
   0.0   0.0   0.0   0.0   0.0   0.0  90.000
$   v1    v2    v3    d1    d2    d3  dfailm  dfails
   0.0   0.0  1.000   0.0   0.0   0.0 0.06000 0.03000
$  tfail   alph   soft   fbrt  ycfac  dfailt  dfailc   efs
 .11530E-8 0.10000 0.73000 0.50000  1.200 0.01640 -0.01300   0.0
$   xc    xt    yc    yt    sc   crit   beta
 103000.0 132000.0 102000.0 112000.0 19000.00  54.000 0.50000
$---+----1----+----2----+----3----+----4----+----5----+----6----+----7----+----8
*DAMPING_PART_STIFFNESS
$   pid   beta
    1 0.05000
*DAMPING_PART_STIFFNESS
$   pid   beta
    2 0.05000
$---+----1----+----2----+----3----+----4----+----5----+----6----+----7----+----8
*BOUNDARY_PRESCRIBED_MOTION_SET_ID
$   id
    1
$  nsid   dof   vad   lcid    sf   vid  death  birth
    5    3    2   123   0.0    0   0.0   0.0
*BOUNDARY_SPC_SET_ID
$   id
    1
$  nsid   cid   dofx   dofy   dofz  dofrx  dofry  dofrz
```

```
    2    0    1    1    1    0    0    0
$---+----1----+----2----+----3----+----4----+----5----+----6----+----7----+----8
*CONTACT_RIGID_NODES_TO_RIGID_BODY_ID
$   cid
    1
$  ssid   msid  sstyp  mstyp  sboxid  mboxid   spr   mpr
    1    19    2    3    0    0    0    0
$   fs    fd    dc    vc   vdc  penchk    bt    dt
 0.50000 0.50000   0.0   0.0   0.0    0   0.0 .1000E+21
$   sfs   sfm   sst   mst   sfst   sfmt   fsf   vsf
  1.000  1.000   0.0   0.0  1.000  1.000  1.000  1.000
$  lcid   fcm    us
    82    2   0.0
$  soft  sofscl  lcidab  maxpar  sbopt  depth  bsort  frcfrq
    0   0.0    0   0.0   0.0    0    0    0
$ penmax  thkopt  shlthk  snlog   isym  i2d3d  sldthk  sldstf
   0.0    0    0    0    0    0   0.0   0.0
$  igap  ignore  dprfac  dtstif  blank  blank  flangl
    1    0   0.0   0.0             0.0
$---+----1----+----2----+----3----+----4----+----5----+----6----+----7----+----8
*DEFINE_CURVE_TITLE
Loading
$  lcid   sidr   sfa   sfo   offa   offo  dattyp
   123    0  1.000  1.000   0.0   0.0    0
$  abscissa (time)  ordinate (value)
    0.000000E+00    0.000000E+00
    0.200000E-01   -0.300000E+01
*DEFINE_CURVE_TITLE
for Contact
$  lcid   sidr   sfa   sfo   offa   offo  dattyp
    82    0  1.000  1.000   0.0   0.0    0
$  abscissa (time)  ordinate (value)
    0.000000E+00    0.000000E+00
    0.100000E+00    0.250000E+02
    0.200000E+00    0.150000E+03
    0.300000E+00    0.750000E+03
$---+----1----+----2----+----3----+----4----+----5----+----6----+----7----+----8
*NODE
$  nid       x       y       z   tc   rc
   1 6.125742275E-17 0.000000000E+00 1.224606354E-16
...
$---+----1----+----2----+----3----+----4----+----5----+----6----+----7----+----8
*ELEMENT_SHELL
$  eid  pid   n1   n2   n3   n4
   1   1  183  185  178  179
...
$---+----1----+----2----+----3----+----4----+----5----+----6----+----7----+----8
*END
```